

# Simultaneous Broadband Vibration Suppression and Energy Harvesting Using a Magnetically Enhanced Piecewise-Linear Nonlinear Energy Sink

#### Haining Li

Department of Mechanical and Mechatronics Engineering

Lakehead University, Thunder Bay, Ontario

#### August 2025

A dissertation submitted in partial fulfillment of the requirements of the degree of Doctor of Philosophy in Mechanical Engineering

Supervisor: Dr. Kefu Liu

Department of Mechanical and Mechatronics Engineering

Co-supervisor: Dr. Jian Deng

Department of Civil Engineering, Lakehead University

Copyright © 2025 by Haining Li

#### **ABSTRACT**

Nonlinear energy sinks (NESs) offer significant potential for simultaneous broadband vibration suppression (VS) and energy harvesting (EH) through the use of an essentially nonlinear spring (ENS). However, realizing an ENS with minimal energy dissipation remains challenging. A piecewise-linear spring (PLS) provides a structurally simple and physically interpretable means to approximate nonlinear stiffness with little added friction. Yet, NESs employing a PLS often require a relatively high initial energy threshold to trigger targeted energy transfer (TET), resulting in reduced performance under low-level excitation. Magnetic springs can introduce bi-stable characteristics that enable snapthrough oscillations, thereby lowering the energy threshold. Existing studies, however, have focused primarily on ungrounded magnetic spring configurations, leaving the influence of a grounded magnetic spring (GMS) on NES's performance largely unexplored.

To address this gap, this research integrates a tunable GMS into a piecewise-linear NES (PLNES) to reduce the energy threshold, thereby facilitating TET activation and enhancing broadband VS and EH performance. Four interconnected studies are undertaken:

- 1. **Magnetic Spring Modelling** A tunable multi-stable piezoelectric energy harvester (PEH) is developed by combining a cantilever beam with an adjustable magnetic assembly capable of achieving mono-, bi-, and tri-stable states. Two magnetic restoring force models, based on the magnetic single-point and two-point dipole approaches, are formulated and optimized via a multi-population genetic algorithm. Parametric sensitivity analyses are conducted for the optimal models.
- 2. **Hybrid Multi-Stable Energy Harvesting** A multi-stable hybrid energy harvester (MSHEH), integrating a PEH and electromagnetic energy harvester (EMEH), is proposed and evaluated numerically and experimentally under various stability states. Optimal load resistances for balanced energy output across configurations are determined through optimization.

- 3. **PLS Design Methodology** A systematic approach for designing a PLS is developed, enabling close emulation of a desired ENS using a cantilever beam constrained by single- or double-stop blocks. The designed PLSs are validated against the target ENS through both simulation and experiment.
- 4. Magnetically Enhanced PLNES (MPLNES) A novel MPLNES is proposed by integrating a PLNES with a tunable GMS and a grounded EMEH. The GMS produces a position-dependent restoring force that shifts the NES's equilibrium, enabling easier activation of large-amplitude oscillations. Numerical and experimental results confirm that the MPLNES triggers TET at lower excitation levels than the corresponding PLNES. A two-objective optimization reveals that the MPLNES achieves superior trade-offs between VS and EH, sustaining energy transfer over a wider range of excitation levels compared with the two other NES designs.

## Keywords

Nonlinear energy sink; vibration suppression; energy harvesting; targeted energy transfer; essentially nonlinear spring; piecewise-linear spring; grounded magnetic spring; piezoelectric energy harvester; electromagnetic energy harvester; multi-stable dynamics.

### **Co-Authorship Statement**

This thesis has been prepared in accordance with the Integrated-Article format stipulated by the Faculty of Graduate Studies at Lakehead University. All external sources used for analysis or discussion have been appropriately cited. The co-authored components of this thesis are as follows:

# Chapter 2, Validation and Optimization of Two Models for the Magnetic Restoring Forces Using a Multi-stable Piezoelectric Energy Harvester

Haining Li, Kefu Liu, Jian Deng and Bing Li, has been published in *Journal of Intelligent Material and Systems and Structures*, 2023, 34(14), 1688-1701. DOI: 10.1177/1045389X221151064. Contributions of the Authors:

Haining Li: Conceptualization, mathematical modelling, analysis, simulation, result acquisition and validation, manuscript preparation including drafting and writing. Kefu Liu: Conceptualization, manuscript review and editing, supervision, and funding acquisition. Jian Deng: Manuscript review and editing, supervision, and funding acquisition. Bing Li: Manuscript review and editing.

#### Chapter 3, Modelling and Evaluation of a Multi-Stable Hybrid Energy Harvester.

Haining Li, Kefu Liu and Jian Deng, has been published in *Vibration*. 2024, 7(3), 662-686; <a href="https://doi.org/10.3390/vibration7030035">https://doi.org/10.3390/vibration7030035</a>. Contributions of the Authors:

Haining Li: Conceptualization, mathematical modelling, analysis, simulation, result acquisition and validation, and manuscript preparation including drafting and writing. Kefu Liu: Conceptualization, manuscript review and editing, supervision, and funding acquisition. Jian Deng: Conceptualization, manuscript review and supervision.

# Chapter 4, Using a Piecewise-Linear Spring to Approximate an Essentially Nonlinear Spring: Design and Validation.

Haining Li, Kefu Liu and Jian Deng, has been published in the Transactions of the Canadian Society for Mechanical Engineering. 2024, 49(2):192-206, DOI: 10.1139/tcsme-

2024-0163. Contributions of the Authors:

Haining Li: Conceptualization, mathematical modelling, analysis, simulation, result acquisition and validation, analysis, and manuscript preparation, drafting and writing. Kefu Liu: Conceptualization, manuscript review and editing, supervision, and funding acquisition. Jian Deng: Conceptualization, manuscript review and supervision.

## Chapter 5, A Magnetically Enhanced Piecewise-Linear Nonlinear Energy Sink: Transient Responses

Haining Li, Kefu Liu and Jian Deng, has been submitted to *Journal of Sound and Vibration*, June 2025. Contributions of the Authors:

Haining Li: Conceptualization, mathematical modelling, analysis, simulation, result acquisition and validation, and manuscript preparation including drafting and writing. Kefu Liu: Conceptualization, manuscript review and editing, supervision, and funding acquisition. Jian Deng: Conceptualization, manuscript review and supervision.

# Appendix A, A Grounded and Tunable Multi-Stable Nonlinear Energy Sink: Transient Responses

Haining Li, Kefu Liu and Jian Deng, the Proceedings of the *CSME International Congress* 2022, June 5-8, 2022, Edmonton, Canada. https://doi.org/10.7939/r3-d4rz-jr10. Contributions of the Authors:

Haining Li: Conceptualization, mathematical modelling, analysis, simulation, result acquisition and validation, and manuscript preparation including drafting and writing. Kefu Liu: Conceptualization, manuscript review and editing and supervision Jian Deng: Manuscript review and editing, supervision, and funding acquisition. Bing Li: Conceptualization, manuscript review and editing.

# Appendix B, Identification of the Restoring Force of a Grounded Nonlinear Energy Sink.

Haining Li, Kefu Liu and Jian Deng, the Proceedings of the *CSME International Congress* 2024, May 26-29, 2024, Toronto, Canada. Contributions of the Authors:

Haining Li: Conceptualization, mathematical modelling, analysis, simulation, result acquisition and validation, and manuscript preparation including drafting and writing. Kefu Liu: Conceptualization, manuscript review and editing, supervision and funding acquisition. Jian Deng: Conceptualization, manuscript review and supervision.

#### Appendix C, Design and Evaluation of Three Variant Nonlinear Energy Sinks.

Haining Li, Kefu Liu, Jian Deng, and Hui Long, was submitted as an abstract and presented as an oral presentation at the *6th International Conference on Vibration and Energy Harvesting Applications*, July 11-14, Hong Kong, China. Contributions of the Authors:

Haining Li: Conceptualization, mathematical modelling, analysis, simulation, result acquisition and validation, and manuscript preparation including drafting and writing. Kefu Liu: Conceptualization, mathematical modelling, manuscript review and editing, supervision and funding acquisition. Jian Deng: Conceptualization, manuscript review and supervision. Hui Long: Validation and manuscript review.

## Dedication

This work is dedicated to my wife, who stood by me through late nights, setbacks, and doubts. Her love and belief in me have been my greatest source of strength.

## Acknowledgment

First and foremost, my deepest and most heartfelt gratitude goes to my supervisor, Dr. Kefu Liu, for his generous and constant support. His expertise in vibration research, along with his unwavering commitment to academic excellence, has profoundly shaped my approach to research and has been instrumental in my development as a scholar. I consider myself truly fortunate to have had him as my supervisor throughout my doctoral journey. I am equally indebted to my co-supervisor, Dr. Jian Deng, whose encouragement and guidance gave me the courage to overcome the many challenges I encountered throughout my research journey. I would also like to extend my sincere appreciation to the coordinator of the PhD program, Dr. Wilson Wang, for his exceptional assistance and dedication. My gratitude further goes to the members of my doctoral thesis examination committee, Dr. Ahmed Elshaer (Civil Engineering) and Dr. Muhammad Khalid (Mechanical and Mechatronics Engineering), for their valuable feedback, constructive comments, and continuous support.

Secondly, I wish to express my appreciation to my colleagues in the Lab, Mr. Youzuo Jin, Mr. Zhangzhe, and Mr. Gairik Partha Banerjee. Learning and working together with them has been a source of inspiration, and their passion for engineering has continually motivated me to move forward. I am deeply thankful to my parents for their unconditional love, sacrifice, and confidence in me over the years. My heartfelt thanks also go to Ms. Ning Jiang, whose advice and support have been indispensable in helping me navigate the complexities of both my personal and professional life.

Finally, I would like to express my heartfelt gratitude to my wife, Zhenxuan Jia, for her love, understanding, and steadfast support throughout the most challenging moments of this journey. Her companionship and encouragement have been an enduring source of strength and comfort, helping me persevere and overcome difficulties. More importantly, her presence has made me a more responsible and complete person.

#### **List of Journal Publications**

- H. Li, K. Liu, J. Deng, B. Li, Validation and optimization of two models for the magnetic restoring forces using a multi-stable piezoelectric energy harvester. *Journal of Intelligent Material Systems and Structures*, 2023, 34(14): 1688-1701. <a href="https://doi.org/10.1177/1045389X221151064">https://doi.org/10.1177/1045389X221151064</a>.
- H. Li, K. Liu, J. Deng, A Tunable Multi-Stable Hybrid Energy Harvester. *Vibration* 2024, 7(3), 662-686; https://doi.org/10.3390/vibration7030035.
- H. Li, K. Liu, J. Deng, Using a Piecewise-Linear Spring to Approximate an Essentially Nonlinear Spring: Design and Validation. *The Transactions of the* Canadian Society for Mechanical Engineering, 2024, 49(2): 192-206. <a href="https://doi.org/10.1139/tcsme-2024-0163">https://doi.org/10.1139/tcsme-2024-0163</a>.
- H. Li, K. Liu, J. Deng, A Magnetically Enhanced Piecewise-Linear Nonlinear Energy Sink: Transient Responses. Submitted to *Journal of Sound and Vibration*, June 2025.

#### **List of Conference Publications**

- H. Li, K. Liu, J. Deng, B. Li, A Grounded and Tunable Multi-Stable Nonlinear Energy Sink: Transient Responses. the Proceedings of the *CSME International Congress* 2022, June 5-8, 2022, Edmonton, Canada. https://doi.org/10.7939/r3-d4rz-jr10.
- H. Li, K. Liu, J. Deng, B. Li, Identification of The Restoring Force of a Grounded Nonlinear Energy Sink. the Proceedings of the *CSME International Congress* 2024, May 26-29, Toronto, Canada.
- H. Li, K. Liu, E. Hamsayeh, L. Li, J. Xu, Development of Optimal Lumped-

Parameter Models for Torsional Vibration of Shafts. the Proceedings of the *CSME International Congress 2025*. May 25-28 Montreal, Canada.

## **Table of Contents**

ABSTRACT	I
KEYWORDS	III
CO-AUTHORSHIP STATEMENT	IV
DEDICATION	VII
ACKNOWLEDGMENT	VIII
LIST OF JOURNAL PUBLICATIONS	IX
LIST OF CONFERENCE PUBLICATIONS	IX
TABLE OF CONTENTS	XI
LIST OF FIGURES	XIV
LIST OF TABLE	XXII
LIST OF ACRONYMS	XXIV
CHAPTER 1. INTRODUCTION	1
CHAPTER 2. VALIDATION AND OPTIMIZATION OF TWO MODELS FOR THE MAGNETIC	
RESTORING FORCES USING A MULTI-STABLE PIEZOELECTRIC ENERGY HARVESTER.	23
2.1 Introduction	23
2.2 Apparatus	26
2.3 THE RESTORING FORCE OF THE SYSTEM	28
2.3.1 Equivalent Magnetic Point Dipole Model	29
2.3.2 Equivalent Magnetic 2-point Dipole Model	30
2.4 Experimental Validation	34
2.5 MODEL OPTIMIZATION	39
2.6 THE PARAMETRIC SENSITIVITY STUDY AND STABILITY STATE REGION	46
2.7 CONCLUSIONS	49
References	50
CHAPTER 3 MODELLING AND EVALUATION OF A MULTI-STABLE HYBRID ENERGY	
HARVESTER	55
2.1 Interoprection	55

3.2 APPARATUS AND MODELLING	58
3.3 DETERMINATION OF THE EMEH'S TRANSDUCTION FACTOR	62
3.4 DETERMINATION OF THE NONLINEAR RESTORING FORCE	70
3.5 EVALUATION OF THE PERFORMANCES OF THE MSHEH	75
3.5.1 High-level Acceleration	76
3.5.2 Low-level Acceleration	81
3.6 PARETO FRONT OPTIMIZATION	83
3.7 Conclusions	89
References	91
CHAPTER 4. USING A PIECEWISE LINEAR SPRING TO APPROXIMATE AN ESSENTIAL	LLY
NONLINEAR SPRING: DESIGN AND VALIDATION	95
4.1 Introduction	95
4.2 Design Procedure	98
4.3 NUMERICAL SIMULATIONS	103
4.4 Experimental Validation	107
4.4.1 Static Experimental Test	108
4.4.2 Dynamic Experimental Test	109
4.5 Conclusions	115
APPENDIX 4A. FIXED BEAM WITH AN OVERHANG	116
References	120
CHAPTER 5. A MAGNETICALLY ENHANCED PIECEWISE-LINEAR NONLINEAR ENERG	GY SINK:
TRANSIENT RESPONSES	124
5.1 Introduction	124
5.2 MPLNES AND MODELLING	129
5.2.1 MPLNES	129
5.2.2 Design of the PLS and GMS	133
5.2.3 Determination of the Transduction Factor	139
5.3 NUMERICAL SIMULATION	143
5.3.1 Transient performances	144
5.3.2 Nonlinear Normal Mode (NNM) Analysis	148
5.4 VS AND EH TRADE-OFF STUDY	156
5.5 EXPERIMENTAL VERIFICATION	162
5.6 CONCLUSIONS	168
APPENDIX 5C. DETERMINATION OF THE EMELL'S TRANSPURSTION EASTER BY COMSOL	171

CHAPTER 6 CONCLUSIONS AND FUTURE WORKS	177
6.1 Conclusions	177
6.2 RECOMMENDATIONS FOR FUTURE WORK	179
APPENDICES	181
APPENDIX A. A GROUNDED AND TUNABLE MULTI-STABLE NONLINEAR ENERGY SINK: TRANS	IENT
RESPONSES	181
A.1 Introduction	181
A.2 The Apparatus and Electromechanical Model	183
A.3 Numerical Simulation	189
A.4 Conclusions	196
References	197
APPENDIX B. IDENTIFICATION OF THE RESTORING FORCE OF A GROUNDED NONLINEAR ENERG	SY SINK 199
B.1 Introduction	199
B.2 Apparatus and Modelling	200
B.3 Fundamental of the linear regression method	206
B.4 Application of the linear regression method	207
B.5 Conclusions	214
References	214
APPENDIX C. DESIGN AND EVALUATION OF THREE VARIANT NONLINEAR ENERGY SINKS	217
Abstract	217

# **List of Figures**

Figure 1.1 A primary system attached with a TMD
Figure 1.2 Two types of NES: (a) a primary system attached with an ungrounded NES;
(b) a primary system attached with a grounded NES4
Figure 1.3 The frequency responses of the primary mass without TMD, with TMD and
with NES.
Figure 1.4 Transient performance $Dc$ verse $fp$ and $V$ : (a) TMD configuration; (b) NES
configuration7
Figure 1.5 Illustration of achieving ENS through mechanical springs: (a) the apparatus;
(b) the design of ENS [16]9
Figure 1.6 Illustration of EMEH: (a) a schematic of EMEH [27]; (b) a lumped-
parameter model of EMEH11
Figure 1.7 Illustration of PEH: (a) a cantilevered PEH [31]; (b) the lumped-parameter
model of the PEH
Figure 1.8 Power dissipated by one of the eight oil-based viscous dampers in the TMD
of Taipei 101 building under wind-induced vibration [33]14
Figure 2.1 Schematic of the apparatus.
Figure 2.2 Spatial positions of the magnets
Figure 2.3 Front view of the apparatus
Figure 2.4 Top view of the apparatus
Figure 2.5 Top view of positions of magnets of the apparatus: (a) magnet B and D; (b)
magnet A and D
Figure 2.6 (a) Photo of the experimental setup; (b) detail of the beam; (c) schematic of
the equivalent lumped parameter model for the experimental setup 36
Figure 2.7 The total restoring forces of: (a) Case (1); (b) Case (2); (c) Case (3); (d) Case
(4)38
Figure 2.8 The flowchart of the MPGA
Figure 2.9 The total restoring forces for: (a) Case (1); (b) Case (2); (c) Case (3); (d)

Case (4) based on the optimized models
Figure 2.10 The total restoring forces for: (a) Case (1); (b) Case (2); (c) Case (3); (d
Case (4) based on the optimized 2 <sup>nd</sup> models with six and five independen
parameters4:
Figure 2.11 The total restoring forces of the optimized and perturbated 1st model for
(a) Case (5); (b) Case (6); (c) Case (7)
Figure 2.12 The total restoring forces of the optimized and perturbated 2 <sup>nd</sup> model for
(a) Case (5); (b) Case (6); (c) Case (7)48
Figure 2.13 Stability state region.
Figure 3.1 (a) Schematic of the MSHEH; Spatial positions of: (b) coils and magnets A
and C; (c) magnets A, B, C and D.
Figure 3.2 Two-dimensional views of the beam and magnets: (a) front view; (b) side
view60
Figure 3.3 Lumped parameter model of the system.
Figure 3.4 Illustration of coils' positions and slicing strategy.
Figure 3.5 Comsol model used to determine Kti: (a) isometric view; (b) front view. 64
Figure 3.6 Magnetic flux distributions of magnets B and C at the different positions: (a
x = -0.0353  m; (b) $x = 0  m$ ; (c) $x = 0.0353  m$
Figure 3.7 Transduction factors of the coils: (a) coil 1, coil 2 and coil 3; (b) coil 4, coi
5 and coil 6; (c) total transduction factor.
Figure 3.8 Experimental setup for verification of transduction factors of coils: (a) the
overview; (b) the detail of the area within the red rectangle in (a)68
Figure 3.9 Illustration of (a) the verification experimental setup. (b) the open circuit
voltage of the coil and the velocity of the magnet.
Figure 3.10 Experimental results of the transduction factors: (a) coil 1; (b) coil 2; (c
coil 4; (d) coil 5
Figure 3.11 Illustration of the equivalent magnetic 2-point dipole model: (a) magnet
A and D; (b) magnets B and D.
Figure 3.12 The total restoring forces: (a) Case (I); (b) Case (II); (c) Case (III); (d) Case
(IV); (e) Case ( \( \)

Figure 3.13	(a) Potential energies of the five cases. (b) Stability state region75
Figure 3.14	Potential energies: (a) varying $d$ and fixing $h$ at 0.002 m; (b) varying $h$ and
	fixing d at 0.035 m
Figure 3.15	The simulation results of the instant power outputs under the frequency up-
	sweep excitation with $A=1.6$ m/s2: (a) the EMEH's; (b) the PEH's77
Figure 3.16	Photos of the experimental setup: (a) the entire system; (b) the EMEH78
Figure 3.17	The experimental results of the instant power outputs under the frequency
	up-sweep excitation with $A = 1.6$ m/s2: (a) the EMEH's; (b) the PEH's.79
Figure 3.18	3 The simulation results of the instant power outputs under the frequency
	down-sweep excitation with $A=1.6$ m/s2: (a) the EMEH's; (b) the PEH's.
	79
Figure 3.19	The experimental results of the instant power outputs under the frequency
	down-sweep excitation $A=1.6$ m/s2: a the EMEH's; b the PEH's80
Figure 3.20	The accumulated harvested energy of the MSHEH under the high-level
	excitation: (a) frequency up-sweep excitation; (b) frequency down-sweep
	excitation81
Figure 3.21	The accumulated harvested energy of the MSHEH under the low-level
	excitation: (a) frequency up-sweep excitation; (b) frequency down-sweep
	excitation82
Figure 3.22	The best Pareto fronts: (a) the linear system excited at 5 Hz; (b) the mono-
	stable system excited at 3 Hz; (c) the bi-stable system excited at 3.5 Hz; (d)
	the tri-stable system excited at 3 Hz85
Figure 3.23	3 The best Pareto fronts of the system under the high-level frequency up-
	sweep excitation: (a) the linear configuration; (b) the mono-stable
	configuration; (c) the bi-stable configuration; (d) the tri-stable
	configuration88
Figure 3.24	The total accumulated harvested energy of the MSHEH under the high-
	level frequency up-sweep excitation89
Figure 4.1(	(a) CAD drawing of the proposed apparatus; (b) schematic of the system
	model99

Figure 4.2 Configurations of the PLSs: (a) with single-stop blocks; (b) with double-stop
blocks
Figure 4.3 Comparison of the restoring forces of the ENS and the optimum PLS10
Figure 4.4 Comparison of the potential energies of the three springs10
Figure 4.5 Simulation results, free response (left) and its WT spectrum (right): (a) (b
with the ENS; (c) (d) with the PLS of single-stop blocks; (e) (f) with the
PLS of double-stop blocks
Figure 4.6 Photo of the static experimental setup
Figure 4.7 Experimental results of the restoring force of PLSs: (a) with single-sto-
blocks; (b) with double-stop blocks
Figure 4.8(a) Photo of the experimental setup for the dynamic experimental test; (b
schematic of the model for the experimental setup
Figure 4.9 Experimental results of the restoring force of PLSs with $z_m = 0.02$ m: (a
with single-stop blocks; (b) with double-stop blocks
Figure 4.10 Experimental results for the free response and corresponding IF of PLS
with $z_m = 0.02$ m: (a) (b) with single-stop blocks; (c) (d) with double-stop
blocks.
Figure 4.11 Experimental results of the restoring force of PLSs with $z_m = 0.01$ m: (a
with single-stop blocks; (b) with double-stop blocks through the restoring
force surface method.
Figure 4.12 Experimental results for time history of the free response with $z\theta = 0.01$ m
and corresponding instantaneous frequency of PLSs (a) with single-stop
blocks; (b) with double-stop blocks when $z_m = 0.01$ m
Figure 4.13 (a) the FBD of the fixed-pinned beam with an overhang; (b) the FBD of th
beam segment between the fixed end and the pin and the FEB of the bean
segment between the pin and the free end
Figure 5.1(a) Schematic of the MPLNES; Spatial positions of: (b) coils and magnets A
and C; (c) magnets A, B, C and D
Figure 5.2 Two-dimensional views of the beam and magnets: (a) side view; (b) from
view; (c) detail of the DSBs13

Figure 5.3 The lumped-parameter model of the combined system
Figure 5.4 Illustration of the equivalent magnetic 2-point dipole model: (a) magnets A
and D; (b) magnets B and D135
Figure 5.5 Illustration of $f_{n2}$ : (a) $f_{n2}$ verse z and $xp$ ; (b) three representative cases of
$f_{n2}$ verse z
Figure 5.6 Illustration of $f_{n1} + f_{n2}$ : (a) the force surface; (b) the potential energy
surface138
Figure 5.7 Validation of the equilibrium positions of the MPLNES: (a) the experimental
setup; (b) comparison of the values from the model and the values measured
experimentally139
Figure 5.8 Transduction factor verses $x_a$ of coil 1 for different $x_p$
Figure 5.9 Experimental results of the $K_{t1}$ when (a) $xp = -0.02$ m; (b) $x_p = 0$ m; (c)
$x_p = 0.02 \text{ m}141$
Figure 5.10 Curve fitting surface and the numerical results of the total transduction
factor versus $x_a$ for different $x_p$
Figure 5.11 Simulation results with MPLNES and $X = 3.0$ mm: (a) $x_p$ ; (b) $x_a$ ; (c) $D_1$ ;
(d) <i>V<sub>out</sub></i> 145
Figure 5.12 Simulation results with PLNES and $X = 3.0 \text{ mm}$ : (a) $x_p$ ; (b) $x_a$ ; (c) $D_1$ ; (d)
V <sub>out</sub> 145
Figure 5.13 WT spectra of the responses with $X = 3$ mm: (a) $x_p$ with MPLNES; (b) $x_p$
with PLNES $x_p$ ; (c) $x_a$ with MPLNES; (d) $x_a$ with PLNES146
Figure 5.14 Simulation results with MPLNES and $X = 7.0$ mm: (a) $x_p$ ; (b) $x_a$ ; (c) $D_1$ ;
(d) $V_{out}$
Figure 5.15 Simulation results with PLNES and $X = 7.0$ mm: (a) $x_p$ ; (b) $x_a$ ; (c) $D_1$ ; (d)
V <sub>out</sub> 148
Figure 5.16 WT spectra of the responses with $X = 7$ mm: (a) $x_p$ with MPLNES; (b) $x_p$
with PLNES; (c) $x_a$ with MPLNES; (d) $x_a$ with PLNES
Figure 5.17 Heatmap of $J_2$ for different $M$ and $N$ .
Figure 5.18 FEPs and WT spectra of the relative displacement z with MPLNES: (a) low

	initial energy $X = 3$ mm; (b) medium initial energy $X = 5.0$ mm; (c) medium
	high initial energy $X = 7.0$ mm; (d) high initial energy $X = 8.0$ mm 155
Figure 5.19	FEPs and WT spectra of the relative displacement z with PLNES: (a) low
	initial energy $X = 3$ mm; (b) medium initial energy $X = 5.0$ mm; (c) medium
	high initial energy $X = 7.0$ mm; (d) high initial energy $X = 8.0$ mm 156
Figure 5.20	Percentage of the initial energy dissipated by the NES: (a) MPLNES; (b)
	PLNES. 158
Figure 5.21	Simulation results with MPLNES and $X = 7.0$ mm, $Rl = 20 \Omega$ : (a) $x_p$ ; (b)
	$x_a$ ; (c) $D_1$ ; (d) $V_{out}$
Figure 5.22	2 Simulation results with PLNES with $X = 7.0$ mm, $Rl = 20 \Omega$ : (a) $x_p$ ; (b)
	$x_a$ ; (c) $D_1$ ; (d) $V_{out}$
Figure 5.23	The Pareto fronts for Case B: (a) MPLNES; (b) PLNES and (c) MPLNES
	without DSBs
Figure 5.24	4 Comparison of the optimum results for the three configurations under
	different initial energy level ranges: (a) $J_1$ ; (b) $J_2$
Figure 5.25	The experimental setup: (a) the entire system; (b) a close-up view of the
	MPLNES and magnet D
Figure 5.26	Experimental results with MPLNES and $X = 3.53$ mm: (a) $x_p$ ; (b) $x_a$ ; (c)
	$D_1$ ; (d) $V_{out}$
Figure 5.27	Experimental results with PLNES and $X = 2.99$ mm: (a) $x_p$ ; (b) $x_a$ ; (c) $D_1$
	(d) <i>Vout</i> 164
Figure 5.28	B WT spectra of the experimental responses: (a) $xp$ with MPLNES; (b) $xp$
	with PLNES $x_p$ ; (c) $x_a$ with MPLNES; (d) $x_a$ with PLNES164
Figure 5.29	Experimental results with MPLNES and $X = 6.87$ mm: (a) $x_p$ ; (b) $x_a$ ; (c)
	$D_1$ ; (d) $V_{out}$
Figure 5.30	Experimental results with PLNES and $X = 6.93$ mm: (a) $x_p$ ; (b) $x_a$ ; (c) $D_1$
S	(d) $V_{out}$
Figure 5.31	WT spectra of the experimental responses: (a) $x_p$ with MPLNES; (b) $x_p$
-6	with PLNES; (c) $x_a$ with MPLNES; (d) $x_a$ with PLNES
	$\alpha$

Figure 5.32. FEPs and WT spectra for the experimental relative displacement $z$ with
MPLNES: (a) low initial energy $X = 3.53$ mm; (b) medium initial energy $X$
= 5.21 mm; (c)medium-high initial energy $X = 6.87$ mm and (d) high initial
energy $X = 8.50 \text{ mm}.$ 167
Figure 5.33 FEPs and WT spectra for the experimental relative displacement z with
PLNES: (a) low initial energy $X = 2.99$ mm; (b) medium initial energy $X =$
4.78 mm; (c) medium-high initial energy $X = 6.93$ mm and (d) high initial
energy $X = 8.11 \text{ mm}$
Figure 5C.1 COMSOL model used to determine $K_{ti}$ : (a) isometric view; (b) side view.
Figure A.1 (a) 3D CAD drawing of a primary system attached by a tunable multi-stable
NES, (b) lumped parameter model
Figure A.2 Spatial positions of the magnets
Figure A.3 (a) Side view and (b) front view of the apparatus
Figure A.4 The potential energy of the different NESs verse $x_a$ when varying x: (a)
MNES; (b) BNES; (c)TNES
Figure A.5 Transient responses of the systems with four different NESs when $A=1.2 \text{ N}$ ,
red dash line and blue solid for the displacement of primary mass with
locked and unlocked NES, green solid line for the NES's displacement: (a)
MNES; (b) BNES; (c) TNES192
Figure A.6 WT spectra of the transient responses of the systems with four different
NESs when $A=1.2$ N, upper plots for the primary displacements and lower
plots for the NES displacements: (a)(d) MNES; (b)(e) BNES; (c)(f) TNES.
Figure A.7 Accumulated energy of the systems with different NESs when $A=1.2~\mathrm{N}.$
Figure A.8 Transient responses of the systems with four different NESs when $A=8\mathrm{N},$
red dash line and blue solid for the displacement of primary mass with
locked and unlocked NES, green solid line for the NES's displacement: (a)
MNES; (b) BNES; (c) TNES

Figure A.9 WT spectra of the transient responses of the systems with four different
NESs when A=8 N, upper plots for the primary systems' displacements and
lower plots for the NESs' displacements: (a)(d) MNES; (b)(e) BNES; (c)(f)
TNES195
Figure A.10 Accumulated energy of the systems with different NESs when $A=8$ N.
196
Figure B.1 3D CAD drawing of the apparatus
Figure B.2 Lumped parameter model of the apparatus202
Figure B.3 Illustration of the equivalent magnetic 2-point dipole model:(a) magnets B
and D; (b) magnets A and D203
Figure B.4 3D plot of the nonlinear restoring force surface of the: (a) case I; (b) case II.
Figure B.5 Free responses of the Case I system with the real force model and the
estimated force model by using the single variable in the candidate
functions matrix
Figure B.6 Free responses of the Case I system with the real force model and the
estimated force model by using a modified candidate functions matrix.210
Figure B.7 Free responses of the Case II system with the real force model and the
estimated force model trained by one data set
Figure B.8 Free responses of the Case II with the real force model and the estimated
force model trained by two data sets212
Figure B.9 Free responses of the Case II with the real force model and the estimated
force model trained by three data sets
Figure B.10 The error of the prediction of the Case II system with identified force model
trained by three different sets of data

## **List of Table**

Table 1.1 Comparison of TMD and NES.
Table 1.2 Summary of advantages and disadvantages of EMEH and PEH13
Table 2.1 Parameter values of the apparatus [42]
Table 2.2 The optimization results of the 1 <sup>st</sup> model and 2 <sup>nd</sup> model42
Table 2.3 The fitness value of Case (I) to (IV) using original and optimized $1^{\text{st}}$ and $2^{\text{nd}}$
model
Table 2.4 The optimization results of the $2^{nd}$ model with six or five parameters45
Table 2.5 Errors for Cases (5), (6) and (7) of the optimized $1^{st}$ and $2^{nd}$ models with detuned
parameters47
Table 3.1 Parameters of the coils
Table 3.2 Parameters of the magnets
Table 3.3 Curve-fitting constants of Eqs. (3.12) and (3.13)67
Table 3.4 Curve-fitting constants of Eqs. (3.12) and (3.13) by using Ne70
Table 3.5 Values of the total charges on the surfaces of different magnets74
Table 3.6 The effective frequency bandwidths of the systems under the high-level
frequency sweep excitation
Table 3.7 The effective frequency bandwidths of the systems under low-level frequency
sweep excitation82
Table 3.8 The optimum load resistance values and total power output for the four
configurations86
Table 3.9 The optimum load resistance values and total power output for the four
configurations. 89
Table 4.1 Parameters value of the system
Table 4.2 The optimum parameters of the PLSs with single- or double-stop blocks $105$
Table 4.3 Estimated results for the parameters of PLSs with single- and double-stop blocks
when $z_m = 0.01 \text{ m}.$ 114
Table 5.1 Curve-fitting constants of Eqs. (5.16) and (5.17)

Table 5.2 Coefficient values in Eq. (5.24).	150
Table 5.3 The optimization results for three NES configurations	161
Table 5A.1 The parameters of the PLSs with DSBs.	170
Table A.1 Parameters value of the apparatus.	191
Table B.2 Paramters value of the Grounded NES.	205

## **List of Acronyms**

BEH Bi-stable Energy Harvester

DVA Dynamic Vibration Absorber

EH Energy Harvesting

EMEH Electromagnetic Energy Harvester

EMF Electromotive Force

ENS Essentially Nonlinear Spring

ET Energy Threshold

FBD Free-Body Diagram

FEP Frequency Energy Plot

GMS Grounded Magnetic Spring

HEH Hybrid Energy Harvester

IF Instantaneous Frequency

MEMS Micro Electromechanical System

MPGA Multi-population Genetic Algorithm

MPLNES Magnetically Enhanced PLNES

MSHEH Multi-Stable Hybrid Energy Harvester

NES Nonlinear Energy Sink

NNM Nonlinear Normal Mode

PEH Piezoelectric Energy Harvester

PLNES Piecewise Linear Nonlinear Energy Sink

PLS Piecewise-Linear Spring

QZS Quazi-zero Stiffness

RF Reflex Sensors

RMS Root-Mean-Square

SMR Strongly Modulated Response

TEH Tri-stable Energy Harvesters

TET Targeted Energy Transfer

TMD Tuned Mass Damper

VEH Vibration Energy Harvester

VS Vibration Suppression

WT Wavelet Transform

### **Chapter 1. Introduction**

### 1.1 Background

### 1.1.1 Vibration Suppression

Vibration control technologies are widely used in both civil engineering and mechanical engineering and can be broadly categorized into passive [1], active [2], and semi-active [3] regimes. Among them, the passive vibration control is the most well-established one due to its inherent robustness, simplicity, and ease of maintenance.

As a passive vibration control device, a dynamic vibration absorber (DVA) or tuned mass damper (TMD) consists of a mass and a linear spring. When a one-degree-of-freedom (DOF) host structure is subjected to a harmonic excitation with a constant frequency, its steady-state vibration can be suppressed by attaching a DVA whose natural frequency is tuned to be the exciting frequency. Adding a DVA to a single-DOF system yields a two-DOF system. The new system has two natural frequencies. One of the shortcomings of the DVA is a narrow operating band. If the exciting frequency drifts, the system may enter a new resonance. Adding a linear damper to a DVA can improve its performance robustness, making it less sensitive to variation of the exciting frequency. In this thesis, a damped DVA is considered. Hereinafter, TMD is used to refer to a secondary linear mass-spring-damper system used to suppress the vibration of a primary system. Commonly, the natural frequency of a TMD is tuned to match the fundamental natural frequency of the primary system. When the primary structure experiences resonance, the TMD vibrates out of phase and the damper will effectively dissipate the vibrational energy, thereby reducing the response of the host structure. Figure 1.1 shows the schematic of a primary system attached with a TMD. In the figure  $w_b$  represents the base excitation,  $x_p$  and  $x_a$  are the displacement of the primary mass and TMD relative to the base, respectively,  $m_p$ ,  $k_p$  and

 $c_p$  are the mass, stiffness and damping coefficient of the primary system, respectively,  $m_a$ ,  $k_a$  and  $c_a$  are the mass, stiffness and damping coefficient of the TMD, respectively. The governing equations of the combined system can be derived based on the Newton's second law:

$$m_{p}\ddot{x}_{p} + c_{p}\dot{x}_{p} + k_{1}x_{p} - k_{a}(x_{a} - x_{p}) - c_{a}(\dot{x}_{a} - \dot{x}_{p}) = -m_{p}\ddot{w}_{b}$$
 (1.1)

$$m_a \ddot{x}_a + c_a (\dot{x}_a - \dot{x}_p) + k_a (x_a - x_p) = -m_a \ddot{w}_b$$
 (1.2)

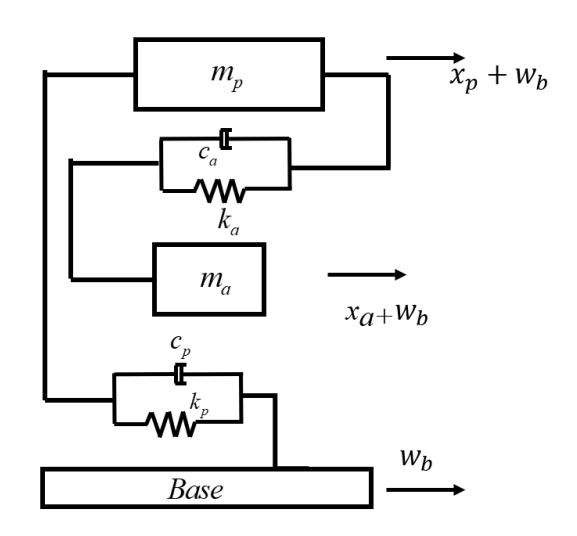


Figure 1.1 A primary system attached with a TMD.

The key limitation of a TMD is that its effectiveness is typically confined to a narrow frequency band, making it less suitable when the host structure is subjected to broadband or transient excitations [4]. Various approaches have been proposed to address this issue, such as employing multiple TMDs tuned to respond to different frequency components [5, 6] or incorporating nonlinearity into the system to broaden the operational bandwidth [7, 8]. As a special nonlinear TMD, a nonlinear energy sink (NES) consists of a small mass, a damper, and an essentially nonlinear spring (ENS). The restoring force of an ENS is a cubic polynomial. As illustrated in Figure 1.2, there are two main NES configurations: ungrounded or grounded. In the ungrounded configuration, the NES is connected to the primary mass through an ENS  $k_n$  and a damper  $c_a$ . The governing equations of the system with the ungrounded NES can be expressed as:

$$m_{p}\ddot{x}_{p} + c_{p}\dot{x}_{p} + k_{p}x_{p} - c_{a}(\dot{x}_{a} - \dot{x}_{p}) - k_{n}(x_{a} - x_{p})^{3} = -m_{p}\ddot{w}_{b}$$
(1.3)

$$m_a \ddot{x}_a + c_a (\dot{x}_a - \dot{x}_p) + k_n (x_a - x_p)^3 = -m_a \ddot{w}_b$$
 (1.4)

As for the grounded configuration, the NES mass is connected to the ground using an ENS  $k_n$  and damper  $c_a$  and weakly coupled to the primary mass via a linear spring  $k_a$ . The governing equations are given by:

$$m_{p}\ddot{x}_{p} + c_{p}\dot{x}_{p} + k_{p}x_{p} - c_{a}(\dot{x}_{a} - \dot{x}_{p}) - k_{a}(x_{a} - x_{p}) = -m_{p}\ddot{w}_{b}$$
(1.5)

$$m_a \ddot{x}_a + c_a \dot{x}_a + k_n x_a^3 - c_a (\dot{x}_a - \dot{x}_p) - k_a (x_a - x_p) = -m_a \ddot{w}_b$$
 (1.6)

The essential nonlinearity of the NES allows it to engage in 1:1 resonance with the primary system, thereby facilitating targeted energy transfer (TET), where energy from the primary system is transferred to the NES in a one-way irreversible fashion [4]. The ungrounded NES is very efficient in terms of TET, and is commonly used to absorb shock or periodic excitations, whereas the grounded NES is less efficient in terms of TET due to the lack of a continuous nonlinear normal mode under excitation [9]. However, the grounded NES has the advantage of being less constrained by the mass ratio [10], and such a configuration is generally used to suppress the transient and steady-state vibration in rotor systems [11].

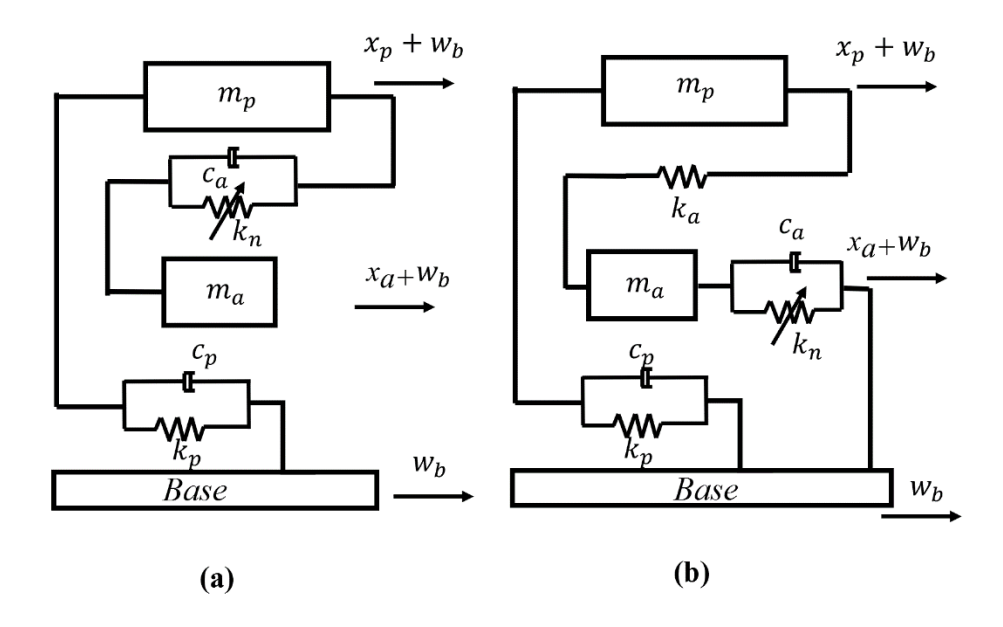


Figure 1.2 Two types of NES: (a) a primary system attached with an ungrounded NES; (b) a primary system attached with a grounded NES.

## 1.1.2 Comparison of TMD and NES

To further explore the difference between the TMD and NES, a numerical simulation is performed to demonstrate the frequency response characteristics of the primary system with TMD and NES based on Eqs. (1.1) - (1.4). The parameter values used in the simulation are taken from Chapter 5. For the primary system:  $m_p = 0.882 \, \mathrm{kg}$ ,  $k_p = 4.605 \times 10^3 \, \mathrm{N/m}$ ,  $c_p = 0.8604 \, \mathrm{Ns/m}$  so that  $f_P = \sqrt{k_P/m_p}/2\pi = 11.5 \, \mathrm{Hz}$  and  $\zeta_p = c_p/(2\sqrt{m_p k_p}) = 0.005$ . For both TMD and NES:  $m_a = 0.9 \, \mathrm{kg}$  and  $c_a = 0.0179 \, \mathrm{Ns/m}$ . For the TMD configuration, its natural frequency is tuned to be  $f_a = 11.5 \, \mathrm{Hz}$  so that  $k_a = (2\pi f_a)m_a = 469.89 \, \mathrm{N/m}$  and  $\zeta_a = c_a/(2\sqrt{m_a k_a}) = 0.049$ . The ratio  $\beta = f_a/f_p$  is referred to as the tuning parameter. Note that in this case, the TMD is designed so that  $\beta = 1$ . For the NES configuration, Using  $f_m = 15 \, \mathrm{Hz}$  and  $z_m = 0.02 \, \mathrm{m}$  in Eq. (4.8) yields  $k_n = 2.6648 \times 10^6 \, \mathrm{N/m}$ . The excitation is modeled as a sinusoidal acceleration applied to the base, with a constant amplitude of  $A_y = 2 \, \mathrm{m/s^2}$  and a frequency range varying from 5 Hz to 25 Hz. As a baseline, the frequency response of the primary mass without the TMD

can be calculated analytically [12]:

$$\left|X_{p}(\omega)\right| = \frac{A_{y}}{\sqrt{\left(\frac{k_{p}}{m_{p}} - \omega^{2}\right)^{2} + \left(\frac{c_{p}\omega}{m_{p}}\right)^{2}}}$$
(1.7)

where  $\omega$  is the frequency of the base excitation. To evaluate the frequency response of the primary mass with the TMD, Eqs. (1.1) and (1.2) can be formulated in the frequency domain as [12]:

$$\left(-\omega^2 M + j\omega C + K\right) X = F \tag{1.8}$$

where M, C, K, are the mass, damping coefficient and stiffness matrices, respectively, which can be expressed as:

$$\boldsymbol{M} = \begin{bmatrix} m_p & 0 \\ 0 & m_a \end{bmatrix}, \boldsymbol{C} = \begin{bmatrix} c_p + c_a & -c_a \\ -c_a & c_a \end{bmatrix}, \boldsymbol{K} = \begin{bmatrix} k_p + k_a & -k_a \\ -k_a & k_a \end{bmatrix}$$
(1.9)

X represents the displacement vector, F is the inertial force vector due to base acceleration. Then the frequency response can be found by X = HF, where  $H = (-\omega^2 M + j\omega C + K)^{-1}$  is the frequency response matrix.

The frequency response of the primary mass with the NES can be obtained through frequency up-sweep and down-sweep simulations. For this purpose, the base excitation is varied as follows:

$$\ddot{w}_b(t) = A_y \cdot \sin(2\pi f_{\text{start}} t + 2\pi r t^2)$$
(1.10)

where  $f_{start} = 5$  Hz (up-sweep) or 25 Hz (down-sweep),  $r = \pm 0.02$  Hz/s is the frequency changing rate, and the time duration of the simulation is 1000 seconds. As illustrated in Figure 1.3, the amplitude of the primary mass without the TMD shows a sharp peak around the natural frequency  $f_p$ , and the introduction of the TMD efficiently reduces this peak, but produces two lower peaks around the new natural frequencies. This indicates that the efficiency of TMD is limited by a narrow frequency bandwidth. In contrast, the up-sweep

and down-sweep responses of the primary mass with the NES exhibit jump phenomena around  $f_p$  due to the nonlinear nature of the coupled system. Although the NES does not suppress the resonance as sharply as the TMD, it offers more robust performance over a wider frequency range.

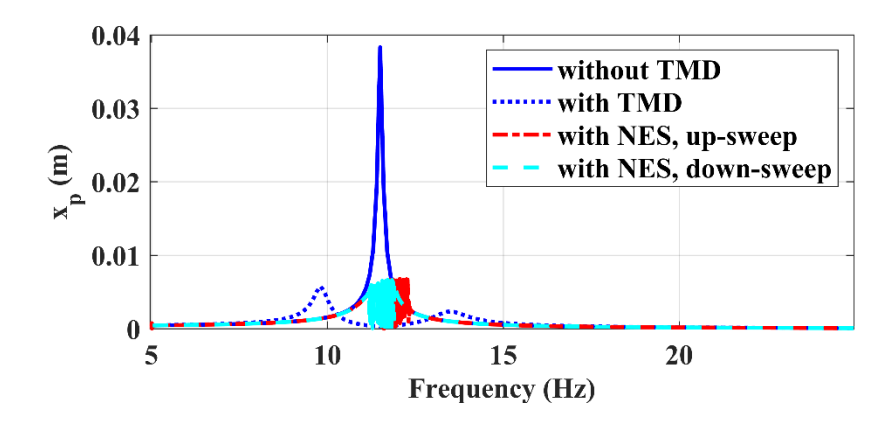


Figure 1.3 The frequency responses of the primary mass without TMD, with TMD and with NES.

To better demonstrate the transient behaviours of TMD and NES, A series of simulations is conducted by varying the primary system's natural frequency  $f_p$  (ranging from 1 - 40 Hz) and initial velocity V (ranging from 0.05 - 2 m/s<sup>2</sup>). Eqs. (1.1) and (1.2) for the TMD configuration, and Eqs. (1.3) and (1.4) for the NES configuration are numerically solved using MATLAB ODE 45 function over a time duration of 10 seconds. It should be mentioned that  $\ddot{w}_b$  is set to zero in the simulation. To evaluate the transient performance, the following index is defined:

$$D_c = \frac{c_a}{E_i} \int_0^T (\dot{x}_a - \dot{x}_p)^2 dt \times 100\%$$
 (1.11)

where  $E_i = m_p V^2/2$  is the initial energy. This index represents the percentage of the initial energy dissipated by the TMD damper or the NES damper over the time duration T. As illustrated in Figure 1.4(a), the performance of the TMD is independent of the initial velocity, a feature of the linear system. The TMD achieves highest efficiency only when its natural frequency  $f_a$  (11.5 Hz) matches the natural frequency  $f_p$  of the primary system,

and the performance drops significantly when  $f_a$  deviates from  $f_p$ . This indicates that the effectiveness of the TMD is limited in a narrow frequency band. In contrast, as shown in Fig. 1.14(b), the performance of the NES is less sensitive to variations in  $f_p$ , demonstrating its robustness. However, amount of the energy dissipated by the NES depends on the initial velocity. Also, beyond a certain value of  $f_p$ , a minimum initial energy threshold is required to trigger TET, making it less efficient under low excitation levels. The above analysis highlights the distinct characteristics of the TMD and NES. Table 1.1 summarises these differences, consolidating the underlying principles, frequency-response behaviour, transient performance, and limitations of the two configurations.

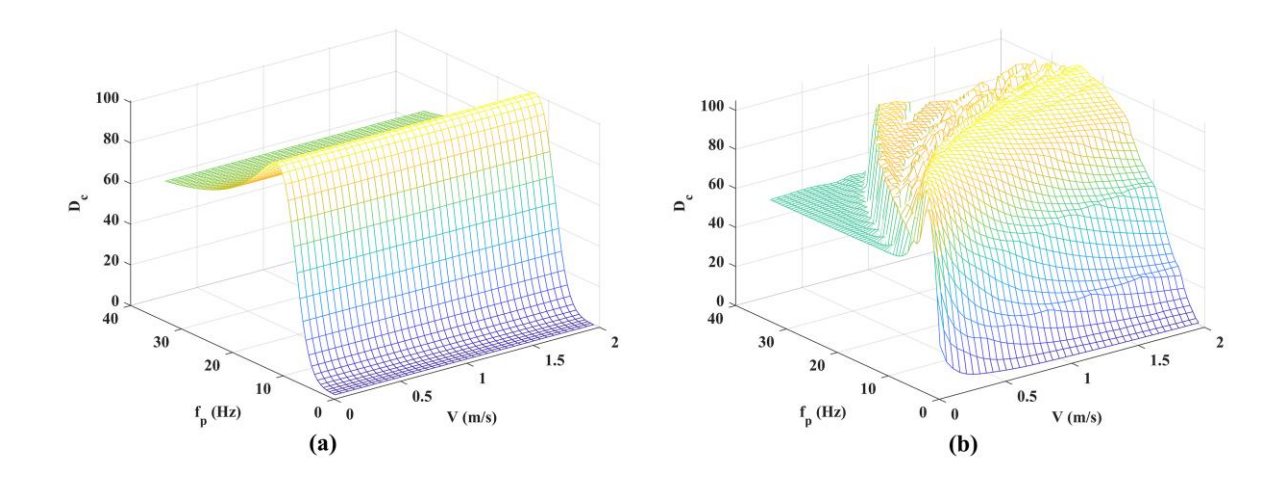


Figure 1.4 Transient performance  $D_c$  verse  $f_p$  and V: (a) TMD configuration; (b) NES configuration.

Table 1.1 Comparison of TMD and NES.

	TMD	NES
Principle	Resonate with the primary structure's natural frequency to maximize energy dissipation.	Uses an essentially nonlinear spring to enable the Targeted Energy Transfer (TET).
Energy flow	Reversible energy exchange	One-way irreversible energy transfer [13]
Steady-state performance	Sharp vibration suppression at the tuned frequency.	More uniform vibration suppression over a broad frequency range.
Transient performance	Independent of initial energy; high efficiency only when $f_p$ matches the tuned value.	Dependent on initial energy; robust to the variation of $f_p$ .
Limitations	Narrow bandwidth; sensitive to detuning.	Less efficient at low level excitation.

#### 1.1.3 Realization of ENS in NES

In TMD design, the tuning parameter  $\beta$  is chosen to be close to 1 or  $\beta \to 1$  so that the TMD is strongly coupled to the primary system. In contrast, the NES can be considered to possess a zero natural frequency or  $\omega_a = 0$  so that  $\beta = 0$ . In this sense, the NES is weakly coupled to the primary system. Achieving an essential nonlinearity in practical implementation remains a challenge, as any real spring inherently exhibits a certain degree of linear stiffness [14]. To realize an ENS, a classic approach is to utilize the geometric nonlinearity [15, 16]. To illustrate this approach, the NES proposed in [16] is used as an example. As shown in Fig. 1.5, the two linear springs with stiffness k and initial length k are connected to the NES mass which can slid along the guide rail where k represents the initial tension in the springs. By considering the force balance in the horizontal direction, the restoring force of the NES is derived:

$$f = 2ku + \frac{2u(P - kl)}{\sqrt{l^2 + u^2}}$$
 (1.12)

which can be further approximated through a Taylor series expansion:

$$f(u) \approx \frac{2P}{l}u + \frac{kl - P}{l^3}u^3 + O(u^5)$$
 (1.13)

Eq. (1.13) reveals that an ideal ENS is attainable only if P equals to zero. Besides the mechanical spring type, several other practical implementations have been proposed, such as cam-roller mechanisms [17, 18], magnetic springs [19, 20], and piecewise linear springs (PLS) [21, 22]. These studies have shown that by making the tuning parameter as small as possible or  $\beta \ll 1$ , a nonlinear oscillator can behave similarly like a true NES, exhibiting the typical TET behaviour. In this thesis, an NES with a small linear stiffness and large nonlinear stiffness is referred to as a variant NES. When a variant NES is attached to a primary system, the tuning parameter is greater than zero or  $\beta > 0$ .

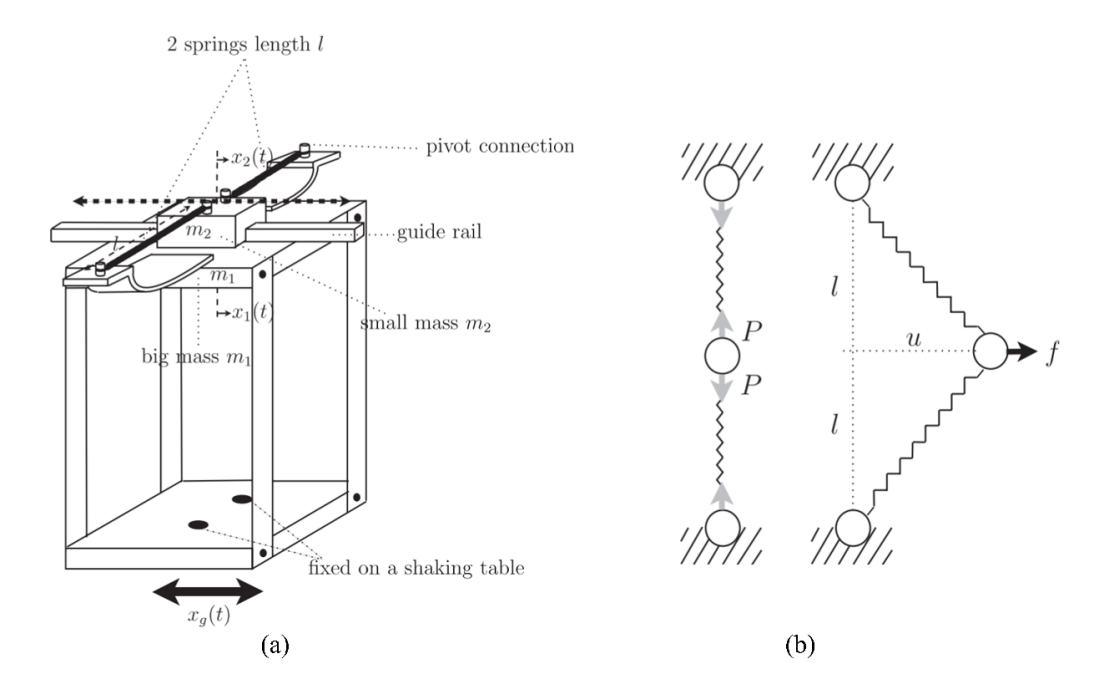


Figure 1.5 Illustration of achieving ENS through mechanical springs: (a) the apparatus; (b) the design of ENS [16].

These designs have their pros and cons. For example, the cam-roller system shows an advantage to customize different stiffness characteristics, while it introduces friction due to contact between the roller and cam surface. The PLS offer a structurally simple and

physically interpretable way to approximate nonlinear stiffness with little added friction. However, the NES constructed with a PLS still faces challenges in triggering TET at low excitation levels. The magnetic springs provide another non-contact means of introducing nonlinearity. But the magnetic forces are sensitive to the alignment, making it challenging to build an accurate magnetic force model for a complex magnet assembly. More details about the design, analysis, and application of NESs are summarized in a recent review paper [23].

## 1.1.4 Energy Harvesting

In recent decades, there has been growing interest in developing vibration energy harvester (VEH) to provide a sustainable power source for wearable electronics and wireless sensor networks. Vibration energy harvesting involves converting ambient mechanical vibrations into usable electrical energy. There are four main kinds of conversion mechanisms, namely, electrostatic [24], triboelectric [25], electromagnetic, and piezoelectric. The first two types are commonly employed **MEMS** (Microelectromechanical Systems) applications, while this thesis focuses primarily on the latter two types.

An electromagnetic energy harvester (EMEH) is designed based on Faraday's law. As illustrated in Figure 1.6(a), an EMEH consists of a magnet suspended by a spring and a coil fixed on the vibrating body. Under base excitation, the relative motion between the magnet and the coil causes the magnetic field lines to cut through the coil, inducing an electric current. The lumped-parameter model of such a single-DOF system is shown in Figure 1.6(b), where x is the magnet's displacement relative to the base, k is the stiffness of the spring, and  $c_m$  is the coefficient of inherent mechanical damping in the system,  $K_t$  is the transduction factor of the EMEH,  $E = K_t \dot{x}$  is the so-called electromotive force (EMF) of the EMEH, I is the output current of the EMEH,  $R_c$  and  $R_c$  are the resistance and inductance of the coil, respectively, and  $R_{le}$  is the resistance of a load resistor connected to the output of the EMEH. By applying Newton's second law and Kirchhoff's law, the governing equations can be derived as:

$$m\ddot{x} + c_m \dot{x} + kx + f_e = -m\ddot{w}_b \tag{1.14}$$

$$L_{c}\frac{dI}{dt} + \left(R_{c} + R_{le}\right)I = K_{t}\dot{x} \tag{1.15}$$

where based on Lenz's law,  $f_e = K_t I$  represents the back electromotive force. If  $\omega L_c \ll R_c + R_{le}$  where  $\omega$  is the frequency of vibration,  $I \approx K_t \dot{x}/(R_c + R_{le})$  from Eq. (1.15). Then Eq. (1.14) becomes

$$m\ddot{x} + (c_m + c_e)\dot{x} + kx = -m\ddot{w}_b$$
 (1.16)

where  $c_e = K_t^2/(R_c + R_{le})$  is referred to as the electrical damping coefficient. Eq. (1.16) indicates that an EMEH with a resistive load is equivalent to an electrical damper. A comprehensive review of EMEH design and modelling can be found in [26].

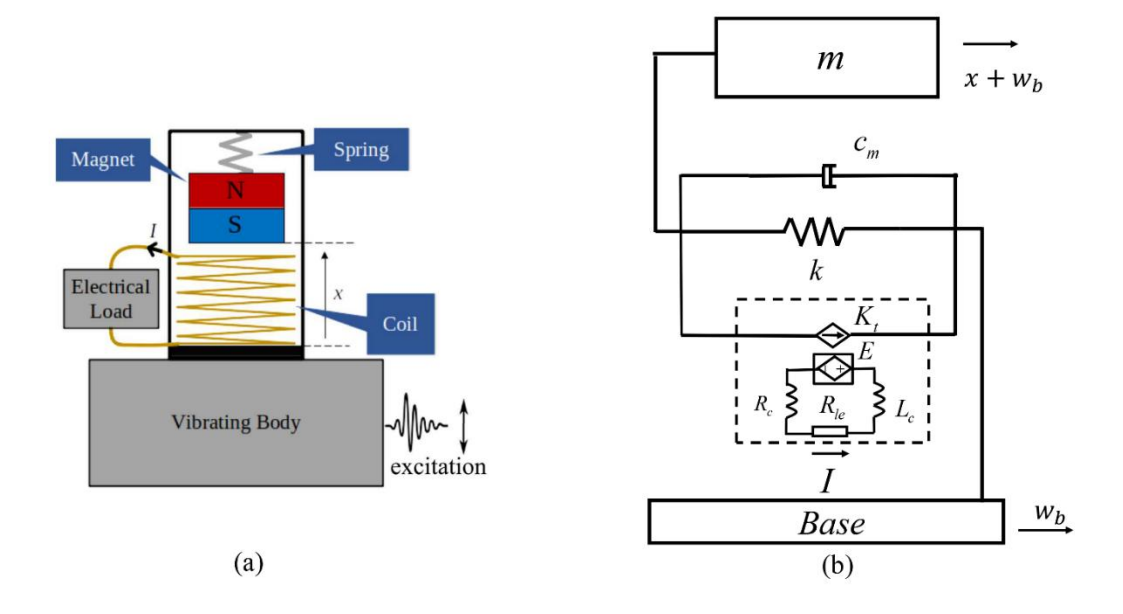


Figure 1.6 Illustration of EMEH: (a) a schematic of EMEH [27]; (b) a lumped-parameter model of EMEH.

The piezoelectric energy harvester (PEH) has two operation modes, namely, d31 mode (the external force is perpendicular to the polarization direction) and d33 mode (the stress has the same direction as the polarization of the material). The classic configuration of PEH in d31 mode is the cantilevered type. Figure 1.7(a) illustrates a typical cantilevered PEH

with a tip mass. Under the base excitation, the tip mass oscillates vertically, causing the beam and piezoelectric plate to deflect. Through the direct piezoelectric effect of the d31 mode, this mechanical deformation is converted into electrical voltage. The lumped-parameter model of a single-DOF PEH is shown in Figure 1.7(b), where  $v_p$  is the voltage over a load resistor connected to the output of the PEH,  $\theta$  is the electromechanical coupling coefficient. The electromechanical coupling can be modelled using a force-voltage analogy. The mechanical deformation produces an output current that is proportional to the strain changing rate [28]. The governing equations of the PEH can be expressed as follows:

$$m\ddot{x} + c_m \dot{x} + kx + \theta v_p = -m\ddot{w}_b \tag{1.17}$$

$$C^{S}\dot{v}_{p} + \frac{v_{p}}{R_{lp}} - \theta \dot{x} = 0 \tag{1.18}$$

where  $C^S$  is the capacitance of the PEH and  $R_{lp}$  is the resistance of the load resistor. With some derivation [29], Eq. (1.17) can be rewritten as

$$m\ddot{x} + (c_m + c_e)\dot{x} + (k + k_e)x = -m\ddot{w}_b$$
 (1.19)

where  $c_e = R_{lp}\theta^2/\left[1 + (\omega R_{lp}c_p)^2\right]$  and  $k_e = (\omega R_{lp}\theta)^2 c_p/\left[1 + (\omega R_{lp}c_p)^2\right]$  are referred to as the electric damping coefficient and the electrical stiffness, respectively. Eq. (1.19) shows that in addition to inducing electrical damping, a PEH with a resistive load adds additional stiffness to the system. Note that in the case of PEH,  $c_e$  and  $k_e$  are frequency dependent. A more detailed discussion on principles and modelling of PEH can be found in a recent review paper [30]. To better compare EMEH and PEH, Table 1.2 summarizes their advantages and disadvantages.

Table 1.2 Summary of advantages and disadvantages of EMEH and PEH.

Energy harvester type	Advantages	Disadvantages		
	Ease of manufacture.	Require magnetic material.		
	High current output.	High electrical damping.		
ЕМЕН	Suitable for low-frequency applications.	Lower energy density.		
	Easy to scale up.			
	Durable over long periods.			
	Simple structure.	Material brittleness may limit durability.		
	High energy density.	Low current output.		
PEH	High voltage output.	Charge leakage.		
	Small electric damping.			
	Easy integration.			
	Robust with no moving parts.			

Moreover, to further increase the energy density of the energy harvesting system, a hybrid energy harvester (HEH) is proposed. It usually combines two or more energy harvesting mechanisms. A more detailed literature review on HEH can be found in Chapter 3.

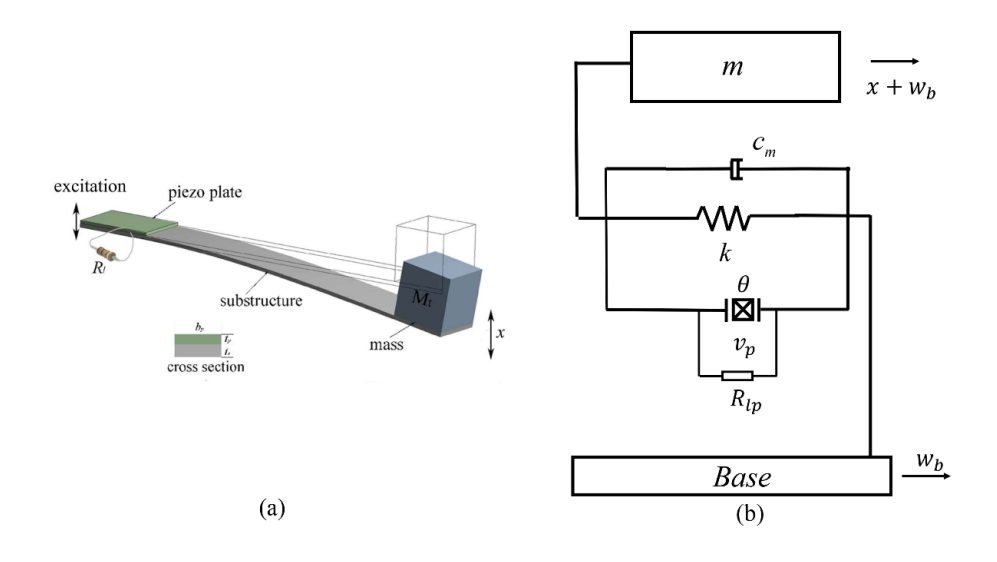


Figure 1.7 Illustration of PEH: (a) a cantilevered PEH [31]; (b) the lumped-parameter model of the PEH.

### 1.1.5 Simultaneous Vibration Suppression and Energy Harvesting

In the last two decades, researchers have been exploring the use of a same device to suppress vibration and harvest energy simultaneously. This dual-functional concept has been particularly explored in the context of large-scale civil engineering structures under the wind-induced vibration. In the study conducted in [32], a scale-down model was used to estimate the amount of energy that can be harvested from a 75-story building. The study found that under the wind load at a wind speed of 13.5 m/s, such a building could yield more than 85 kW of harvestable power. To corroborate this magnitude, the field measurements from the TMD installed in Taipei 101 reported a peak energy dissipation of about 40 kW from a single viscous damper (Figure 1.8) [33]. Nowadays, oil-based viscous dampers are commonly used in large-scale TMDs. As such viscous dampers simply convert vibrational energy into thermal energy generated heat imposes stringent thermal design requirements, including provisions for forced cooling and the use of heat-resistant components [34]. A dual-functional TMD provides an alternative solution. Once vibration energy is passively transferred into the TMD, it can be partially converted into electricity by integrating the TMD with an appropriate VEH. For instance, if the TMD is coupled with an EMEH, the system is referred to as a TMD-EMEH [35-37], while coupling it with a PEH yields a TMD-PEH [38, 39]. The harvested energy can be stored in rechargeable elements (e.g., batteries or supercapacitors) via power-management circuits [40], or used to power wireless sensor nodes for structural health monitoring [35].

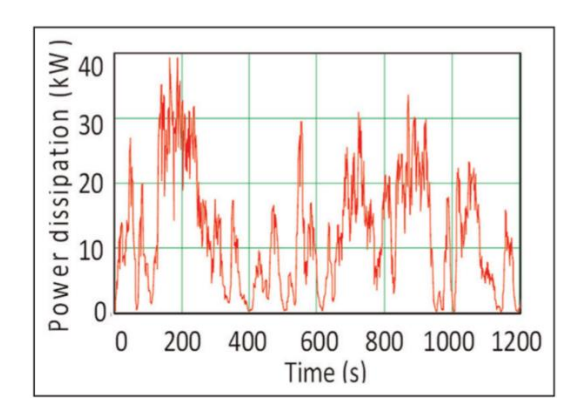


Figure 1.8 Power dissipated by one of the eight oil-based viscous dampers in the

However, as pointed out in Section 1.1.2, the TMD has a narrow operating band and its VS and EH performances remain limited under broadband or transient excitations. Introducing essential nonlinearity through an NES can efficiently broaden the operational bandwidth. Building on this concept, various NES-based VEHs have been proposed, including NES-EMEH [41, 42] and NES-PEH [43, 44]. Furthermore, an NES integrated with both PEH and EMEH was proposed in [45], and the parametric studies showed that adjusting external resistance and coil parameters significantly affects both VS and EH performance. More detailed literature about the dual-functional NES can be found in the introduction of Chapter 5.

# 1.2 Research Gaps and Objectives

As pointed out previously, it is challenging to realize a true ENS without introducing friction. Any mechanical damping in a dual-functional NES should be kept as low as possible to maximize harvested energy, yielding a variant NES. A major limitation of the variant NES designs lies in their inefficiency under low-energy excitation, primarily due to the relatively high initial energy threshold required to trigger TET. Reducing this threshold remains particularly challenging. Recent studies have utilized magnetic springs to create bi-stable nonlinear characteristics in NES to achieve both VS and EH [46, 47]. The snap-through oscillation enables the NES to perform a large-amplitude response under low-level excitation. However, most of these efforts focus on ungrounded magnetic spring configurations.

One of the author's previous works [48] demonstrates that integrating a grounded magnetic spring (GMS) into a variant NES offers distinct advantages. The GMS applies a position-dependent magnetic force to a movable magnet attached to the NES mass, dynamically shifting the equilibrium position of the NES in response to the motion of the primary system. This unique feature significantly lowers the energy threshold required to trigger TET, thereby presenting a promising approach to enhancing both VS and EH

#### performance.

Nevertheless, to the best of the author's knowledge, the following research gaps remain unexplored and warrant further investigation: design a tunable magnetic spring that is suitable for a grounded NES; design a PLS to emulate a desirable ENS closely; develop a GMS to enhance the TET performance in terms of both VS and EH in a wide operating band; incorporate an EMEH into the GMS; overcome new challenges in modeling and analyzing. To address these gaps, the study intends to accomplish the following four objectives:

- Develop a multi-stable PEH consisting of a cantilever beam and an adjustable magnetic assembly capable of achieving mono-stable, bi-stable, or tri-stable states by tuning its geometric parameters. Establish an accurate model for the magnetic restoring force for such a spring through optimization. Validate the model accuracy experimentally.
- Design a HEH that incorporates both PEH and EMEH in a cantilever beam configuration. This also serves as a basis for the theoretical modelling and practical implementation of a suitable energy harvester for a NES system.
- Develop a systematic methodology to design a PLS consisting of a cantilever beam constrained by a pair of single- or double-stop blocks to emulate a desired ENS. Evaluate the designed PLS numerically and experimentally.
- Develop a magnetically enhanced piecewise-linear nonlinear energy sink (MPLNES) by integrating a GMS into a PLNES and a grounded EMEH. Establish the modelling and analysis approaches for the MPLNES. Evaluate VS and EH performances of the MPLNES via numerical simulation and experimental validation.

### 1.3 Organization of Thesis

The thesis is presented in an "integrated-article" format and is organized into six

chapters:

Chapter 1. This chapter introduces the background of the research and identifies the research gaps in the current literature. Then, the research objectives are established to address these gaps.

Chapter 2. This chapter presents a tunable multi-stable piezoelectric energy harvester consisting of a cantilever beam and a magnet assembly capable of achieving mono-stable, bi-stable, and tri-stable configurations. Two analytical models for the magnetic restoring force are developed using point dipole and two-point dipole approximations, respectively. Dynamic tests are conducted to validate the models, and a multi-population genetic algorithm is used to optimize the model parameters. The resulting models are analyzed for parameter sensitivity and used to map the stability regions of the system. This study establishes a foundation for accurately modelling compact magnetic assemblies for NES applications.

Chapter 3. This chapter introduces a multi-stable hybrid energy harvester (MSHEH) combining a PEH and an EMEH. A modelling method is developed to compute the EMEH transduction factor and derive the magnetic restoring force using the two-point dipole model. The system's performance is evaluated under various configurations including linear, mono-stable, bi-stable, and tri-stable states, using simulations and experiments. Pareto optimization is applied to identify optimal load resistances for a balanced energy output.

Chapter 4. This chapter proposes a systematic design method for a PLS that emulates an ENS closely. The PLS is realized using a cantilever beam constrained by single or double stop blocks. A target restoring force is defined based on equivalent stiffness theory, and optimal stop block parameters are obtained using least squares fitting. Simulations and experiments are performed to evaluate the force-displacement behavior, potential energy distribution, and instantaneous frequency variation.

Chapter 5. This chapter presents a magnetically enhanced piecewise-linear nonlinear energy sink (MPLNES) for achieving both vibration suppression and energy harvesting.

The proposed system includes a small secondary mass, a PLS, a GMS, and a grounded EMEH. Two-variable mathematical models are developed to describe the nonlinear restoring force and transduction factor of EMEH. Time response analyses, wavelet spectra, and frequency-energy plots are used to compare the performance of the MPLNES with that of a conventional PLNES. A two-objective optimization identifies optimal initial energies and load resistances for three NES configurations. Experimental validations agree well with simulations, confirming the effectiveness of the MPLNES for dual-function applications.

Chapter 6. This chapter summarizes the key insights and conclusions observed in the research. Then, the future studies are proposed.

In addition, two conference papers and one conference abstract that are related to this thesis are included as appendices. Appendix A reports the development of a piezoelectric energy harvester that is integrated with a grounded and tunable multi-stable nonlinear energy sink, including the system design, modelling, and transient response analysis. Appendix B addresses identification of the restoring force of a grounded multi-stable NES with a tunable magnetic spring, where a polynomial model is formulated and linear regression is applied to determine its coefficients. Appendix C deals with the design and evaluation of three variant nonlinear energy sinks

#### References

- [1] P. S. Balaji and K. Karthik SelvaKumar, "Applications of nonlinearity in passive vibration control: a review," *Journal of Vibration Engineering & Technologies*, vol. 9, no. 2, pp. 183-213, 2020, doi: 10.1007/s42417-020-00216-3.
- [2] R. Alkhatib and M. Golnaraghi, "Active structural vibration control: a review," *Shock and Vibration Digest*, vol. 35, no. 5, p. 367, 2003, doi:10.1177/05831024030355002
- [3] A. M. A. Soliman and M. M. S. Kaldas, "Semi-active suspension systems from research to mass-market A review," *Journal of Low Frequency Noise, Vibration and Active Control*, vol. 40, no. 2, pp. 1005-1023, 2019, doi: 10.1177/1461348419876392.
- [4] A. F. Vakakis, O. V. Gendelman, L. A. Bergman, D. M. McFarland, G. Kerschen,

- and Y. S. Lee, Nonlinear targeted energy transfer in mechanical and structural systems. Dordrecht, The Netherlands: Springer, 2009.
- [5] A. J. Clark, "Multiple passive tuned mass dampers for reducing earthquake induced building motion," in *Proceedings of the 9th world conference on earthquake engineering*, vol. 5: Tokyo-Kyoto JAPAN, pp. 779-784, 1988, .
- [6] H. Zuo, K. Bi, and H. Hao, "Using multiple tuned mass dampers to control offshore wind turbine vibrations under multiple hazards," *Engineering Structures*, vol. 141, pp. 303-315, 2017, doi: 10.1016/j.engstruct.2017.03.006.
- [7] F. Arnold, "Steady-state behavior of systems provided with nonlinear dynamic vibration absorbers," *Journal of Applied Mechanics*, 22(4): pp. 487-492, 1955, doi: 10.1115/1.4011141.
- [8] L. Pipes, "Analysis of a nonlinear dynamic vibration absorber," *Journal of Applied Mechanics*, 20(4): pp. 515-518, 1953, doi: 10.1115/1.4010757 1953.
- [9] X. Kang, J. Tang, G. Xia, J. Wei, F. Zhang, Z. Sheng "Design, optimization, and application of nonlinear energy sink in energy harvesting device," *International Journal of Energy Research*, vol. 2024, no. 1, 2024, doi: 10.1155/2024/2811428.
- [10] K. Dekemele, L. D. Knop, P. V. Torre, and M. Loccufier, "Equivalence of grounded and non-grounded nes tuning and performance in mitigating transient vibrations," in *Advances in Nonlinear Dynamics*, (NODYCON Conference Proceedings Series, ch. Chapter 3, pp. 27-37, 2022, doi: 10.1007/978-3-030-81166-2\_3.
- [11] H. Yao, Y. Cao, Z. Ding, and B. Wen, "Using grounded nonlinear energy sinks to suppress lateral vibration in rotor systems," *Mechanical systems and signal processing*, vol. 124, pp. 237-253, 2019, doi: 10.1016/j.ymssp.2019.01.054.
- [12] D. J. Inman and R. C. Singh, *Engineering vibration*. Prentice Hall Englewood Cliffs, NJ, 1994.
- [13] S. Roundy, P. K. Wright, and J. Rabaey, "A study of low level vibrations as a power source for wireless sensor nodes," *Computer communications*, vol. 26, no. 11, pp. 1131-1144, 2003, doi: 10.1016/S0140-3664(02)00248-7.
- [14] X.-F. Geng, H. Ding, J.-C. Ji, K.-X. Wei, X.-J. Jing, and L.-Q. Chen, "A state-of-the-art review on the dynamic design of nonlinear energy sinks," *Engineering Structures*, vol. 313, 2024, doi: 10.1016/j.engstruct.2024.118228.
- [15] D. M. McFarland, G. Kerschen, J. J. Kowtko, Y. S. Lee, L. A. Bergman, and A. F. Vakakis, "Experimental investigation of targeted energy transfers in strongly and nonlinearly coupled oscillators," *The Journal of the Acoustical Society of America*, vol. 118, no. 2, pp. 791-799, 2005, doi: 10.1115/DETC2005-84497.
- [16] E. Gourdon, N. A. Alexander, C. A. Taylor, C. H. Lamarque, and S. Pernot, "Nonlinear energy pumping under transient forcing with strongly nonlinear coupling: Theoretical and experimental results," *Journal of Sound and Vibration*, vol. 300, no. 3-5, pp. 522-551, 2007, doi: 10.1016/j.jsv.2006.06.074.

- [17] J. Zhou, X. Wang, D. Xu, and S. Bishop, "Nonlinear dynamic characteristics of a quasi-zero stiffness vibration isolator with cam-roller-spring mechanisms," *Journal of Sound and Vibration*, vol. 346, pp. 53-69, 2015, doi: 10.1016/j.jsv.2015.02.005.
- [18] X. Wang, J. Zhou, D. Xu, H. Ouyang, and Y. Duan, "Force transmissibility of a two-stage vibration isolation system with quasi-zero stiffness," *Nonlinear Dynamics*, vol. 87, no. 1, pp. 633-646, 2016, doi: 10.1007/s11071-016-3065-x.
- [19] X. Geng, H. Ding, X. Jing, X. Mao, K. Wei, and L. Chen, "Dynamic design of a magnetic-enhanced nonlinear energy sink," *Mechanical Systems and Signal Processing*, vol. 185, 2023, doi: 10.1016/j.ymssp.2022.109813.
- [20] B. Mann and N. Sims, "Energy harvesting from the nonlinear oscillations of magnetic levitation," *Journal of sound and vibration*, vol. 319, no. 1-2, pp. 515-530, 2009. doi: 10.1016/j.jsv.2008.06.011.
- [21] X.-F. Geng, H. Ding, X.-Y. Mao, and L.-Q. Chen, "A ground-limited nonlinear energy sink," *Acta Mechanica Sinica*, vol. 38, no. 5, 2022, doi: 10.1007/s10409-022-09027-x.
- [22] Y. Sun, "Experimental modelling and amplitude-frequency response analysis of a piecewise linear vibration system," *IEEE Access*, vol. 9, pp. 4279-4290, 2021, doi: 10.1109/access.2020.3047655.
- [23] H. Ding and L.-Q. Chen, "Designs, analysis, and applications of nonlinear energy sinks," *Nonlinear Dynamics*, vol. 100, no. 4, pp. 3061-3107, 2020, doi: 10.1007/s11071-020-05724-1.
- [24] S. Boisseau, G. Despesse, and B. A. Seddik, "Electrostatic conversion for vibration energy harvesting," *Small-scale energy harvesting*, vol. 5, 2012, doi: 10.5772/51360.
- [25] F.-R. Fan, Z.-q. Tian, and Z. L. Wang, "Flexible triboelectric generator," *Nano Energy*, vol. 1, pp. 328-334, 2012, doi: 10.1016/j.nanoen.2012.01.004.
- [26] A. Muscat, S. Bhattacharya, and Y. Zhu, "Electromagnetic vibrational energy harvesters: A review," *Sensors*, vol. 22, no. 15, p. 5555, 2022. doi: 10.3390/s22155555.
- [27] L. Costanzo, A. Lo Schiavo, A. Sarracino, and M. Vitelli, "Stochastic thermodynamics of an electromagnetic energy harvester," *Entropy (Basel)*, vol. 24, no. 9, Aug 31 2022, doi: 10.3390/e24091222.
- [28] Y. Yang and L. Tang, "Equivalent circuit modeling of piezoelectric energy harvesters," *Journal of Intelligent Material Systems and Structures*, vol. 20, no. 18, pp. 2223-2235, 2009, doi: 10.1177/1045389x09351757.
- [29] L. Xiong, L. Tang, K. Liu, and B. R. Mace, "Effect of electromechanical coupling on dynamic characteristics of a piezoelectric nonlinear energy sink system," *Journal of Vibration Engineering & Technologies*, vol. 9, no. 4, pp. 687-699, 2020,

- doi: 10.1007/s42417-020-00255-w.
- [30] H. S. Kim, J.-H. Kim, and J. Kim, "A review of piezoelectric energy harvesting based on vibration," *International Journal of Precision Engineering and Manufacturing*, vol. 12, no. 6, pp. 1129-1141, 2011, doi: 10.1007/s12541-011-0151-3.
- [31] Z. Yang, "High-performance nonlinear piezoelectric energy harvesting in compressive mode." Ph.D. dissertation, University of Toronto (Canada), 2016.
- [32] T. Ni, L. Zuo, and A. Kareem, "Assessment of energy potential and vibration mitigation of regenerative tuned mass dampers on wind excited tall buildings," in *International Design Engineering Technical Conferences and Computers and Information in Engineering Conference*, vol. 54785, pp. 333-342, 2011. doi: 10.1115/DETC2011-48728
- [33] T. Haskett, B. Breukelman, J. Robinson, and J. Kottelenberg, "Tuned mass dampers under excessive structural excitation," *Report of the Motioneering Inc., Guelph, Ontario, Canada,* 2004.
- [34] L. Zuo and X. Tang, "Large-scale vibration energy harvesting," *Journal of Intelligent Material Systems and Structures*, vol. 24, no. 11, pp. 1405-1430, 2013, doi: 10.1177/1045389x13486707.
- [35] W.-a. Shen, S. Zhu, and Y.-l. Xu, "An experimental study on self-powered vibration control and monitoring system using electromagnetic TMD and wireless sensors," *Sensors and Actuators A: Physical*, vol. 180, pp. 166-176, 2012. doi: 10.1016/j.sna.2012.04.011
- [36] A. Gonzalez-Buelga, L. R. Clare, A. Cammarano, S. A. Neild, S. G. Burrow, and D. J. Inman, "An optimised tuned mass damper/harvester device," *Structural Control and Health Monitoring*, vol. 21, no. 8, pp. 1154-1169, 2014, doi: 10.1002/stc.1639.
- [37] S. Zhu, W. Shen, H.-P. Zhu, and Y.-l. Xu, "Electromagnetic energy harvesting from structural vibrations during earthquakes," *Smart Structures and Systems, An International Journal*, vol. 18, no. 3, pp. 449-470, 2016, doi:10.12989/sss.2016.18.3.449.
- [38] P. Pan, D. Zhang, X. Nie, and H. Chen, "Development of piezoelectric energy-harvesting tuned mass damper," *Science China Technological Sciences*, vol. 60, no. 3, pp. 467-478, 2016, doi: 10.1007/s11431-016-0280-5.
- [39] S. F. Ali and S. Adhikari, "Energy harvesting dynamic vibration absorbers," *Journal of Applied Mechanics*, vol. 80, no. 4, 2013, doi: 10.1115/1.4007967.
- [40] S. Zelenika *et al.*, "Energy harvesting technologies for structural health monitoring of airplane components-a review," *Sensors (Basel)*, vol. 20, no. 22, Nov 22 2020, doi: 10.3390/s20226685.
- [41] G. Pennisi, B. P. Mann, N. Naclerio, C. Stephan, and G. Michon, "Design and

- experimental study of a Nonlinear Energy Sink coupled to an electromagnetic energy harvester," *Journal of Sound and Vibration*, vol. 437, pp. 340-357, 2018, doi: 10.1016/j.jsv.2018.08.026.
- [42] D. Kremer and K. Liu, "A nonlinear energy sink with an energy harvester: transient responses," *Journal of Sound and Vibration*, vol. 333, no. 20, pp. 4859-4880, 2014, doi: 10.1016/j.jsv.2014.05.010.
- [43] X. Li, Y. Zhang, H. Ding, and L. Chen, "Integration of a nonlinear energy sink and a piezoelectric energy harvester," *Applied Mathematics and Mechanics*, vol. 38, no. 7, pp. 1019-1030, 2017, doi: 10.1007/s10483-017-2220-6.
- [44] L. Xiong, L. Tang, K. Liu, and B. R. Mace, "Broadband piezoelectric vibration energy harvesting using a nonlinear energy sink," *Journal of Physics D: Applied Physics*, vol. 51, no. 18, 2018, doi: 10.1088/1361-6463/aab9e3.
- [45] L. Wang, W. Liu, X. Lin, Z. Yan, and X. Nie, "Study of vibration suppression and energy harvesting for a Vibration-based Piezoelectric–Electromagnetic energy harvester with nonlinear energy sink," *Journal of Magnetism and Magnetic Materials*, vol. 602, 2024, doi: 10.1016/j.jmmm.2024.172200.
- [46] M. Rezaei, R. Talebitooti, and W.-H. Liao, "Investigations on magnetic bistable PZT-based absorber for concurrent energy harvesting and vibration mitigation: Numerical and analytical approaches," *Energy*, vol. 239, 2022, doi: 10.1016/j.energy.2021.122376.
- [47] M. Rezaei, R. Talebitooti, and W.-H. Liao, "Exploiting bi-stable magneto-piezoelastic absorber for simultaneous energy harvesting and vibration mitigation," *International Journal of Mechanical Sciences*, vol. 207, p. 106618, 2021/10/01/2021, doi: 10.1016/j.ijmecsci.2021.106618.
- [48] H. Li, K. Liu, J. Deng, and B. Li, "A grounded and tunable multi-stable nonlinear energy sink: transient responses," *In Proceedings of the Canadian Society for Mechanical Engineering International Congress* vol. Volume 5, 2022, doi: 10.7939/r3-d4rz-jr10.

### Chapter 2. Validation and Optimization of Two Models for

### the Magnetic Restoring Forces Using a Multi-stable

### Piezoelectric Energy Harvester

#### 2.1 Introduction

In this century, wireless sensor networks have been playing an important role in the Internet of Things (IoT). Normally, the wireless sensors are powered by batteries which are not eco-friendly. It has been much desirable to use vibration energy harvesters to solve costly battery replacement problem and make wireless sensor networks autonomous [1]. Ambient vibration can be converted to electricity by four methods: piezoelectric [2, 3], electromagnetic [4-7], electrostatic [8-10] and triboelectric [11, 12]. The main advantages of the piezoelectric vibration energy harvesters (PVEHs) are their large power densities and ease of operation.

A traditional PVEH is a single-degree-of-freedom linear oscillator that performs efficiently only at resonance [13-15]. To broaden the response frequency bandwidth, various nonlinear energy harvesters have been proposed [16-19]. According to the system stability, the nonlinear PVEHs can be classified as mono-stable and multistable, such as bi-stable or tri-stable. The nonlinearity can be realized by introducing the nonlinear restoring forces to the piezoelectric beam. Applying magnetic forces to the beam is one of the convenient ways to achieve that. In [20], a PVEH is proposed that consists of a piezoelectric cantilever beam with a tip magnet, the system is subjected to an external magnetic field generated by a pair of fixed magnets. Such a mono-stable energy harvester can exhibit softening or hardening behaviors when the magnetic interaction is adjusted. By applying different external magnet tuning

strategies, two kinds of bi-stable energy harvester (BEH) can be achieved: attractive magnetic force type [21, 22] or repulsive magnetic force type [23-25]. The study in [26] found that, for a certain range of excitation intensity, the BEH can largely enhance the power output performance due to its snap-through characteristic. Further, in order to reduce the potential barrier of BEHs, tri-stable energy harvesters (TEH) have been proposed by introducing a middle potential well between BEH's two potential wells. Based on the configuration of the BEH proposed in [27], TEHs were achieved by tuning the angular orientations [28, 29] or the spatial positions [30, 31] of the two fixed magnets. However, the disadvantage of the aforementioned tunable multi-stable PVEHs is that they need more than one fixed magnet to achieve the tri-stable state. Thus, installing multiple fixed magnets would take more space, which is undesirable in realization through a micro-electromechanical system (MEMS). And also, an asynchronous operation of tuning the angle or position of the fixed magnets will lead to the asymmetric potential wells for the TEH.

In the dynamic modelling of a tunable multi-stable PVEH, an accurate magnetic force model is crucial. Generally, the magnetic force between two magnets is complicated, especially when the separation distance between them is relatively small. There are several commonly used models for this purpose. The most widely used one is the so-called equivalent magnetic point dipole approach [32-34] which treats each magnet as a point dipole at its center. However, this approach has a limitation as it can offer a reliable prediction only when the distance between the magnets is much greater than their dimensions. In light of this limitation, a magnetic force modelling method based on the equivalent magnetizing current theory was proposed [35, 36]. The study indicates that the magnetizing current model offers better accuracy than the equivalent magnetic point dipole model. Accordingly, an equivalent magnetic 2-point dipole approach is proposed in [37], which only counts the magnetizing current on the permanent magnet's left and right polarized surfaces and uses two total surface charges to represent a magnet. It has been proved that the accuracy of the equivalent magnetic

2-point dipole model was significantly improved by using the proposed method [22, 37-39]. Currently, such approach is mainly used in the modelling of the magnetic force between thin cubic permanent magnets, the accuracy of the magnetic force model of the thick cylinder magnets based on such approach still needs to be examined.

In this study, a new tunable multi-stable piezoelectric energy harvester is proposed. Different from the existing design which employs multiple fixed magnets to achieve a tri-stable state, the proposed apparatus consists of a stationary magnet and a cantilever beam whose free end is attached by an assembly of two cylindrical magnets that can be moved along the beam and a small cylindrical magnet that is fixed at the beam tip. By varying the gap between the stationary magnet and the tip magnet, and the distance between the magnet assembly and the tip magnet, the system can assume three stability states: tri-stable, bi-stable, and mono-stable, respectively. Modelling the magnetic restoring forces for a tunable multi-stable energy harvester poses a challenge as a reliable model should give an accurate prediction over a wide range of the tuning parameters. For this purpose, the developed apparatus is used to dynamically validate two commonly used models: the equivalent magnetic point dipole approach and the equivalent magnetic 2-point dipole approach proposed in [37]. The study shows that although the second model offers more accurate results than the first model, it still fails to predict the restoring forces in some cases. A numerical optimization is carried out to improve the accuracy of both models. The study shows that by using the optimal parameters, both models can achieve a comparable accuracy.

The rest of the chapter is organized as follows. Section 2 presents the proposed apparatus. Section 3 derives the magnetic restoring force models based on the equivalent magnetic point dipole approach and the equivalent magnetic 2-point dipole approach, respectively. Section 4 validates the two models dynamically. Section 5 conducts a model optimization. Section 6 uses the optimum model for the parametric sensitivity study and the stability region determination. Finally, Section 7 draws the main conclusions of the study.

### 2.2 Apparatus

Figure 2.1 shows a CAD drawing of the developed apparatus. A cantilever beam is constructed by connecting a piezoelectric transducer (S128-J1FR-1808YB, Midé) to a thin stainless-steel plate. One end of the cantilever beam is clamped to a stand that is fastened to a base, while its other end is fixed with a small cylindrical magnet B and attached with a holder for an assembly of two identical cylindrical magnets A and C. The holder for magnets A and C can slide along the beam. A large cylindrical magnet D is fixed in a stand that can slide along the base. When the cantilever beam is at its equilibrium position or undeflected, the four magnets situate on the same vertical plane and magnets B and D are collinear. By sliding the stand for magnet D, the distance between magnet B and magnet D can be adjusted. By sliding the holder along the beam, the distance between magnet B and magnets A, C can be varied. Figure 2.2 illustrates the spatial positions and polarities of the four magnets where  $m_A$ ,  $m_B$ ,  $m_C$ ,  $m_D$  are the magnetic moment vectors,  $A_0$ ,  $B_0$ ,  $C_0$  and A, B, C denote the center positions of magnets A, B and C when the beam is undeformed and deformed, respectively, and the origin of the coordinate system is also located at  $B_0$ ,  $r_{DA}$  represents a vector from A to D,  $r_{DB}$  represents a vector from B to D, and the vector  $r_{DA}$ 's projection on the x-y plane is represented by  $r_{DAxy}$ .

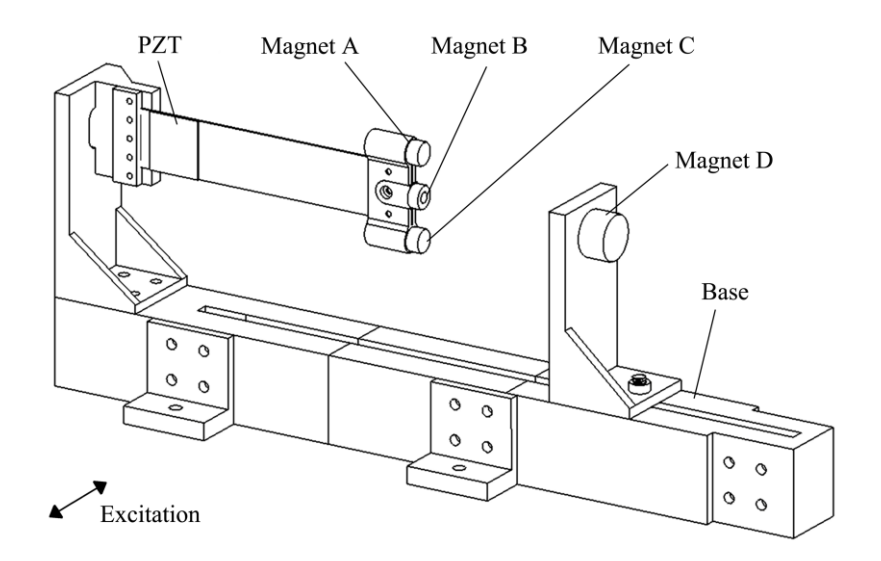


Figure 2.1 Schematic of the apparatus.

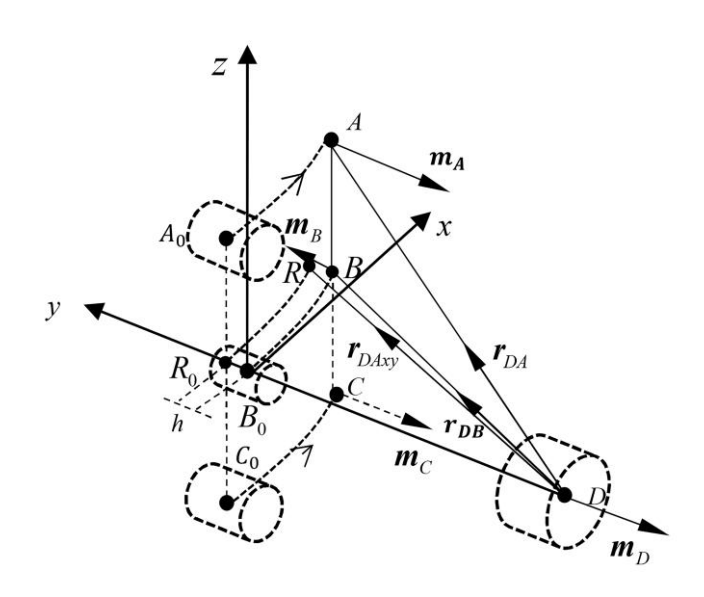


Figure 2.2 Spatial positions of the magnets.

Figure 2.3 and 2.4 show the front view and top view of Figure 2, respectively, where d is the distance between magnet D and magnet B when the beam is undeformed, and h is the distance between magnet A or C and magnet B, l is the length of the cantilever beam, and w is the distance between the axis of magnet B and that of magnet A or C.

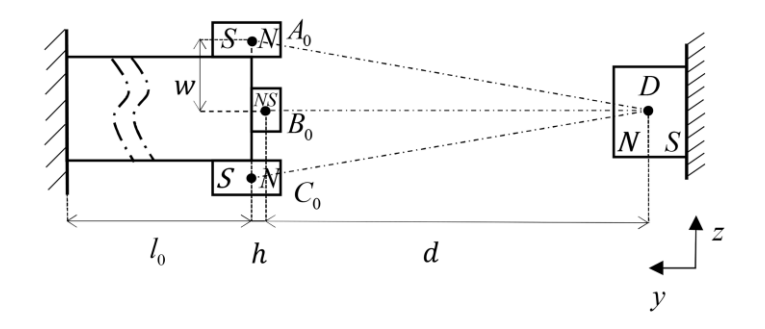


Figure 2.3 Front view of the apparatus.

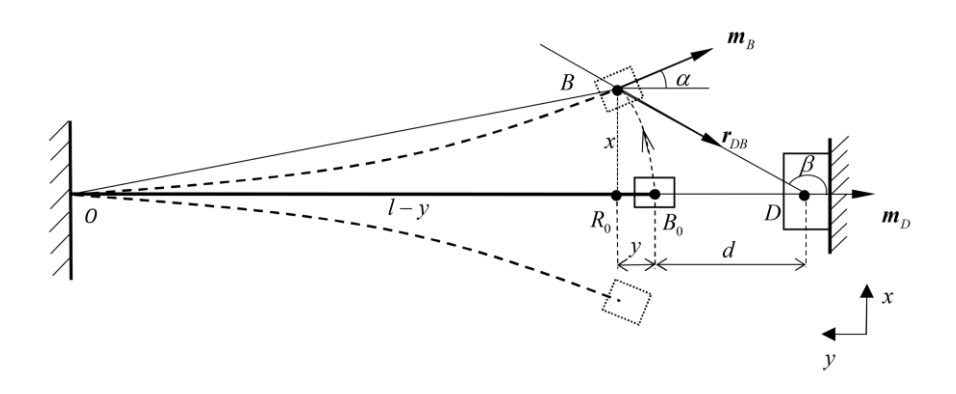


Figure 2.4 Top view of the apparatus.

# 2.3 The Restoring Force of the System

The total restoring force  $f_x$  of the system in the x-direction consists of a restoring force  $f_e$  due to the beam's elasticity, an attractive magnetic force  $f_{DBx}$  between magnet D and magnet B and two repulsive magnetic forces  $f_{DAx}$  between magnet D and magnet A, and  $f_{DCx}$  between magnet D and magnet C. Since magnets A and C are identical and symmetrical about the central line of the beam, the values of  $f_{DAx}$  and  $f_{DCx}$  are equal. Then the total restoring force can be expressed as:

$$f_x = f_e + f_{DBx} + f_{DAx} + f_{DCx} = k_b x + f_{DBx} + 2f_{DAx}$$
 (2.1)

where  $k_b$  is the stiffness of the beam which can be determined experimentally. In what follows, the analytical restoring forces  $f_{DBx}$  and  $f_{DAx}$  will be found using two approaches.

### 2.3.1 Equivalent Magnetic Point Dipole Model

Commonly, a pair of magnets is regarded as equivalent magnetic point dipoles by assuming that the magnet sizes are much smaller than their separation distance [40]. Firstly, the magnetic force between magnet B and magnet D is considered. According to this approach, the force exerted by magnet B on magnet D is given by:

$$\boldsymbol{f}_{DB} = \nabla \left( \boldsymbol{B}_{DB} \cdot \boldsymbol{m}_{B} \right) \tag{2.2}$$

where  $\nabla$  denotes the vector gradient operator and  $\mathbf{B}_{DB}$  is the magnetic flux density generated by magnet D upon B. Eq. (2.2) can be expanded as:

$$f_{DB} = \frac{3\mu_0 m_D m_B}{4\pi r_{DB}^4} \left[ \hat{\mathbf{r}}_{DB} \left( \hat{\mathbf{m}}_B \cdot \hat{\mathbf{m}}_D \right) - 5\hat{\mathbf{r}}_{DB} \left( \hat{\mathbf{m}}_D \cdot \hat{\mathbf{r}}_{DB} \right) \left( \hat{\mathbf{r}}_{DB} \cdot \hat{\mathbf{m}}_B \right) + \hat{\mathbf{m}}_B \left( \hat{\mathbf{m}}_D \cdot \hat{\mathbf{r}}_{DB} \right) + \hat{\mathbf{m}}_D \left( \hat{\mathbf{m}}_B \cdot \hat{\mathbf{r}}_{DB} \right) \right] (2.3)$$

where  $m_B$ ,  $m_D$ , and  $r_{BD}$  are the magnitude of  $m_B$ ,  $m_D$ , and  $r_{DB}$ , respectively,  $\hat{m}_B$ ,  $\hat{m}_D$  and  $\hat{r}_{DB}$  are the unit vector of  $m_B$ ,  $m_D$ , and  $r_{DB}$ , respectively. These unit vectors can be expressed as:

$$\hat{\boldsymbol{m}}_{B} = [\sin(\alpha) - \cos(\beta) \ 0], \ \hat{\boldsymbol{m}}_{D} = [0 \ -1 \ 0], \ \hat{\boldsymbol{r}}_{DB} = [-\sin(\beta) \cos(\beta) \ 0]. \tag{2.4}$$

Substituting the above unit vectors in Eq. (2.3) and the magnetic force in the *x*-direction can be obtained in the following form:

$$f_{DBx} = -\frac{3\mu_0 m_D m_B}{4\pi r_{BD}^4} \left\{ \sin(\beta) \left[ \cos(\alpha) - 5\cos(\beta)\cos(\beta - \alpha) \right] + \sin(\alpha)\cos(\beta) \right\}. \tag{2.5}$$

Since the slope of the beam's tip is relatively small, it is assumed that  $\angle BOB_0 \approx \alpha$ . Also, it is noted that  $\beta$  can be found from the triangle  $DR_0B$ . Thus, Eq. (2.5) can be expressed as follows:

$$f_{DBx} = -\frac{3\mu_0 m_D m_B x}{4\pi r_{DB}^5 l} \left\{ l - 2y - d - \frac{5}{r_{DB}^2} \left[ -y^3 + \left(l - 2d\right) y^2 + \left(2dl - d^2\right) y + d^2l - \left(y + d\right) x^2 \right] \right\} (2.6)$$

where  $y = l - \sqrt{l^2 - x^2}$ . Similarly, the magnetic force between magnet A and magnet D in the *x*-direction can be found as:

$$f_{DAx} = \frac{3\mu_0 m_D m_A x}{4\pi r_{DA}^4 l_0} \left\{ \frac{l_0 - 2y - d_0}{r_{DAxy}} - \frac{5}{r_{DAxy}^3} \left[ -y^3 + \left(l_0 - 2d_0\right) y^2 + \left(2d_0 l_0 - d_0^2\right) y + d_0^2 l_0 - \left(y + d_0\right) x^2 \right] \right\}$$
(2.7)

where  $d_0 = d + h$  and  $l_0 = l - h$ . Substituting Eqs. (2.6) and (2.7) into Eq. (2.1) yields the analytical model of the total restoring force. In Eqs. (2.6) and (2.7), the magnitudes of the magnetic moment vectors are determined by:

$$m_A = MV_A, m_B = MV_B, m_D = MV_D,$$
 (2.8)

where  $V_A$ ,  $V_B$  and  $V_D$  are the volume of the magnets A, B and D, respectively,  $M = B_r/\mu$  is the magnetization of magnets A, B and D, where  $B_r = 1.46$  T is the magnetic residual flux density and  $\mu = 4\pi \times 10^{-7}$  H/m is the vacuum permeability.

# 2.3.2 Equivalent Magnetic 2-point Dipole Model

As mentioned in [35], the equivalent magnetic point dipole approach's accuracy deteriorates when the separation space between the magnets becomes small. In light of such limitation, an improved approach was proposed in [37]. In this study, such an improved approach is named as equivalent magnetic 2-point dipole model as the approach treats a magnet as a 2-point dipole. In what follows, the magnetic restoring force of the system is developed using this improved method. Figures 2.5(a) and (b) show the top view of the apparatus when the beam is deformed.

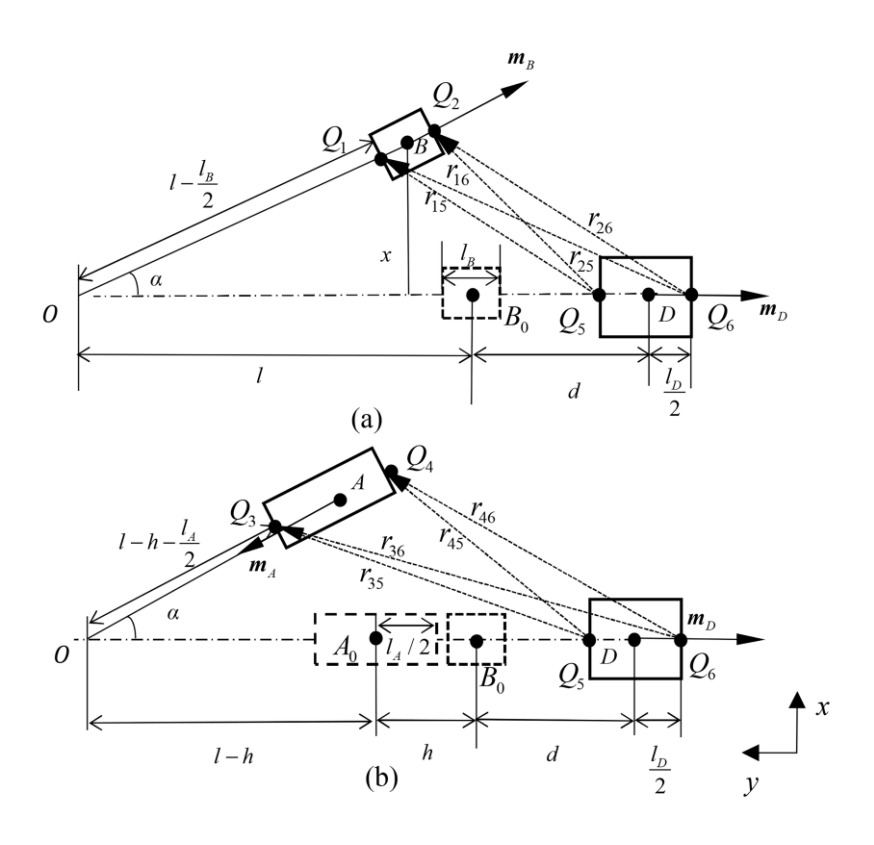


Figure 2.5 Top view of positions of magnets of the apparatus: (a) magnet B and D; (b) magnet A and D.

As shown in Figures 2.5 (a) and (b), the origin of the coordinate system locates at  $B_0$ , the centers of the magnet A, B, and D are represented by points A, B and D, respectively, point  $A_0$  and  $B_0$  depict the positions of the magnets A and B when the beam is undeformed,  $l_B$ ,  $l_D$  and  $l_A$  are the length of magnet B, magnet D and magnet A, respectively, and h is the distance between magnet A or C and magnet B in y-direction, l is the length of the cantilever beam,  $r_{15}$ ,  $r_{25}$ ,  $r_{35}$  and  $r_{45}$  are the vectors from  $Q_5$  to  $Q_1$ ,  $Q_2$ ,  $Q_3$  and  $Q_4$ , respectively, and  $r_{16}$ ,  $r_{26}$ ,  $r_{36}$  and  $r_{46}$  are the vectors from  $Q_6$  to  $Q_1$ ,  $Q_2$ ,  $Q_3$  and  $Q_4$  respectively,  $Q_1$  and  $Q_2$ , are the total charges of the left and the right surfaces of magnet B, respectively,  $Q_3$  and  $Q_4$  are the total charges of the left and the right surfaces of magnet A, respectively,  $Q_5$  and  $Q_6$  are the total charges of the left and right surfaces of magnet D, respectively. The total surface charges can be expressed as

follow:

$$Q_1 = -MS_B$$
  $Q_2 = MS_B$   $Q_3 = MS_A$   $Q_4 = -MS_A$   $Q_5 = -MS_D$   $Q_6 = MS_D$  (2.9)

where  $S_B$ ,  $S_A$  and  $S_D$  are the surface area of magnets B, A and D, respectively, and M is the magnetization of the magnets defined previously.

Similar to the previous section, the magnetic force between magnet B and magnet D is considered first. Based on the Boit-Savart law, the magnetic force exerted by magnet B on magnet D is the combination of the magnetic force exerted from  $Q_1$  and  $Q_2$  to  $Q_5$  and  $Q_6$ , which is given in the following equation:

$$\mathbf{f}_{DB} = \mathbf{B}_1 Q_1 + \mathbf{B}_2 Q_2 \tag{2.10}$$

where  $\mathbf{B}_1$  and  $\mathbf{B}_2$  are the magnetic current density at  $Q_1$  and  $Q_2$  generated by  $Q_5$  and  $Q_6$  which can be defined as follows:

$$\mathbf{B}_{1} = \frac{\mu_{0}}{4\pi} \left( Q_{5} \frac{\mathbf{X}_{5} - \mathbf{X}_{1}}{\left| \mathbf{X}_{5} - \mathbf{X}_{1} \right|^{3}} + Q_{6} \frac{\mathbf{X}_{6} - \mathbf{X}_{1}}{\left| \mathbf{X}_{6} - \mathbf{X}_{1} \right|^{3}} \right),$$

$$\mathbf{B}_{2} = \frac{\mu_{0}}{4\pi} \left( Q_{5} \frac{\mathbf{X}_{5} - \mathbf{X}_{2}}{\left| \mathbf{X}_{5} - \mathbf{X}_{2} \right|^{3}} + Q_{6} \frac{\mathbf{X}_{6} - \mathbf{X}_{2}}{\left| \mathbf{X}_{6} - \mathbf{X}_{2} \right|^{3}} \right)$$
(2.11)

where  $X_1$ ,  $X_1$ ,  $X_5$  and  $X_6$  are the position vectors of  $Q_1$ ,  $Q_2$ ,  $Q_5$  and  $Q_6$ , respectively, and they can be obtained from Figure 2.5(a):

$$\boldsymbol{X}_{1} = \left(x - \frac{l_{B}}{2}\sin\alpha\right)\boldsymbol{i} + \left[l - \left(l - \frac{l_{B}}{2}\right)\cos\alpha\right]\boldsymbol{j}, 
\boldsymbol{X}_{2} = \left(x + \frac{l_{B}}{2}\sin\alpha\right)\boldsymbol{i} + \left[l - \left(l + \frac{l_{B}}{2}\right)\cos\alpha\right]\boldsymbol{j}, 
\boldsymbol{X}_{5} = -\left(d - \frac{l_{D}}{2}\right)\boldsymbol{j}, \quad \boldsymbol{X}_{6} = -\left(d + \frac{l_{D}}{2}\right)\boldsymbol{j}$$
(2.12)

where i and j are the unit vector on x and y-axis. By substituting Eqs. (2.11) and (2.12)

into Eq. (2.10), the magnetic force between magnet B and magnet D can be obtained. It should be noted that the total magnetic force between magnet B and magnet D can be separated into two components: one is in the *y*-direction  $f_{DBy}$ , another one is in the *x*-direction  $f_{DBx}$ . According to Eq. (2.1), to obtain the total restoring force, only the  $f_{DBx}$  is considered, which can be expressed as follows:

$$f_{DBx} = -\frac{\mu_0}{4\pi} \left\{ Q_1 \left[ Q_5 \frac{\left( x - \frac{l_B}{2} \sin \alpha \right)}{\gamma_1} + Q_6 \frac{\left( x - \frac{l_B}{2} \sin \alpha \right)}{\gamma_2} \right] + Q_6 \frac{\left( x - \frac{l_B}{2} \sin \alpha \right)}{\gamma_2} \right]$$

$$+ Q_2 \left[ Q_5 \frac{\left( x + \frac{l_B}{2} \sin \alpha \right)}{\gamma_3} + Q_6 \frac{\left( x + \frac{l_B}{2} \sin \alpha \right)}{\gamma_3} \right]$$

$$(2.13)$$

where  $\gamma_1,\,\gamma_2,\,\gamma_3$  and  $\gamma_4$  can be expressed as follows:

$$\gamma_1 = \left\{ \left\{ -\left[ d - \frac{l_D}{2} \right] - \left( l - \left( l - \frac{l_B}{2} \right) \cos \alpha \right) \right\}^2 + \left( x - \frac{l_B}{2} \sin \alpha \right)^2 \right\}^{3/2}$$
(2.14)

$$\gamma_2 = \left\{ \left\{ -\left[ d + \frac{l_D}{2} \right] - \left( l - \left( l - \frac{l_B}{2} \right) \cos \alpha \right) \right\}^2 + \left( x - \frac{l_B}{2} \sin \alpha \right)^2 \right\}^{3/2}$$
(2.15)

$$\gamma_3 = \left\{ \left\{ -\left[ d - \frac{l_D}{2} \right] - \left( l - \left( l + \frac{l_B}{2} \right) \cos \alpha \right) \right\}^2 + \left( x + \frac{l_B}{2} \sin \alpha \right)^2 \right\}^{3/2}$$
(2.16)

$$\gamma_4 = \left\{ \left\{ -\left[d + \frac{l_D}{2}\right] - \left(l - \left(l + \frac{l_B}{2}\right)\cos\alpha\right) \right\}^2 + \left(x + \frac{l_B}{2}\sin\alpha\right)^2 \right\}^{3/2}$$
(2.17)

By following the same process, the magnetic force between magnet A and D in the *x*-direction can also be obtained as:

$$f_{DAx} = -\frac{\mu_0}{4\pi} \left\{ Q_3 \left[ Q_5 \frac{\left( x - h \sin \alpha - \frac{l_A}{2} \right)}{\gamma_5} + Q_6 \frac{\left( x - h \sin \alpha - \frac{l_A}{2} \right)}{\gamma_6} \right] + Q_4 \left[ Q_5 \frac{\left( x - h \sin \alpha + \frac{l_A}{2} \right)}{\gamma_7} + Q_6 \frac{\left( x - h \sin \alpha + \frac{l_A}{2} \right)}{\gamma_8} \right] \right\}$$
(2.18)

where  $\gamma_5, \gamma_6, \gamma_7$  and  $\gamma_8$  can be expressed as follows:

$$\gamma_{5} = \left\{ \left\{ -\left[ d - \frac{l_{D}}{2} \right] - \left( l - \left( l - h - \frac{l_{A}}{2} \right) \cos \alpha \right) \right\}^{2} + \left( x - h \sin \alpha - \frac{l_{A}}{2} \sin \alpha \right)^{2} \sin^{2} \alpha + w^{2} \right\}^{3/2}$$
(2.19)

$$\gamma_{6} = \left\{ \left\{ -\left[d + \frac{l_{D}}{2}\right] - \left(l - \left(l - h - \frac{l_{A}}{2}\right)\cos\alpha\right) \right\}^{2} + \left(x - h\sin\alpha - \frac{l_{A}}{2}\sin\alpha\right)^{2}\sin^{2}\alpha + w^{2} \right\}^{3/2}$$
 (2.20)

$$\gamma_{7} = \left\{ \left\{ -\left[d - \frac{l_{D}}{2}\right] - \left(l - \left(l - h + \frac{l_{A}}{2}\right)\cos\alpha\right) \right\}^{2} + \left(x - h\sin\alpha + \frac{l_{A}}{2}\sin\alpha\right)^{2}\sin^{2}\alpha + w^{2} \right\}^{3/2}$$
 (2.21)

$$\gamma_{8} = \left\{ \left\{ -\left[d + \frac{l_{D}}{2}\right] - \left(l - \left(l - h + \frac{l_{A}}{2}\right)\cos\alpha\right) \right\}^{2} + \left(x - h\sin\alpha + \frac{l_{A}}{2}\sin\alpha\right)^{2}\sin^{2}\alpha + w^{2} \right\}^{3/2}$$
 (2.22)

where w is the distance between magnets A and B in the z-direction, which can be observed in Figure 2.3. By substituting Eqs. (2.13) and (2.18) into Eq. (2.1), the total restoring force can be obtained.

# 2.4 Experimental Validation

With the models established, a natural question arises regarding their accuracy and reliability. To this end, an experimental model validation is conducted. For simplicity, hereinafter, the equivalent magnetic point dipole model and 2-point dipole model are referred to as 1<sup>st</sup> model and 2<sup>nd</sup> model, respectively. The restoring force surface method [41] is employed to determine the total restoring forces dynamically. Figures 2.6(a) and (b) show the experimental setup and the detail of the magnets' positions, respectively.

Figure 2.6(c) shows a schematic of the equivalent lumped parameter model that represents the experimental setup, where  $x_b$  is the base's displacement and x is the displacement of the cantilever beam's tip relative to the base, m represents the total mass of the assembly of magnets A and C and magnet B, c is the damping coefficient, and  $k_n$  represents the stiffness of the combined spring. The lumped parameter model is commonly employed for multi-stable energy harvesters [35]. The equation of motion of this setup is given by:

$$m(\ddot{x} + \ddot{x}_h) + c\dot{x} + f_x(x) = 0$$
 (2.23)

where  $f_x(x)$  denotes the restoring force of the combined spring. Eq. (2.23) can be rewritten as:

$$F(x,\dot{x}) = -m(\ddot{x} + \ddot{x}_h) \tag{2.24}$$

where  $F(x,\dot{x})$  is the so-called restoring force surface.

As shown in Figure 2.6(a), the apparatus is mounted on a slipping table that is driven by a shaker (2809, Brüel & Kjær) through a stinger. The shaker is driven by an amplifier (2718, Brüel & Kjær). Two laser reflex sensors (RF) (CP24MHT80, Wenglor) are used to measure the transverse displacement of the beam's tip and the base's displacement, respectively. A computer equipped with the dSPACE dS1104 data acquisition board is used to collect sensor data and send voltage signal to the power amplifier to drive the shaker. The control program is developed by using the MATLAB Simulink which is interfaced with dSPACE Controldesk Desktop software. The velocity and acceleration are obtained by numerical differentiation of the measured displacement signals.

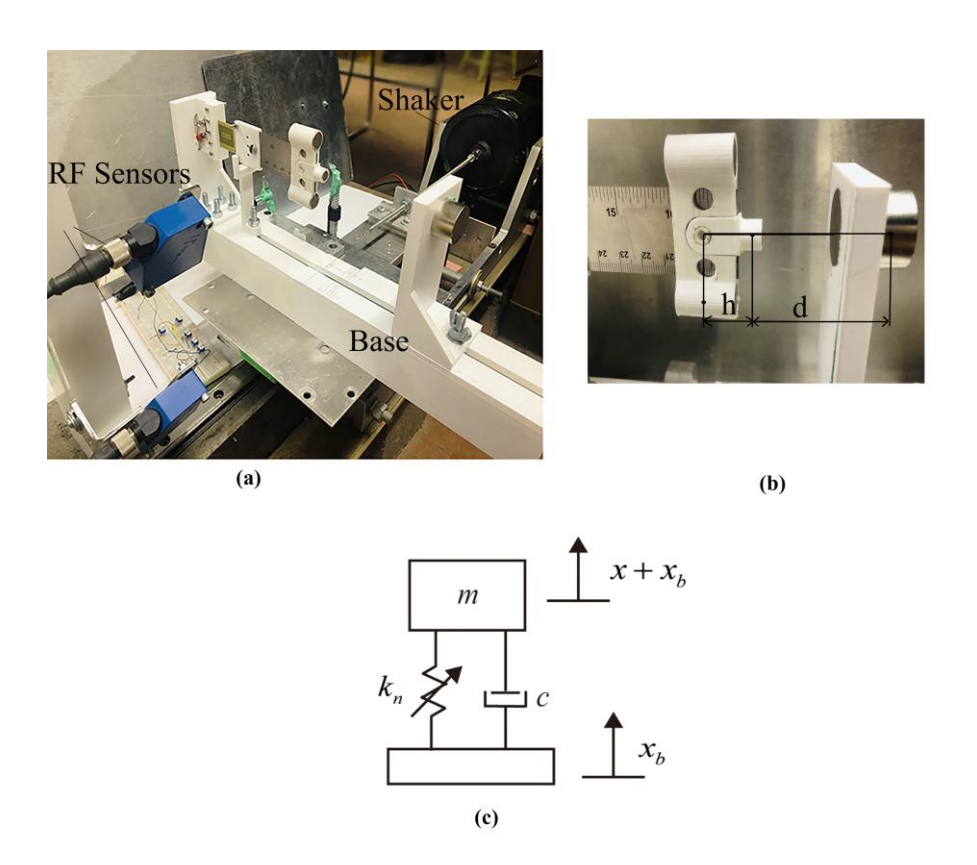


Figure 2.6 (a) Photo of the experimental setup; (b) detail of the beam; (c) schematic of the equivalent lumped parameter model for the experimental setup.

To apply the restoring force method properly, the responses should sufficiently cover the phase plane. The exciting signal should be persistently strong so that both intrawell and interwell responses are established. For this purpose, a harmonic signal with a slowly modulated amplitude is employed

$$x_b(t) = X_b \cos(0.2\pi t) \times \cos(2\pi f_n t)$$
 (2.25)

where  $X_b$  and  $f_n$  are the amplitude and exciting frequency, respectively. The general guidelines for choosing proper values of  $X_b$  and  $f_n$  are that  $X_b$  should be large enough to achieve interwell responses and  $f_n$  should be close to the natural frequency of the linearized system around the equilibrium position. In the experiment,  $X_b$  and  $f_n$  are chosen on a case-by-case basis by trial and error. A great number of experiments are conducted to examine the relationship between the stability states and the tuning

parameters. For the sake of comparison, the following four configurations are chosen: Case (1) d = 0.0407 m, h = 0.0187 m; Case (2) d = 0.0457 m, h = 0.0162 m; Case (3) d = 0.0517 m, h = 0.0187 m; Case (4) d = 0.0507 m, h = 0.0187 m. The purple circles in Figure 2.7 show the identified restoring force values. As shown in the figures, the system is transferred from a tri-stable one in Case (1) to a mono-stable one in Case (4). By using the parameter values given in Table 2.1 in the derived models, the analytical restoring forces are found. The blue dashed lines and red solid lines in Figure 2.7 show the restoring force values based on the 1<sup>st</sup> model and the 2<sup>nd</sup> model, respectively. It can be seen that the 1<sup>st</sup> model fails to predict Cases (1), (3), and (4). On the other hand, the 2<sup>nd</sup> model shows a better agreement with the measured data for Cases (1), (2), and (3) than the 1<sup>st</sup> model. But it fails to predict both the magnitude and trend for Case (4).

Table 2.1 Parameter values of the apparatus [42].

Symbol	Description	Value
$V_A$ , $V_C$ (m <sup>3</sup> )	Volume of magnet A and C	3.21×10 <sup>-6</sup>
$V_B  (\mathrm{m}^3)$	Volume of magnet B	3.93×10 <sup>-7</sup>
$V_D (\mathrm{m}^3)$	Volume of magnet D	1.29×10 <sup>-5</sup>
$S_A$ , $S_C$ (m <sup>2</sup> )	End surface area of magnet A and C	3.22×10 <sup>-5</sup>
$S_B (m^2)$	End surface area of magnet B	3.93×10 <sup>-5</sup>
$S_D$ (m <sup>2</sup> )	End surface area of magnet D	1.29×10 <sup>-5</sup>
$k_b$ (N/m)	Stiffness of the cantilever beam	26.17
$l\left(\mathbf{m}\right)$	Length of the cantilever beam	0.12
m (kg)	Mass of the system	0.086
c (Ns/m)	Damping coefficient	0.0668

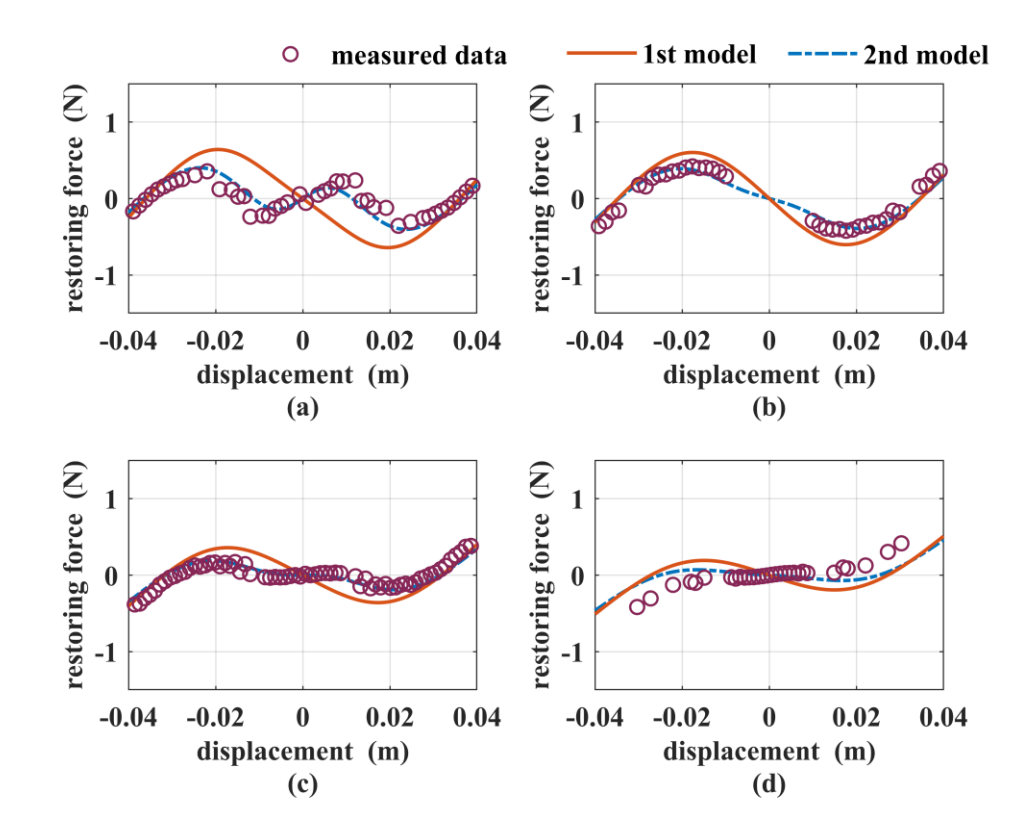


Figure 2.7 The total restoring forces of: (a) Case (1); (b) Case (2); (c) Case (3); (d) Case (4).

### 2.5 Model Optimization

As shown in the previous section, although the 2<sup>nd</sup> model gives a better prediction for the restoring force than the 1<sup>st</sup> model in Cases (1), (2), and (3), it fails to do so in Case (4). It is natural to ask a question of whether both models can be improved by optimization. For this purpose, an optimization based on the multi-population genetic algorithm (MPGA) [43] is carried out to identify the magnitudes of the magnetic vectors for the 1st model, and the amounts of the total charges for the 2nd model. Different from the standard genetic algorithm, which only has a single population group, the MPGA initializes the whole population as multiple population groups to operate the selection, crossover and mutation independently. Figure 2.8 shows the flowchart of the MPGA. Note that the flowchart only shows two population groups as an example. In the beginning, the initial ranges of the parameters, the population size, the population group number, and the maximum iteration number need to be specified. After the initialization, the individuals of the first population are randomly generated within the specified ranges, and they are arranged into different population groups. Then, the fitness values or objective functions are evaluated. The best individual of each population group will immigrate to the other population groups and participate in the respective groups' selection, crossover, and mutation operation process. The main purpose of the immigration operator is to prevent the decrease in genetic diversity of a single population group. After that, the new offspring will be generated and prepared for the evaluation process in the next iteration. On the other hand, the best individual of each iteration will always be collected to the quintessence population group. As the maximum iteration number is reached, the individual in the quintessence population who has the minimum fitness value will be chosen as the optimum individual.

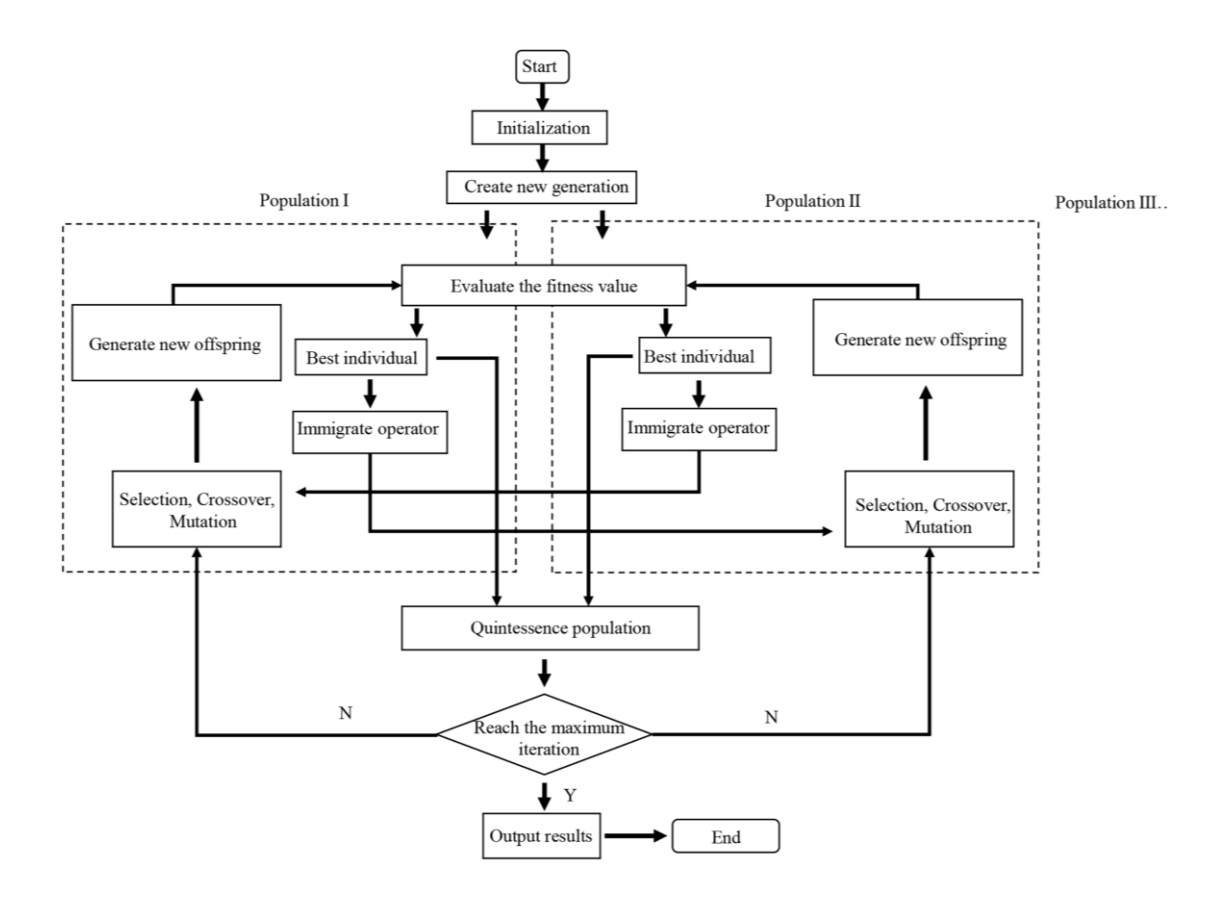


Figure 2.8 The flowchart of the MPGA.

The training data of the optimization are chosen from the measured restoring forces of the three different configurations of the system: Case (5) d = 0.0587 m, h = 0.0187 m; Case (6) d = 0.0502 m, h = 0.0162 m; Case (7) d = 0.0372 m, h = 0.0162 m, which make the system exhibit mono-stable, bi-stable, and tri-stable stability state, respectively. The main reason for choosing the configuration cases different from Cases (1) to (4) is to prevent the local minima problem to happen in optimization. In this way, it will guarantee that the optimized model is able to predict any configuration in the system's parameters region. The parameters to be optimized for the 1<sup>st</sup> model are chosen to be  $m_A$ ,  $m_B$ , and  $m_D$ . First, to have a fair comparison, the parameters to be optimized for the 2<sup>nd</sup> model are chosen to be  $Q_A$ ,  $Q_B$ , and  $Q_D$  where  $Q_1 = -Q_B$ ,  $Q_2 = Q_B$ ,  $Q_3 = -Q_A$ ,  $Q_4 = Q_A$ ,  $Q_5 = -Q_D$ ,  $Q_6 = Q_D$ . The fitness function used in the optimization for the 1<sup>st</sup> model is defined as:

$$J_1(m_A, m_B, m_D) = \sqrt{\frac{1}{3N} \sum_{j=5}^{7} \sum_{i=1}^{N} (f_{jm}(x_i) - f_{ja1}(x_i))^2}$$
 (2.26)

and the fitness function used in the optimization for the  $2^{nd}$  model is defined as

$$J_2(Q_A, Q_B, Q_D) = \sqrt{\frac{1}{3N} \sum_{j=5}^{7} \sum_{i=1}^{N} (f_{jm}(x_i) - f_{ja2}(x_i))^2}$$
 (2.27)

where  $f_{jm}(x_i)$  is the measured restoring forces that are smoothened by a spline fitting,  $f_{a1}(x_i)$  is the analytical restoring forces based on the 1<sup>st</sup> model,  $f_{a2}(x_i)$  is the analytical restoring forces based on the 2<sup>nd</sup> model, and N=81 is the number of data. The reasons for interpolating the measured restoring forces with spline fitting are twofold: to alleviate the influence of measurement noise and to use the same amount of data in optimization for all cases that have different numbers of the raw data. The parameter search ranges for the 1<sup>st</sup> model are chosen as  $0 \le m_A \le 10$ ,  $0 \le m_B \le 1$  and  $0 \le m_D \le 30$ , and the parameter search ranges for the 2<sup>nd</sup> model are chosen as  $0 \le Q_A \le 400$ ,  $0 \le Q_B \le 200$  and  $0 \le Q_D \le 1200$ . For both models, the maximum number of iterations is set to be 200, and the number of the population group and the size of each group are set to 100 and 500, respectively.

Table 2.2 lists the optimization results where the differences between the original values and the optimized values are represented by  $\sigma$ . It can be seen that the original magnitudes of the magnetic vectors are underestimated for  $m_A$  and  $m_B$  and overestimated for  $m_D$ . And there is a significant difference between the original magnitude and optimized magnitude for  $m_B$ . On the other hand, for the 2<sup>nd</sup> model, the original amounts of the total charges are underestimated for  $Q_B$  and  $Q_A$  and overestimated for  $Q_D$ . Accordingly, for both modelling approaches, the effect of magnet B is underestimated while the effect of magnet D is overestimated, which is the leading cause of the errors in prediction, as shown in Figure 2.7.

Table 2.2 The optimization results of the 1<sup>st</sup> model and 2<sup>nd</sup> model.

	1 <sup>st</sup> model		σ%	2 <sup>nd</sup> model with three independent parameters		σ%
	Original	Optimize d		Original	Optimized	
Magnet A	$m_A = 3.74$	$m_A^* = 3.802$	1.6	$Q_A = 147.17$	$Q_A^* = 209.14$	42.10
Magnet B	$m_B = 0.46$	$m_B^* = 0.803$	74.56	$Q_B = 57.49$	$Q_B^*=80.13$	39.38
Magnet D	$m_D = 14.95$	$m_D^* = 11.96$	-20	$Q_D = 588.71$	$Q_D^* = 334.78$	-43.13

Using the optimum parameters, the simulations of the restoring forces for Cases (1), (2), (3) and (4) are conducted, and the results are shown in Figure 2.9. The blue dashed lines and red solid lines represent the values of the restoring force based on the optimized 1<sup>st</sup> model and the optimized 2<sup>nd</sup> model, respectively. It can be seen that both optimized models fit the measured values well for all four cases. Table 2.3 gives a quantitative comparison of the fitness values for the four cases. It can be seen that the fitness value for the 1<sup>st</sup> model is drastically reduced and becomes slightly smaller than the fitness value for the 2<sup>nd</sup> model. Clearly, the proposed optimization significantly improves the accuracy of the 1<sup>st</sup> model.

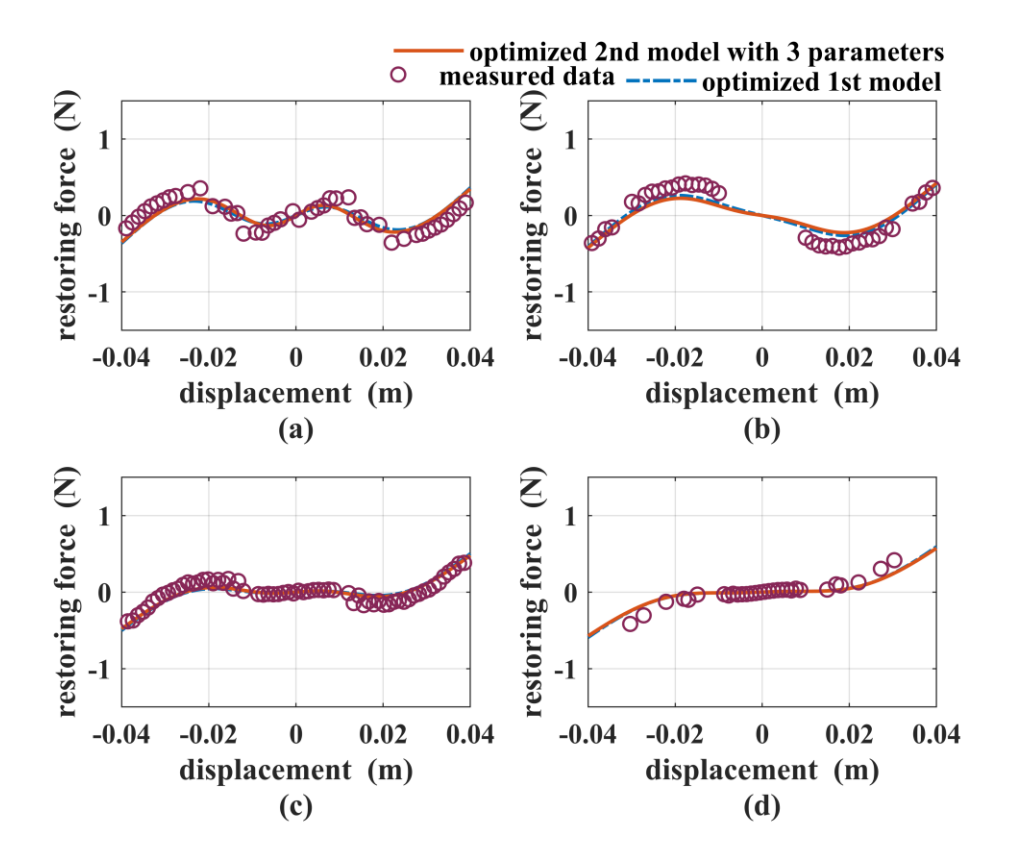


Figure 2.9 The total restoring forces for: (a) Case (1); (b) Case (2); (c) Case (3); (d) Case (4) based on the optimized models.

Table 2.3 The fitness value of Case (I) to (IV) using original and optimized  $1^{st}$  and  $2^{nd}$  model.

	Model categories	fitness values	
Original model	Original 1st model	0.248	
Original model	Original 2 <sup>nd</sup> model	0.131	
	Optimized 1 <sup>st</sup> model	0.104	
	Optimized 2 <sup>nd</sup> model with three independent	0.111	
	parameters	0.111	
Optimized model	Optimized 2 <sup>nd</sup> model with six independent		
	parameters		
	Optimized 2 <sup>nd</sup> model with five independent		
	parameters	0.0917	

The above optimization indicates that both optimum models offer a comparable accuracy for the prediction of the restoring forces. As the second approach treats a magnet as a 2-point dipole, it provides more freedom for controlling the model accuracy. One of the possible ways to further improve the model accuracy is to consider all the total charges  $Q_1,\,Q_2,\,Q_3,\,Q_4,\,Q_5,$  and  $Q_6$  as independent parameters. A six-parameter optimization is conducted by using the same parameter ranges and initialization process mentioned above. Note that the fitness function in Eq. (2.27) now becomes  $J_2(Q_1,Q_2,Q_3,Q_4,Q_5,Q_6)$ . The results are given in Tables 2.3 and 2.4. Table 2.3 shows that the accuracy model can be further improved if all the total charges are identified. And as shown in Table.2.4, the almost zero value for the optimum charge  $Q_3^*$  warrants an investigation. A plausible explanation is that, as shown in Figure 2.5, the left surface of magnets A and C is farthest away from magnet D, which means the effect of this surface is less critical in the magnetic force model. Thus, an assumption can be made that the total charge  $\mathcal{Q}_3$  can be neglected so that there are five independent parameters to be optimized. By defining the fitness function as  $J_2(Q_1,Q_2,Q_4,Q_5,Q_6)$ , a fiveparameter optimization is conducted. The results are shown in Tables 2.3 and 2.4 as well. It can be seen that the fitness values for the 2<sup>nd</sup> models with six and five independent parameters are almost the same. After conducting simulations for Cases (1) to (4) based on such two models, the results are shown in Figure 2.10, The red solid lines and the blue dashed lines in Figure 2.10 represent the values of the restoring force based on the optimized 2<sup>nd</sup> model with six and five independent parameters, respectively. It's found that both two models fit the measured ones well for all four cases and their predicted values are almost the same. The results validate the assumption that the total charge  $Q_3$  of the  $2^{\rm nd}$  model can be neglected in the optimization, and it also proves that the simplified five-parameter optimization can make the 2<sup>nd</sup> model reach the same accuracy level as the optimum six-parameter model

does.

Table 2.4 The optimization results of the 2<sup>nd</sup> model with six or five parameters.

	2 <sup>nd</sup> model with six independent parameters		σ%	2 <sup>nd</sup> model with five independent parameters		σ%
	Original	Optimized		Original	Optimized	
Magnet	$Q_3 = 147.17$	$Q_3^*=0.0017$	-99.99	$Q_3 = 147.17$	$Q_3^* = 0$	-100
A	$Q_4$ =147.17	$Q_4^*$ =227.05	54.27	$Q_4$ =147.17	$Q_4^*$ =295.67	100.9
Magnet	$Q_1 = 57.49$	$Q_1^*=13.15$	-77.13	$Q_1 = 57.49$	$Q_1^*=11.96$	-79.19
В	$Q_2 = 57.49$	$Q_2^* = 55.95$	-2.68	$Q_2 = 57.49$	$Q_2^* = 70.72$	23.01
Magnet	$Q_5 = 588.71$	$Q_5^* = 497.74$	-15.45	$Q_5 = 588.71$	$Q_5^* = 388.73$	-33.96
D	$Q_6 = 588.71$	$Q_6^*$ =892.90	51.67	$Q_6 = 588.71$	$Q_6^*$ =698.95	18.72

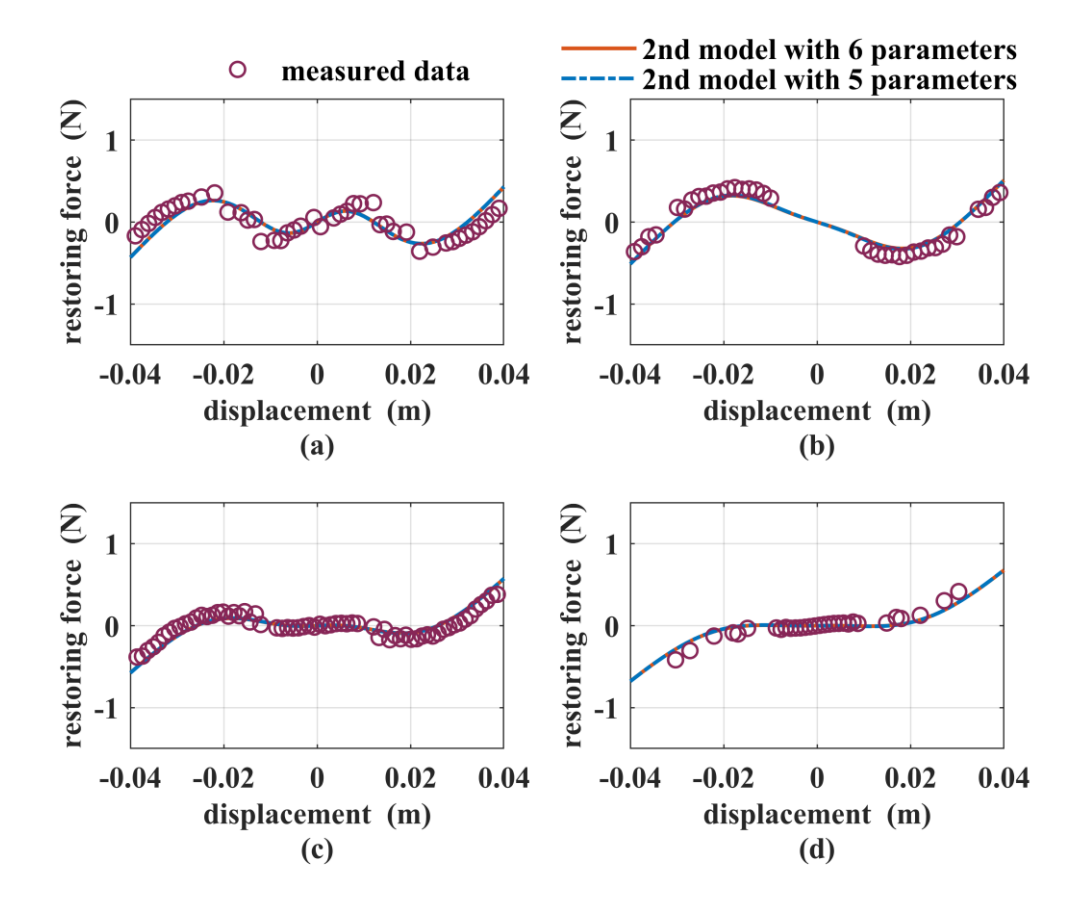


Figure 2.10 The total restoring forces for: (a) Case (1); (b) Case (2); (c) Case (3);

(d) Case (4) based on the optimized 2<sup>nd</sup> models with six and five independent parameters.

### 2.6 The Parametric Sensitivity Study and Stability State Region

The sensitivity study intends to evaluate the model robustness against parametric variation. For this purpose, each of the three parameters in the optimum  $1^{st}$  model and the optimum  $2^{nd}$  model with three parameters is perturbated by  $\pm 10\%$ . The error between the optimum  $1^{st}$  model and perturbated  $1^{st}$  model is defined as:

$$e_{j} = \sqrt{\frac{1}{N} \sum_{i=1}^{N} (f_{ja1}^{P}(x_{i}) - f_{ja1}^{*}(x_{i}))^{2}} \qquad j = 5, 6, 7$$
 (2.28)

where  $f_{jal}^*(x_i)$  and  $f_{jal}^P(x_i)$  are the restoring forces of the optimum 1<sup>st</sup> model and the perturbated 1<sup>st</sup> model, respectively, N=81 is the number of the data used. The error between the optimum 2<sup>nd</sup> model and the perturbated 2<sup>nd</sup> model is defined as:

$$e_{j} = \sqrt{\frac{1}{N} \sum_{i=1}^{N} (f_{ja2}^{P}(x_{i}) - f_{ja2}^{*}(x_{i}))^{2}} \qquad j = 5, 6, 7$$
 (2.29)

where  $f_{ja2}^*(x_i)$  and  $f_{ja2}^P(x_i)$  are the restoring forces of the optimum  $2^{\rm nd}$  model and the perturbated  $2^{\rm nd}$  model, respectively. Table 2.5 lists the errors by perturbating one parameter by 10%. It should be noted that if the parameter is perturbated by -10%, the errors remain unchanged. Based on the results, several observations can be drawn for both models. The parameter variation of magnet A and C affects the restoring forces most significantly. The tri-stable state is most sensitive to the parameter variation while the mono-stable state is least sensitive to the parameter variation. In addition, based on the average errors given in the last column of Table 2.5, the  $2^{\rm nd}$  model is slightly more robust than the  $1^{\rm st}$  model when the parameters of magnets A (C) and B are perturbated, and both models have equal robustness when the parameter of magnet D is perturbated.

Figures 2.11 and 2.12 shows the restoring forces values based on the optimum

models and perturbated model. The blue lines represent the restoring forces of the optimum 1<sup>st</sup> model or 2<sup>nd</sup> model, and the red, yellow and purple lines are the restoring forces of both models when varying the parameters of magnet A, magnet B and magnet D, respectively. The figures confirm the observations made above. The figures also show the effect of the parameter variation on the trends of the restoring forces. As shown in Figures 2.11(a) (b) and 2.12(a) (b), an increase in  $m_B$  or  $Q_B$  strengthens the mono-stable or tri-stable state most significantly while an increase of  $m_A$  or  $Q_A$  weakens the mono-stable or tri-stable state most significantly. As shown in Figures 2.11(c) and 2.12(c), an increase of  $m_A$  or  $Q_A$  results in a stronger bi-stable state while an increase of  $m_B$  or  $Q_B$  results in a weaker bi-stable state. Such effects are expected as magnet B is critical for the mono-stable state or tri-stable state while magnets A and C are critical for the bi-stable state. The opposite effects occur when the parameters are decreased by 10%.

Table 2.5 Errors for Cases (5), (6) and (7) of the optimized 1<sup>st</sup> and 2<sup>nd</sup> models with detuned parameters

	Parameter	$e_5$	$e_6$	$e_7$	$\overline{e}$
Model	s	Mono- stable	Tri-stable	Bi-stable	$=\frac{e_5+e_6+e_7}{3}$
	$1.1m_A^*, m_B^*, m_D^*$	5.2×10 <sup>-2</sup>	16.0×10 <sup>-2</sup>	9.0×10 <sup>-2</sup>	10.1×10 <sup>-2</sup>
1	$m_A^*, 1.1 m_B^*, m_D^*$	2.0×10 <sup>-2</sup>	10.9×10 <sup>-2</sup>	3.6×10 <sup>-2</sup>	5.5×10 <sup>-2</sup>
	$m_A^*, m_B^*, 1.1 m_D^*$	3.2×10 <sup>-2</sup>	7.0×10 <sup>-2</sup>	5.5×10 <sup>-2</sup>	5.2×10 <sup>-2</sup>
2	$1.1Q_A^*, Q_B^*, Q_D^*$	4.2×10 <sup>-2</sup>	11.9×10 <sup>-2</sup>	7.1×10 <sup>-2</sup>	7.7×10 <sup>-2</sup>
	$Q_A^*, 1.1Q_B^*, Q_D^*$	1.0×10 <sup>-2</sup>	6.9×10 <sup>-2</sup>	2.0×10 <sup>-2</sup>	3.3×10 <sup>-2</sup>
	$Q_A^*, Q_B^*, 1.1Q_D^*$	3.2×10 <sup>-2</sup>	7.1×10 <sup>-2</sup>	5.2×10 <sup>-2</sup>	5.2×10 <sup>-2</sup>

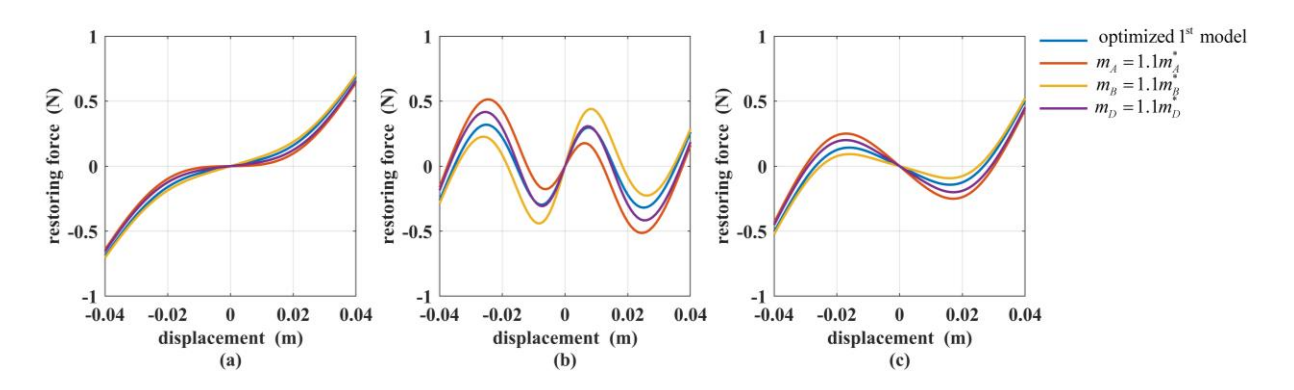


Figure 2.11 The total restoring forces of the optimized and perturbated 1<sup>st</sup> model for: (a) Case (5); (b) Case (6); (c) Case (7).

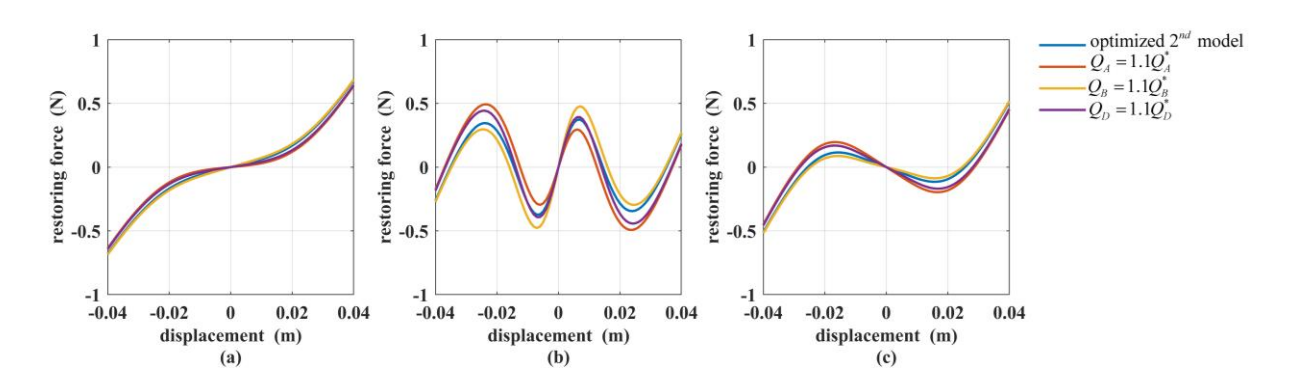


Figure 2.12 The total restoring forces of the optimized and perturbated 2<sup>nd</sup> model for: (a) Case (5); (b) Case (6); (c) Case (7).

With the optimum models, the so-called stability state region can be generated by varying the tuning parameters d and h. Figure 2.13 shows such plot by using the optimum  $2^{nd}$  model with five independent parameters, where S, M and W denote the strong, medium and weak stability state based on the depth of potential wells, respectively. The stability state region clearly shows that by tuning d and h, the proposed apparatus can achieve the tri-stable, bi-stable, and mono-stable stability states, respectively.

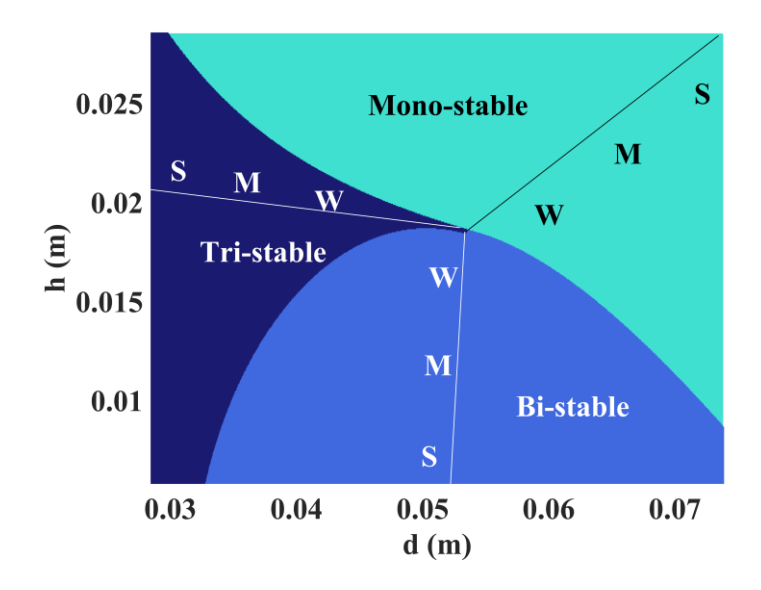


Figure 2.13 Stability state region.

## 2.7 Conclusions

In this study, a tunable multi-stable piezoelectric energy harvester has been developed for applications in an ambient vibration environment with a broad frequency band. The apparatus can be manually tuned to achieve tri-stable, bi-stable, and monostable stability states. The magnetic restoring forces of the apparatus have been derived by using two approaches named as 1<sup>st</sup> model and 2<sup>nd</sup> model, respectively. An experimental validation of both models has been conducted. It has been found that although the 2<sup>nd</sup> model is more accurate than the 1<sup>st</sup> model, it has its own limitation. A model optimization has been carried out by using the multi-population genetic algorithm (MPGA). The magnitudes of the magnetic vectors and the amounts of the surface charges of the three magnets have been chosen as parameters to be optimized for the 1<sup>st</sup> and 2<sup>nd</sup> model, respectively. The results show that two optimum models can achieve almost the same level of accuracy. The results also show that the optimum 2<sup>nd</sup> model has a larger error in predicting the restoring force of the bi-stable state case than the optimum 1<sup>st</sup> model. To further improve the accuracy of the 2<sup>nd</sup> model, the six-parameter optimization has been carried out by assuming that the two surface charges

of an individual magnet are different. The results show that the accuracy of the 2<sup>nd</sup> model with six independent parameters can be further improved. The results also show that the optimum value of  $Q_3$  is almost zero, as the corresponding surface is farthest away from magnet D. Based on this observation, magnets A and C can be treated as one point dipole so that the number of independent parameters can be reduced to five in the optimization. The results show that the optimum 2<sup>nd</sup> model with five parameters has the highest accuracy among all the three optimum models. With the optimum models, the parametric sensitivity has been investigated by perturbating each of the three parameters by  $\pm 10\%$ . The following observations have been drawn. The parameter variation of magnet A affects the restoring forces most significantly. The tristable state is most sensitive to the parameter variation, while the mono-stable state is least sensitive to the parameter variation. In addition, the 2<sup>nd</sup> model is slightly more robust than the 1st model when the parameters of magnets A and B are perturbated, and both models have equal robustness when the parameter of magnet D is perturbated. With the optimum 2<sup>nd</sup> model, the stability state region has been generated to show that the developed apparatus possesses a large parameter tuning space.

## References

- [1] W. Tian, Z. Ling, W. Yu, and J. Shi, "A review of MEMS scale piezoelectric energy harvester," *Applied Sciences*, vol. 8, no. 4, 2018, doi: 10.3390/app8040645.
- [2] Q. Lu, F. Scarpa, L. Liu, J. Leng, and Y. Liu, "An E-shape broadband piezoelectric energy harvester induced by magnets," *Journal of Intelligent Material Systems and Structures*, vol. 29, no. 11, pp. 2477-2491, 2018, doi: 10.1177/1045389x18770871.
- [3] M. Derayatifar, R. Sedaghati, S. Chandramohan, M. Packirisamy, and R. Bhat, "Dynamic analysis of a functionally graded piezoelectric energy harvester under magnetic interaction," *Journal of Intelligent Material Systems and Structures*, vol. 32, no. 9, pp. 986-1000, 2021, doi: 10.1177/1045389x21990886.

- [4] C. B. Williams and R. B. Yates, "Analysis of a micro-electric generator for microsystems," *Sensors and Actuators A: Physical*, vol. 52, no. 1, pp. 8-11, 1996/03/01/1996, doi: https://doi.org/10.1016/0924-4247(96)80118-X.
- [5] Y. Pan *et al.*, "Modeling and field-test of a compact electromagnetic energy harvester for railroad transportation," *Applied Energy*, vol. 247, pp. 309-321, 2019.
- [6] M. A. Halim, H. Cho, and J. Y. Park, "Design and experiment of a human-limb driven, frequency up-converted electromagnetic energy harvester," *Energy Conversion and Management*, vol. 106, pp. 393-404, 2015.
- [7] B. Zaghari, E. Rustighi, and M. Ghandchi Tehrani, "Phase dependent nonlinear parametrically excited systems," *Journal of Vibration and Control*, vol. 25, no. 3, pp. 497-505, 2019, doi: 10.1177/1077546318783566.
- [8] Y. Zhang, T. Wang, A. Luo, Y. Hu, X. Li, and F. Wang, "Micro electrostatic energy harvester with both broad bandwidth and high normalized power density," *Applied energy*, vol. 212, pp. 362-371, 2018.
- [9] H. Koga, H. Mitsuya, H. Honma, H. Fujita, H. Toshiyoshi, and G. Hashiguchi, "Development of a cantilever-type electrostatic energy harvester and its charging characteristics on a highway viaduct," *Micromachines*, vol. 8, no. 10, p. 293, 2017.
- [10] D.-H. Choi, C.-H. Han, H.-D. Kim, and J.-B. Yoon, "Liquid-based electrostatic energy harvester with high sensitivity to human physical motion," *Smart materials and structures*, vol. 20, no. 12, p. 125012, 2011.
- [11] P. Wang *et al.*, "An ultra-low-friction triboelectric-electromagnetic hybrid nanogenerator for rotation energy harvesting and self-powered wind speed sensor," *ACS Nano*, vol. 12, no. 9, pp. 9433-9440, Sep 25 2018, doi: 10.1021/acsnano.8b04654.
- [12] K. Tao *et al.*, "Origami-inspired electret-based triboelectric generator for biomechanical and ocean wave energy harvesting," *Nano Energy*, vol. 67, 2020, doi: 10.1016/j.nanoen.2019.104197.
- [13] S. Roundy and P. K. Wright, "A piezoelectric vibration based generator for wireless electronics," *Smart Materials and Structures*, vol. 13, no. 5, pp. 1131-1142, 2004, doi: 10.1088/0964-1726/13/5/018.
- [14] S. Roundy, P. K. Wright, and J. Rabaey, "A study of low level vibrations as a power source for wireless sensor nodes," *Computer Communications*, vol. 26, no. 11, pp. 1131-1144, 2003/07/01/ 2003, doi: https://doi.org/10.1016/S0140-3664(02)00248-7.

- [15] S. Yu and S. He, "Accurate free vibration analysis of cantilever piezoelectric panel carrying a rigid mass," *Journal of Vibration and Control*, vol. 19, no. 8, pp. 1187-1198, 2013, doi: 10.1177/1077546312444657.
- [16] J. Twiefel and H. Westermann, "Survey on broadband techniques for vibration energy harvesting," *Journal of Intelligent Material Systems and Structures*, vol. 24, no. 11, pp. 1291-1302, 2013, doi: 10.1177/1045389x13476149.
- [17] Z. Yang, S. Zhou, J. Zu, and D. Inman, "high-performance piezoelectric energy harvesters and their applications," *Joule*, vol. 2, no. 4, pp. 642-697, 2018, doi: 10.1016/j.joule.2018.03.011.
- [18] R. Ramlan, M. J. Brennan, B. R. Mace, and I. Kovacic, "Potential benefits of a non-linear stiffness in an energy harvesting device," *Nonlinear Dynamics*, vol. 59, no. 4, pp. 545-558, 2009, doi: 10.1007/s11071-009-9561-5.
- [19] K. Yang, J. Wang, and D. Yurchenko, "A double-beam piezo-magneto-elastic wind energy harvester for improving the galloping-based energy harvesting," *Applied Physics Letters*, vol. 115, no. 19, 2019, doi: 10.1063/1.5126476.
- [20] S. C. Stanton, C. C. McGehee, and B. P. Mann, "Reversible hysteresis for broadband magnetopiezoelastic energy harvesting," *Applied Physics Letters*, vol. 95, no. 17, 2009, doi: 10.1063/1.3253710.
- [21] H. Fu and E. M. Yeatman, "Rotational energy harvesting using bi-stability and frequency up-conversion for low-power sensing applications: Theoretical modelling and experimental validation," *Mechanical Systems and Signal Processing*, vol. 125, pp. 229-244, 2019/06/15/ 2019, doi: https://doi.org/10.1016/j.ymssp.2018.04.043.
- [22] M. Rezaei, R. Talebitooti, and W.-H. Liao, "Exploiting bi-stable magneto-piezoelastic absorber for simultaneous energy harvesting and vibration mitigation," *International Journal of Mechanical Sciences*, vol. 207, p. 106618, 2021/10/01/2021, doi: https://doi.org/10.1016/j.ijmecsci.2021.106618.
- [23] Z. Xie, C. A. Kitio Kwuimy, T. Wang, X. Ding, and W. Huang, "Theoretical analysis of an impact-bistable piezoelectric energy harvester," *The European Physical Journal Plus*, vol. 134, no. 5, 2019, doi: 10.1140/epjp/i2019-12569-2.
- [24] G. Wang, W.-H. Liao, B. Yang, X. Wang, W. Xu, and X. Li, "Dynamic and energetic characteristics of a bistable piezoelectric vibration energy harvester with an elastic magnifier," *Mechanical Systems and Signal Processing*, vol. 105, pp. 427-446, 2018, doi: 10.1016/j.ymssp.2017.12.025.
- [25] S. Bae and P. Kim, "Load resistance optimization of a broadband bistable piezoelectric energy harvester for primary harmonic and subharmonic behaviors," *Sustainability*, vol. 13, no. 5, 2021, doi: 10.3390/su13052865.

- [26] S. Zhao and A. Erturk, "On the stochastic excitation of monostable and bistable electroelastic power generators: relative advantages and tradeoffs in a physical system," *Applied Physics Letters*, vol. 102, no. 10, 2013, doi: 10.1063/1.4795296.
- [27] A. Erturk, J. Hoffmann, and D. J. Inman, "A piezomagnetoelastic structure for broadband vibration energy harvesting," *Applied Physics Letters*, vol. 94, no. 25, 2009, doi: 10.1063/1.3159815.
- [28] S. Zhou, J. Cao, A. Erturk, and J. Lin, "Enhanced broadband piezoelectric energy harvesting using rotatable magnets," *Applied Physics Letters*, vol. 102, no. 17, p. 173901, 2013, doi: 10.1063/1.4803445.
- [29] J. Cao, S. Zhou, W. Wang, and J. Lin, "Influence of potential well depth on nonlinear tristable energy harvesting," *Applied Physics Letters*, vol. 106, no. 17, p. 173903, 2015, doi: 10.1063/1.4919532.
- [30] L. Haitao, Q. Weiyang, L. Chunbo, D. Wangzheng, and Z. Zhiyong, "Dynamics and coherence resonance of tri-stable energy harvesting system," *Smart Materials and Structures*, vol. 25, no. 1, p. 015001, 2016, doi: 10.1088/0964-1726/25/1/015001.
- [31] G. Wang *et al.*, "Nonlinear magnetic force and dynamic characteristics of a tristable piezoelectric energy harvester," *Nonlinear Dynamics*, vol. 97, no. 4, pp. 2371-2397, 2019, doi: 10.1007/s11071-019-05133-z.
- [32] S. C. Stanton, C. C. McGehee, and B. P. Mann, "Nonlinear dynamics for broadband energy harvesting: Investigation of a bistable piezoelectric inertial generator," *Physica D: Nonlinear Phenomena*, vol. 239, no. 10, pp. 640-653, 2010, doi: 10.1016/j.physd.2010.01.019.
- [33] L. Tang and Y. Yang, "A nonlinear piezoelectric energy harvester with magnetic oscillator," *Applied Physics Letters*, vol. 101, no. 9, p. 094102, 2012, doi: 10.1063/1.4748794.
- [34] S. Fang, X. Fu, and W.-H. Liao, "Asymmetric plucking bistable energy harvester: Modeling and experimental validation," *Journal of Sound and Vibration*, vol. 459, p. 114852, 2019, doi: 10.1016/j.jsv.2019.114852.
- [35] Y. Leng, D. Tan, J. Liu, Y. Zhang, and S. Fan, "Magnetic force analysis and performance of a tri-stable piezoelectric energy harvester under random excitation," *Journal of sound and vibration*, vol. 406, pp. 146-160, 2017.
- [36] D. Tan, Y. G. Leng, and Y. J. Gao, "Magnetic force of piezoelectric cantilever energy harvesters with external magnetic field," *The European Physical Journal Special Topics*, vol. 224, no. 14, pp. 2839-2853, 2015/11/01 2015, doi: 10.1140/epjst/e2015-02592-6.

- [37] G. Wang, H. Wu, W.-H. Liao, S. Cui, Z. Zhao, and J. Tan, "A modified magnetic force model and experimental validation of a tri-stable piezoelectric energy harvester," *Journal of Intelligent Material Systems and Structures*, vol. 31, no. 7, pp. 967-979, 2020, doi: 10.1177/1045389X2090597.
- [38] Y. Ju, Y. Li, J. Tan, Z. Zhao, and G. Wang, "Transition mechanism and dynamic behaviors of a multi-stable piezoelectric energy harvester with magnetic interaction," *Journal of Sound and Vibration*, vol. 501, p. 116074, 2021/06/09/2021, doi: https://doi.org/10.1016/j.jsv.2021.116074.
- [39] Y. Zhang, J. Cao, W. Wang, and W.-H. Liao, "Enhanced modeling of nonlinear restoring force in multi-stable energy harvesters," *Journal of Sound and Vibration*, vol. 494, p. 115890, 2021/03/03/ 2021, doi: https://doi.org/10.1016/j.jsv.2020.115890.
- [40] K. W. Yung, P. B. Landecker, and D. D. Villani, "An analytic solution for the force between two magnetic dipoles," *Physical Separation in Science and Engineering*, vol. 9, no. 1, pp. 39-52, 1998.
- [41] K. Worden, "Data processing and experiment design for the restoring force surface method, part I: integration and differentiation of measured time data," *Mechanical Systems and Signal Processing*, vol. 4, no. 4, pp. 295-319, 1990/07/01/1990, doi: https://doi.org/10.1016/0888-3270(90)90010-I.
- [42] H. Li, "A tunable multi-stable piezoelectric vibration energy harvester," Mechanical engineering, Lakehead University, published, 2021. [Online]. Available: https://knowledgecommons.lakeheadu.ca/handle/2453/4966
- [43] J.-O. Kim and P. Khosla, "A multi-population genetic algorithm and its application to design of manipulators," Proceedings of the IEEE/RSJ International Conference on Intelligent Robots and Systems, 1992, July 07-10 Raleigh, NC, USA.

# Chapter 3. Modelling and Evaluation of a Multi-Stable

# **Hybrid Energy Harvester**

#### 3.1 Introduction

A vibration energy harvester (VEH) is a device that converts ambient mechanical energy into electrical energy. There are various ambient mechanical energies that can be captured, such as structural vibration [1], machinery vibration [2], and human motion [3]. The VEH provides a promising solution to a growing demand for self-sustainable power supply for wearable electronic devices and wireless sensor node networks, especially when deploying conventional power sources such as power lines or batteries is inconvenient or impractical [4].

In general, a traditional VEH consists of a linear oscillator that has a narrow operation frequency bandwidth. Over the last two decades, there has been a growing interest in enhancing the working bandwidth and energy harvesting efficiency of VEHs for different environments. Introducing nonlinearity is one of the promising solutions to broaden the working bandwidth of VEHs. Various nonlinear VEHs have been proposed [5]. According to the system stability state, the nonlinear VEHs can be classified as mono-stable and multi-stable, such as bi-stable or tri-stable. A mono-stable energy harvester reported in [6] consists of a piezoelectric cantilever beam with a tip magnet subjected to an external magnetic field generated by a pair of fixed magnets. Such a mono-stable system can exhibit softening or hardening behaviors when the magnetic interaction is adjusted. The energy harvesting performance of a mono-stable energy harvester was investigated in [7]. The study showed that the high-branch oscillation leads to a high energy harvesting efficiency. A bi-stable energy harvester can be used to improve energy harvesting performance by utilizing the snappingthrough feature. As proved in [8], the inter-well oscillation of a bi-stable energy harvester can significantly enhance its power output performance. The study reported in [9] showed that a bi-stable energy harvester with an elastic magnifier can provide

higher power output and wider working bandwidth. One of the drawbacks of bi-stable energy harvesters is the requirement of a sufficient excitation level in order to overcome the barrier of the potential wells. Tri-stable energy harvester was proposed to address this drawback. Based on the configuration of the bi-stable energy harvester in [8], a tri-stable energy harvester was achieved by tuning the orientation 43s [10] and the positions [11,12] of the two fixed magnets. Moreover, the performance of an asymmetric tri-stable energy harvester was investigated in [12]. The studies showed that the proposed tri-stable energy harvester outperforms the bi-stable energy harvesters under the low-level excitation in terms of the voltage output.

On the other hand, the concept of hybrid systems has been proposed to enhance both the energy density and the power output. There are two kinds of hybrid systems: the first one can convert multiple energy sources such as solar, thermal or vibration into electricity [13]; the second one can convert a single energy source such as vibration into electricity through multiple conversion mechanisms [14]. This study considers the second type. There are three main transduction mechanisms for the VEH, namely piezoelectric [15], electromagnetic [16], and electrostatic [17]. Each of them has its own advantages and disadvantages. For example, the piezoelectric energy harvester (PEH) has high energy density and easy to deploy, the electromagnetic energy harvester (EMEH) shows the benefits of high current output and ease of maintenance, and the electrostatic energy harvester has the advantages of compact design and wider working bandwidth. A VEH combined with two or more transduction mechanisms is referred to as hybrid energy harvester (HEH), yielding better efficiency and robustness [18,19]. This paper focuses on the HEH consisting of a PEH and an EMEH.

A HEH proposed in [20] consists of a cantilever beam patched with a PEH and attached with a tip magnet that moves inside a coil placed on the base. The study provided an approach of coupling the PEH and EMEH to increase the power output. A power management circuit was designed in [21] to overcome the impedance mismatching issue of the HEH. The HEHs proposed in [22] and [23] utilized a 2-degree-freedom structure to improve the power output. To enhance the performance of the HEH under ultra-low frequency excitation, the frequency up-conversion design of the HEH was proposed in [24]. In addition, a multi-modal HEH was developed in [25] to make the system able to operate at four different resonant modes, significantly

widening the operation bandwidth. There have been conflicting views on the benefits of a linear HEH under harmonic excitation. For example, a recent study [26] showed that under harmonic excitation, an idealized two-port linear HEH with electrical loss neglected offers little benefit in terms of the maximum output power. On the other hand, introducing nonlinearity to the HEH has been explored by some researchers. For example, a mono-stable HEHs proposed in [27,28] showed that the nonlinearity can significantly boost the energy density and widen the frequency bandwidth. A bi-stable HEH was proposed in [29] to improve the power output. In the study, an approximate method was used to simplify the modelling of the coupled system. A bi-stable HEH developed in [30] used the tunable stiffness design to achieve better adaptability for various environments. Further, the studies reported in [31,32] showed that the tri-stable HEH is beneficial for enhancing both operation bandwidth and output power compared with the mono-stable and bi-stable HEHs.

The above review indicates a need for a nonlinear HEH whose stability states can be adjusted in order to achieve better adaptability in terms of power output and frequency bandwidth. To address such a need, based on our previous study [33], a tunable multi-stable hybrid energy harvester (MSHEH) is proposed in this study. Different from the existing designs that use two external magnets [34-37], the MSHEH employs a single external magnet, which makes the magnetic spring more compact and makes implementation of an EMEH easy. The EMEH is realized by placing one set of six coils above and one set of six coils below the two moving magnets. With this novel arrangement, the magnetic flux on both the moving magnets' upper surface and the lower surface can be effectively utilized, and the space efficiency of the EMEH can be improved compared with the existing designs, such as the ones in [29,38,39].

The contributions of the present study lie in four aspects. Firstly, the proposed MSHEH is novel in terms of stability tuning and the EMEH design. Secondly, a numerical modelling procedure is developed to determine the transduction factor of the EMEH. Thirdly, a comparative study is conducted to evaluate the energy harvesting performances of four different configurations subjected to the frequency sweep excitation. Fourthly, a Pareto front optimization is conducted to maximize the power output of both EMEH and PEH under harmonic excitations with various exciting frequencies. In addition, further optimization is conducted to maximize the

accumulated harvested energy for both EMEH and PEH under high-level frequency upsweep excitation.

# 3.2 Apparatus and modelling

Figure 3.1(a) shows a solid modelling drawing of the proposed MSHEH. As shown in the figure, a thin stainless-steel beam is clamped to a platform which is fastened to a base by using four aluminum extrusions. Each side of the upper end of the beam is attached by a piezoelectric transducer or PZT (S128-J1FR-1808YB, Midé), while its lower end is fixed with a small cylindrical magnet B and attached with a holder for an assembly of two identical cylindrical magnets A and C. The holder can be fixed on any position along the beam by sliding. A large cylindrical magnet D is fixed in a holder that can slide vertically in a stand on the base. When the cantilever beam is at its equilibrium position or undeflected, the four magnets are situated on the same vertical plane, and magnets B and D are collinear. By sliding the holder for magnet D, the distance between magnet B and magnet D can be adjusted. By sliding the holder for magnets A and C along the beam, the distance between magnets A, C and magnets B, D can be adjusted.

To add an EMEH to the system, 12 coils are placed symmetrically between magnets A and C, i.e., 6 coils above and 6 coils below. Each of the coils is held in a holder that allows individual adjustment of the coil's position and orientation. Through adjustment, the end surfaces of the coils are approximately parallel to the oscillation trajectory of magnets A and C. Figure 3.1(b) illustrates the spatial positions of the coils, those on the side of magnet C are labelled as 1 to 6 while those on the side of magnet A are labelled as 1' to 6'. Figure 3.1(c) shows the polarities of the four magnets where  $m_A$ ,  $m_B$ ,  $m_C$ ,  $m_D$  are the magnetic moment vectors,  $A_0$ ,  $B_0$ ,  $C_0$  and A, B, C represent the center positions of magnets A, B, and C when the beam at undeformed and deformed states, respectively. Note that the origin of the coordinate system is fixed at  $B_0$ .

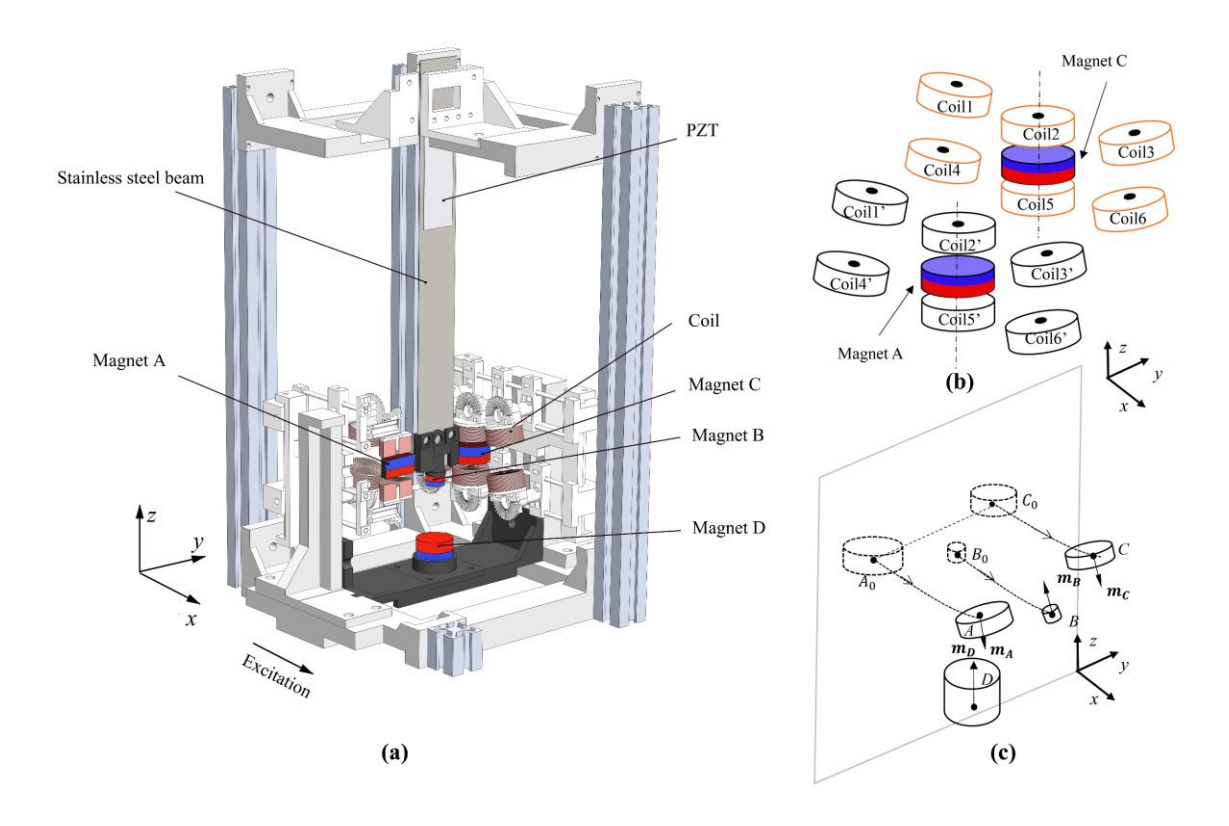


Figure 3.1 (a) Schematic of the MSHEH; Spatial positions of: (b) coils and magnets A and C; (c) magnets A, B, C and D.

Figures 3.2(a) and (b) show the front view and side view of Figure 3.1(a), respectively, where d is the distance between magnet B and magnet D when the beam is undeformed, and h is the distance between magnet B and magnets A, C, l is the length of the cantilever beam, and  $d_t$  is the distance between the axis of magnet B and that of magnets A and C. As shown in Figure 3.2(b), x and z represent the transverse and longitudinal displacements of the center of magnet B relative to  $B_0$ , respectively.  $\alpha$  is the angle between  $m_B$  and  $m_D$ , Since the slope of the beam's tip is relatively small, it is assumed that  $\angle BOB_0 \approx \alpha$ .

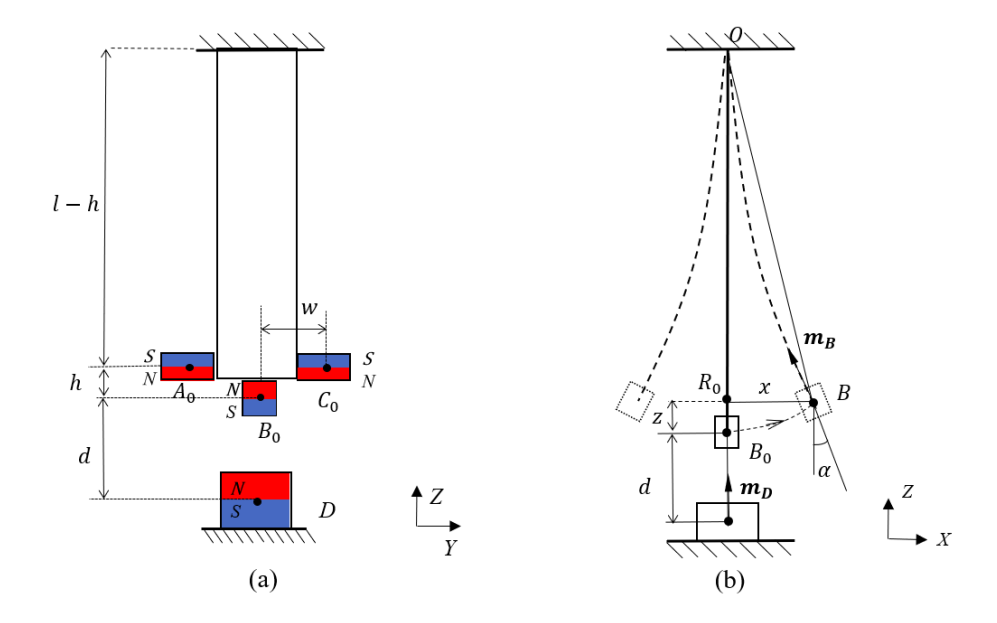


Figure 3.2 Two-dimensional views of the beam and magnets: (a) front view; (b) side view.

Figure 3.3 shows a lumped parameter model for the simplified system. In the figure, m = 0.09 Kg represents the equivalent mass at the tip of the beam,  $w_b$  and x are the displacement of the base and the equivalent mass relative to the base, respectively,  $c_m = 0.0058$  N/m which is the mechanical damping coefficient of the system,  $k_n$  is the nonlinear stiffness including the effects of the cantilever beam and the magnetic interaction. The PEH's circuit is given on the right side of the figure, where  $\theta = 8.515 \times 10^{-3}$  N/V is the electromechanical coefficient of the PEH which is identified by the experimental method proposed in [40],  $R_{lp}$  is the resistance of a load resistor connected to the output of the PEH. The EMEH's circuit is given on the left side of the figure, where  $K_t$  is the total transduction factor of the EMEH,  $v_{em}$  is the inductive voltage or so-called electromotive force (EMF) of the EMEH,  $R_c$  and  $R_c$  are resistance and inductance of one coil, respectively, and  $R_{le}$  is the resistance of a load resistor connected to the output of the EMEH. Note that as the 12 coils are connected in series, their total resistance and inductance are  $12R_c$  and  $12L_c$ , respectively.

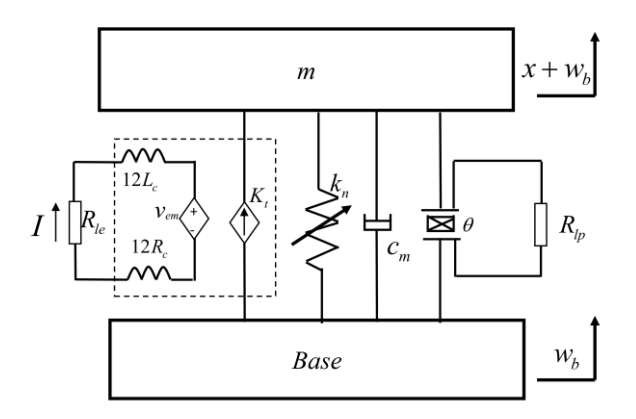


Figure 3.3 Lumped parameter model of the system.

Based on the Newton's second law and Kirchhoff's current law, the governing equations of the system can be derived as follows:

$$m\ddot{x} + c_m \dot{x} + f_e + f_n + \theta v = -m\ddot{w}_b \tag{3.1}$$

$$c_p \dot{v} + \frac{v}{R_{lp}} - \theta \dot{x} = 0 \tag{3.2}$$

where  $v_p$  is the voltage over the load resistor of the PEH,  $c_p = 50 \times 10^{-9}$  F is the capacitance of the PEH,  $f_n$  is the total restoring force,  $f_e$  is the electromagnetic force caused by the changes in the magnetic flux through the coils. Based on the Lenz's law, the electromagnetic force can be expressed as follows:

$$f_e = K_t I \tag{3.3}$$

where  $K_t = 2\sum_{i=1}^6 K_{ti}$  is the total transduction factor with  $K_{ti}$  as the transduction factor for the  $i^{th}$  coil and I is the current in the EMEH's circuit. Note that the values of the transduction factors of coils 1 to 6 and coils 1' to 6' are equal since they have identical configurations at the upper and lower sides of magnet C and magnet A, respectively, and Applying Kirchoff's law to the circuit of the EMEH yields:

$$12L_{c}\frac{dI}{dt} + (12R_{coil} + R_{le})I = v_{em}$$
 (3.4)

By using a multimeter, it is found that  $R_{coil} = 0.9 \Omega$ . By using an inductance meter, it is found that  $L_c = 0.454$  mH. Since the frequency of vibration considered in this study does not exceed 20 Hz, the inductive impedance of the coil is negligible compared with  $R_{coil}$ . Thus, the current can be written in the following form:

$$I = \frac{v_{em}}{12R_{coil} + R_{le}} \tag{3.5}$$

## 3.3 Determination of the EMEH's Transduction Factor

Due to the unique design of the EMEH, the determination of its total transduction factor is not straightforward. In what follows, a numerical method is employed for this purpose. According to Faraday's law, the EMF of the EMEH can be expressed as:

$$v_{em} = -2\sum_{i=1}^{6} \frac{d\Phi_i}{dt} = -2\sum_{i=1}^{6} \frac{\partial \Phi_i}{\partial x} \dot{x}$$
(3.6)

where  $\Phi_i$  is the total magnetic flux through the  $i^{th}$  coil. In fact, the magnetic flux is not evenly distributed throughout the whole coil due to the complex orientation of the magnets. Thus, each coil is sliced into n layers and the magnetic flux in the  $j^{th}$  layer is assumed to be uniformly distributed and denoted as  $\phi_{ij}$ .

As shown in Figure 3.4, the layer closest to magnet A or C is labelled as layer 1, which means the bottom layer for the upper side coil and the top layer for the lower side coil are the first layer. Thus, the total magnetic flux in the  $i^{th}$  coil can be expressed as:

$$\Phi_i = \frac{N}{n} \sum_{j=1}^n \phi_{ij} \tag{3.7}$$

where N is the turns of the coil. The magnetic flux in the j<sup>th</sup> layer for the i<sup>th</sup> coil is given by

$$\phi_{ij} = \iint_{A} \left( B_{zij} \cos \beta + B_{xij} \sin |\beta| \right) dA$$
 (3.8)

where  $B_{xij}$  and  $B_{zij}$  is the magnetic flux density in the x and z direction at that layer, respectively,  $\beta$  is the angle of the coil from the horizontal, and A is the area of the end surface of the coil. Substituting Eq. (3.7) into Eq. (3.6) gives:

$$v_{em} = -2\frac{N}{n} \sum_{i=1}^{6} \sum_{j=1}^{n} \frac{\partial \phi_{ij}}{\partial x} \dot{x} = K_{t} \dot{x}$$
 (3.9)

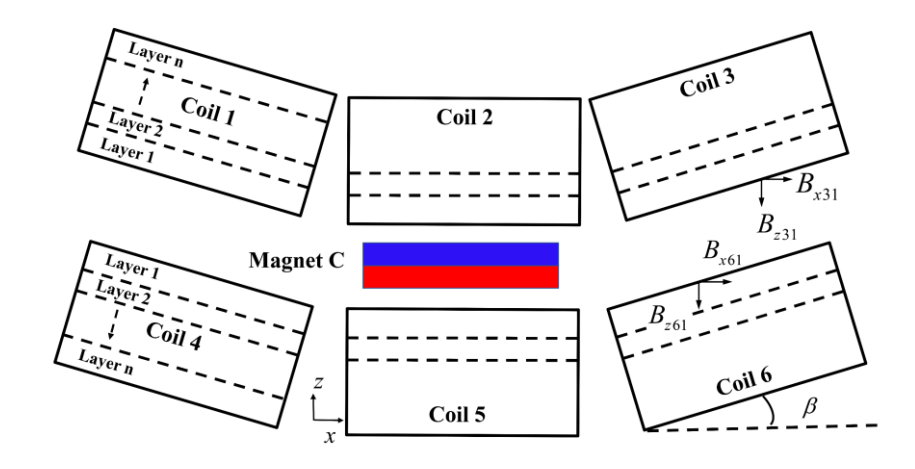


Figure 3.4 Illustration of coils' positions and slicing strategy.

According to Eq. (3.9), the transduction factor  $K_{ti}$  for each coil can be defined as follows:

$$K_{ti} = -\frac{N}{n} \sum_{i=1}^{n} \frac{\partial \phi_{ij}}{\partial x}$$
 (3.10)

which is a function of the change rate of the magnetic flux with respective to the displacement x. In this study, a finite element analysis software, COMSOL Multiphysics is utilized to compute the change rates of the magnetic flux of the six coils 1 to 6 when magnets C and B are oscillating through them. For the sake of simplicity, the influence of magnet A on the coils 1 to 6 is ignored. The geometry of the model built in COMSOL is shown in Figure 3.5(a) It should be noted that each of the coils is modelled as n disks to represent the n layers and meshed individually. As shown in Figure 3.5(b),  $D_{coil}$  and  $h_{coil}$  are the diameter and height of the coil, respectively,  $d_g$  is the air gap between the end surfaces of magnet C and the coils 2, 5,  $d_s$  is the lateral distance between the bottom center of the coils 4, 6 and the center of magnet D. All the values of the parameters of the coils and magnets used in the simulation are listed in Tables 3.1 and 3.2, respectively.

In the simulation, the number n of layers for each coil is set to 12, and magnets B and C oscillate from x = -0.065 m to x = 0.065 m. In order to simulate the trajectory of magnets B and C, the displacement of the center of magnets B and C in the z-axis is

modelled as z(x) which can be derived from the trigonometric relationship in the triangle  $OR_0B_0$  in Figure 2b as follow:

$$z(x) = l - \sqrt{l^2 - x^2}, (3.11)$$

and  $\alpha$  is the angle of magnets B and C from the horizontal and is approximated as  $\sin^{-1}(x/l)$  based on the triangle  $OR_0B_0$ .

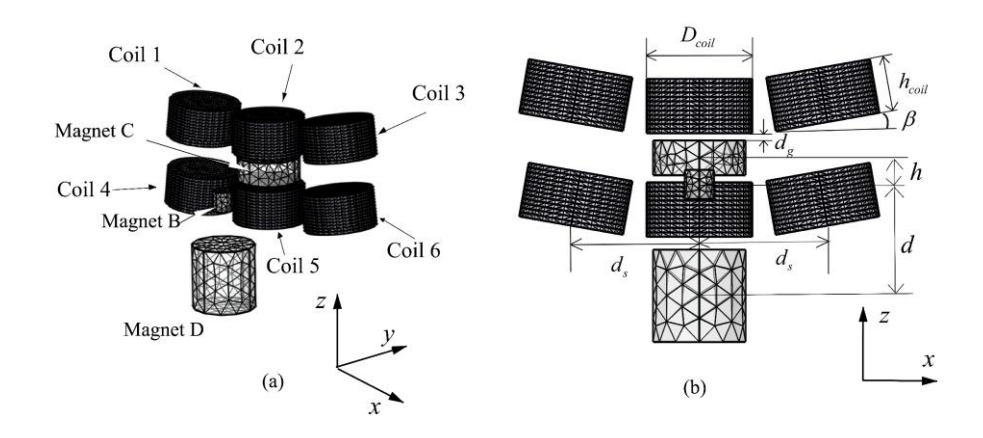


Figure 3.5 COMSOL model used to determine  $K_{ti}$ : (a) isometric view; (b) front view.

Table 3.1 Parameters of the coils.

Symbol	Name	Coils 1,	Coils 2,	Coils 3,
		4	5	6
$D_{coil}$ (m)	Diameter of the coil	0.029	0.029	0.029
$h_{coil}$ (m)	Hight of the coil	0.015	0.015	0.015
β (degree)	Angle of the coil from the horizontal	-10	0	10
N	Turn number	245	245	245
$d_s$ (m)	Distance from the center of magnet D	-0.0353	0	0.0353
$d_g$ (m)	Air gap between the magnet C and coils 2, 5	0.002	0.002	0.002

Table 3.2 Parameters of the magnets.

Symbol	Name	Magnet A & C	Magnet B	Magnet D
$D_{mag}$ (m)	Diameter of magnet	$2.54 \times 10^{-2}$	$7.94 \times 10^{-3}$	$2.54 \times 10^{-2}$
$l_A$ , $l_C$ , $l_B$ , $l_D$ (m)	Hight of magnets	9.525×10 <sup>-3</sup>	$7.94 \times 10^{-3}$	$2.54 \times 10^{-2}$
$B_r$ (T) Residual flux density		1.44	1.28	1.28
	Material	N50	N42	N42

Figure 3.6 shows the magnetic flux distributions when magnets B and C move from the farthest left position to the farthest right position. In particular, Figures 3.6(a), b and c illustrate the situations when magnet C is concentric with coils 1, 2 and 3, respectively. During the simulation, the change rate of the magnetic flux through each layer of the coils with the different displacements is recorded.

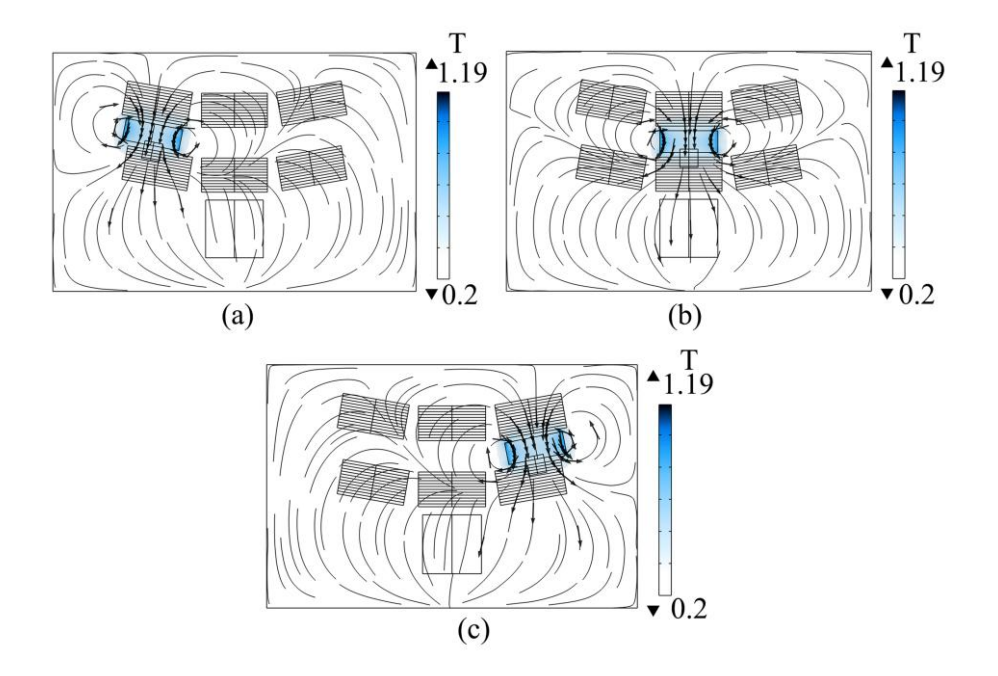


Figure 3.6 Magnetic flux distributions of magnets B and C at the different positions: (a) x = -0.0353 m; (b) x = 0 m; (c) x = 0.0353 m.

Based on Eq. (3.10), the transduction factors for all six coils can be computed, and the results are shown as solid lines in Figure 3.7(a) and (b). Then, these results are curve-fitted using piecewise functions, which are the sum of three sine functions in the specific displacement ranges and can be defined as follows:

$$K_{ti}(x) = \begin{cases} \sum_{j=1}^{3} (-1)^{i} a_{uj} \sin(b_{uj}(x+c_{i})) & d_{i}^{\min} \le x \le d_{i}^{\max} \quad (i=1,2,3) \\ 0 & x < d_{i}^{\min} & x > d_{i}^{\max} \quad (i=1,2,3) \end{cases}$$
(3.12)

$$K_{ii}(x) = \begin{cases} \sum_{j=1}^{3} (-1)^{i-1} a_{lj} \sin(b_{lj}(x+c_i)) & d_i^{\min} \le x \le d_i^{\max} \quad (i=4,5,6) \\ 0 & x < d_i^{\min} & x > d_i^{\max} \quad (i=4,5,6) \end{cases}$$
(3.13)

where  $a_{uj}$  and  $b_{uj}$  are the curve-fitting constants for coils 1, 2, 3 and  $a_{lj}$ ,  $b_{lj}$  are the curve-fitting constants for coils 4, 5, 6,  $d_i^{\min}$  and  $d_i^{\max}$  are the equation limits for the *i*th coil,  $c_i$  is the coordinate translation for the  $i^{th}$  coil. The equation limits are  $d_1^{\min} = -0.0706$  m,  $d_4^{\min} = -0.0690$  m,  $d_1^{\max} = d_4^{\max} = 0$ ,  $d_2^{\min} = -0.0353$  m,  $d_5^{\min} = -0.0345$  m,  $d_2^{\max} = 0.0353$  m,  $d_5^{\min} = 0.0345$  m,  $d_3^{\min} = d_6^{\min} = 0$ ,  $d_3^{\max} = 0.0706$  m,  $d_4^{\max} = 0.0690$  m. The coordinate translations are  $c_1 = 0.0353$  m,  $c_4 = 0.0345$  m,  $c_2 = 0.0345$  m,  $c_3 = 0.0690$  m. The coordinate translations are  $c_4 = 0.0353$  m,  $c_4 = 0.0345$  m,  $c_5 = 0.0345$  m,  $c_7 = 0.0345$  m,  $c_8 = 0.0345$  m,  $c_8 = 0.0345$  m,  $c_9 = 0$ 

 $c_5 = 0$ ,  $c_3 = -0.0353$  m,  $c_6 = -0.0345$  m, and Table 3.3 lists the obtained curve-fitting constants. The curve-fitting results are shown in dotted lines in Figures 3.7(a) and b. Overall, the curve-fitting results agree well with the numerical results. Figure 3.7(c) shows the total transduction factor, which is a strongly nonlinear function of x, reaching the maximum values around |x| = 0.017 m and |x| = 0.045 m, respectively.

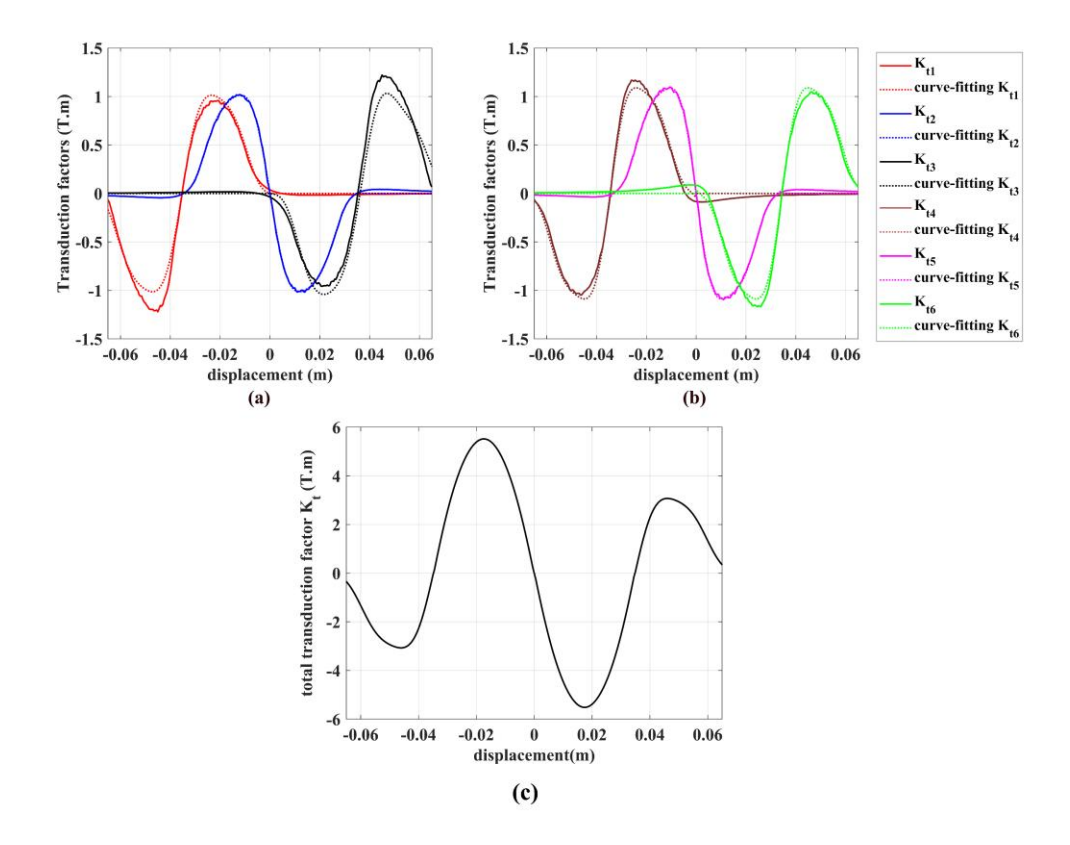


Figure 3.7 Transduction factors of the coils: (a) coil 1, coil 2 and coil 3; (b) coil 4, coil 5 and coil 6; (c) total transduction factor.

Table 3.3 Curve-fitting constants of Eqs. (3.12) and (3.13).

Constants	$a_{u1}$	$b_{ul}$	$a_{u2}$	$b_{u2}$	$a_{u3}$	$b_{u3}$
Value	-0.94	88.80	-0.29	179.47	-0.06	344.84
Constants	$a_{l1}$	$b_{l1}$	$a_{l2}$	$b_{l2}$	$a_{l3}$	$b_{l3}$
Value	-1.06	99.08	-0.28	207.30	-0.084	376.82

An experiment is carried out to verify the computed transduction factors for the six coils. To measure the transduction factor value for each coil at different displacements x, an experimental setup shown in Figure 3.8 is developed according to the verification

method proposed in [41]. As shown in Figure 3.8(a), the apparatus is placed horizontally and fixed on the test platform, the six coils on magnet A side are removed, and the tip of the cantilever beam is connected to the shaker (Model 2025E) through an adjustable stinger. The shaker is driven by an amplifier (SmartAmp<sup>TM</sup> 2100E21), and a vibrometer (Metrolaser 500V) is placed at the left side of the apparatus to measure the velocity of magnet C, the voltage signals of the coils are collected by the data acquisition system (Brüel & Kjær PULSE Type 3560) which is controlled by a computer. As illustrated in Figure 3.8(b), a scale placed at magnet A's side is used to control the initial position of each test.

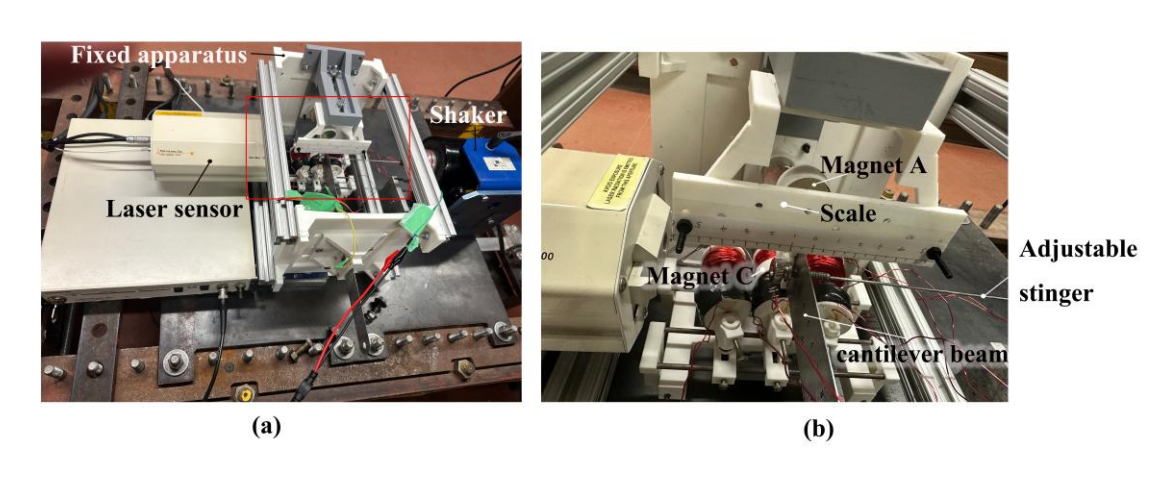


Figure 3.8 Experimental setup for verification of transduction factors of coils: (a) the overview; (b) the detail of the area within the red rectangle in (a).

The principle of the experimental verification is demonstrated in Figure 3.9. The transduction factor for the coils when magnet C is at a specific position can be treated as a constant when the magnet is doing a very small oscillation around that position. Thus, the critical part of the experimental verification is to measure the transduction factor at an initial position, and then change the initial position to do another measurement till the position covers the displacement range of the magnet. In this study, the amplitude and frequency of the oscillation for the magnet are set to be 1 mm and 3 Hz, respectively. As illustrated in Figure 3.9(a), a stinger is inserted into a hole at the center of the shaker's head and fastened with the shaker's head by using a collet. For each test, the length of the stinger is adjusted to make magnet C reach the desired positions, And the angle  $\alpha$  also needs to be adjusted for each test to guarantee that the stinger is perpendicular to the end segment of the cantilever beam. The measured open

circuit voltage of the single coil  $E_i$  and oscillation velocity  $\dot{x}$  can be treated as two sine waves as shown in Figure 3.9(b), where i represents the  $i^{th}$  coil. According to the Faraday's law,  $E_i$  and  $\dot{x}$  will both reach the maximum values when the magnet crosses the initial position x, and the transduction factor can be obtained by calculating the ratio of the peak or root mean square (RMS) value of the voltage and that of the velocity.

Since the functions of the transduction factor of coils 3 and 6 are symmetric with coils 1 and 4, in this case, only the transduction factors of coils 1, 2, 4 and 5 need to be measured. The range of the initial displacement position x has been chosen from -0.04 m to 0 m with an interval of 0.005 m. The measurement results are shown in Figure 2.10. It can be seen that the experimental results (blue stars) are slightly lower than the original simulation results (red lines). One possible explanation is that in Eq. (3.10), the coil turn number N is overestimated. In the simulation, all the turns of the coil have been considered active when calculating the EMF of the coil, but in fact, when the edge of magnet C has passed the central point of the coils, the magnetic flux change only happens in the turns located the outside of the coil. In this case, the equivalent turn number  $N_e$  for the coils need to be estimated. Based on the obtained experimental results, an approximate equivalent turns number is found to be 180 through trial and error. Based on the simulation results for coils 2 and 5, the constants of the curve fitting functions shown in Eqs. (3.12) and (3.13) can be obtained and listed in Table 3.4. As shown in Figure 3.10, the measured data, the simulation results based on the equivalent turn number  $N_e$  (green lines) and the curve fitting functions (black lines) match well.

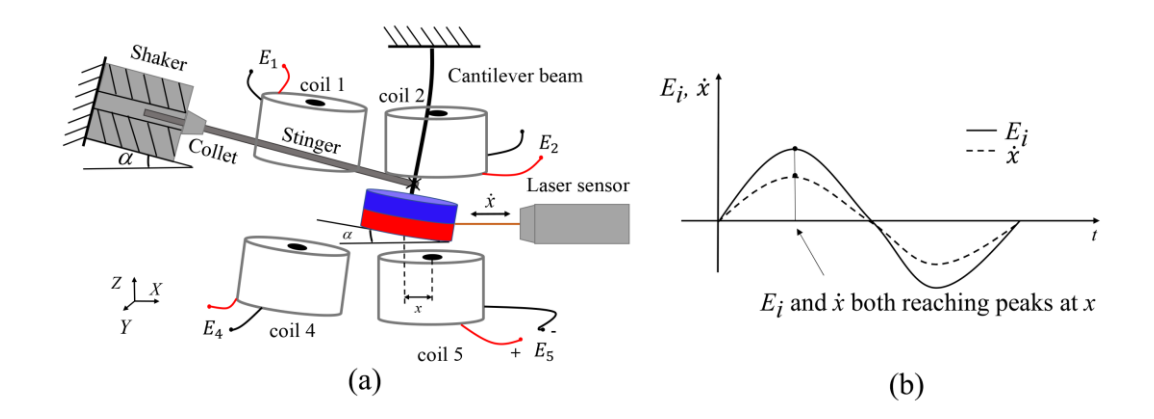


Figure 3.9 Illustration of (a) the verification experimental setup. (b) the open circuit voltage of the coil and the velocity of the magnet.

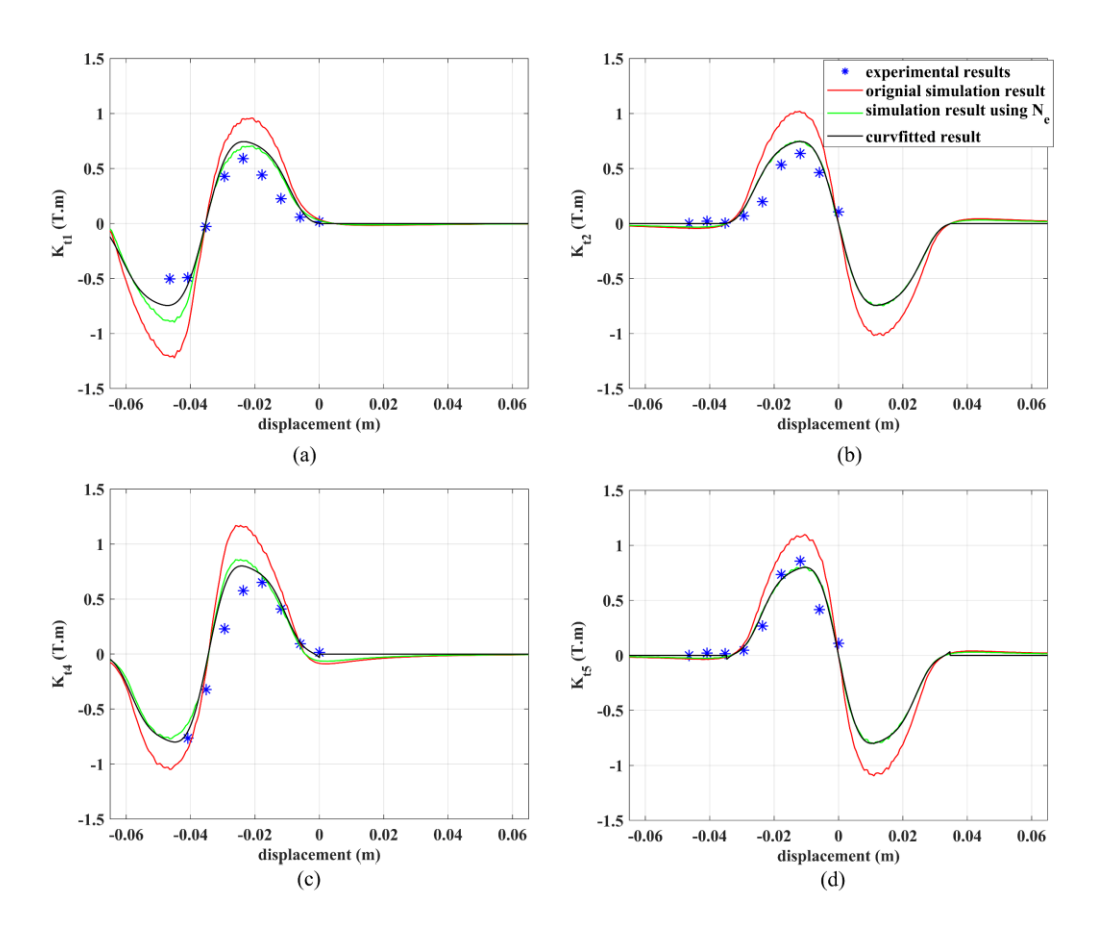


Figure 3.10 Experimental results of the transduction factors: (a) coil 1; (b) coil 2; (c) coil 4; (d) coil 5.

Table 3.4 Curve-fitting constants of Eqs. (3.12) and (3.13) by using  $N_e$ .

Constants	$a_{u1}$	$b_{u1}$	$a_{u2}$	$b_{u2}$	$a_{u3}$	$b_{u3}$
Value	-0.68	87.93	-0.22	177.48	-0.05	343.65
Constants	$a_{l1}$	$b_{l1}$	$a_{l2}$	$b_{l2}$	$a_{l3}$	$b_{l3}$
Value	-0.78	99.08	-0.20	207.30	-0.06	376.81

# 3.4 Determination of the Nonlinear Restoring Force

The total restoring force  $f_n$  of the system in the x-direction consists of an equivalent force  $f_g$  due to the gravity, a restoring force  $f_b$  due to the beam's elasticity, an attractive magnetic force  $f_{DBx}$  between magnet D and magnet B and two repulsive magnetic forces:  $f_{DAx}$  between magnet D and magnet A, and  $f_{DCx}$  between magnet D and magnet

C. Since magnets A and C are identical and symmetrical about the central line of the beam, the values of  $f_{DAx}$  and  $f_{DCx}$  are equal. Then the total restoring force can be expressed as:

$$f_n = f_g + f_b + f_{DBx} + f_{DAx} + f_{DCx} = mg \cdot \tan(\alpha) + k_b x + f_{DBx} + 2f_{DAx}$$
 (3.14)

where  $k_b$  =90.1 N/m is the stiffness of the beam which can be determined experimentally. In what follows, the analytical restoring forces  $f_{DBx}$  and  $f_{DAx}$  will be found using the equivalent magnetic 2-point dipole model proposed in [42]. To have a better understanding of the magnetic force model, Figures 3.11(a) and (b) show the front view of the apparatus when the beam is undeformed and deformed.

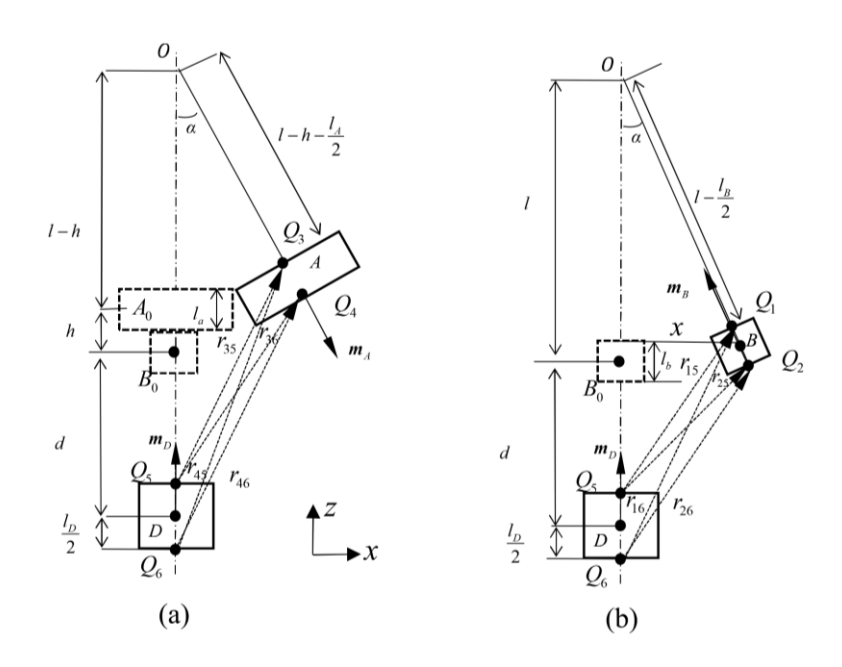


Figure 3.11 Illustration of the equivalent magnetic 2-point dipole model: (a) magnets A and D; (b) magnets B and D.

As shown in Figures 3.11(a) and b,  $r_{15}$ ,  $r_{25}$ ,  $r_{35}$  and  $r_{45}$  are the vectors from  $Q_5$  to  $Q_1$ ,  $Q_2$ ,  $Q_3$  and  $Q_4$ , respectively, and  $r_{16}$ ,  $r_{26}$ ,  $r_{36}$  and  $r_{46}$  are the vectors from  $Q_6$  to  $Q_1$ ,  $Q_2$ ,  $Q_3$  and  $Q_4$  respectively, where  $Q_i$ , i=1,...,6 are the total surface charges of the magnets defined by:

$$Q_1 = -MS_B$$
  $Q_2 = MS_B$   $Q_3 = MS_A$   $Q_4 = -MS_A$   $Q_5 = -MS_D$   $Q_6 = MS_D$  (3.15)

where  $S_A = 5.07 \times 10^{-4} \text{ m}^2$ ,  $S_B = 4.95 \times 10^{-5} \text{ m}^2$  and  $S_D = 5.07 \times 10^{-4} \text{ m}^2$  are the surface area of magnets B, A and D, respectively,  $M = B_r / \mu$  is the magnetization of magnets A, B and D, where  $B_r$  is the magnetic residual flux density, their values are listed in Table 3.2, and  $\mu = 4\pi \times 10^{-7} \text{H/m}$  is the vacuum permeability.

The magnetic force between magnet B and magnet D is considered first. Based on the Boit-Savart law, the magnetic force exerted by magnet B on magnet D is the combination of the magnetic force exerted from  $Q_1$  and  $Q_2$  to  $Q_5$  and  $Q_6$ , which is given in the following equation:

$$f_{DB} = Q_1 \frac{\mu_0}{4\pi} \left( Q_5 \frac{\mathbf{r}_{15}}{|\mathbf{r}_{15}|^3} + Q_6 \frac{\mathbf{r}_{16}}{|\mathbf{r}_{16}|^3} \right) + Q_2 \frac{\mu_0}{4\pi} \left( Q_5 \frac{\mathbf{r}_{25}}{|\mathbf{r}_{25}|^3} + Q_6 \frac{\mathbf{r}_{26}}{|\mathbf{r}_{26}|^3} \right)$$
(3.16)

where  $r_{15}$ ,  $r_{16}$ ,  $r_{25}$  and  $r_{26}$  can be derived from the are the position vectors of  $Q_1$ ,  $Q_2$ ,  $Q_5$  and  $Q_6$ , respectively. According to Eq.(3.14), to obtain the total restoring force, only the  $f_{DBx}$  is considered, which can be expressed as follows [33]:

$$f_{DBx} = -\frac{\mu_0}{4\pi} \left[ Q_1 \left( x - \frac{l_B}{2} \sin \alpha \right) \left( \frac{Q_5}{\gamma_1} + \frac{Q_6}{\gamma_2} \right) + Q_2 \left( x + \frac{l_B}{2} \sin \alpha \right) \left( \frac{Q_5}{\gamma_3} + \frac{Q_6}{\gamma_3} \right) \right]$$
(3.17)

where the expression  $\gamma_1$ ,  $\gamma_2$ ,  $\gamma_3$  and  $\gamma_4$  are given in [33]. Further, the magnetic force between magnet A and D in the x-direction can also be obtained as:

$$f_{DAx} = -\frac{\mu_0}{4\pi} \left[ Q_3 \left( x - h \sin \alpha - \frac{l_A}{2} \right) \left( \frac{Q_5}{\gamma_5} + \frac{Q_6}{\gamma_6} \right) + Q_4 \left( x - h \sin \alpha + \frac{l_A}{2} \right) \left( \frac{Q_5}{\gamma_7} + \frac{Q_6}{\gamma_8} \right) \right] (3.18)$$

where  $\gamma_5$ ,  $\gamma_6$ ,  $\gamma_7$  and  $\gamma_8$  are also defined in [33]. By substituting Eqs (3.17) and (3.18) into Eq.(3.14), the total restoring force can be obtained.

To validate the model, the five different configurations are considered: Case (I) d = 0.0605 m, h = 0.0035 m; Case (II) d = 0.0496 m, h = 0.0058 m; Case (III) d = 0.0452 m, h = 0.0058 m; Case (IV) d = 0.0339 m, h = 0.0092 m; Case (V) d = 0.0330 m, h = 0.0079 m. Among them, the first case is the mono-stable configuration, the second and third cases are the bi-stable configurations. By applying the original values of the total charges that are listed in the first column of Table 3.5, the simulation results are plotted as red lines in Figure 3.12. To verify the accuracy of the model, the total restoring forces

of the system under various configurations are measured by using the restoring force surface method [33]. The results corresponding to the five chosen cases are plotted as black dots in Figure 3.12 By comparing the measured data and the simulation results using the original values of  $Q_1$  to  $Q_6$ , it can be found that the model fails to predict the magnitudes of Cases III, IV, and V or the bi-stable and tri-stable cases.

To improve the accuracy of the model, a genetic algorithm-based identification approach proposed in [33] is applied. In this approach,  $Q_1$  to  $Q_6$  are treated as six independent parameters to be identified by minimizing an objective or fitness function defined below

$$J_1(Q_1, Q_2, Q_3, Q_4, Q_5, Q_6) = \sqrt{\frac{1}{5N_d} \sum_{j=1}^5 \sum_{i=1}^{N_d} (f_{jm}(x_i) - f_{ja}(x_i))^2}$$
(3.19)

where  $f_{jm}(x_i)$  is the measured restoring forces that are smoothened by a spline fitting,  $f_a(x_i)$  is the analytical restoring forces based on Eq.(3.14), and  $N_d = 101$  is the number of training data for each case. According to [33]. Once the six parameters has been identified, the neglectable parameter (with an almost zero value) can be set to zero, then an optimization for the five independent parameters can be conducted. All the identified values of the total charges and their corresponding fitness values are listed in Table 3.5. As shown in the table, the five-parameter optimization has the lowest fitness value. With the results, the recalculated restoring forces are plotted as blue lines in Figure 3.12.

In what follows, the optimal values with the five-parameter optimization are used. By integrating the total restoring forces with respect to x, the potential energies of the five cases can be found and plotted in Figure 13(a). By varying the tuning parameters d and h, the stability state region can be generated and plotted in Figure 13(b). This Figure reveals the tunability of the system. For both the lower limit and upper limit of the parameter d, the system is a mono-stable one regardless of the value of h. To have a bi-stable system, the distance d should be around the middle of the tuning range so that the repelling force between magnets A, C and magnet D is strong enough. And keep decrease the parameter d, a tri-stable system can be achieved. Figure 14(a) shows the potential energies vs. x and d by fixing h at 0.02 m where C1, C2 and C3 represent the crossing points of the line C and the borderline between the strong mono-stable and

tri-stable; tri-stable and bi-stable, bi-stable and week mono-stable, respectively while Figure 14(b) shows the potential energies vs. x and h by fixing d at 0.035 m, where D1 and D2 represent the crossing points of the line D and the borderline between the medium mono-stable and tri-stable; tri-stable and bi-stable, respectively. It can be found that the region for the tri-stable is the narrowest one, which indicates that the tri-stable system has the highest sensitivity when changing the parameters.

Table 3.5 Values of the total charges on the surfaces of different magnets.

		Original values	Optimum values	Optimum values
			(6 parameters)	(5 parameters)
Magnet	$Q_3$	580.64	1150	642.36
A	$Q_4$	580.64	1516.7	903.53
Magnet	$Q_1$	50.4	0.16	0
В	$Q_2$	50.4	58.83	35.62
Magnet	$Q_5$	516.12	207.12	353.39
D	$Q_6$	516.12	321.6	577.56
$J_1$		0.3420	0.0786	0.0784

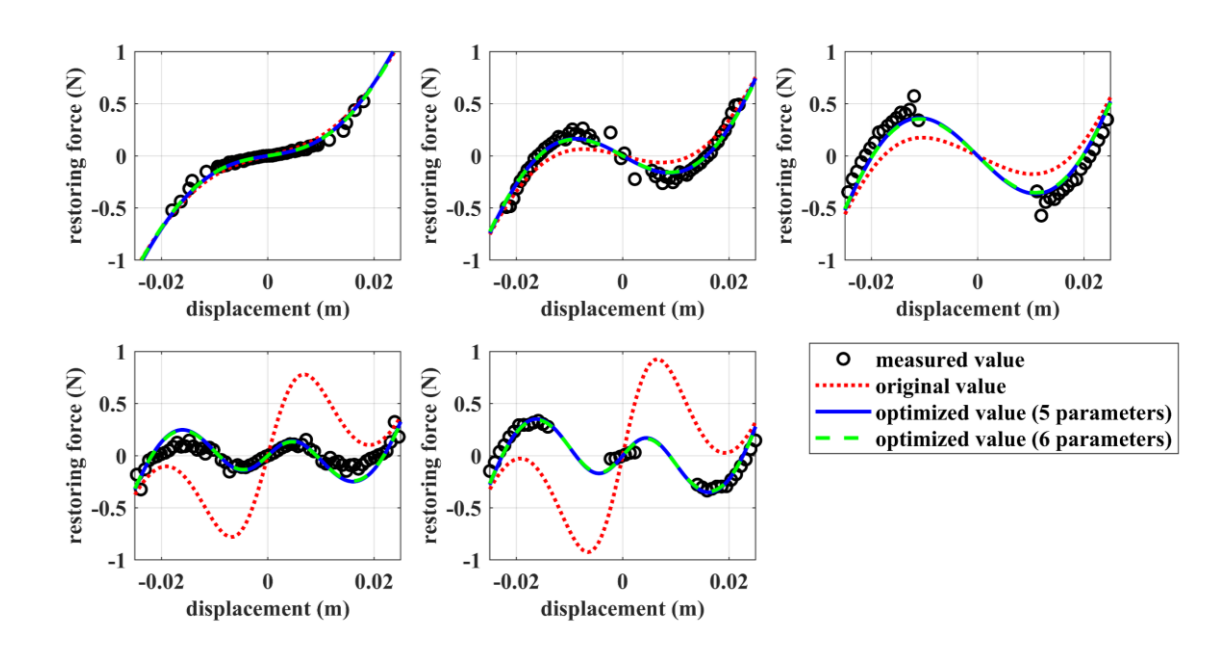


Figure 3.12 The total restoring forces: (a) Case (I); (b) Case (II); (c) Case (III); (d) Case (IV); (e) Case (V).

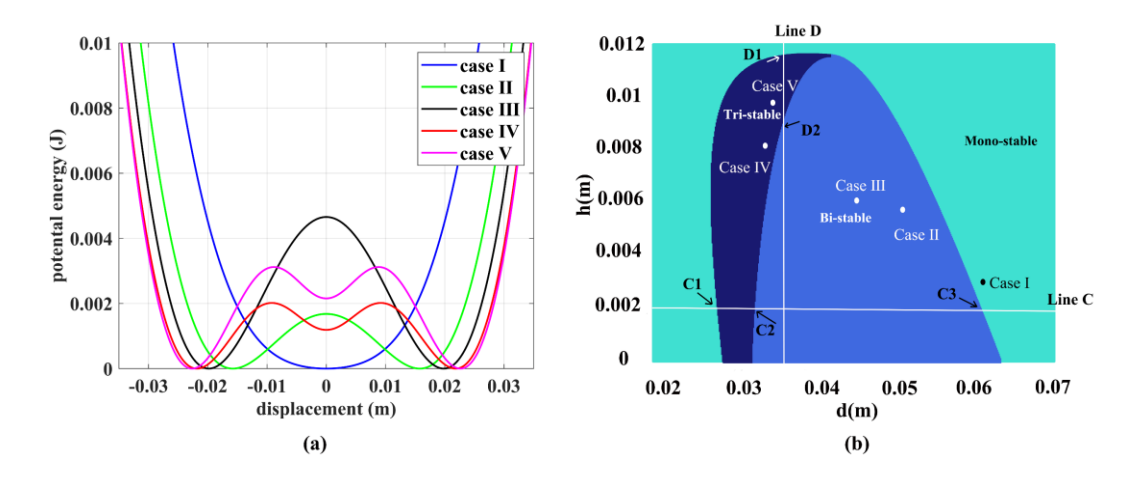


Figure 3.13 (a) Potential energies of the five cases. (b) Stability state region.

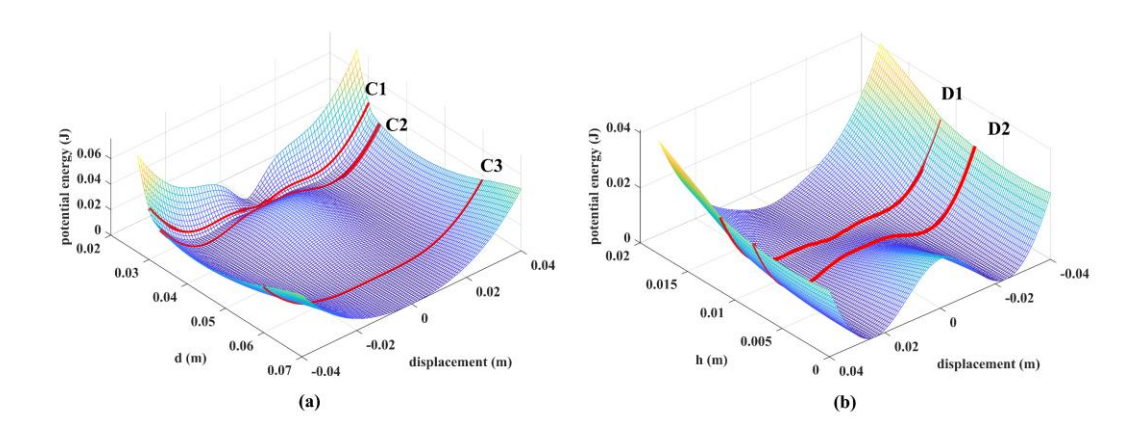


Figure 3.14 Potential energies: (a) varying d and fixing h at 0.002 m; (b) varying h and fixing d at 0.035 m.

## 3.5 Evaluation of the Performances of the MSHEH

In this section, the performances of the MSHEH are evaluated under harmonic frequency sweeping excitation. Both up-sweep and down-sweep excitations are conducted numerically and experimentally. For this purpose, four different configurations are considered: linear, mono-stable, bi-stable and tri-stable. The restoring force of the linear system is defined by setting  $f_{DBx}$ ,  $f_{DAx}$ ,  $f_{DCx}$  to be zero in Eq. (3.14) while the last three configurations are Case (I), Case (III) and Case (IV) defined in the previous section. The load resistances for the EMEH and PEH are set to the optimum values given in red in Table 3.8.

## 3.5.1 High-level acceleration

In the simulation, the acceleration amplitude is set to be 1.6 m/s<sup>2</sup>. The frequency of the harmonic excitation is varied by

$$f = f_i + \frac{f_e - f_i}{T}t {(3.20)}$$

where for the up-sweep,  $f_i = 2$  Hz and  $f_e = 8$  Hz, for the down-sweep,  $f_i = 8$  Hz and  $f_e = 2$  Hz, and  $f_e = 2$  Hz and  $f_e = 2$  Hz, and  $f_e = 2$ 

Figure 3.15(a) clearly shows that for the EMEH, the linear and tri-stable configurations outperform the mono-stable and bi-stable configurations in terms of the peak output powers. The EMEH with the mono-stable and tri-stable configurations show obvious hardening behaviors, which leads to a wider effective energy harvesting bandwidth. With the frequency rising, the bi-stable system first switches between the intra-well oscillation and chaotic inter-well oscillation at 3.7 Hz and then resumes the intra-well motion after 4.4 Hz. And owing to its lower potential barriers, the tri-stable system starts with the periodic inter-well oscillation at 2 Hz and then switches to the intra-well oscillation at 4.3 Hz. It can be seen that the periodic inter-well motion of the tri-stable system generates more power compared to the chaotic inter-well motion of the bi-stable system, and the intra-well motion has the lowest energy harvesting efficiency among the three motion modes.

As shown in Figure 3.15(b), the trends for the power outputs of the PEH of the four

configurations are similar to those of the EMEH. In addition, it should be noted that the value of the instant power output of the EMEH under the mono-stable and tri-stable configurations are close to each other from 2 Hz to 3.4 Hz. However, the value of the power output of the PEH under the mono-stable configuration is lower than that under the tri-stable configuration. The main reason is that the voltage output of the EMEH is only related to the transduction factor and the velocity of the moving magnets according to Eq. (3.9). Since both the mono-stable system and tri-stable system perform the large amplitude oscillation under the low-frequency excitation (lower than 3.4 Hz), the velocity of the moving magnets of the two systems are close when passing the high-power output regions ( $x = \pm 0.017$  m), which explains the similar power output level. On the other hand, the power output of the PEH mainly depends on the displacement of the cantilever beam's tip. The two side potential wells of the tri-stable system lead to a larger amplitude response at the inter-well oscillation mode than that of the mono-stable system. Thus, the PEH with the tri-stable configuration shows higher power output than the PEH with the mono-stable configuration.

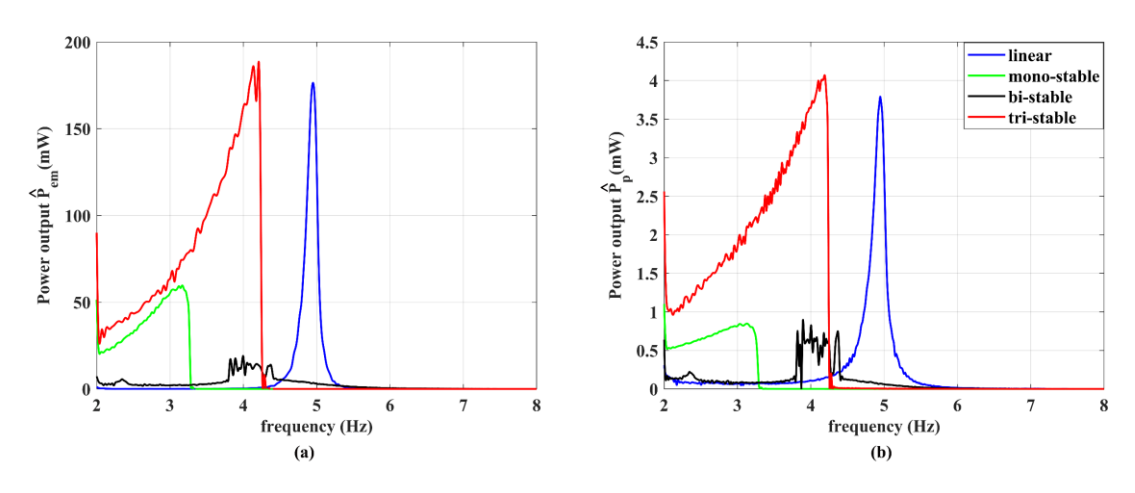


Figure 3.15 The simulation results of the instant power outputs under the frequency up-sweep excitation with  $A = 1.6 \text{ m/s}^2$ : (a) the EMEH's; (b) the PEH's.

To validate the above simulation, an experiment is conducted. As shown in Figure 3.16, the apparatus is fixed on a slip table that is driven by a shaker (2809, Brüel & Kjær) through a stinger. The shaker is driven by an amplifier (2718, Brüel & Kjær). Two laser reflex sensors (CP24MHT80, Wenglor) are used to measure the displacements of the beam's tip and the base, respectively. A computer equipped with

dSPACE dS1104 data acquisition board is used to collect the signals from the laser sensors and the voltage signals of the EMEH's load resistor and the PEH's load resistor, output the exciting voltage signal to the power amplifier. To control the experiment, a program is developed by using the MATLAB Simulink which is interfaced with dSPACE Controldesk Desktop software.

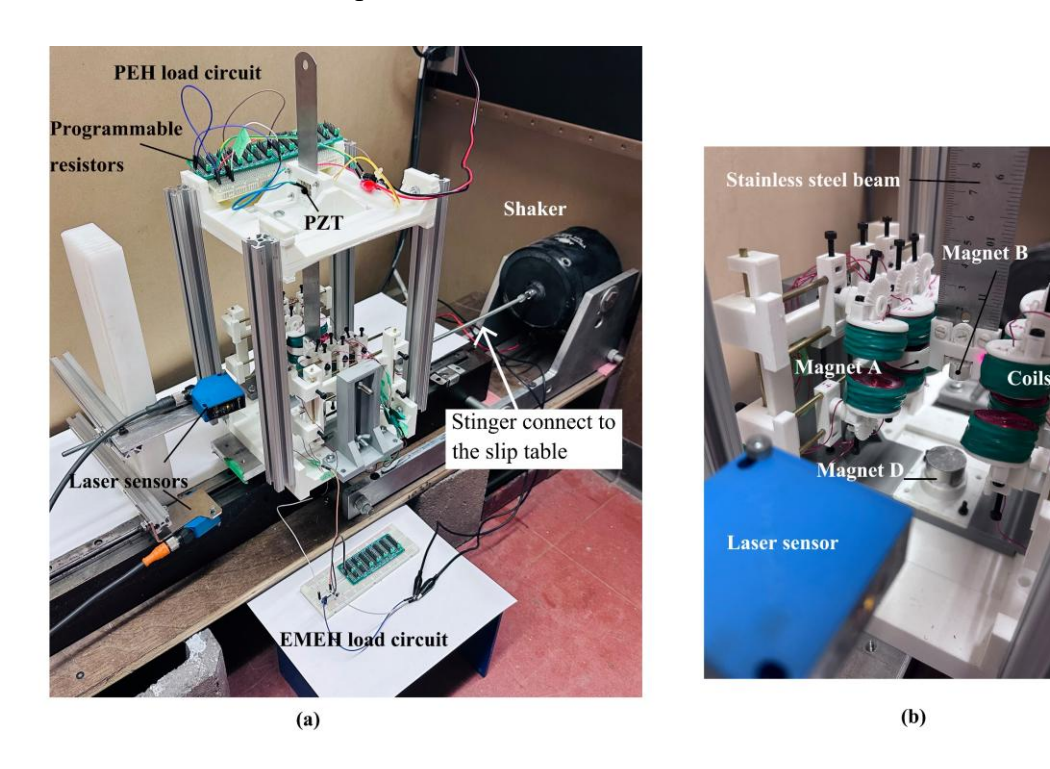


Figure 3.16 Photos of the experimental setup: (a) the entire system; (b) the EMEH.

The experimental results are shown in Figure 3.17. It can be seen that the trends of the results agree with the simulation ones for the higher frequency region. However, for the lower frequency region, the experimental results for the four systems are lower than their simulation counterparts. Such discrepancy can be attributed to the limit of the shaker because 4 Hz exceeds the lower limit of the ideal working range of the shaker, which causes the actual acceleration of the excitation is much lower than 1.6 m/s<sup>2</sup>. Nevertheless, the experiment results indicate that the model used in the simulation is valid. In what follows, more simulation is carried out to further evaluate the performance of the MSHEH.

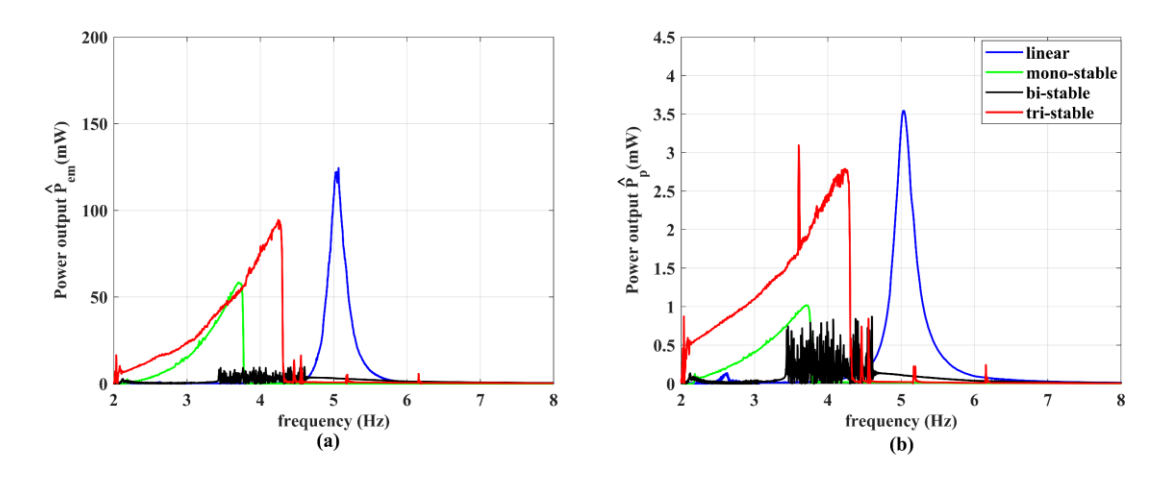


Figure 3.17 The experimental results of the instant power outputs under the frequency up-sweep excitation with  $A = 1.6 \text{ m/s}^2$ : (a) the EMEH's; (b) the PEH's.

Figure 3.18 shows the simulation results of the power outputs for the EMEH and PEH under the frequency down-sweep (8 to 2 Hz) excitation. The overall trends of the power outputs of the linear, mono-stable and bi-stable configurations are similar to those from the frequency up-sweep excitation. While the power output of the tri-stable system is not as high as in the up-sweep test since it mainly performs the intra-well oscillation. The bi-stable and tri-stable systems start to jump when the frequency decreases to 4.3 Hz and 3.5 Hz, respectively, which is the situation when the two systems just overcome the threshold of their local potential well and switch to the chaotic inter-well oscillation mode. As shown in Figure 3.19, the experimental results generally agree with the simulation one.

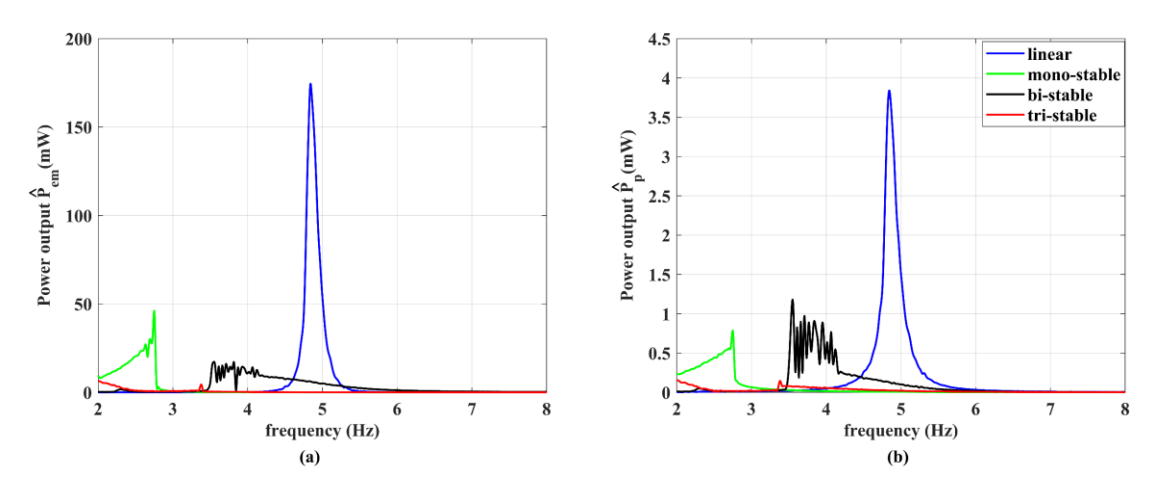


Figure 3.18 The simulation results of the instant power outputs under the frequency

down-sweep excitation with  $A = 1.6 \text{ m/s}^2$ : (a) the EMEH's; (b) the PEH's.

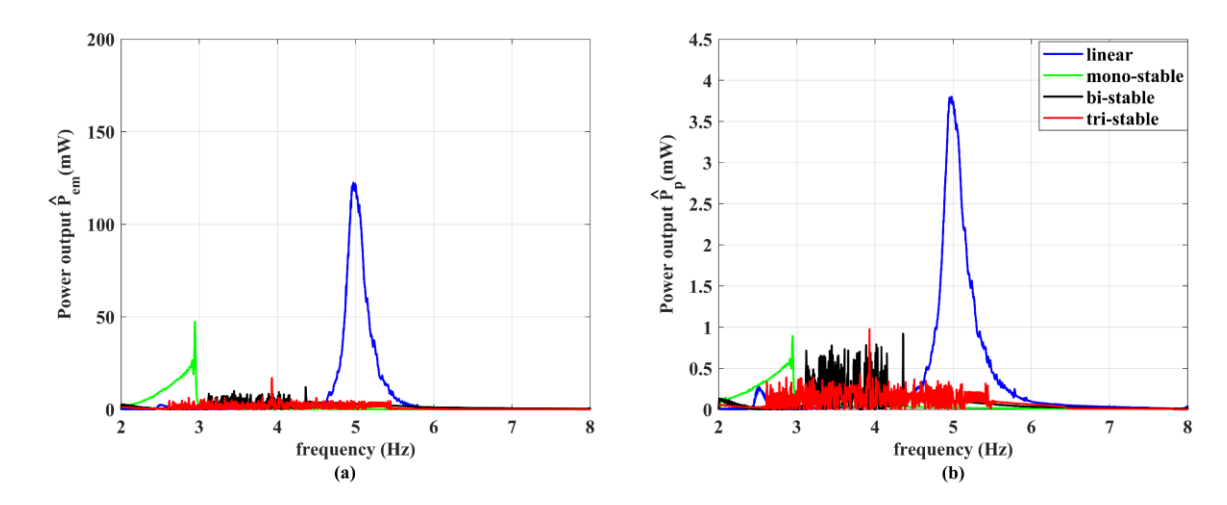


Figure 3.19 The experimental results of the instant power outputs under the frequency down-sweep excitation  $A = 1.6 \text{ m/s}^2$ : a the EMEH's; b the PEH's.

To better measure the bandwidth of the MSHEH, the accumulated harvested energy  $E_{em}$  of the EMEH and the accumulated harvested energy  $E_p$  of the PEH are defined as:

$$E_{em}(t) = \int_{0}^{t} P_{em}(\tau) d\tau$$
 (3.21)

$$E_p(t) = \int_0^t P_p(\tau) d\tau \tag{3.22}$$

where  $P_{em}$  and  $P_p$  are the instantaneous power of the EMEH and PEH, respectively. Figures 3.20(a) and (b) show the total accumulated harvested energy  $E(t) = E_{em}(t) + E_p(t)$  under the frequency up-sweep excitation and down-sweep excitation, respectively. Note that the relationship between the time t and the frequency f is defined by Eq. (3.20) The effective frequency range of energy harvesting can be defined as the region where the increase rate of E(t) is equal to or greater than 0.1 J/Hz. The total bandwidth can be obtained by taking the sum of the frequency range of the up-sweep and down-sweep tests. For example, the effective energy harvesting bandwidth for the tri-stable system is 2.36 Hz (ranging from 2 Hz to 4.36 Hz) and 0.1 Hz (ranging from 2 Hz to 2.1 Hz) for the frequency up-sweep and down-sweep excitations, respectively, and the total bandwidth will be 2.36 Hz. In addition, the total accumulated harvested energy for each configuration is represented by  $E_{em}(T)$  under the up-sweep excitation. All the results

are listed in Table 5, and the results clearly show all three nonlinear configurations show wider bandwidth compared to the linear one. The tri-stable system has the largest total bandwidth and total accumulation harvested energy among the four configurations as it is able to enter the periodic inter-well oscillation mode.

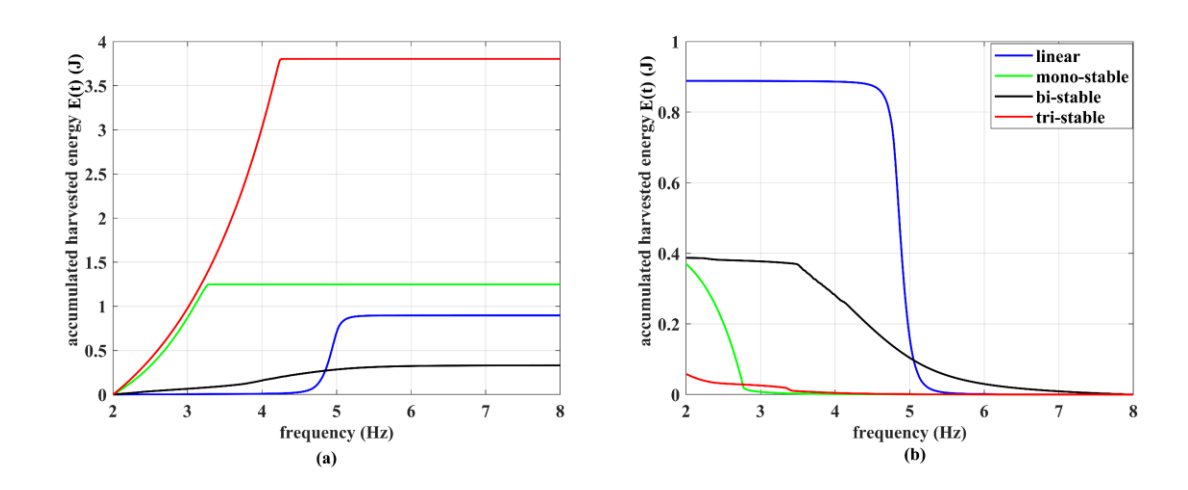


Figure 3.20 The accumulated harvested energy of the MSHEH under the high-level excitation: (a) frequency up-sweep excitation; (b) frequency down-sweep excitation.

Table 3.6 The effective frequency bandwidths of the systems under the high-level frequency sweep excitation.

	Up-sweep frequency range (Hz)	Down-sweep frequency range (Hz)	Total bandwidth (Hz)	<i>E</i> ( <i>T</i> )(J)
Linear	4.53-5.23	4.54-5.24	0.71	1.78
Mono-stable	2.00-3.73	2-2.88	1.37	1.62
Bi-stable	3.68-4.83	3.48-5.26	1.78	0.72
Tri-stable	1.66-4.36	2.00-2.10	2.36	3.86

# 3.5.2 Low-level acceleration

To investigate the energy harvesting performances of the system under the excitation with low-level acceleration, a series of simulations are conducted. In the

simulation, the acceleration amplitude is set to 0.3 m/s<sup>2</sup> and the frequency varies from 2 to 8 Hz (up-sweep) and 8 to 2 Hz (down-sweep) in a duration of 360 seconds, and the same initial conditions as those in the previous section are used. In this time, the bistable and tri-stable will perform the low-amplitude intra-well oscillation at their side potential wells and middle potential well, respectively.

By following the same procedure discussed previously, E(t) for the system under frequency up-sweep and down-sweep excitation can be obtained and shown in Figure 3.21. As the values of E(t) under low-level excitation are much lower than those under the high-level excitation, the threshold of increase slop is chosen as  $2 \times 10^{-3}$  J/Hz when the effective frequency range is identified. The effective bandwidth of the system and the E(T) of the different configurations are both summarized in Table 3.7. The results indicate that the bi-stable and tri-stable possess a wider efficient energy harvesting bandwidth, The bi-stable system, in particular, can harvest more energy compared to other configurations. The higher energy harvesting efficiency is attributed to the high-power output regions of EMEH located around the equilibrium points of the bi-stable system (at |x| = 0.02 m). And this can guarantee the high efficiency of energy harvesting even when the bi-stable system performs the low-amplitude intra-well oscillation.

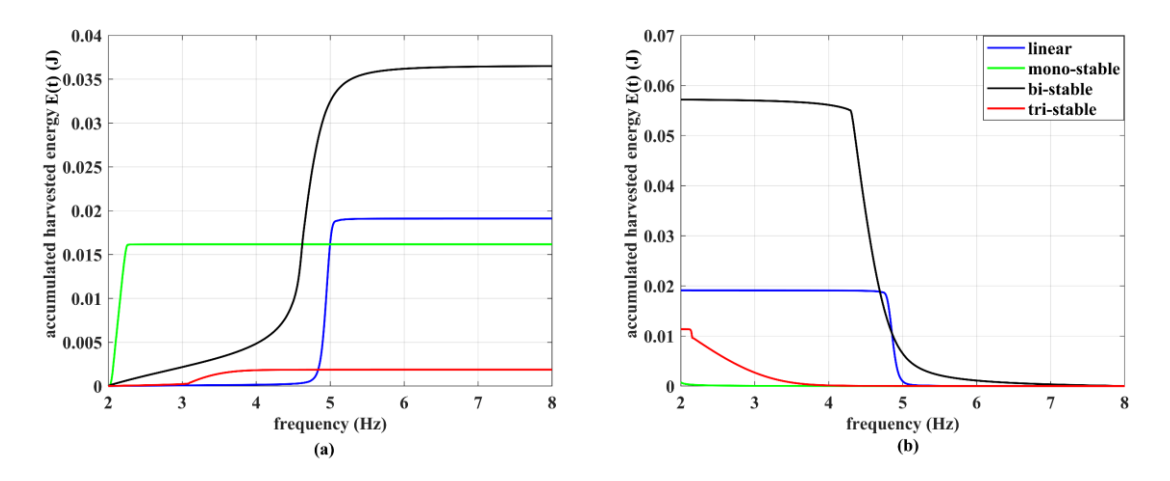


Figure 3.21 The accumulated harvested energy of the MSHEH under the low-level excitation: (a) frequency up-sweep excitation; (b) frequency down-sweep excitation.

Table 3.7 The effective frequency bandwidths of the systems under low-level

frequency sweep excitation.

	<b>Up-sweep frequency</b>	Down-sweep frequency	Total bandwidth	<b>E</b> ( <b>T</b> ) ( <b>I</b> )
	range (Hz)	range (Hz)	(Hz)	E(T) (J)
Linear	4.60-5.10	4.62-5.12	0.52	3.82×10 <sup>-2</sup>
Mono-stable	2.00-2.37	2.00-2.08	0.37	1.69×10 <sup>-2</sup>
Bi-stable	3.07-5.34	4.14-5.72	2.65	9.35×10 <sup>-2</sup>
Tri-stable	3.07-3.44	2.00-3.66	1.66	1.32×10 <sup>-2</sup>

### 3.6 Pareto Front Optimization

To maximize the power output of the system, it is crucial to determine the optimum resistance value. Traditionally, this involves applying impedance matching to each component within a hybrid energy harvester [19]. However, the complex coupling effect between the PEH and the EMEH warrants further consideration. A traditional impedance matching may not be sufficient to ensure the optimum overall performance of the system. The explanation is shown as follows: In this apparatus, the deployment of a large number of coils results in a significantly high peak value for  $K_t$ , leading to substantial electromagnetic damping forces from the EMEH. The force will significantly impact the dynamics of the system, particularly in multi-stable configuration cases. Although higher currents in the EMEH can increase its power output, the resulting large damping force may hinder the system from performing the inter-well oscillations. In other words, increasing the power output of the EMEH may scarify the power output of the PEH. Therefore, a proper compromise between the power output of EMEH and PEH needs to be considered when one chooses the optimum  $R_{le}$  and  $R_{lp}$ .

In this study, the MATLAB Global Optimization Toolbox based on the genetic algorithm is employed to solve such a multiple-objective optimization problem. The average power outputs of the EMEH and PEH are defined as follows:

$$\overline{P}_{em} = I_{rms}^2 R_{le}, \tag{3.23}$$

And

$$\overline{P}_p = \frac{v_{rms}^2}{R_{lp}},\tag{3.24}$$

respectively, where  $I_{rms}$  and  $v_{rms}$  are the root mean square value of the output current of EMEH and voltage of the PEH, respectively. The search range is from 0.1  $\Omega$  to 300  $\Omega$  for  $R_{le}$  and from 0.1 M $\Omega$  to 5 M $\Omega$  for  $R_{lp}$ . Since the program is based on the minimization of the objective functions, the two objective functions are set to  $-\overline{P}_{em}$  and  $-\overline{P}_p$  The population size and the maximum number of the generation are set to 500 and 50, respectively, and the same initial conditions as those in Section 5 are used and the amplitude of the acceleration of the harmonic excitation is set to 2 m/s<sup>2</sup>.

After implementing the optimization program to the four systems under the excitation with six different frequencies (2.5 Hz, 3 Hz, 3.5 Hz, 4 Hz, 4.5 Hz and 5 Hz), the best results of the so-called Pareto-front are shown as black dots in Figure 3.22. To find the best trade-off point, the distance between the origin of the plot and each best result is evaluated. The point with the shortest distance is considered to have the best trade-off between  $-\overline{P}_{em}$  and  $-\overline{P}_{p}$ , shown as red dots in Figure 3.22. Then, the total power output  $\overline{P}_t$  is the sum of  $-\overline{P}_{em}$  and  $-\overline{P}_p$  corresponding to this point. It is important to note that the results presented on the Pareto front offer decision support for configuring the system to meet diverse application requirements. In practical scenarios, the priority may lean towards either the EMEH or the PEH, dictating that the optimal point could be selected from either the left or right side of the best trade-off point identified in this study. Table 3.8 highlights the optimum results  $R_{le}^*$  and  $R_{lp}^*$ , and the corresponding  $\overline{P}_t$  of the four configurations when reaching the maximum at a different exciting frequency: 5 Hz (linear); 3 Hz (mono-stable); 3.5 Hz (bi-stable); 3 Hz (tristable). As summarized in [19], the power output of HEH consisting of a PEH and EMEH generally ranges from 1  $\mu$ W to 100 mW, Therefore, the power output level for the proposed apparatus in this study is considered reasonable.

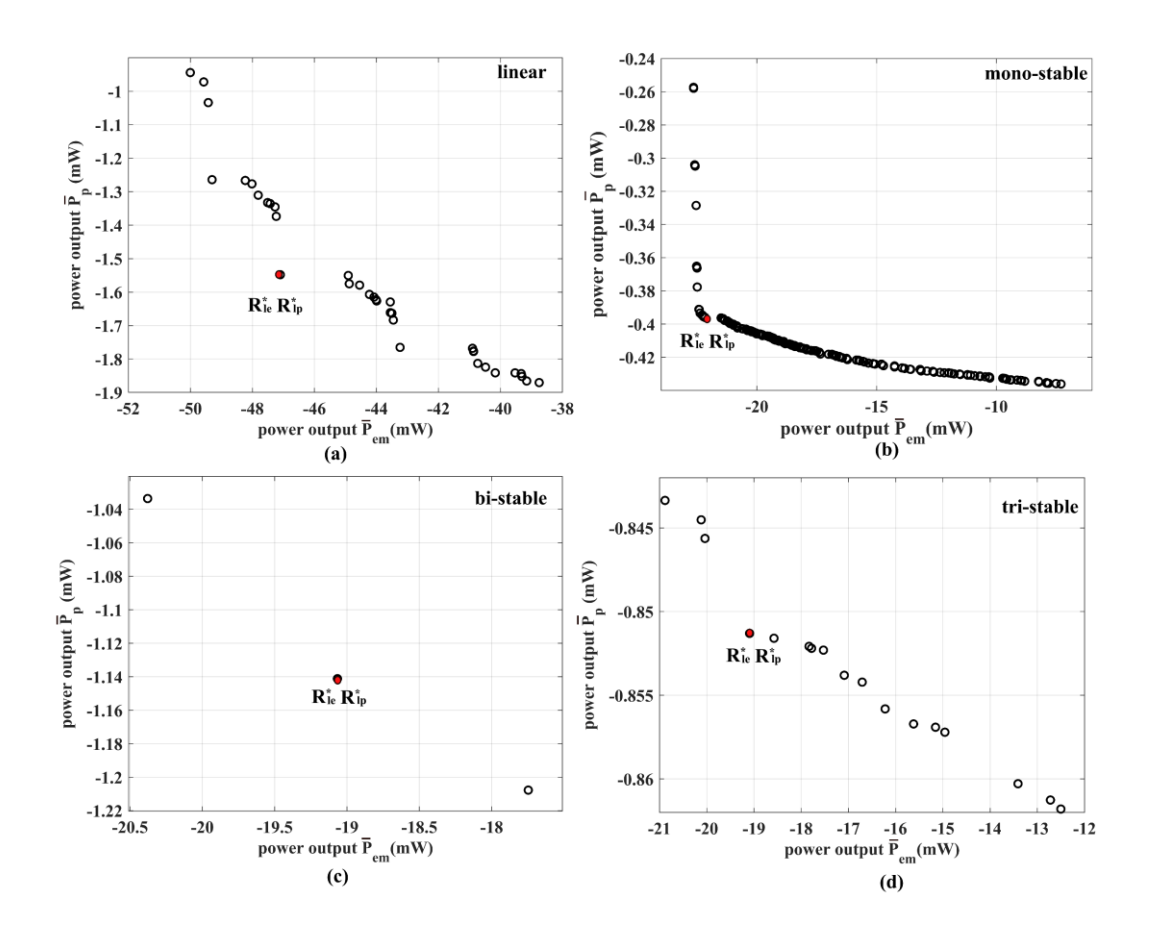


Figure 3.22 The best Pareto fronts: (a) the linear system excited at 5 Hz; (b) the mono-stable system excited at 3 Hz; (c) the bi-stable system excited at 3.5 Hz; (d) the tri-stable system excited at 3 Hz.

Table 3.8 The optimum load resistance values and total power output for the four configurations.

Configuration	Frequency (Hz)	$R_{le}^{*}\left( \Omega  ight)$	$R_{lp}^{*}$ (M $\Omega$ )	$\overline{P}_{em}$ (mW)	$\overline{P}_p$ (mW)	$\overline{P}_t$ (mW)
	2.5	82.612	1.49	0.03	0.004	0.03
Linear	3	19.25	1.11	0.44	0.04	0.48
	3.5	13.76	0.92	0.10	0.02	0.12
	4	44.69	0.77	0.44	0.04	0.48
	4.5	49.30	0.74	6.45	0.16	6.61
	5	204.18	0.60	47.10	1.54	48.64
	2.5	43.00	1.23	10.34	0.23	10.56
	3	54.36	1.04	21.36	0.39	21.76
Mana stabla	3.5	24.42	0.93	0.22	0.02	0.24
Mono-stable	4	14.92	0.87	0.08	0.01	0.09
	4.5	15.26	0.77	0.03	0.01	0.04
	5	15.97	0.67	0.02	0.01	0.02
	2.5	69.19	1.03	0.54	0.01	0.54
	3	256.11	0.73	12.76	0.75	13.51
Bi-stable	3.5	282.41	1.37	19.07	1.14	20.21
	4	43.90	0.79	12.94	0.12	13.06
	4.5	123.43	1.23	5.75	0.16	5.90
	5	75.73	0.63	6.90	0.06	6.97
Tri-stable	2.5	94.56	1.41	17.76	0.55	18.31
	3	164.22	1.04	19.09	0.85	19.94
	3.5	54.67	1.58	4.81	0.12	4.93
	4	46.17	2.06	4.35	0.10	4.46
	4.5	34.74	0.61	7.26	0.05	7.31
	5	19.07	0.62	0.10	0.02	0.11

In the above optimization, the maximum harvested powers of the EMEH and PEH are chosen as the objective functions and the harmonic excitation with a constant frequency is considered. The result shows that the linear configuration outperforms the other three ones, confirming the well-known knowledge that the linear energy harvester is the best choice if the ambient vibration is harmonic with a fixed frequency. In the previous frequency sweep excitation simulation, the best compromised values in Table 3.8 were used in order to compare the four configurations based on the benchmark of the linear configuration. The results have shown that the nonlinear configurations outperform the linear one in terms of the accumulated harvested energy and the frequency bandwidth. A natural question arises what the best load resistances are if the MSHEH is subjected to a frequency sweep excitation and the accumulated harvested

energies are chosen to be the objective functions.

To answer this question, a further optimization is conducted. The MSHEH is subjected to the high-level frequency up-sweep excitation. The two objectives are set as  $-E_{em}(T)$  and  $-E_p(T)$ , respectively. By following the same simulation procedure as outlined for the high-level frequency up-sweep tests in the previous section, E(t) for each configuration can be obtained. The setting of the optimization is same as the above, and the same initial conditions are used as those in Section 5. Considering the computational cost, the duration of the excitation signal is chosen as T = 100 second. The obtained Pareto fronts for the four configurations are shown in Figure 3.23, where the best trade-off points are identified by red circles. The optimum resistance values  $R_{le}^*$  and  $R_{lp}^*$ , and the corresponding accumulated harvested energy for the EMEH and PEH  $E_{em}^*(T)$  and  $E_P^*(T)$ , and total accumulated harvested energy  $E^*(T)$  are listed in Table 3.9. It can be seen that  $E^*(T)$  for nonlinear configurations outperform the linear configuration. Figure 3.24 compares the E(t) (solid lines) of the MSHEH with the optimum load resistances from Table 3.8, referred to as Opt 1 and those (dashed lines) with the optimum load resistances from Table 3.9, referred to as Opt 2. Several observations can be made. Here E(T) represents the E(t)s' value at 8Hz. Firstly, the E(T)s from the linear configuration remain almost unchanged for both cases. Secondly, the E(T) from the bi-stable configuration for Opt 2 sees an increase compared with that for Opt 1. Thirdly, the E(T) from the mono-stable configuration for Opt 2 increases significantly. Fourthly, the tri-stable configuration for Opt 2 still exhibits the best performance than the other three.

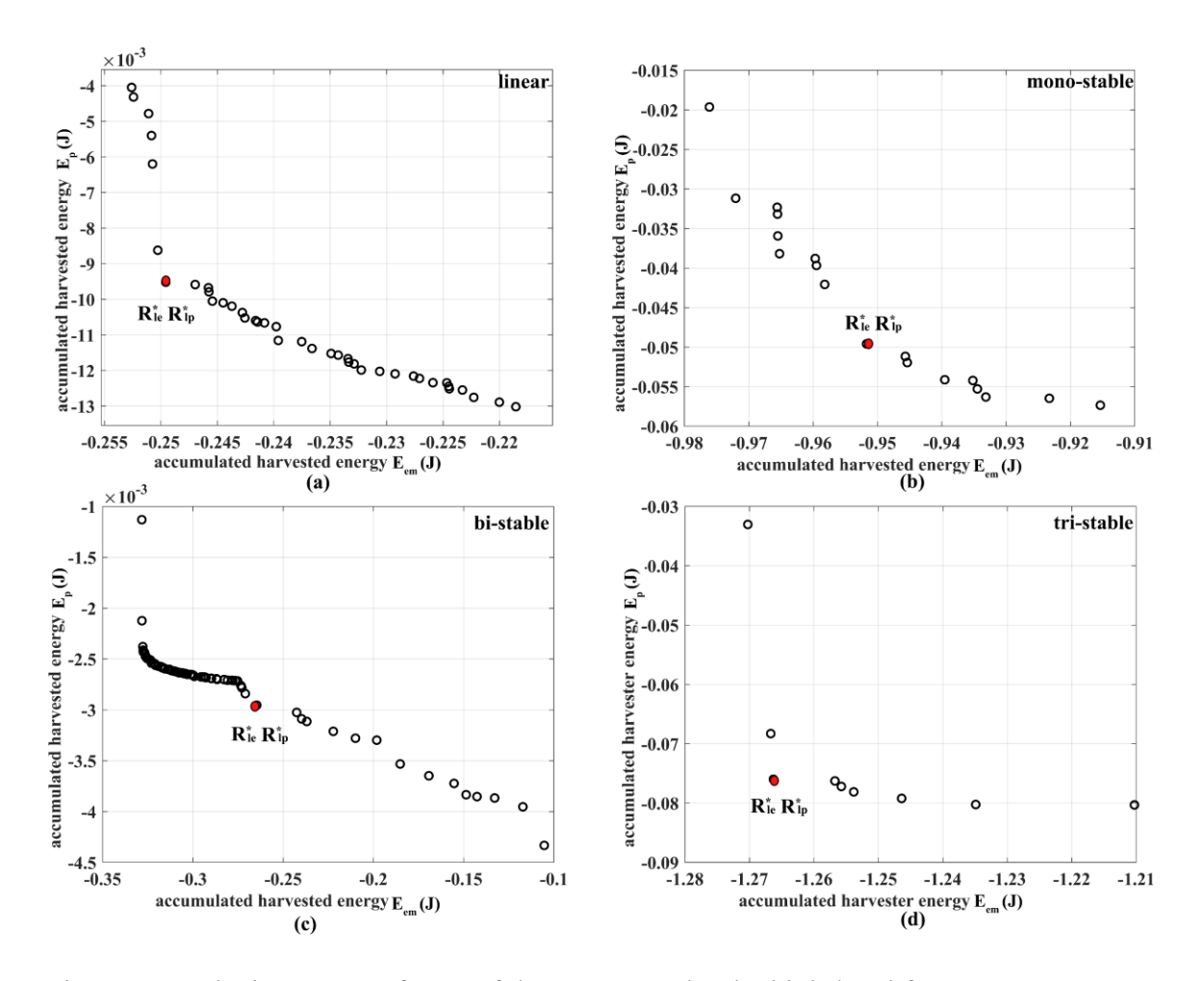


Figure 3.23 The best Pareto fronts of the system under the high-level frequency upsweep excitation: (a) the linear configuration; (b) the mono-stable configuration; (c) the bi-stable configuration; (d) the tri-stable configuration.

Table 3.9 The optimum load resistance values and total power output for the four configurations.

Configuration	$R_{le}^{*}\left(\Omega\right)$	$R_{lp}^{*}\left( \mathrm{M}\Omega  ight)$	$E_{em}^{*}(T)$ (J)	$E_p^*(\mathbf{T})$ (J)	$E^*(T)(J)$
Linear	194.80	0.54	0.24	1.0×10 <sup>-2</sup>	0.25
Mono-stable	256.86	0.58	0.95	5.0×10 <sup>-2</sup>	1.00
Bi-stable	66.28	0.91	0.26	0.3×10 <sup>-2</sup>	0.26
Tri-stable	258.21	1.09	1.26	7.6×10 <sup>-2</sup>	1.34

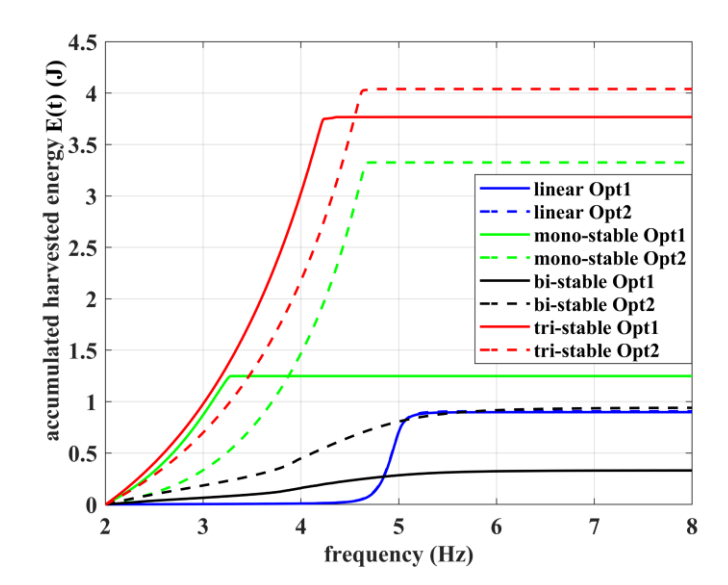


Figure 3.24 The total accumulated harvested energy of the MSHEH under the high-level frequency up-sweep excitation.

### 3.7 Conclusions

In this study, we present the development and evaluation of a multi-stable hybrid energy harvester (MSHEH). The system is equipped with both an electromagnetic energy harvester (EMEH) and a piezoelectric energy harvester (PEH), offering two tuning variables (h and d) for selecting the different stability states. A novel arrangement of coils in the EMEH has been implemented to enhance energy harvesting efficiency across various oscillation modes. A numerical approach is employed to determine the transduction factor for the EMEH. The obtained results are validated experimentally. The magnetic restoring force model is established based on the

equivalent magnetic 2-point dipole model and validated experimentally. The accuracy of the model is further improved by the genetic algorithm identification approach. This refined model was used to map the stability state region. Four different configurations of the MSHEH, namely linear, mono-stable, bi-stable, and tri-stable, were chosen to evaluate the energy harvesting performances of the MSHEH through both simulation and experiment.

In the performance evaluation, the MSHEH's four configurations are subjected to frequency up-sweep or down-sweep base excitation with high-level acceleration and low-level acceleration, respectively. The results revealed that under the high-level excitation, the mono-stable and multi-stable configurations exhibit a wider working bandwidth than the linear one. Particularly, owing to the shallower barrier of the potential wells, the tri-stable system is able to perform the large amplitude periodic inter-well oscillation, which makes it have the widest frequency bandwidth (2.36 Hz) and highest total accumulated harvested energy (3.86 J) among the four configurations. When the system is under low-level excitation, both bi-stable and tri-stable harvesters perform the low amplitude intra-well oscillation around the side potential wells and the middle potential well, respectively. The results show the bi-stable system outperforms the others in terms of effective bandwidth (2.65 Hz) and total accumulated harvested energy (9.35×10<sup>-2</sup> J). Due to the high power output regions of the EMEH are located around the two side equilibriums of the bi-stable configuration, the EMEH's power output remains sufficiently high, even though the system only performs low amplitude intra-well oscillations.

In the end, a Pareto front optimization is employed to find the optimum values for  $R_{le}$  and  $R_{lp}$  by balancing the power output for the EMEH and PEH when the system is under harmonic excitation with various frequencies. The results demonstrate that the value of the optimum  $R_{le}$  is higher when the amplitude of the oscillation is larger, and the values of the optimum  $R_{lp}$  are inversely proportional to the frequency of the excitation. In addition, another Pareto optimization is conducted to further improve the accumulated harvested energy for both EMEH and PEH under the high-level frequency up-sweep excitation. the results demonstrate that the total accumulated harvested energies of the nonlinear configurations outperform the linear one.

#### References

- [1] R. Hidalgo-Leon *et al.*, "Powering nodes of wireless sensor networks with energy harvesters for intelligent buildings: A review," *Energy Reports*, vol. 8, pp. 3809-3826, 2022, doi: 10.1016/j.egyr.2022.02.280.
- [2] I. Ahmad, L. M. Hee, A. M. Abdelrhman, S. A. Imam, and M. S. Leong, "Scopes, challenges and approaches of energy harvesting for wireless sensor nodes in machine condition monitoring systems: A review," *Measurement*, vol. 183, 2021, doi: 10.1016/j.measurement.2021.109856.
- [3] N. Zhou, Z. Hou, Y. Zhang, J. Cao, and C. R. Bowen, "Enhanced swing electromagnetic energy harvesting from human motion," *Energy*, vol. 228, 2021, doi: 10.1016/j.energy.2021.120591.
- [4] W. Zhou, D. Du, Q. Cui, C. Lu, Y. Wang, and Q. He, "Recent research progress in piezoelectric vibration energy harvesting technology," *Energies*, vol. 15, no. 3, 2022, doi: 10.3390/en15030947.
- [5] Z. Yang, S. Zhou, J. Zu, and D. Inman, "High-performance piezoelectric energy harvesters and their applications," *Joule*, vol. 2, no. 4, pp. 642-697, 2018, doi: 10.1016/j.joule.2018.03.011.
- [6] S. C. Stanton, C. C. McGehee, and B. P. Mann, "Reversible hysteresis for broadband magnetopiezoelastic energy harvesting," *Applied Physics Letters*, vol. 95, no. 17, 2009, doi: 10.1063/1.3253710.
- [7] S. Zhou, J. Cao, and J. Lin, "Theoretical analysis and experimental verification for improving energy harvesting performance of nonlinear monostable energy harvesters," *Nonlinear Dynamics*, vol. 86, no. 3, pp. 1599-1611, 2016, doi: 10.1007/s11071-016-2979-7.
- [8] A. Erturk, J. Hoffmann, and D. J. Inman, "A piezomagnetoelastic structure for broadband vibration energy harvesting," *Applied Physics Letters*, vol. 94, no. 25, 2009, doi: 10.1063/1.3159815.
- [9] G. Wang, W.-H. Liao, B. Yang, X. Wang, W. Xu, and X. Li, "Dynamic and energetic characteristics of a bistable piezoelectric vibration energy harvester with an elastic magnifier," *Mechanical Systems and Signal Processing*, vol. 105, pp. 427-446, 2018, doi: 10.1016/j.ymssp.2017.12.025.
- [10] Y. Zhang, J. Cao, W. Wang, and W.-H. Liao, "Enhanced modeling of nonlinear restoring force in multi-stable energy harvesters," *Journal of Sound and Vibration*, vol. 494, 2021, doi: 10.1016/j.jsv.2020.115890.
- [11] L. Haitao, Q. Weiyang, L. Chunbo, D. Wangzheng, and Z. Zhiyong, "Dynamics and coherence resonance of tri-stable energy harvesting system," *Smart*

- Materials and Structures, vol. 25, no. 1, p. 015001, 2016, doi: 10.1088/0964-1726/25/1/015001.
- [12] X. Ma, H. Li, S. Zhou, Z. Yang, and G. Litak, "Characterizing nonlinear characteristics of asymmetric tristable energy harvesters," *Mechanical Systems and Signal Processing*, vol. 168, 2022, doi: 10.1016/j.ymssp.2021.108612.
- [13] S. Guo, Q. Liu, J. Sun, and H. Jin, "A review on the utilization of hybrid renewable energy," *Renewable and Sustainable Energy Reviews*, vol. 91, pp. 1121-1147, 2018, doi: 10.1016/j.rser.2018.04.105.
- [14] H. Liu, H. Fu, L. Sun, C. Lee, and E. M. Yeatman, "Hybrid energy harvesting technology: From materials, structural design, system integration to applications," *Renewable and Sustainable Energy Reviews*, vol. 137, 2021, doi: 10.1016/j.rser.2020.110473.
- [15] H. Liu, J. Zhong, C. Lee, S.-W. Lee, and L. Lin, "A comprehensive review on piezoelectric energy harvesting technology: Materials, mechanisms, and applications," *Applied Physics Reviews*, vol. 5, no. 4, 2018, doi: 10.1063/1.5074184.
- [16] A. Muscat, S. Bhattacharya, and Y. Zhu, "Electromagnetic vibrational energy harvesters: a review," *Sensors (Basel)*, vol. 22, no. 15, Jul 25 2022, doi: 10.3390/s22155555.
- [17] F. U. Khan and M. U. Qadir, "State-of-the-art in vibration-based electrostatic energy harvesting," *Journal of Micromechanics and Microengineering*, vol. 26, no. 10, 2016, doi: 10.1088/0960-1317/26/10/103001.
- [18] M. Iqbal *et al.*, "Vibration based piezoelectric, electromagnetic, and hybrid energy harvesters for microsystems applications: A contributed review," *International Journal of Energy Research*, vol. 45, no. 1, pp. 65-102, 2020, doi: 10.1002/er.5643.
- [19] M. M. Ahmad and F. U. Khan, "Review of vibration based electromagnetic—piezoelectric hybrid energy harvesters," *International Journal of Energy Research*, vol. 45, no. 4, pp. 5058-5097, 2020, doi: 10.1002/er.6253.
- [20] V. R. Challa, M. G. Prasad, and F. T. Fisher, "A coupled piezoelectric–electromagnetic energy harvesting technique for achieving increased power output through damping matching," *Smart Materials and Structures*, vol. 18, no. 9, 2009, doi: 10.1088/0964-1726/18/9/095029.
- [21] M. Kundurthi, D. Mallick, and A. Jain, "System level modeling and optimization of hybrid vibration energy harvesters," in 2020 IEEE International Symposium on Circuits and Systems (ISCAS), 2020: IEEE, pp. 1-5.

- [22] F. Shen *et al.*, "A hybrid energy harvester based on piezoelectric and electromagnetic mechanisms," in *Journal of Physics: Conference Series*, 2023, vol. 2418, no. 1: IOP Publishing, p. 012067.
- [23] M. Rajarathinam and S. F. Ali, "Energy generation in a hybrid harvester under harmonic excitation," *Energy Conversion and Management*, vol. 155, pp. 10-19, 2018, doi: 10.1016/j.enconman.2017.10.054.
- [24] K. Fan, S. Liu, H. Liu, Y. Zhu, W. Wang, and D. Zhang, "Scavenging energy from ultra-low frequency mechanical excitations through a bi-directional hybrid energy harvester," *Applied Energy*, vol. 216, pp. 8-20, 2018/04/15/ 2018, doi: https://doi.org/10.1016/j.apenergy.2018.02.086.
- [25] R. M. Toyabur, M. Salauddin, H. Cho, and J. Y. Park, "A multimodal hybrid energy harvester based on piezoelectric-electromagnetic mechanisms for low-frequency ambient vibrations," *Energy Conversion and Management*, vol. 168, pp. 454-466, 2018, doi: 10.1016/j.enconman.2018.05.018.
- [26] B. D. Truong, C. P. Le, and S. Roundy, "Are piezoelectric-electromagnetic hybrid energy harvesting systems beneficial?," *Smart Materials and Structures*, vol. 32, no. 9, 2023, doi: 10.1088/1361-665X/acec23.
- [27] S. Mahmoudi, N. Kacem, and N. Bouhaddi, "Enhancement of the performance of a hybrid nonlinear vibration energy harvester based on piezoelectric and electromagnetic transductions," *Smart Materials and Structures*, vol. 23, no. 7, 2014, doi: 10.1088/0964-1726/23/7/075024.
- [28] K. Fan, J. Hao, Q. Tan, and M. Cai, "A monostable hybrid energy harvester for capturing energy from low-frequency excitations," *Journal of Intelligent Material Systems and Structures*, vol. 30, no. 18-19, pp. 2716-2732, 2019, doi: 10.1177/1045389x19873420.
- [29] M. A. Karami, P. S. Varoto, and D. J. Inman, "Analytical approximation and experimental study of bi-stable hybrid nonlinear energy harvesting system," in *International Design Engineering Technical Conferences and Computers and Information in Engineering Conference*, 2011, vol. 54785, pp. 265-271.
- [30] J. Xing, S. Fang, X. Fu, and W.-H. Liao, "A rotational hybrid energy harvester utilizing bistability for low-frequency applications: Modelling and experimental validation," *International Journal of Mechanical Sciences*, vol. 222, 2022, doi: 10.1016/j.ijmecsci.2022.107235.
- [31] T. Yang and Q. Cao, "Dynamics and performance evaluation of a novel tristable hybrid energy harvester for ultra-low level vibration resources," *International Journal of Mechanical Sciences*, vol. 156, pp. 123-136, 2019, doi: 10.1016/j.ijmecsci.2019.03.034.
- [32] Z. Peng, F. Song, and Y. Xiong, "A tri-stable structure of piezoelectric-electromagnetic composite energy harvester (TPEEH)," *Microsystem*

- *Technologies*, vol. 29, no. 2, pp. 243-251, 2023, doi: 10.1007/s00542-023-05416-x.
- [33] H. Li, K. Liu, J. Deng, and B. Li, "Validation and optimization of two models for the magnetic restoring forces using a multi-stable piezoelectric energy harvester," *Journal of Intelligent Material Systems and Structures*, vol. 34, no. 14, pp. 1688-1701, 2023, doi: 10.1177/1045389x221151064.
- [34] S. Zhou, J. Cao, D. J. Inman, J. Lin, S. Liu, and Z. Wang, "Broadband tristable energy harvester: Modeling and experiment verification," *Applied Energy*, vol. 133, pp. 33-39, 2014, doi: 10.1016/j.apenergy.2014.07.077.
- [35] M. Panyam and M. F. Daqaq, "Characterizing the effective bandwidth of tristable energy harvesters," *Journal of Sound and Vibration*, vol. 386, pp. 336-358, 2017, doi: 10.1016/j.jsv.2016.09.022.
- [36] L. Hai-Tao, D. Hu, J. Xing-Jian, Q. Wei-Yang, and C. Li-Qun, "Improving the performance of a tri-stable energy harvester with a staircase-shaped potential well," *Mechanical Systems and Signal Processing*, vol. 159, 2021, doi: 10.1016/j.ymssp.2021.107805.
- [37] G. Wang, Z. Zhao, W.-H. Liao, J. Tan, Y. Ju, and Y. Li, "Characteristics of a tri-stable piezoelectric vibration energy harvester by considering geometric nonlinearity and gravitation effects," *Mechanical Systems and Signal Processing*, vol. 138, 2020, doi: 10.1016/j.ymssp.2019.106571.
- [38] M. A. Karami and D. J. Inman, "Nonlinear hybrid energy harvesting utilizing a piezo-magneto-elastic spring," in *Active and Passive Smart Structures and Integrated Systems 2010*, 2010, vol. 7643: SPIE, pp. 245-255.
- [39] H. Xia, R. Chen, and L. Ren, "Parameter tuning of piezoelectric–electromagnetic hybrid vibration energy harvester by magnetic force: Modeling and experiment," *Sensors and Actuators A: Physical*, vol. 257, pp. 73-83, 2017.
- [40] L. Tang, Y. Yang, and H. Wu, "Modeling and experiment of a multiple-DOF piezoelectric energy harvester," in *Active and Passive Smart Structures and Integrated Systems* 2012, 2012, vol. 8341: SPIE, pp. 429-441.
- [41] D. Spreemann and Y. Manoli, "*Electromagnetic Vibration Energy Harvesting Devices*," Springer Series in Advanced Microelectronics 2012, doi: 10.1007/978-94-007-2944-5.
- [42] G. Wang, H. Wu, W.-H. Liao, S. Cui, Z. Zhao, and J. Tan, "A modified magnetic force model and experimental validation of a tri-stable piezoelectric energy harvester," *Journal of Intelligent Material Systems and Structures*, vol. 31, no. 7, pp. 967-979, 2020.

## Chapter 4. Using a Piecewise-Linear Spring to

## Approximate an Essentially Nonlinear Spring: Design

#### and Validation

#### 4.1 Introduction

An essentially nonlinear spring (ENS) is a hardening spring with a zero stiffness at its undeformed position. Mathematically, its restoring force can be expressed as an odd-order polynomial without the first-order term. In particular, the ENS with a cubic nonlinearity is considered in this study. The ENS has been widely used for vibration isolation such as quazi-zero stiffness (QZS) isolators [1] and vibration suppression such as nonlinear energy sink (NES) [2]. In the latter, the unique properties of the ENSs enable an NES to weakly couple with a primary system so that the 1:1 resonance can be trigged and the targeted energy transfer (TET) can be established if the excitation level exceeds a threshold [3]. Additionally, the ENS has also been widely employed in the construction of nonlinear vibration energy harvesters to overcome the narrow bandwidth limitation of traditional linear oscillators. This enhancement significantly improves the robustness and efficiency of vibration energy harvesters in real-world environments [4]. Various means have been developed to realize an ENS, including near buckling beam, zero-tension string, cam-roller-spring, magnetic spring, and piecewise linear spring (PLS), etc.

Mechanical springs are the most common approach to realizing ENS characteristics. The classic three-spring structure was first proposed in [5]. This design utilizes a vertical coil spring to provide positive stiffness and two oblique springs to provide negative stiffness. By carefully balancing the positive stiffness and negative stiffness, the desired ENS behaviour can be achieved. Various designs were developed based on such a principle [6]. For example, a design employing two buckled beams as negative stiffness elements was introduced in [7]. The design in [8-10] utilized multiple pairs of

oblique springs to enlarge the low-stiffness range of QZS isolators to provide a better isolation performance under low frequency excitation. In [11, 12], a design that uses only two springs combined with rigid links to achieve QZS is proposed. In [13], a novel spring arrangement that combines with an X-shape structure presented to achieve an even better low frequency vibration isolation performance.

Cam-roller-spring construction provides another approach to realizing ENS. Such a device usually consists of a spring-supported roller. When the roller moves on a curved surface, the restoring force of the spring will change in a nonlinear way along the curved surface. In [14], a typical cam-roller-spring design is proposed and conducted a systematical analysis of its static and dynamic behaviours. The design proposed in [15] combined a vertical liner spring with two parallel cam-roller-spring structures. The study in [16] proposed a customized surface for the cam to enable the isolator to perform both hardening and softening spring behaviours. A novel design proposed in [17] allowed the isolator to show essentially nonlinearity in two directions simultaneously.

Magnetic spring constructions have also been widely studied to achieve ENS behaviour. These assemblies typically use magnetic attraction or repulsion properties between magnet poles to generate a negative or positive stiffness spring. The nonlinear nature of the force between two magnets makes magnetic springs ideal for achieving ENS characteristics. in [18], a typical design was proposed by allowing a magnet to move between two fixed magnets in a tube. On the other hand, the magnetic springs can combine with other components like beam [19, 20], coil springs [21, 22] or wire rope [23] to make the system more stable.

Each of the aforementioned methods presents both advantages and limitations. For instance, an ENS realized by a zero-tension string is generally straightforward in design and tuning. However, it requires a supporting track, which introduces unwanted friction, and its bulky design can limit its use in compact applications. The cam-roller spring can precisely achieve complex nonlinearity, but the contact between the cam surface and the roller can lead to significant friction, reducing overall efficiency. A magnetic spring offers contactless operation, which prevents wear and tear, but often requires complex and precise adjustments to achieve the desired nonlinearity. It should

also be noted that these methods strive to approximate an ideal ENS as any spring inherently possesses a certain degree of linear stiffness. Another promising approach to approximate an ENS is to use a PLS. This approach involves dividing the nonlinear force-displacement relationship into several linear segments, each representing a different stiffness characteristic. By carefully selecting the breakpoints and slopes of these segments, it is possible to closely approximate the nonlinear behaviors of the ENS system while retaining the mathematical simplicity of linear analysis within each segment. The simplest PLS configuration involves a cantilever beam constrained by a pair of stop blocks. The study in [24] developed a PLS with tunable piecewise linear stiffness by using a cantilever beam and a pair of movable single-stop blocks. A PLS developed in [25] employs a cantilever beam with a pair of double-stop blocks. Based on such a concept, some designs by using continuous stop blocks were developed [26, 27]. Note that this kind of design no longer belongs to the piecewise linear category.

PLS offers several advantages. For example, the non-smooth nonlinearity of the PLS has been proven to have a high vibration reduction effect, which brought benefits when employing PLS in the NES design [28]. Moreover, PLS provides a flexible and computationally efficient approach for modeling complex nonlinear behaviors, which facilitates integration with existing analytical methods, such as the harmonic balance method. This versatility makes PLS design especially valuable in the design and optimization of mechanical vibration absorbers, energy harvesters, and other systems where nonlinearities play a critical role. Despite these advantages, existing implementations of PLS, particularly those employing beams with double-stop blocks such as the one proposed in [25], often rely on the trial-and-error method to determine configuration parameters. Few studies provide a systematic design method for PLS consisting of a cantilever beam with single-stop or double-stop blocks. This study intends to address this gap. The contributions of the present work lie in four aspects. First, a systematic design procedure is developed to use a cantilever beam-based PLS with single- or double-stop blocks to approximate an ENS. To the best of our knowledge, no such study has been reported. Second, comparative simulations are conducted to evaluate the performances of the optimum PLSs statically and dynamically. Such method of evaluation is applicable in similar studies. Third, an apparatus with a tunable design is developed to validate the simulation results. Fourth,

the limitation of using a cantilever beam-based PLS to approximate an ENS is revealed, and the remedy is proposed.

The rest of the Chapter is organized as follows: In Section 2, a design procedure is presented to find the optimum parameters of a PLS with single- or double-stop blocks based on a desired ENS. In Section 3, numerical simulations are conducted to evaluate the behaviors of the designed PLSs. In Section 4, experiments are carried out to validate the simulation results statically and dynamically. The main conclusions of the study are given in Section 5.

#### 4.2 Design Procedure

As mentioned in the Introduction, a PLS with low linear stiffness and high nonlinear stiffness can be achieved by placing a cantilever beam between a pair of single- or double-stop blocks. In what follows, a procedure is developed to design such a PLS. For this purpose, an apparatus with four tunable stop-blocks is developed. Figure 4.1(a) shows a CAD drawing of the developed apparatus. The frame of the apparatus is constructed by connecting a top block to a base block using four aluminum extrusions. A stainless steel beam is clamped in the middle of the top block, and its free end is attached by a pair of magnets acting as an oscillating mass. On each side of the beam, there are two stop blocks. Each of the four stop blocks is held in place by a holder, which is attached to a movable bar that can slide up and down. Individual block can be slid horizontally inside of its holder. The top block, the base block, and the stop blocks are made of PLA filament through 3D printing.

Figure 4.1(b) illustrates a schematic of the system model, where z denotes the displacement of the tip mass relative to the base, m is the tip mass, c and  $k_n$  represent the damping coefficient and nonlinear stiffness of the steel beam, respectively. Based on the model, the equation of motion can be derived as follows:

$$m\ddot{z} + c\dot{z} + f_{pl} = 0 \tag{4.1}$$

where  $f_{pl}$  is the piecewise linear restoring force of the PLS which has two distinct forms:  $f_{pls}$  for the single-stop configuration and  $f_{pld}$  for the double-stop configuration.

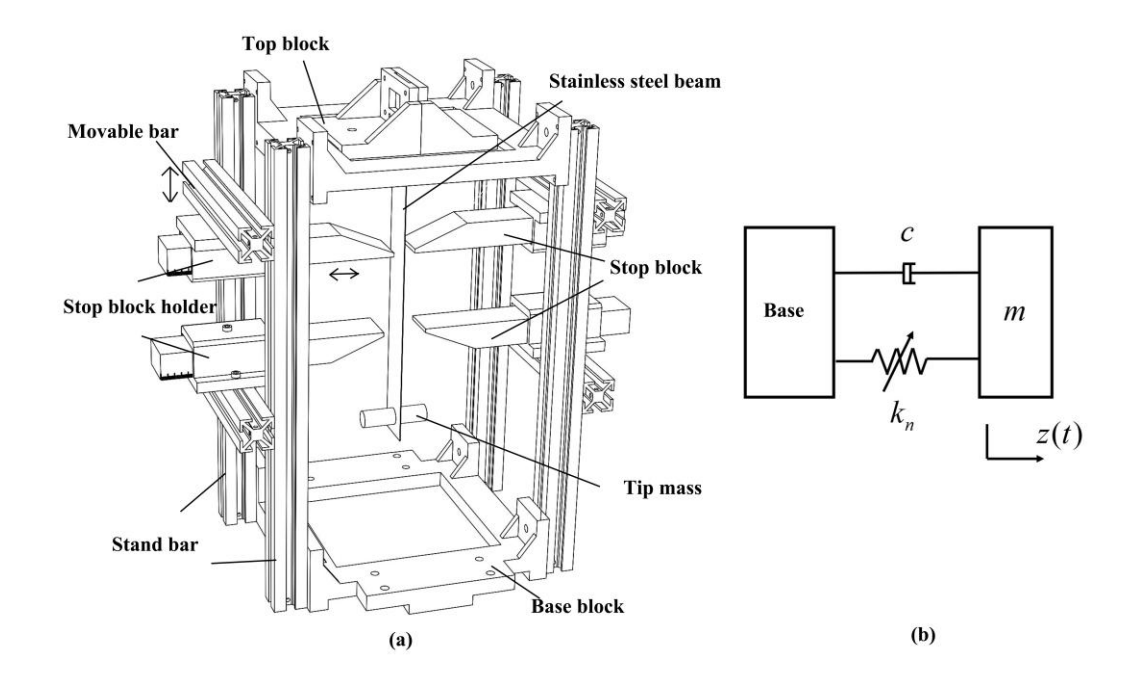


Figure 4.1(a) CAD drawing of the proposed apparatus; (b) schematic of the system model.

Figure 4.2(a) shows the configuration of the PLS with single-stop blocks where l denotes the length of the beam, h the location of the stop block, and d the gap between the undeformed beam and the stop block, and  $z_s$  the critical displacement when the beam just contacts tip A. The critical displacement  $z_s$  divides the piecewise linear restoring force into two sections: unconstrained and constrained. They have two incremental piecewise linear stiffness  $k_{s1}$  and  $k_{s2}$ . Then the restoring force of the PLS with single-stop blocks within the range of  $-z_m \le z \le z_m$  can be expressed as:

$$f_{pls}(z) = \begin{cases} k_{s2}(z+z_s) - k_{s1}z_s & -z_m \le z < -z_s \\ k_{s1}z & -z_s \le z \le z_s \\ k_{s2}(z-z_s) + k_{s1}z_s & z_s < z \le z_m \end{cases}$$
(4.2)

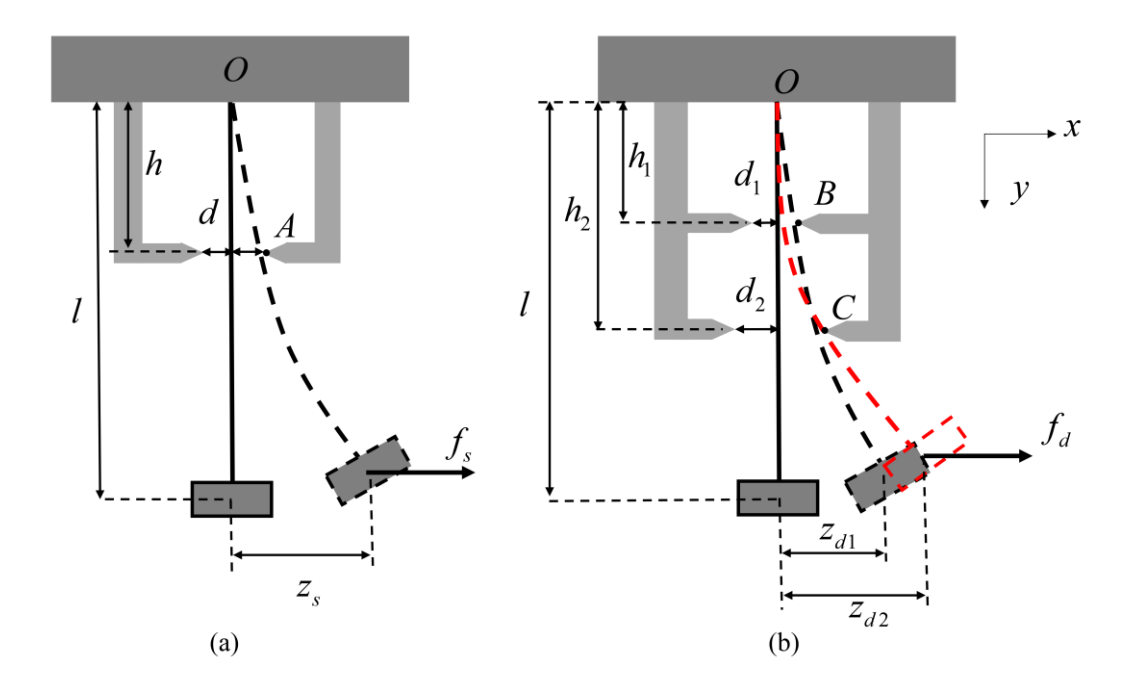


Figure 4.2 Configurations of the PLSs: (a) with single-stop blocks; (b) with double-stop blocks.

Figure 4.2(b) shows the configuration of the PLS with double-stop blocks where l denotes the length of the beam,  $h_1$  and  $d_1$  are the location and the gap of the first pair of stop blocks,  $h_2$  and  $d_2$  are the location and the gap of the second pair of stop blocks,  $z_{d1}$  the critical displacement when the beam just contacts the first block tip B and  $z_{d2}$  the critical displacement when the beam just contacts the second block tip C. The piecewise linear restoring force can be separated into three sections: one unconstrained and two constraineds. They are characterized by three incremental piecewise linear stiffness  $k_{d1}$ ,  $k_{d2}$  and  $k_{d3}$ , respectively. Then the restoring force of the PLS with double-stop blocks within the range of  $-z_m \le z \le z_m$  can be expressed as:

$$f_{pld}(z) = \begin{cases} k_{d3}(z + z_{d2}) - k_{d2}(z_{d2} - z_{d1}) - k_{d1}z_{d1} & -z_{m} \le z < -z_{d2} \\ k_{d2}(z + z_{d1}) - k_{d1}z_{d1} & -z_{d2} \le z < -z_{d1} \\ k_{d1}z & -z_{d1} \le z \le z_{d1} \\ k_{d2}(z - z_{d1}) + k_{d1}z_{d1} & z_{d1} < z \le z_{d2} \\ k_{d3}(z - z_{d2}) + k_{d2}(z_{d2} - z_{d1}) + k_{d1}z_{d1} & z_{d2} < z \le z_{m} \end{cases}$$

$$(4.3)$$

As mentioned above, the design objective is to use a PLS to approximate an ENS with a cubic nonlinearity. Thus, the desired restoring force is defined by:

$$f_{en}(z) = k_n z^3 \tag{4.4}$$

where  $k_n$  is the nonlinear stiffness. The value of  $k_n$  can be determined based on applications. In the case of the NES, the maximum displacement  $z_m$  of the mass and its corresponding instantaneous frequency  $\omega_m$  are chosen first. For example,  $z_m$  can be chosen according to the space limit and the beam deformation limit and  $\omega_m$  can be chosen according to the 1:1 resonance requirement. Then, the concept of the equivalent stiffness  $k_{eq}$  [24, 29] is used to relate  $k_n$  to  $z_m$  and  $\omega_m$ . Based on this concept, the equivalent stiffness  $k_{eq}$  of a nonlinear spring with an odd-order polynomial restoring force is related to the instantaneous frequency at  $z_m$  by:

$$k_{eq} \approx \omega_m^2 m \tag{4.5}$$

On the other hand, the equivalent stiffness can be estimated by:

$$k_{eq} = \frac{f_{cp}(z_m) + f_{cp}(z_m/2)}{z_m + z_m/2}$$
(4.6)

Substituting Eq. (4.4) into Eq. (4.6) yields:

$$k_{eq} = \frac{3}{4} k_n z_m^2 (4.7)$$

Substituting Eq. (4.5) into the above equation yields:

$$k_n = \frac{4\omega_m^2 m}{3z_{\dots}^2} \tag{4.8}$$

Now, based on eq. (4.4), the desired restoring force  $f_{en}(z)$  within  $0 \le z \le z_m$  can be determined. As defined in Eq. (4.2), there are three parameters  $k_{s1}$ ,  $k_{s2}$ ,  $z_s$  to be determined to approximate such a nonlinear force by using the PLS with single-stop blocks. When the cantilever beam is chosen,  $k_{s1}$  is specified by the formula  $k_{s1} = 3EI/l^3$ . Then the optimum values for  $k_{s2}$  and  $z_s$  can be found by minimizing the following objective function:

$$J(k_{s2}, z_s) = \sum_{i=1}^{N} (f_{pls}(z_i) - f_{en}(z_i))^2$$
(4.9)

where N is the number of discretized terms,  $z_i$  is the i<sup>th</sup> discretized displacement. With the found optimum values  $k_{s2}^*$  and  $z_s^*$ , the parameters h and d can be found in the following procedure. After the beam contacts the tip A, the beam can be treated as a fixed-pinned beam with an overhang [24]. As derived in the Appendix 4A, the stiffness of such a beam is defined by:

$$k_{s2}^* = \frac{12EI}{(l-h)^2(4l-h)} \tag{4.10}$$

The above equation can be expanded into a  $3^{rd}$ -order polynomial in terms of h:

$$-h^{3} + 6lh^{2} - 9l^{2}h + 4l^{3} - \frac{12EI}{k_{s2}^{*}} = 0$$
 (4.11)

Substituting l, EI and  $k_{s2}^*$  into the above equation yields three roots. The smallest root should be chosen as h. On the other hand, the force that causes the cantilever beam's tip to deflect  $z_s^*$  is given by:

$$f_s = \frac{3EI}{I^3} z_s^* {(4.12)}$$

With this force, the deflection of the cantilever beam at h is chosen to be d, i.e.,

$$d = \frac{3EI}{l^3} z_s^* \frac{h^2 (3l - h)}{6EI} = \frac{z_s^* h^2}{2l^3} (3l - h)$$
 (4.13)

As for the PLS with double-stop blocks, based on the restoring force defined in Eq. (4.3), there are five parameters  $k_{d1}$ ,  $z_{d1}$ ,  $k_{d2}$ ,  $z_{d2}$  and  $k_{d3}$  to be determined. When the cantilever beam is chosen,  $k_{d1}$  is specified by the formula  $k_{d1} = 3EI/l^3$ . Then, the optimum values for  $z_{d1}$ ,  $k_{d2}$ ,  $z_{d2}$  and  $k_{d3}$  can be found by minimizing the following objective function:

$$J(k_{d2}, z_{d1}, k_{d3}, z_{d2}) = \sum_{i=1}^{N} (f_{pld}(z_i) - f_{en}(z_i))^2$$
(4.14)

With the found optimum values  $k_{d2}^*$ , the smallest root of the following equation should be chosen to  $h_1$ :

$$-h^{3} + 6lh^{2} - 9l^{2}h + 4l^{3} - \frac{12EI}{k_{d2}^{*}} = 0$$
 (4.15)

With the found optimum value  $z_{d1}^*$  and  $h_1$ ,  $d_1$  can be found as:

$$d_1 = \frac{z_{d1}^* h_1^2}{2l^3} (3l - h_1) \tag{4.16}$$

With the found optimum values  $k_{d3}^*$ , the smallest root of the following equation should be chosen to be  $h_2$ :

$$-h^{3} + 6lh^{2} - 9l^{2}h + \left(4l^{3} - \frac{12EI}{k_{d3}^{*}}\right) = 0$$
 (4.17)

To find  $d_2$ , the fixed-pinned beam with an overhang and the pin at  $h_1$  is considered. As derived in Appendix 4A, the force that causes its tip to deflect  $z_{d2}^*$  is given by

$$f_d(z_{d2}^*) = \frac{6EI(3ld_1 - 2h_1z_{d2}^* - h_1d_1)}{h_1(h_1^3 - 6lh_1^2 + 9l^2h_1 - 4l^3)}$$
(4.18)

Then  $d_2$  can be found according to the displacement function along the beam shown in Eq. (4A.20):

$$d_{2} = \frac{f_{d}(z_{d2}^{*}) \left[ 3(h_{2} - h_{1})ah_{1}^{2} + 4a^{3}h_{1} - 6a^{2}h_{1}(l - h_{2}) + 2(l - h_{2})^{3}h_{1} \right] + 6EId_{1}(3h_{2} - h_{1})}{12EIh_{1}} (4.19)$$

where  $a = l - h_1$  is introduced to shorten the equation.

### 4.3 Numerical Simulations

Based on the values of the system's parameters provided in Table 4.1, the desired nonlinear restoring force can be derived as:

$$f_{en}(z) = 2.665 \times 10^6 z^3 \tag{4.20}$$

Table 4.1 Parameters value of the system.

Symbol	ymbol Name	
$\omega_m$ (rad/s)	The instantaneous frequency of the NES at $z_m$	$2\pi(15)=94.26$
m (kg)	Tip mass	0.09
c (Ns/m)	Damping coefficient	0.033
$z_m$ (m)	Maximum displacement	0.02
EI (N m <sup>2</sup> )	Transverse rigidity of the cantilever beam	0.158
l(m)	Length of the cantilever beam	0.174
$k_{s1}$ (N/m)	1st stiffness of the PLS with single-stop blocks	90.205
<i>k</i> <sub>d1</sub> (N/m)	1st stiffness of the PLS with double-stop blocks	90.205

To approximate such a force, the nonlinear least squares optimization approach is employed to determine the other paramters of the PLS. For an optimal PLS with single-stop blocks, the objective function defined in Eq. (4.9) is minimized to find  $k_{s2}^*$  and  $z_s^*$  while for an optimal PLS with double-stop blocks, the objective function defined by Eq. (4.14) is minimized to find  $k_{d2}^*$ ,  $z_{d1}^*$ ,  $k_{d3}^*$ , and  $z_{d2}^*$   $k_{s2}^*$ . The MATLAB optimization toolbox is used for the optimization. In the first optimization, the searching ranges of the parameters are set as  $0 < k_{s2} < 1 \times 10^4$  N/m and  $0 < z_s < 0.02$  m, the initial guess of  $k_{s2}$  and  $z_s$  are chosen as  $1 \times 10^3$  N/m and 0.015 m, respectively.

In the second optimization, the searching ranges of the parameters are set as  $0 < k_{d2}$ ,  $k_{d3} < 1 \times 10^4$  N/m and  $0 < z_{d1}$ ,  $z_{d2} < 0.02$  m, the initial guess of  $z_{d1}$ ,  $k_{d2}$ ,  $z_{d2}$ , and  $k_{d3}$  are chosen as 0.005 m,  $1 \times 10^3$  N/m, 0.015 m and  $1 \times 10^3$  N/m, respectively. In both cases,  $z_i$  varies from 0 to 0.02 m, and the total data amount N is 100, the tolerance for the gradient norm is set as  $1 \times 10^{-6}$ .

The obtained optimum parameters are listed in Table 4.2. It can be found that the error obtained for the PLS with single-stop blocks is larger than that for the PLS with double-stop blocks, indicating that the latter provides a better approximation for the desired ENS in terms of the restoring force. Figure 4.3 compares the restoring forces of the three springs. It can be observed that  $f_{pld}$  has a smoother curve and exhibits a better fitting to the desired nonlinear force than  $f_{pls}$ . As the configuration of double-stop

blocks provides one more linear segment to approximate a continuous curve, a better approximation is expected. On the other hand, the configuration of single-stop blocks is easier to construct. As any engineering design, there is a trade-off between the approximation accuracy and construction cost. Additionally, the potential energies  $P_{en}$ ,  $P_{pls}$  and  $P_{pld}$  of the three springs can be obtained by taking the integral of  $f_{en}$ ,  $f_{pls}$  and  $f_{pld}$  over  $f_{pld}$  over  $f_{pld}$  over  $f_{pld}$  when the displacement is larger than 0.007 m, which means the PLS with single-stop blocks is able to have a larger displacement when the excitation is not high enough to make the PLS move to  $f_{pld}$  but beyond a specific threshold. On the other hand,  $f_{pld}$  agrees better with  $f_{en}$  when the deflection increases.

Table 4.2 The optimum parameters of the PLSs with single- or double-stop blocks.

	PLS with single-stop block		PLS with double-stop block		
	Symbols	values	Symbols	values	
Estimated	$z_s^*(m)$	0.009	$z_{d1}^*(m)$	0.008	
parameters	$k_{s2}^*$ (N/m)	1673.322	$k_{d2}^*$ (N/m)	985.764	
of PLSs			$z_{d2}^*(m)$	0.0143	
			$k_{d3}^*$ (N/m)	2370.967	
Geometry	h (m)	0.129	$h_1$	0.116	
parameters	d(m)	0.006	$d_1$	0.004	
of the			$h_2$	0.136	
blocks			$d_2$	0.007	
Errors	67.916		7.37	,	

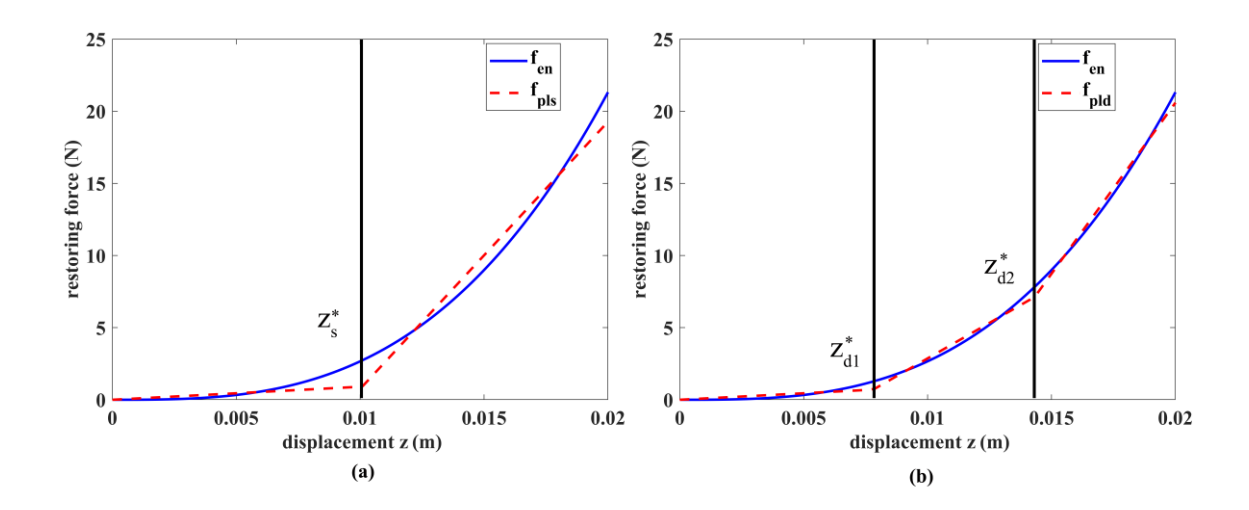


Figure 4.3 Comparison of the restoring forces of the ENS and the optimum PLS.

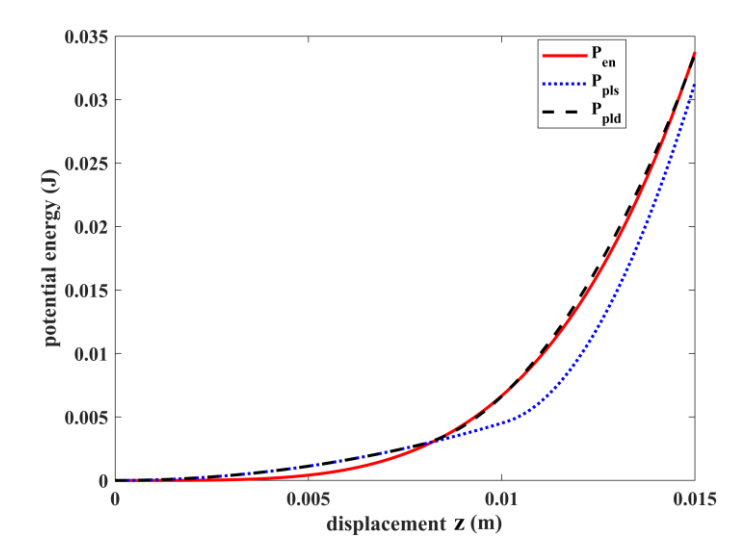


Figure 4.4 Comparison of the potential energies of the three springs.

To compare the dynamic behaviors of the three systems, a numerical simulation is conducted to obtain the free response of each of them by solving Eq. (4.1) through MATLAB ODE45 solver. The initial conditions are chosen as  $(z, \dot{z}) = (0.02, 0)$ . The wavelet transform (WT) is applied to the time response. The frequency corresponding to the maximum WT spectrum value is chosen as the instantaneous frequency (IF) of the system. Figure 4.5 shows the simulation results where the time responses and the WT spectra are given on the left and on the right, respectively. It can be observed that for the system with the ENS, the IF reduces from about 15 Hz to 5 Hz within 10 seconds smoothly. Two observations can be made. First, the use of the equivalent stiffness to

determine the value for  $k_n$  serves the purpose, i.e.,  $\omega_m$  is about 94.26 rad/s or 15 Hz. Second, the system with the ENS does not possess a natural frequency or it can respond to any frequency as long as the initial energy exceeds the required threshold. On the other hand, the IF transition of both PLS systems is less smooth and not continuous. For the system with the PLS of single-stop blocks, its IF becomes about 5 Hz after 7 seconds while for the system with the PLS of double-stop blocks, its IF becomes about 5 Hz after 8 seconds. Once again, the PLS with double-stop blocks gives a better approximation to the ENS.

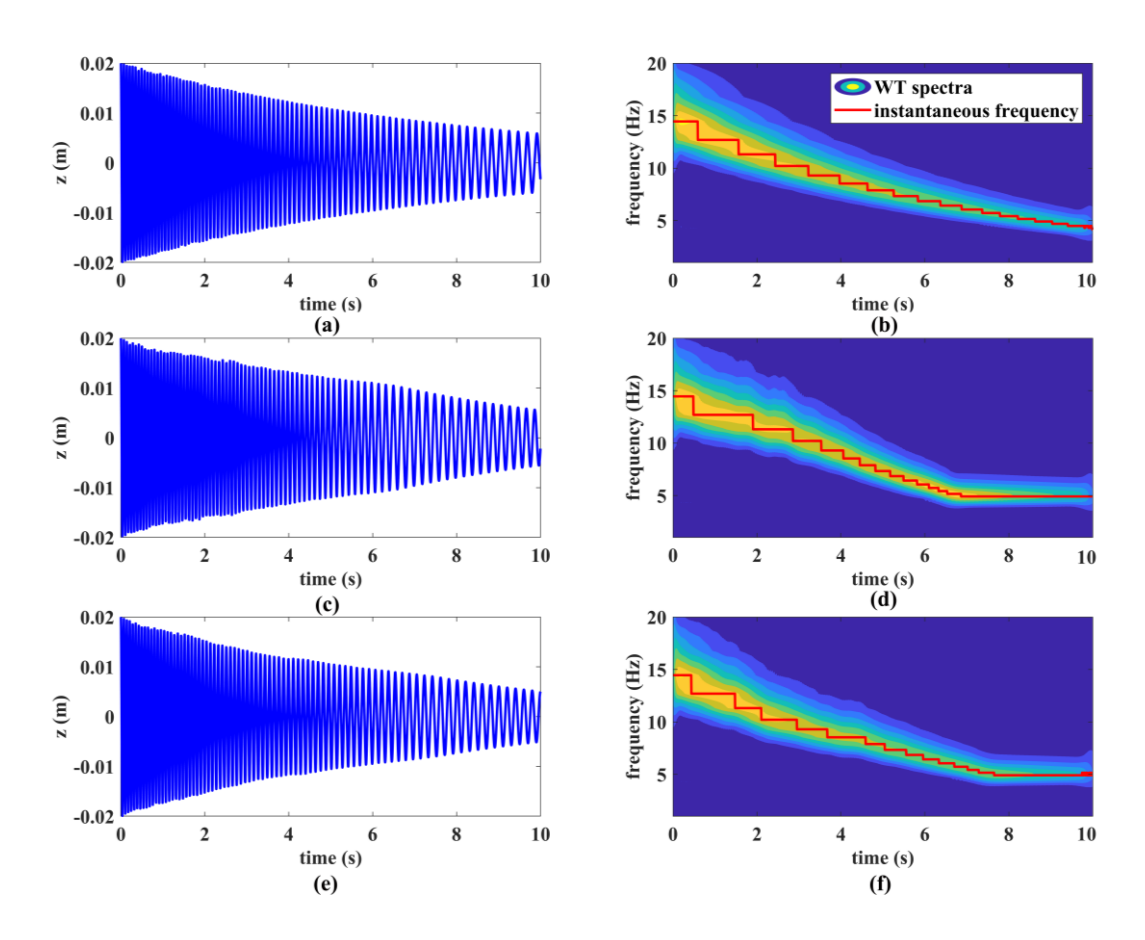


Figure 4.5 Simulation results, free response (left) and its WT spectrum (right): (a) (b) with the ENS; (c) (d) with the PLS of single-stop blocks; (e) (f) with the PLS of double-stop blocks.

# 4.4 Experimental Validation

In this section, the restoring forces of the designed PLSs are validated through static and dynamic experimental tests. In the experimental tests, both single- and double-stop blocks configurations are considered. The lower two stop blocks can be removed to achieve the single-stop block configuration.

### 4.4.1 Static Experimental Test

Figure 6 shows the experimental setup for measuring the restoring force of the PLS with double-stop blocks. As depicted in Figure 4.6, the apparatus is mounted on a slipping table, which is connected to a linear displacement sensor. A force sensor (RCbenchmark Series 1520) is fastened to an aluminum extrusion stand behind the apparatus. The force sensor is made to contact the free end of the beam via a steel rod.

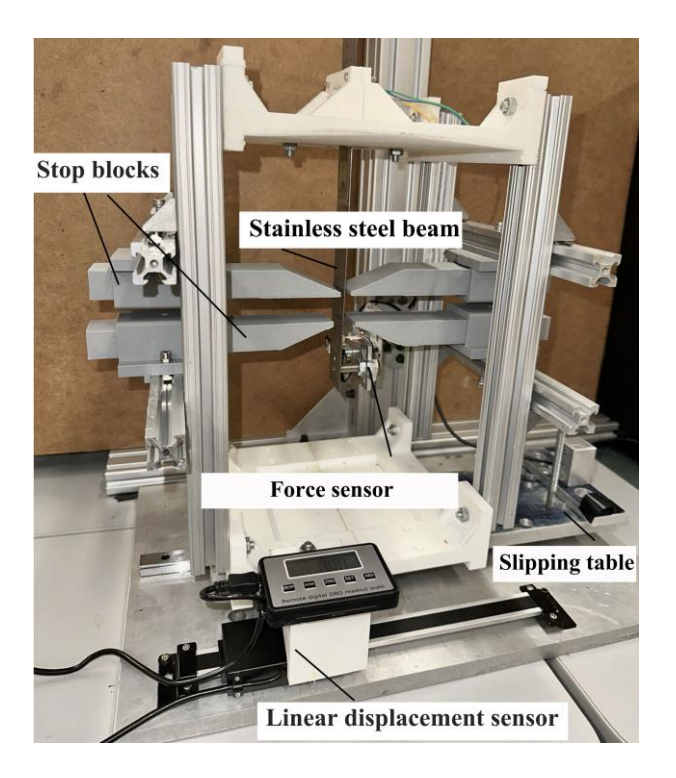


Figure 4.6 Photo of the static experimental setup.

At the beginning of the test, the beam is at its undeformed position. When the apparatus is manually slid to the right, the beam tip is being blocked by the force sensor, causing the beam to deform to the left. During this process, the linear displacement sensor records the displacement of the apparatus which corresponds to the deflection of the beam at an interval of 0.002 m. By increasing the deflection from 0 to 0.02 m, the force-displacement curve can be obtained by collecting the force measured by the force sensor and the deflection measured by the linear displacement sensor. Figure 4.7

compares the measured restoring forces with the predicted one and the desired one for the two PLSs. It can be observed that the experimental results show good agreement with the predicted results, verifying the accuracy of the model statically.

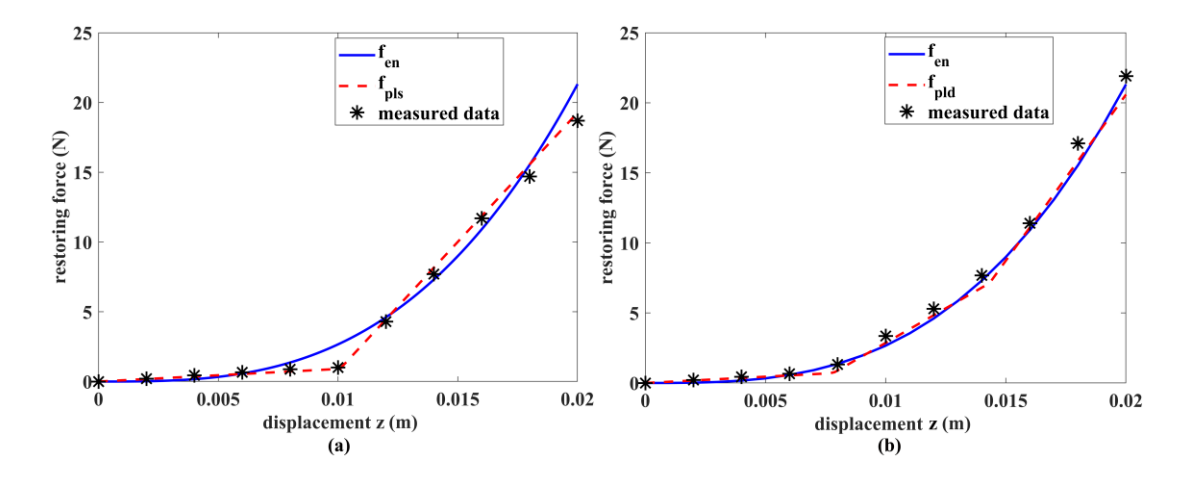


Figure 4.7 Experimental results of the restoring force of PLSs: (a) with single-stop blocks; (b) with double-stop blocks.

## 4.4.2 Dynamic Experimental Test

A dynamic experimental test is conducted to measure the restoring force by using the restoring force surface method [25]. Figure 4.8(a) shows a photo of the experimental setup. The apparatus is mounted on a slipping table that is driven by a shaker (2809, Brüel & Kjær) through a stinger. The shaker is driven by an amplifier (2718, Brüel & Kjær). Two laser reflex sensors (CP24MHT80, Wenglor) are used to measure the transverse displacement of the beam's tip and the base's displacement, respectively. A computer equipped with the dSPACE dS1104 data acquisition board is used to collect the sensor data and send the exciting signal to the power amplifier to drive the shaker. A control program is developed by using the MATLAB Simulink which is interfaced with dSPACE Controldesk Desktop software.

Based on the schematic of the experimental setup shown in Figure. 4.8(b), the equations of motion of the system is given by:

$$m(\ddot{z} + \ddot{y}) + c\dot{z} + f_{pl} = 0$$
 (4.21)

where y is the base displacement, z represents the relative displacement between the

base and the mass at the beam's tip. Equation (4.21) can be reformulated as:

$$F(z,\dot{z}) = -m(\ddot{y} + \ddot{z}) \tag{4.22}$$

A 3-dimensional plot of  $F(z, \dot{z})$  verse z and  $\dot{z}$  is referred to as the restoring force surface [28]. After the displacements of the base and the mass are measured by the laser reflex sensors, their derivatives can be obtained by numerical differentiation. Therefore, the restoring force surface can be established. It should be noticed that the excitation signal should be selected to ensure good coverage in the phase plane. In this study, it is chosen as a harmonic function with a slowly modulated amplitude:

$$y = A\cos(0.01\pi t)\cdot\cos(2\pi f_e t) \tag{4.23}$$

where A=0.0013 m is the amplitude of the exciting signal,  $f_e$  represents the exciting frequency which is chosen from 6.5 Hz to 9.5 Hz by trial and error. By taking the section at  $\dot{z}=0$  of the restoring force surface, the restoring force of the PLS can be found as:  $f_{pl}(z)=F(z,0)$ .

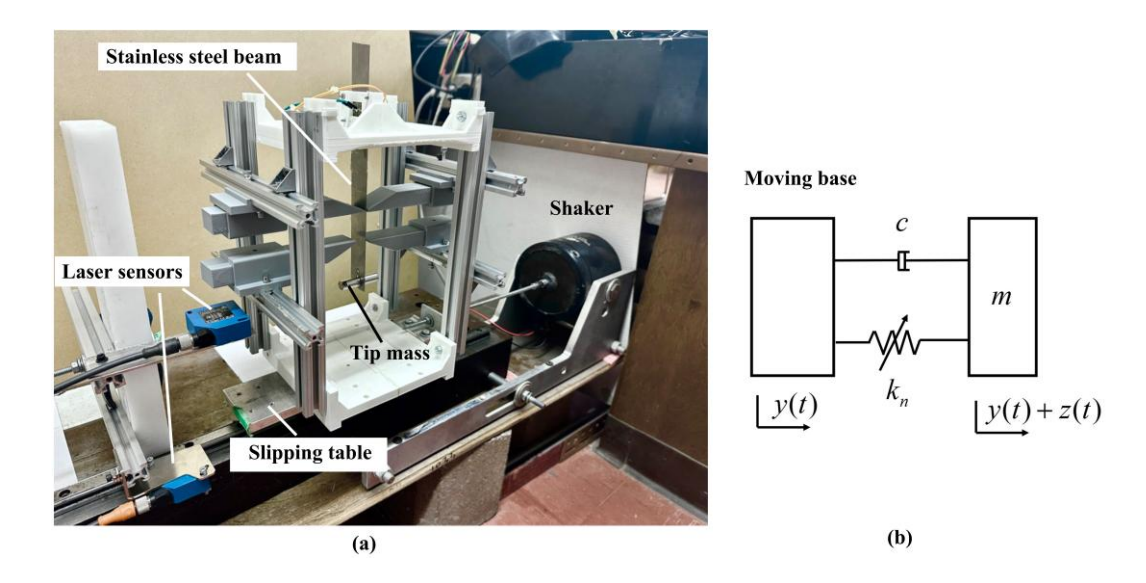


Figure 4.8(a) Photo of the experimental setup for the dynamic experimental test; (b) schematic of the model for the experimental setup.

Figure 4.9 compares the restoring force determined by the force surface method with that of the optimum PLS with single- or double-stop blocks. It is noted that the experimental results are unable to cover the entire range of displacement. The reason

can be attributed to an insufficient excitation level to provide enough inertial force for the tip mass to achieve larger displacement. In the experimental testing, though the shaker is working under its maximum capacity, the maximum displacement of the tip mass can only reach 0.015 m for the two configurations. Within the range of -0.015 m-0.015 m, there is a good agreement between the experimental result and the analytical one. In particular, the experimental restoring force of the PLS with single-stop blocks is able to demonstrate  $k_{s2}$  while the experimental restoring force of the PLS with double-stop blocks fails to reveal  $k_{d3}$ . As shown in Figure. 4.9(b), the maximum displacement just reaches to  $z_{d2}^*$ , which means the beam is not able to touch the lower pair of stop blocks. This will make the equivalent stiffness of the PLS with double-stop blocks much lower than the desired one.

To further demonstrate that, two sets of experimental tests are conducted to obtain the free responses for both two configurations with an initial position  $z_0 = 0.015$  m, then based on the time history of free responses, the IF can be found by picking the peak frequency of the wavelet transform spectra. Figure 4.10 shows the experimental results of the time history and the corresponding IF. It can be found that the IF starts from 8.5 Hz and then decreases to 5 Hz within 2 seconds for both two configurations, the starting frequency is much lower than the desired value of 15 Hz, which further verifies that the equivalent stiffness is lower than the desired value.

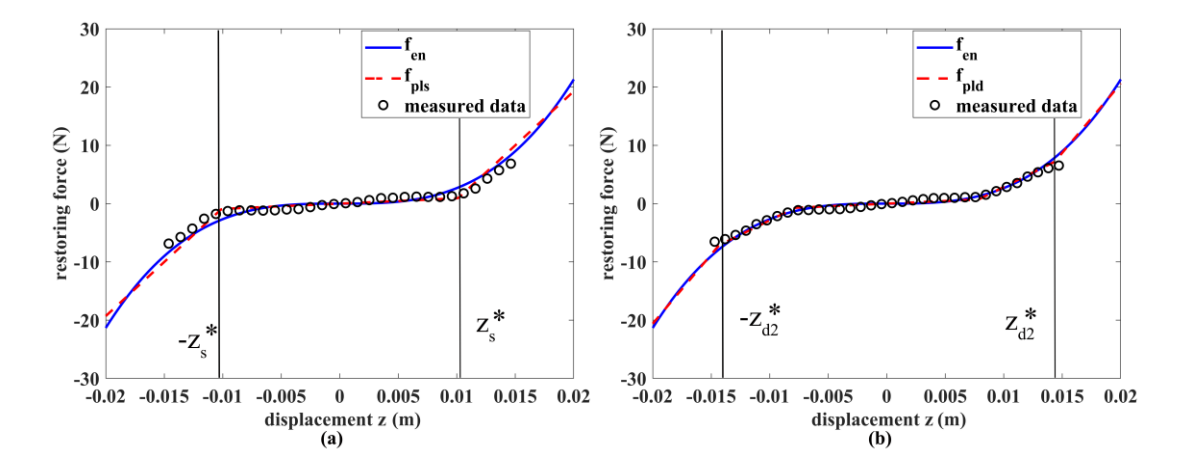


Figure 4.9 Experimental results of the restoring force of PLSs with  $z_m = 0.02$  m: (a) with single-stop blocks; (b) with double-stop blocks.

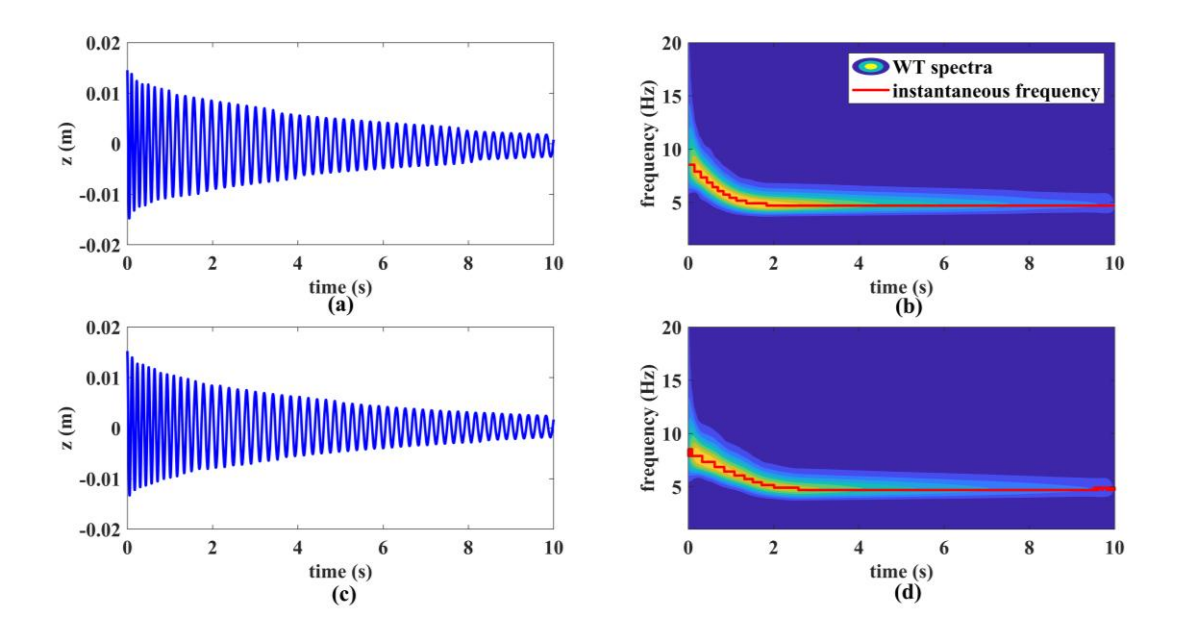


Figure 4.10 Experimental results for the free response and corresponding IF of PLSs with  $z_m = 0.02$  m: (a) (b)with single-stop blocks; (c) (d) with double-stop blocks.

To remedy this problem, one solution is by increasing the excitation level to provide sufficient inertial force for the tip mass. Specifically, the amplitude of the inertial force should be equal or greater than the restoring force corresponding to  $z_m$ . If it is not practical to reach a higher excitation level, an alternative approach involves redesigning the desired nonlinear force with a smaller  $z_m$ .

In this study, due to the limitation imposed by the shaker's capacity, the latter approach is chosen. In the new design,  $z_m$  is chosen as 0.01 m. By following the proposed design procedure, the optimum parameters are obtained and listed in Table 4.3. Compared the results in Table 4.2, it is noted that reducing the range of displacement affects only d in the single-stop blocks configuration and  $d_1$  and  $d_2$  in the double-stop blocks configuration. Using the same excitation condition, the force surface method is implemented again. Figure 4.11 compares the two results with  $z_m = 0.01$  m. It can be seen that the displacement range of the experiment results are able to cover the designed range and the experimental values agree well to the analytical ones.

The experiments to get the free response and IF for the two configurations are conducted again by choosing  $z_0 = 0.01$  m. The results are shown in Figure 4.12. It can

be found that the IF begins at 12 Hz and decreases to 5 Hz within 2 seconds for both configurations. The amplitude of the free response diminishes more rapidly than that in the simulation, and the difference between the IF transitions of the two configurations is less pronounced compared to that in the simulation. This discrepancy can be attributed to the impact caused by the stoppers, which absorb a portion of the kinetic energy of the PLS. In this case, the damping coefficient of the system with the PLS is no longer constant. In the future work, it will be important to consider the impact effect in the theoretical modelling and select proper stopper material to minimize the impact effect.

Table 4.3 Estimated results for the parameters of PLSs with single- and double-stop blocks when  $z_m = 0.01$  m.

	PLS with single-stop block		PLS with double-stop block		
Estimated parameters	Symbols	values	Symbols	values	
of PLSs	$z_s^*(m)$	0.005	$z_{d1}^*(\mathbf{m})$	0.004	
	$k_{s2}^*$ (N/m)	1673.322	$k_{d2}^*$ (N/m)	985.764	
			$z_{d2}^*(\mathbf{m})$	0.007	
			$k_{d3}^*$ (N/m)	2370.967	
Geometry	h (m)	0.129	$h_1$	0.116	
parameters of the blocks	d(m)	0.003	$d_1$	0.002	
			$h_2$	0.136	
			$d_2$	0.003	

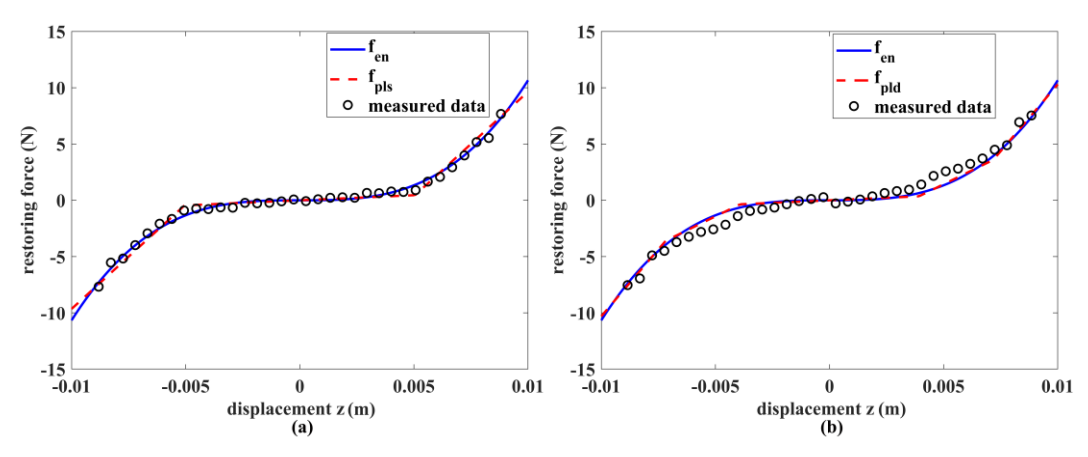


Figure 4.11 Experimental results of the restoring force of PLSs with  $z_m = 0.01$  m: (a) with single-stop blocks; (b) with double-stop blocks through the restoring force surface method.

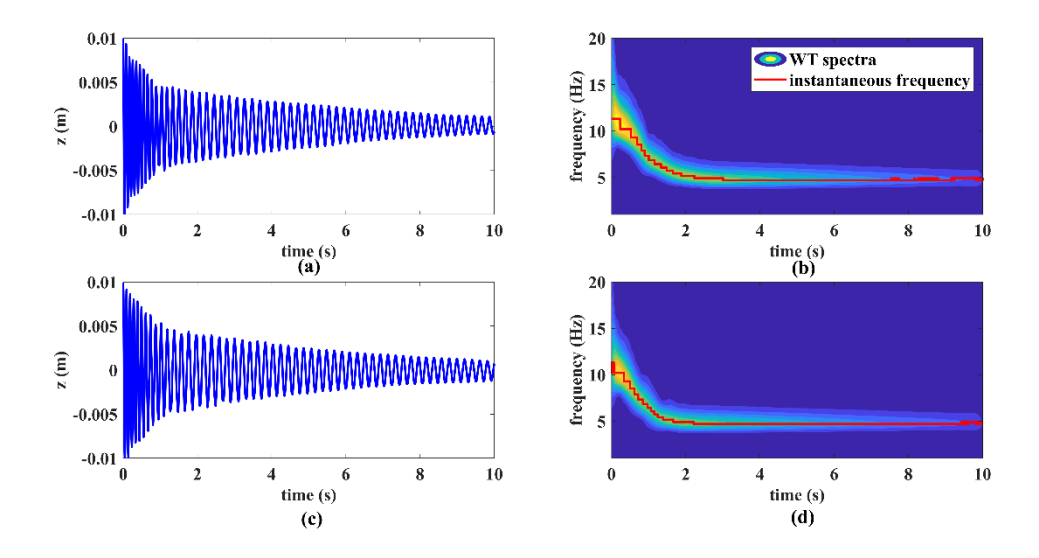


Figure 4.12 Experimental results for time history of the free response with  $z_0 = 0.01$  m and corresponding instantaneous frequency of PLSs (a) with single-stop blocks; (b) with double-stop blocks when  $z_m = 0.01$  m.

### 4.5 Conclusions

This study has developed a design procedure to use a piecewise linear spring (PLS) to approximate an essentially nonlinear spring (ENS). The PLS is constructed by placing a cantilever beam between a pair of single- or double-stop blocks. After the beam contacts a stop block, it is treated as a fixed-pinned beam with an overhang. Thus, the configuration of single-stop blocks is defined by two parameters h and d while the configuration of double-stop blocks is defined by four parameters  $h_1$ ,  $d_1$ ,  $h_2$  and  $d_2$ . The design starts with the determination of the restoring force of the desired ENS using the equivalent stiffness which quantifies the characteristics of a cubic polynomial roughly. Then, a least squares optimization is conducted to find the optimum values  $z_s^*$  and  $k_{s2}^*$  for the PLS with single-stop blocks and  $z_{d1}^*$ ,  $k_{s2}^*$ ,  $z_{d2}^*$  and  $k_{d3}^*$  for the PLS with double-stop blocks. The further steps are presented to find h and d with  $z_s^*$  and  $k_{s2}^*$  and  $h_1$ ,  $d_1$ ,  $h_2$  and  $d_2$  with  $z_{d1}^*$ ,  $k_{s2}^*$ ,  $z_{d2}^*$  and  $k_{d3}^*$ .

A numerical simulation has been conducted to evaluate the performances of the optimum PLSs statically and dynamically. The results show that the PLS with double-stop blocks provides a better approximation to the ENS than the PLS with single-stop

blocks in terms of the restoring force and potential energy. The wavelet transform (WT) spectra of the free responses reveal that both PLS systems are able to initiate the desired instantaneous frequency (IF) as the ENS system under the same initial conditions. However, unlike the system with the ENS, the IF of the system with the PLS settles down to a constant. The PLS with double-stop blocks provides a longer and smoother IF transition than the PLS with single-stop blocks.

An experimental apparatus has been developed to validate the designed PLSs. The apparatus allows to easily configurate into single-stop blocks setup or double-stop blocks setup. The restoring force of each of the PLSs is measured. The measured values show a good agreement with its predicted counterpart, validating the accuracy of the model statically. Further, the restoring force surface method has been employed to determine the restoring force of the PLS systems dynamically. The results show that within the achievable range, the measured values agree well with the predicted ones. However, this achievable range is smaller than the design value  $z_m$  due to an insufficient exciting force. This limitation is also manifested by the smaller range of the IF shown in the WT spectra of the free responses. A solution has been proposed to address this issue. To achieve the desired equivalent stiffness, the PLS should be redesigned by reducing  $z_m$  to an appropriate value so that the displacement range can be covered with the exciting force available. By reducing  $z_m$  by half, the PLSs are redesigned, and the experiments are reconducted. The improved results are obtained, showing that the measured restoring forces have a wider cover range, and the IFs achieve a larger transition. It is also noted that the free responses from the experiment decay much faster than those from the experiment. This may be attributed to the two reasons. First, the damping may not be constant. Second, the impact effect may not be negligible. Future studies should explore the impact effects to better understand their influence on the dynamic response of the PLS system.

# Appendix 4A. Fixed Beam with an Overhang

The stiffness equation and curvature function of the fixed-pinned beam with an overhang are important in the proposed design procedure. Several different expressions exist in the literature [24] To verify their correctness, a detailed derivation is presented

below. Figure 4A.1 shows the free body diagram (FBD) of the fixed-pinned beam with an overhang under a tip load f. As shown in Fig. A1a, three coordinates are used in the analysis, namely,  $0 < y_1 \le h$ ,  $0 < y_2 \le a$  where a = l - h, and  $0 < y \le l$ . It should be mentioned that  $y_1$  and  $y_2$  are introduced only for the purpose of derivation, y is the same coordinate used in the paper. As for the displacement, assume that the right direction is positive. It should be noted that such supports result in an indeterminate beam.

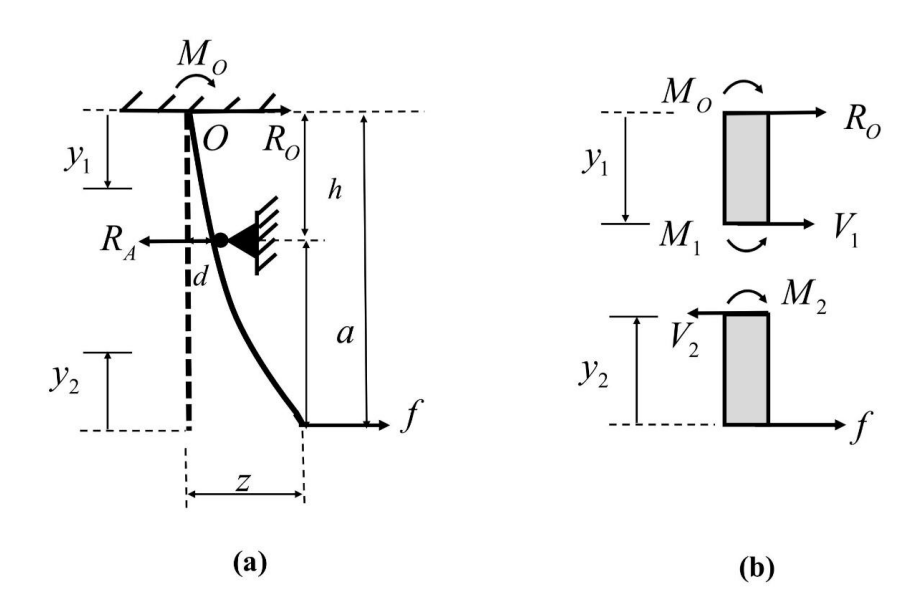


Figure 4A.1 (a) the FBD of the fixed-pinned beam with an overhang; (b) the FBD of the beam segment between the fixed end and the pin and the FEB of the beam segment between the pin and the free end.

From the FBD in Fig. A1a, the sum of the moments at *O* and the sum of forces should be zero:

which yields:

$$M_O = f(l-h) - R_O h \tag{4A.2}$$

From the FBD of the two beam segments shown in Fig. A1b:

$$\wedge + \sum M_{y1} = 0 \qquad M_1 = M_O + R_O y_1 \qquad (4A.3)$$

For  $0 < y_1 \le h$ , based on the double integration method, Eq. (4A.3) can be rewritten as:

$$EI\frac{d^2z_1}{dy_1^2} = M_O + R_O y_1 \tag{4A.5}$$

where  $z_1$  represents the displacement at  $y_1$ . By taking the integration for the above equation twice yields:

$$EI\frac{dz_1}{dy_1} = M_O y_1 + \frac{1}{2}R_O y_1^2 + C_1$$
 (4A.6)

$$EIz_{1} = \frac{1}{2}M_{O}y_{1}^{2} + \frac{1}{6}R_{O}y_{1}^{3} + C_{1}y_{1} + C_{2}$$
(4A.7)

Similarly for  $M_2$ , For  $0 < y_2 \le a$ , Eq. (4A.4) results:

$$EI\frac{d^2z_2}{dy_2^2} = fy_2 (4A.8)$$

where  $z_2$  represents the displacement at  $y_2$ . By taking the integration for above equation twice yields:

$$EI\frac{dz_2}{dv_2} = \frac{1}{2}fy_1^2 + C_3 \tag{4A.9}$$

$$EIz_2 = \frac{1}{6}fy_2^3 + C_3y_2 + C_4 \tag{4A.10}$$

To find the expression for  $C_1$ ,  $C_2$ ,  $C_3$  and  $C_4$ , the following five boundary conditions are considered:

$$\begin{cases} z_{1} = 0 & at \ y_{1} = 0 \\ \frac{dz_{1}}{dy_{1}} = 0 & at \ y_{1} = 0 \\ z_{1} = d & at \ y_{1} = h \\ z_{2} = d & at \ y_{2} = l - h \\ \frac{dz_{1}}{dy_{1}} = -\frac{dz_{2}}{dy_{2}} & at \ y_{1} = h, y_{2} = l - h \end{cases}$$

$$(4A.11)$$

By substituting the first two conditions into Eqs. (4A.7) and (4A.6), respectively,  $C_1$  and  $C_2$  can easily be found to be zeros. Based on the latter three conditions, the following equations can be derived:

$$EId = \frac{1}{2}M_O h^2 + \frac{1}{6}R_O h^3 \tag{4A.12}$$

$$EId = \frac{1}{6}f(l-h)^3 + C_3(l-h) + C_4$$
 (4A.13)

$$M_O y_1 + \frac{1}{2} R_O y_1^2 = -\frac{1}{2} f y_1^2 - C_3$$
 (4A.14)

Based on Eqs (4A.13). and (4A.14),  $C_3$  and  $C_4$  can be given as:

$$C_3 = -\left(M_O h + \frac{1}{2}R_O h^2 + \frac{1}{2}f(l-h)^2\right)$$
 (4A.15)

$$C_4 = EId + \frac{1}{3}f(l-h)^3 + aM_Oh + \frac{1}{2}aR_Oh^2$$
 (4A.16)

Now, the only unknown parameters in the above equations are  $M_O$  and  $R_O$ . Based on Eqs. (4A.2) and (4A.12), the expression of  $M_O$  and  $R_O$  can be found as follows:

$$M_O = -\left(\frac{1}{2}f(l-h) + \frac{3EId}{h^2}\right)$$
 and  $R_O = 3\left(\frac{1}{2h}f(l-h) + \frac{EId}{h^3}\right)$  (4A.17)

By substituting Eq. (4A.17) into Eq. (4A.7), the relationship between  $z_1$  and f can be founded as:

$$z_{1}(y_{1}) = \frac{\left[f(h-l)(h-y_{1})h^{2} + 2EId(3h-y_{1})\right]y_{1}^{2}}{4EIh^{3}}$$
(4A.18)

By substituting Eq. (4A.17) into Eqs. (4A.15) and (4A.16) first, and then substituting  $C_3$  and  $C_4$  into Eq. (4A.10), the relationship between  $z_2$  and f can be found:

$$z_{2}(y_{2}) = \frac{f\left[3(l-h-y_{2})(l-h)h^{2} + 4(l-h)^{3}h - 6(l-h)^{2}hy_{2} + 2y_{2}^{3}h\right] + 6EId(3l-3y_{2}-h)}{12EIh}$$
(4A.19)

Accordingly, the displacement in *y* coordinate or so-called curvature function can be found:

$$z(y) = \begin{cases} \frac{\left[f(h-l)(h-y)h^2 + 2EId(3h-y)\right]y^2}{4EIh^3} & 0 \le y < h \\ \frac{f\left[3(y-h)(l-h)h^2 + 4(l-h)^3h - 6(l-h)^2h(l-y) + 2(l-y)^3h\right] + 6EId(3y-h)}{12EIh} & h \le y \le l \end{cases}$$

$$(4A.20)$$

Then, the relationship between tip displacement z and tip load f can be found when y = l:

$$z(l) = \frac{f(3(l-h)^2h + 4(l-h)^3)h + 6EId(3l-h)}{12EIh}$$
(4A.21)

or

$$f = \frac{6EI(-3ld + 2hz + hd)}{h(l-h)^2(4l-h)}$$
(4A.22)

Since the restoring force of the beam shares the same value with f, the stiffness of the fixed-pinned beam with an overhang can be found as:

$$k = \frac{12EI}{(l-h)^2(4l-h)} \tag{4A.23}$$

### References

- [1] Z. Ma, R. Zhou, and Q. Yang, "Recent advances in quasi-zero stiffness vibration isolation systems: an overview and future possibilities," *Machines*, vol. 10, no. 9, 2022, doi: 10.3390/machines10090813.
- [2] X. Geng, H. Ding, J. Ji, K. Wei, X. Jing, and L. Chen, "A state-of-the-art review on the dynamic design of nonlinear energy sinks," *Engineering Structures*, vol. 313, 2024, doi: 10.1016/j.engstruct.2024.118228.
- [3] A. Vakakis, O. Gendelman, L. Bergman, D. McFarland, G. Kerschen, and Y. Lee, *Nonlinear targeted energy transfer in mechanical and structural systems*. Springer Science & Business Media, 2008.
- [4] Y. Jia, "Review of nonlinear vibration energy harvesting: Duffing, bistability, parametric, stochastic and others," *Journal of Intelligent Material Systems and Structures*, vol. 31, no. 7, pp. 921-944, 2020, doi: 10.1177/1045389x20905989.
- [5] W. Molyneux, "Supports for vibration isolation," *Technical Report ARC/CP-322, Aeronautical Research Council.*, 1957. Technical Report ARC/CP-322, Aeronautical Research Council.

- [6] P. Alabuzhev, Vibration protection and measuring systems with quasi-zero stiffness. CRC Press, 1989.
- [7] X. Huang, X. Liu, J. Sun, Z. Zhang, and H. Hua, "Vibration isolation characteristics of a nonlinear isolator using Euler buckled beam as negative stiffness corrector: A theoretical and experimental study," *Journal of Sound and Vibration*, vol. 333, no. 4, pp. 1132-1148, 2014, doi: 10.1016/j.jsv.2013.10.026.
- [8] F. Zhao, J. C. Ji, K. Ye, and Q. Luo, "Increase of quasi-zero stiffness region using two pairs of oblique springs," *Mechanical Systems and Signal Processing*, vol. 144, 2020, doi: 10.1016/j.ymssp.2020.106975.
- [9] F. Zhao, J. Ji, K. Ye, and Q. Luo, "An innovative quasi-zero stiffness isolator with three pairs of oblique springs," *International Journal of Mechanical Sciences*, vol. 192, 2021, doi: 10.1016/j.ijmecsci.2020.106093.
- [10] F. Zhao, J. Ji, Q. Luo, S. Cao, L. Chen, and W. Du, "An improved quasi-zero stiffness isolator with two pairs of oblique springs to increase isolation frequency band," *Nonlinear Dynamics*, vol. 104, pp. 349-365, 2021.
- [11] A. D. Shaw, G. Gatti, P. J. P. Gonçalves, B. Tang, and M. J. Brennan, "Design and test of an adjustable quasi-zero stiffness device and its use to suspend masses on a multi-modal structure," *Mechanical Systems and Signal Processing*, vol. 152, 2021, doi: 10.1016/j.ymssp.2020.107354.
- [12] G. Gatti, A. D. Shaw, P. J. P. Gonçalves, and M. J. Brennan, "On the detailed design of a quasi-zero stiffness device to assist in the realisation of a translational Lanchester damper," *Mechanical Systems and Signal Processing*, vol. 164, 2022, doi: 10.1016/j.ymssp.2021.108258.
- [13] Y. Chai, X. Jing, and X. Chao, "X-shaped mechanism based enhanced tunable QZS property for passive vibration isolation," *International Journal of Mechanical Sciences*, vol. 218, 2022, doi: 10.1016/j.ijmecsci.2022.107077.
- [14] J. Zhou, X. Wang, D. Xu, and S. Bishop, "Nonlinear dynamic characteristics of a quasi-zero stiffness vibration isolator with cam-roller-spring mechanisms," *Journal of Sound and Vibration*, vol. 346, pp. 53-69, 2015, doi: 10.1016/j.jsv.2015.02.005.
- [15] X. Wang, J. Zhou, D. Xu, H. Ouyang, and Y. Duan, "Force transmissibility of a two-stage vibration isolation system with quasi-zero stiffness," *Nonlinear Dynamics*, vol. 87, no. 1, pp. 633-646, 2016, doi: 10.1007/s11071-016-3065-x.
- [16] D. Zou, G. Liu, Z. Rao, Y. Zi, and W.-H. Liao, "Design of a broadband piezoelectric energy harvester with piecewise nonlinearity," *Smart Materials and Structures*, vol. 30, no. 8, 2021, doi: 10.1088/1361-665X/ac112c.

- [17] K. Ye, J. C. Ji, and T. Brown, "A novel integrated quasi-zero stiffness vibration isolator for coupled translational and rotational vibrations," *Mech Syst Signal Process*, vol. 149, p. 107340, Feb 15 2021, doi: 10.1016/j.ymssp.2020.107340.
- [18] B. P. Mann and N. D. Sims, "Energy harvesting from the nonlinear oscillations of magnetic levitation," *Journal of Sound and Vibration*, vol. 319, no. 1-2, pp. 515-530, 2009, doi: 10.1016/j.jsv.2008.06.011.
- [19] Z. Li, L. Xiong, L. Tang, W. Yang, K. Liu, and B. Mace, "Modeling and harmonic analysis of energy extracting performance of a piezoelectric nonlinear energy sink system with AC and DC interface circuits," *Mechanical Systems and Signal Processing*, vol. 155, 2021, doi: 10.1016/j.ymssp.2021.107609.
- [20] S. C. Stanton, C. C. McGehee, and B. P. Mann, "Reversible hysteresis for broadband magnetopiezoelastic energy harvesting," *Applied Physics Letters*, vol. 95, no. 17, 2009.
- [21] S. Wang, W. Xin, Y. Ning, B. Li, and Y. Hu, "Design, experiment, and improvement of a quasi-zero-stiffness vibration isolation system," *Applied Sciences*, vol. 10, no. 7, 2020, doi: 10.3390/app10072273.
- [22] X. Liu, H. Ding, X. Geng, K. Wei, S. Lai, and L. Chen, "A magnetic nonlinear energy sink with quasi-zero stiffness characteristics," *Nonlinear Dynamics*, vol. 112, no. 8, pp. 5895-5918, 2024, doi: 10.1007/s11071-024-09379-0.
- [23] X. Geng, H. Ding, X. Jing, X. Mao, K. Wei, and L. Chen, "Dynamic design of a magnetic-enhanced nonlinear energy sink," *Mechanical Systems and Signal Processing*, vol. 185, 2023, doi: 10.1016/j.ymssp.2022.109813.
- [24] X. Shui and S. Wang, "Investigation on a mechanical vibration absorber with tunable piecewise-linear stiffness," *Mechanical Systems and Signal Processing*, vol. 100, pp. 330-343, 2018, doi: 10.1016/j.ymssp.2017.05.046.
- [25] X. Li, K. Liu, L. Xiong, and L. Tang, "Development and validation of a piecewise linear nonlinear energy sink for vibration suppression and energy harvesting," *Journal of Sound and Vibration*, vol. 503, 2021, doi: 10.1016/j.jsv.2021.116104.
- [26] L. Wang *et al.*, "Uniform stress distribution of bimorph by arc mechanical stopper for maximum piezoelectric vibration energy harvesting," *Energies*, vol. 15, no. 9, 2022, doi: 10.3390/en15093268.
- [27] Y. Jin, K. Liu, L. Xiong, and L. Tang, "A non-traditional variant nonlinear energy sink for vibration suppression and energy harvesting," *Mechanical Systems and Signal Processing*, vol. 181, 2022, doi: 10.1016/j.ymssp.2022.109479.

- [28] J. Chen, M. Sun, W. Hu, J. Zhang, and Z. Wei, "Performance of non-smooth nonlinear energy sink with descending stiffness," *Nonlinear Dynamics*, vol. 100, pp. 255-267, 2020, doi: 10.1007/s11071-020-05528-3.
- [29] S. Wang and M. Wiercigroch, "Forced oscillators with non-linear spring: A simple analytical approach," *Chaos, Solitons & Fractals*, vol. 41, no. 4, pp. 1784-1790, 2009, doi: 10.1016/j.chaos.2008.07.048.

# **Chapter 5. A Magnetically Enhanced Piecewise-Linear**

### **Nonlinear Energy Sink: Transient Responses**

#### 5.1 Introduction

A dynamic vibration absorber (DVA) or Tuned mass damper (TMD) is a widely used passive device that suppresses structural vibrations by matching their natural frequency to that of the host system. However, the effectiveness of TMDs is limited to narrow frequency bands, making them less suitable for broadband or time-varying excitations. Nonlinear vibration absorbers were proposed for broadband vibration suppression [1]. On the other hand, over the past two decades, there has been growing interest in developing vibration energy harvesters (VEHs) to provide sustainable power sources for wearable electronics and wireless sensor networks. Traditional VEHs typically employ linear oscillators to convert ambient vibration energy to electricity through piezoelectric [2], electromagnetic [3], and electrostatic [4] mechanisms. Similar to TMDs, the effectiveness of traditional VEHs is confined to narrow frequency bands. To overcome this limitation, nonlinear oscillators have been incorporated to enable broadband energy harvesting. A comprehensive review of nonlinear energy harvesting can be found in [5].

Owing to the structural similarities between the TMD and the VEH, researchers have naturally explored the potential for combining vibration suppression (VS) and energy harvesting (EH) in a single multifunctional device. In [6], a piezoelectric energy harvester (PEH) was placed between a linear DVA and its host system to achieve dual purposes of VS and EH, and its performance was evaluated under various excitation conditions and electrical loadings. The study reported in [7] investigated the feasibility of using a linear oscillator simultaneously as a DVA and a VEH under both broadband and single-frequency excitations. To widen the operational bandwidth, many studies have been conducted on devices capable of achieving dual functionality [8, 9]. In [10], a comparative study was

carried out to evaluate the VS and EH performance for linear and nonlinear vibration absorbers under various excitation conditions. The results reveal that the nonlinear vibration absorber provides superior broadband performance.

A nonlinear energy sink (NES) is a specific nonlinear vibration absorber consisting of a small mass, a linear damper, and an essentially nonlinear spring (ENS). Characterized by essential nonlinearity, the NES exhibits unique dynamic phenomena such as Targeted Energy Transfer (TET) and Strongly Modulated Response (SMR). With TET, the energy of the primary system can be transferred irreversibly to the NES through the 1:1 resonance [11]. NESs can be categorized based on their configuration as either grounded (I) or nongrounded (II). In configuration I, NES is connected to ground using an ENS and weakly coupled to the primary mass via a linear spring. In [12], the concept of passive energy pumping in grounded NESs was first introduced and its dynamics in both two-DOF systems and semi-infinite chains was analyzed. Later, in [13], a design methodology was proposed based on nonlinear normal modes (NNMs) of the underlying conservative system to enhance the TET efficiency of grounded NESs. These foundational works formed the theoretical basis for many modern grounded NES designs [14, 15]. In configuration II, NES is connected to the primary mass directly, offering greater design flexibility for compact systems. The study in [16] used the NNM analysis to examine how essential stiffness nonlinearities in a non-grounded NES facilitate TET and energy localization under different system parameters. In [17], the complicated dynamics of a linear primary system coupled with a lightweight non-grounded NES, revealed that the structure of periodic orbits of the undamped system greatly influences the damped dynamics. Moreover, the lightweight NES shows strong resonant interactions with the primary system in a wide frequency range. There have been some attempts that incorporate a grounded spring into a non-grounded NES. In [18], a ground-limit spring was used to prevent excessive displacement of the NES under strong excitations and enhance the robustness of the system. It was found that if the ground-limit NES parameters are not chosen properly, the VS performance deteriorates. Response mechanism of NES with an inerter and grounded spring was investigated in [19]. The study found that the introduction of a grounded spring reduces the Hopf bifurcation area and the required excitation amplitude. The system

investigated in [20] consists of an ungrounded NES and a grounded linear spring. The study focused on the elimination of high-branch response by global parameter optimization.

For the NES design, achieving an essential nonlinearity in practical implementation remains a challenge, as any real spring inherently exhibits a certain degree of linear stiffness [21]. To approximate ENS behavior in NES, several practical implementations have been proposed, including mechanical springs with special configurations [22, 23], cam-roller mechanisms [24, 25], magnetic springs [26], and piecewise linear springs (PLS) [18, 27]. These studies have shown that a well-designed spring can make the nonlinear oscillator behave like a true NES, exhibiting typical TET behavior. As this study employs the PLS and magnetic spring, the following review will focus on these two types of ENS implementations. The PLS approximates the nonlinear force—displacement relationship by dividing it into multiple linear segments with distinct stiffness values. By carefully selecting the breakpoints and slopes of these segments, the system can mimic the nonlinear behavior of the ENS while retaining the mathematical simplicity of linear analysis within each segment [28]. A NES incorporating a PLS is commonly referred to as a piecewiselinear NES (PLNES). In [29], a PLNES was constructed by constraining a cantilevered beam by a pair of adjustable stop blocks, where the segment stiffness and transition displacements can be tuned in real time to optimize energy transfer under varying excitation conditions. In [30], a PLNES was formed using a cantilever beam constrained by a pair of double stop blocks, enabling both vibration suppression and broadband energy harvesting. A segmented NES composed of straight beams with varying gap distances was proposed in [31] to suppress torsional vibrations of a gear shaft system. The results show that the proposed PLNES can improve steady-state vibration suppression rates significantly. A magnetic spring composed of single or multiple permanent magnet pairs, which can also be used to achieve the essential nonlinear characteristics required for NES. Two main configurations are employed for different purposes. In the first configuration, the magnetic interaction becomes dominant at large displacements, sharply increasing stiffness and thus limiting the NES mass's motion (e.g., [26, 32, 33]). In the second configuration, the linear stiffness of the NES is reduced by introducing a negative stiffness to cancel the positive stiffness from the main spring such as beam [34] or coil spring [32, 35]. Moreover, by

carefully tuning the magnetic interaction, the NES can exhibit bi-stable [36, 37] or even tri-stable behaviors [38, 39]. The snap-through motion between different potential wells efficiently reduces the energy threshold required to trigger the TET in NES.

Recently, the integration of NES into energy harvester systems such as PEH or EMEH has garnered increasing attention for achieving both VS and EH. In [40], a coupled NES-PEH system was proposed. Both grounded and non-grounded configurations were investigated under shock excitation, and system parameters were globally optimized to maximize both VS and EH performances. The design proposed in [41] integrated a magnetic plucking frequency-up-conversion PEH into an NES to improve VS and EH performance in low and broadband frequency ranges. The study reported in [42] demonstrated that combining a non-grounded NES with an EMEH can induce intentional high-frequency dynamic instabilities via essential nonlinearities, significantly improving VS under impulsive excitation. A vibro-impact NES coupled with an EMEH was investigated in [43]. The analytical study showed that the robustness of TET can be improved through the combined effects of electric and impact damping. An enhanced trimagnet monostable and bistable nonlinear energy sink equipped with an EMEH was proposed in [44]. The study demonstrated that simultaneous high-efficiency VS and EH can be achieved through a multi-objective optimization of magnet spacing and load resistance. In terms of damping enhancement, PEHs and EMEHs each offer distinct advantages: PEHs typically provide higher energy density and high-voltage, low-current output, while EMEHs produce higher current, yielding stronger electrical damping that can further enhance NES-based VS performance.

In our previous study [45], an NES with a tunable grounded magnetic spring (GMS) was developed for the dual-purpose of VS and EH. The GMS is incorporated with a cantilevered beam, which can produce mono-stable, bi-stable or tri-stable potential wells for the NES by tuning the magnet spacings. As the primary system oscillates, the grounded magnets exert a position-dependent magnetic force on the movable magnet attached to the NES mass, causing the equilibrium position of the NES to shift dynamically with the motion of the primary system. This unique feature significantly lowers the energy threshold

required to trigger TET and simultaneously enhances EH performance.

As point out in [46], a major limitation of conventional NES designs is their inefficiency under low-energy excitation, primarily due to the relatively high initial energy threshold required to trigger TET. Reducing this threshold remains particularly challenging, especially when aiming to design an NES capable of both VS and EH. To overcome this challenge, this study proposes a magnetically enhanced piecewise-linear nonlinear energy sink (MPLNES) that integrates a GMS into a conventional PLNES configuration. With the GMS, an additional nonlinear restoring force is induced so that the equilibrium position of the NES shifts in response to the motion of the primary mass. This design enhances the essential nonlinearity and enables the NES to engage more effectively, even under low initial energy levels. Furthermore, such a grounded configuration facilitates the incorporation of an EMEH, enabling the simultaneous VS and EH. The novelty of this work lies in the following key aspects: 1. Unique MPLNES design: to the best of our knowledge, the proposed MPLNES configuration is original and has not been previously reported; 2. Grounded EMEH integration: The use of a grounded electromagnetic energy harvester provides enhanced flexibility in system installation and enables effective mass distribution; 3. Comprehensive modeling and analysis: By addressing the challenges posed by the MPLNES's unique architecture, this study offers new insights into: (1) optimal emulation of the ENS; (2) modeling of the restoring force and transduction factor that possess two-variable dependence; (3) performance comparison of the PLNES vs the MPLNES; (4) trade-off analysis between VS and EH performance for three different configurations.

The rest of the chapter is organized as follows. Section 2 presents the development and modelling of the apparatus. Section 3 examines the transient performances of the proposed system through numerical simulation. Section 4 discussed the trade-off between the VS and EH performance. Section 5 presents the experimental validation for the numerical analysis. Section 6 summarizes the main conclusions of the study.

### 5.2 MPLNES and Modelling

#### **5.2.1 MPLNES**

Figure 5.1(a) shows a schematic diagram of a primary system attached by the proposed magnetically enhanced piecewise-linear nonlinear energy sink (MPLNES). As shown in the figure, the primary system consists of a primary block serving as the primary mass, and two stainless steel beams functioning as the primary spring. The MPLNES consists of a stainless-steel beam situated between a pair of so-called double-stop blocks (DSBs), acting as a piece-wise linear spring (PLS). The upper end of the beam is clamped to the primary block, while its lower end is fixed with a small cylindrical magnet B and attached with a holder for an assembly of two identical cylindrical magnets A and C. The holder's position can be adjusted by sliding along the beam. A large cylindrical magnet D is fixed in a holder that can slide vertically along two stands fastened the base structure. The three magnets A, B, and C serve three distinct functions: they act as the NES mass, form a tunable GMS through interaction with magnet D, and enable an electromagnetic energy harvester (EMEH) by interacting with four coils. When both the primary beams and the cantilever beam are undeformed, the four magnets are situated on the same vertical plane, and magnets B and D are collinear. By sliding the holder for magnet D, the distance d (see Fig. 3) between magnet B and magnet D can be adjusted. By sliding the holder for magnets A and C along the beam, the distance h (see Fig. 3) between magnets A, C and magnet B can be adjusted. As discussed in the previous study [37], the tunable feature of the magnet positions can make the system exhibit mono-stable, bi-stable, and even tri-stable behaviors. However, the present study primarily focuses on the mono-stable configuration.

Figure 5.1(b) illustrates two deformed positions of the cantilever beam corresponding to equal displacements of the primary mass along the positive (solid line) and negative (dotted line) X-axis directions where O' represents the midpoint of the upper end of the cantilever beam,  $x_p$  and  $x_a$  denote the displacements of the primary mass and the NES mass relative to the base, respectively,  $z = x_p - x_a$  is the relative displacement between

the primary mass and the NES mass. The figure also depicts the spatial positions and polarities of the four magnets where  $m_A$ ,  $m_B$ ,  $m_C$ ,  $m_D$  are the magnetic moment vectors,  $A_0$ ,  $B_0$ ,  $C_0$  and A, B, C denote the center positions of magnets A, B and C when the beam is undeformed and deformed, respectively. As shown in Fig. 1(c), the EMEH is constructed by placing two coils 1, 2 below A and two coils 1', 2' below C symmetrically about the Y-Z plane.

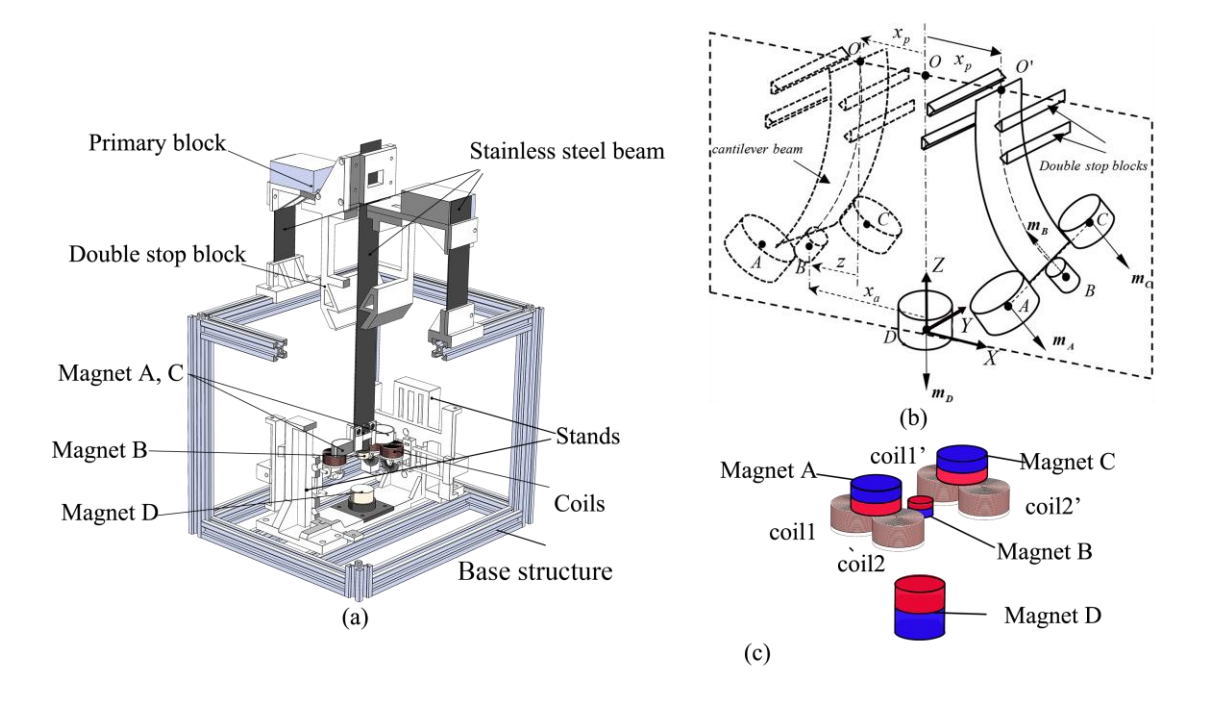


Figure 5.1(a) Schematic of the MPLNES; Spatial positions of: (b) coils and magnets A and C; (c) magnets A, B, C and D.

Figures 2(a) and (b) show the side view and front view of Fig. 1(c), respectively, where d is the distance between magnet B and magnet D when the beam is undeformed, d and h is the distance between magnet B and magnets A, C, l is the length of the cantilever beam, and w is the distance between the axis of magnet B and that of magnet A or C. As shown in Fig. 2(b), when the primary mass displaces by  $x_p$ , the NES mass displaces by  $x_p + z$  horizontally and  $\delta$  vertically,  $\alpha$  is the angle between  $m_B$  and  $m_D$ . Since the slope of the beam's tip is relatively small, it is assumed that  $\angle BOB_0 \approx \theta = \sin^{-1}(z/l)$ . Fig. 2(c) shows the configuration of the DSBs where  $l_1$  and  $g_1$  are the location and the gap of the first pair

of stop blocks,  $l_2$  and  $g_2$  are the location and the gap of the second pair of stop blocks.

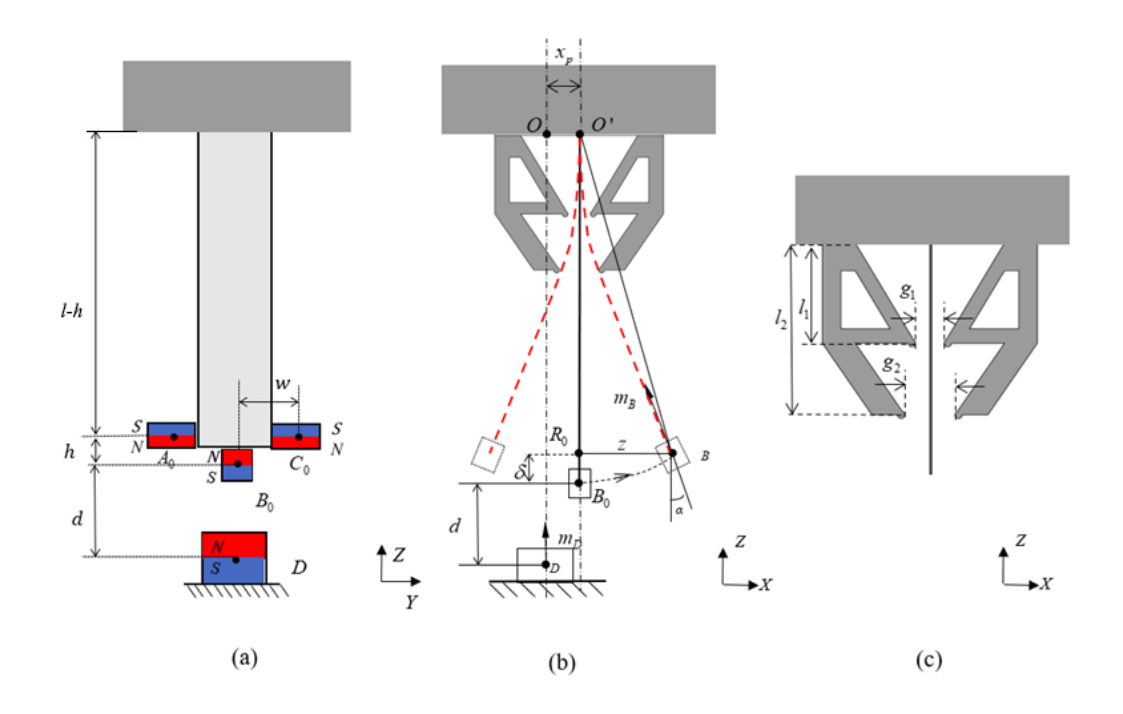


Figure 5.2 Two-dimensional views of the beam and magnets: (a) side view; (b) front view; (c) detail of the DSBs.

Figure. 5.3 shows a lumped-parameter model for the combined system where  $m_p$ ,  $c_p$  and  $k_p$  represent the mass, damping coefficient and stiffness of the primary system, respectively,  $m_a$  and  $c_a$  are the mass and mechanical damping coefficient of the NES, respectively,  $k_{n1}$  represents the nonlinear stiffness of the NES spring and  $k_{n2}$  represents the nonlinear stiffness of the grounded magnetic spring. Since this study focuses on the transient response of the system, the base is assumed to be fixed or  $w_b = 0$ . The figure also shows the circuit of the EMEH where  $K_t$  and E are the total transduction factor and the electromotive force (EMF) of the EMEH, respectively,  $R_c$  and  $L_c$  are the resistance and inductance of one coil, respectively, and  $R_l$  is the resistance of a load resistor connected to the output of the EMEH.

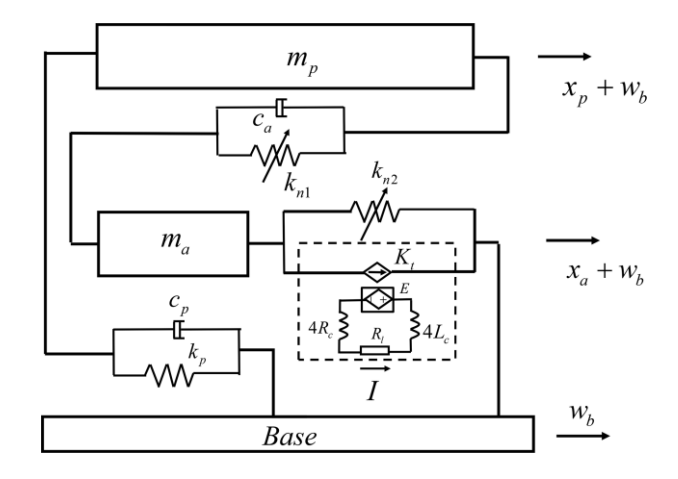


Figure 5.3 The lumped-parameter model of the combined system.

Based on Newton's second law, the governing equations of the system can be derived as follows:

$$m_{p}\ddot{x}_{p} + c_{p}\dot{x}_{p} + k_{1}x_{p} - f_{n1} = 0$$
 (5.1)

$$m_a \ddot{x}_a + c_a \dot{z} + f_e + f_{n1} + f_{n2} = 0$$
 (5.2)

where  $f_{n1}$  is the restoring force of the NES's spring,  $f_{n2}$  is the restoring force of the GMS,  $f_e$  is the electromagnetic force caused by the changes in the magnetic flux through the coils. Based on the Lenz's law, the electromagnetic force can be expressed as follows:

$$f_e = K_t I \tag{5.3}$$

where I is the current in the EMEH's circuit and  $K_t = 2(K_{t1} + K_{t2})$  with  $K_{t1}$  as the transduction factor for coil 1 and  $K_{t2}$  as the transduction factor for coil 2. Note that owing to the symmetric arrangement, coils 1 and 1' have identical transduction factors, as do coils 2 and 2'. Since the inductance of the coils is very small and the frequency of vibration considered in this study does not exceed 20 Hz, the inductive impedance of the coil is negligible compared with  $R_{coil}$ . Thus, the current can be approximated as:

$$I = \frac{K_t \,\dot{x}_a}{4R_{coil} + R_l} \tag{5.4}$$

Then substituting Eq. (5.4) into Eq. (5.3) yields the coefficient of electrical damping  $c_{ae}$ :

$$c_{ae} = \frac{K_t^2}{4R_{coil} + R_t} \tag{5.5}$$

## 5.2.2 Design of the PLS and GMS

The NES mass is subjected to the two nonlinear restoring forces:  $f_{n1}$  and  $f_{n2}$ . As  $f_{n1}$  is due to the beam's elasticity and constraints imposed by the DSBs, it can be defined by:

$$f_{n1} = \begin{cases} k_{g3}(z + z_{g2}) - k_{g2}(z_{g2} - z_{g1}) - k_{g1}z_{g1} & -z_{m} \leq z < -z_{g2} \\ k_{g2}(z + z_{g1}) - k_{g1}z_{g1} & -z_{g2} \leq z < -z_{g1} \\ k_{g1}z & -z_{g1} \leq z \leq z_{g1} \\ k_{g2}(z - z_{g1}) + k_{g1}z_{g1} & z_{g1} < z \leq z_{g2} \\ k_{g3}(z - z_{g2}) + k_{g2}(z_{g2} - z_{g1}) + k_{g1}z_{g1} & z_{g2} < z \leq z_{m} \end{cases}$$

$$(5.6)$$

where  $k_{g1}$ ,  $k_{g2}$ , and  $k_{g3}$  are three incremental linear stiffnesses,  $z_{g1}$  is the relative displacement when the beam just contacts the tip of the first block and  $z_{g2}$  the relative displacement when the beam just contacts the tip of the second block,  $z_m$  is the maximum relative displacement.

The determination of the parameters in Eq. (5.6) is based on the design procedure proposed in [28]. The design objective is to use the piecewise linear spring (PLS) to approximate an essentially nonlinear spring whose restoring force is defined by

$$f_n = k_n z^3 \tag{5.7}$$

where the value of  $k_n$  can be determined based on the instantaneous frequency  $f_m$  of the NES at the maximum displacement  $z_m$ . As the design parameters,  $z_m$  can be chosen based on the space available or the beam deformation limit and  $f_m$  can be chosen based on the 1:1 resonance requirement. In this study,  $z_m$  is chosen as 0.02 m and  $f_m$  is selected as 15 Hz which is slightly higher than the primary system's natural frequency  $f_p = 11.5$  Hz. Then, the concept of the equivalent stiffness  $k_{eq}$  [29, 47] is used to relate  $k_n$  to  $z_m$  and  $f_m$ :

$$k_n = \frac{4(2\pi f_m)^2 m_a}{3z_m^2} \tag{5.8}$$

With the desired cubic nonlinear restoring force, the parameters in Eq. (5.6) can be obtained by applying the least square optimization. Subsequently, the geometric parameters of the DSBs are determined based on the force-deflection model of a cantilevered beam with an overhang. All parameters used in this study are directly adopted from [28], and are summarized in Appendix 5A, Table 5A.1.

The second restoring force  $f_{n2}$  consists of an equivalent force  $f_g$  due to gravity, an attractive magnetic force  $f_{DBx}$  between magnet D and magnet B and two repulsive magnetic forces:  $f_{DAx}$  between magnet D and magnet A, and  $f_{DCx}$  between magnet D and magnet C. Since magnets A and C are identical and symmetrical about the central line of the beam, the values of  $f_{DAx}$  and  $f_{DCx}$  are equal. Then the second nonlinear restoring force can be expressed as:

$$f_{n2} = f_g + f_{DBx} + f_{DAx} + f_{DCx} = mg \cdot \tan(\theta) + f_{DBx} + 2f_{DAx}$$
 (5.9)

where  $\tan(\theta) = z/\sqrt{l^2 - z^2}$  based on the triangle  $OR_0B_0$  shown in Figure 52(b). In what follows, the analytical restoring forces  $f_{DBx}$  and  $f_{DAx}$  will be developed using the equivalent magnetic 2-point dipole model proposed in [48].

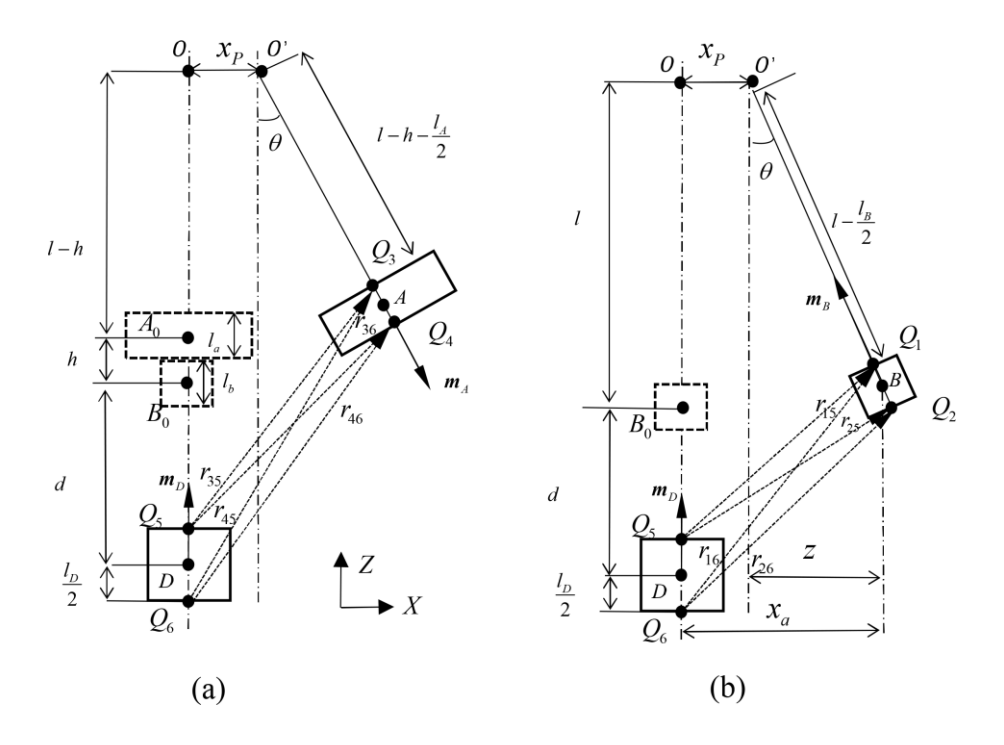


Figure 5.4 Illustration of the equivalent magnetic 2-point dipole model: (a) magnets A and D; (b) magnets B and D.

Figure 5.4 shows the front view of the apparatus when the beam is undeformed and deformed. As shown, the origin of the coordinate system is located at  $B_0$ , the centers of magnets A, B, and D are represented by points A, B and D, respectively, point  $A_0$  and  $B_0$  depict the positions of magnets A/C and B when the beam is undeformed,  $l_B$ ,  $l_D$  and  $l_A$  are the lengths of magnets B, D, and A, respectively. In the figure,  $Q_1$  and  $Q_2$  represent the total charges on the top and bottom surfaces of magnet B, respectively. Similarly,  $Q_3$  and  $Q_4$  denote the total charges of magnet A, and  $Q_5$  and  $Q_6$  denote the total charges of magnet D.

The magnetic force between magnet B and magnet D is considered first. Based on the Boit-Savart law, the magnetic force exerted by magnet B on magnet D is the combination of the magnetic force exerted from  $Q_1$  and  $Q_2$  to  $Q_5$  and  $Q_6$ , which is given in the following equation:

$$f_{DB} = Q_1 \frac{\mu_0}{4\pi} \left( Q_5 \frac{\mathbf{r}_{15}}{|\mathbf{r}_{15}|^3} + Q_6 \frac{\mathbf{r}_{16}}{|\mathbf{r}_{16}|^3} \right) + Q_2 \frac{\mu_0}{4\pi} \left( Q_5 \frac{\mathbf{r}_{25}}{|\mathbf{r}_{25}|^3} + Q_6 \frac{\mathbf{r}_{26}}{|\mathbf{r}_{26}|^3} \right)$$
(5.10)

where  $\mu = 4\pi \times 10^{-7}$  H/m is the vacuum permeability,  $r_{15}$ ,  $r_{16}$ ,  $r_{25}$  and  $r_{26}$  are the position vectors as shown in Figure. 5.4, and their amplitudes are defined in Appendix 5B. According to Eq. (5.9), only the horizontal magnetic forces are considered. Therefore, Eq. (5.10) yields:

$$f_{DBx} = -\frac{\mu_0}{4\pi} \left[ Q_1 \left( x_p + z - \frac{l_B}{2} \sin \theta \right) \left( \frac{Q_5}{|\mathbf{r}_{15}|^3} + \frac{Q_6}{|\mathbf{r}_{16}|^3} \right) + Q_2 \left( x_p + z + \frac{l_B}{2} \sin \theta \right) \left( \frac{Q_5}{|\mathbf{r}_{25}|^3} + \frac{Q_6}{|\mathbf{r}_{26}|^3} \right) \right]$$
(5.11)

Similarly, the horizontal magnetic force between magnets A and D can be obtained as:

$$f_{DAx} = -\frac{\mu_0}{4\pi} \left[ Q_3 \left( x_p + z - h \sin \theta - \frac{l_A}{2} \right) \left( \frac{Q_5}{|\mathbf{r}_{35}|^3} + \frac{Q_6}{|\mathbf{r}_{36}|^3} \right) + Q_4 \left( x_p + z - h \sin \theta + \frac{l_A}{2} \right) \left( \frac{Q_5}{|\mathbf{r}_{45}|^3} + \frac{Q_6}{|\mathbf{r}_{46}|^3} \right) \right]$$
(5.12)

where the amplitudes of  $r_{35}$ ,  $r_{36}$ ,  $r_{45}$  and  $r_{46}$  are defined in Appendix 5B. By substituting Eqs. (5.11) and (5.12) into Eq. (5.9),  $f_{n2}$  is obtained. It should be noted that the magnetic restoring forces  $f_{DBx}$  and  $f_{DAx}$  are functions of both  $x_p$  and z, a unique feature of the GMS.

As mentioned in Introduction, the purpose of introducing the GMS is to enhance the essential nonlinearity of the NES. Thus, the objective of tuning d and h is to achieve a quasi-zero stiffness around the position of equilibrium while maintaining an overall monostable system. Based on this principle, a weak mono-stable configuration is sought by considering the following restoring force:

$$f_n = k_{g1}z + f_{n2}(d, h, x_p)\Big|_{x_p = 0}$$
(5.13)

The rationale for setting  $x_p = 0$  is to ensure the mono-stability at the position of

equilibrium. Two key criteria are considered when the optimal tuning parameters are searched. First, the resulting nonlinear restoring force function  $f_n$  must be an odd and monotonically increasing function with respect to the relative displacement z. Second, to enhance the essential nonlinearity of the NES, the ratio  $\beta = f_a/f_p$  should be further reduced where  $f_a$  is the natural frequency of the linearized NES.

For the NES that employs only the PLS,  $f_a$ =5.03 Hz, resulting in  $\beta$  = 0.437. For the NES that employs both the PLS and the GMS, the design target is to achieve  $\beta$  =0.246, which is substantially lower than the value of the NES with only the PLS. Using the optimal values of the total magnetic charges obtained in [49] (see Table 3.5 in Chapter 3.4), a numerical search is conducted by varying d and h within their tuning regions. It is found that this design target is achieved when d = 0.0373 m and h = 0.0148 m.

Figure 5.5(a) shows the restoring force surface of the GMS. As shown,  $f_{n2}$  is asymmetric about the line  $x_p = -z$  (black dashed line). This indicates that the dominant force in the magnetic force is the repulsive force. To better illustrate the force's dependence on both  $x_p$  and z, Figure 5.5(b) gives three cross sections of the force surface cut at  $x_p = -0.01$  m,  $x_p = 0$  m, and  $x_p = 0.01$  m, respectively. When  $x_p = 0$  (red line),  $f_{n2}$  is asymmetric about the point  $(z, f_{n2}) = (0, 0)$ . When  $x_p = -0.01$  m,  $f_{n2}$  shifts upward and the zero-crossing point moves to z = 0.01 m, indicating that the repulsive force becomes more dominant. When  $x_p = 0.01$  m,  $f_{n2}$  exhibits the opposite behavior. This asymmetric behaviour indicates a position-dependent magnetic nonlinearity, where the restoring force shifts depending on  $x_p$ . Figure 5.6(a) shows the total restoring force vs  $x_p$  and z. Clearly, due to the enhancement of the GMS, the total restoring force changes little around the position of equilibrium, i.e., exhibiting a quazi-zero stiffness characteristic. Figure 5.6(b) shows the total potential energy vs  $x_p$  and z where the circles represent the equilibrium positions or minimum potential energy points of the MPLNES. These equilibrium positions can be curve-fitted by a piecewise function  $z_0$ :

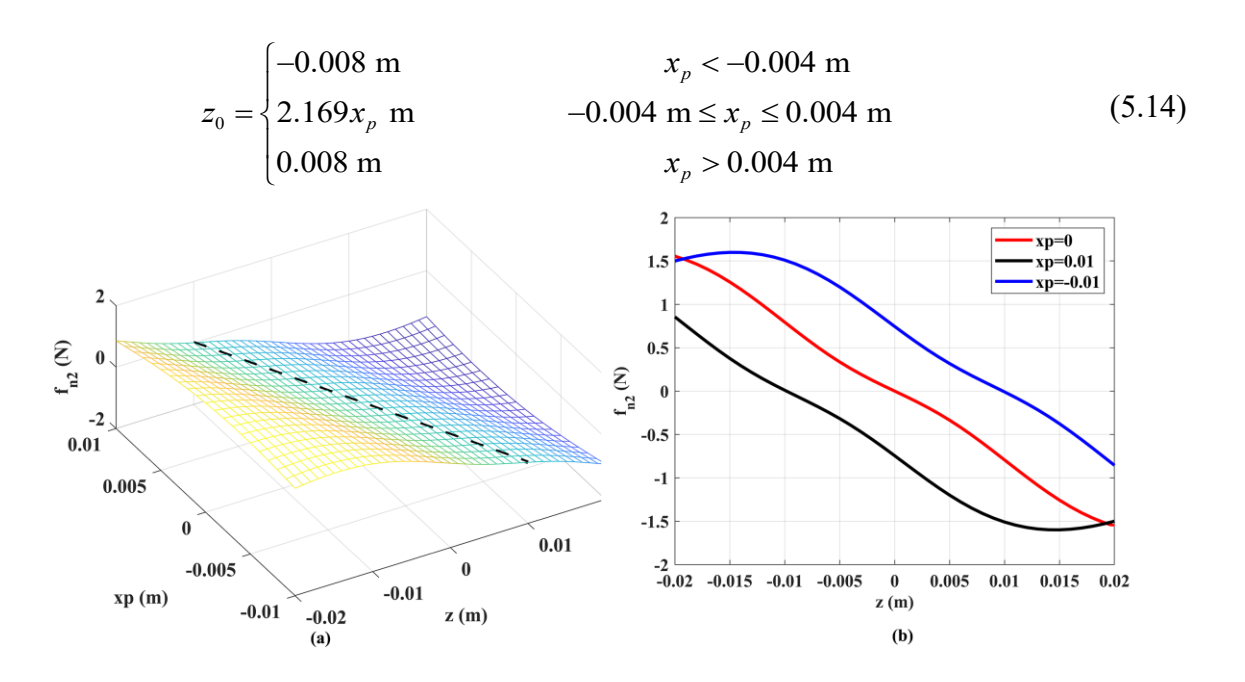


Figure 5.5 Illustration of  $f_{n2}$ : (a)  $f_{n2}$  verse z and  $x_p$ ; (b) three representative cases of  $f_{n2}$  verse z.

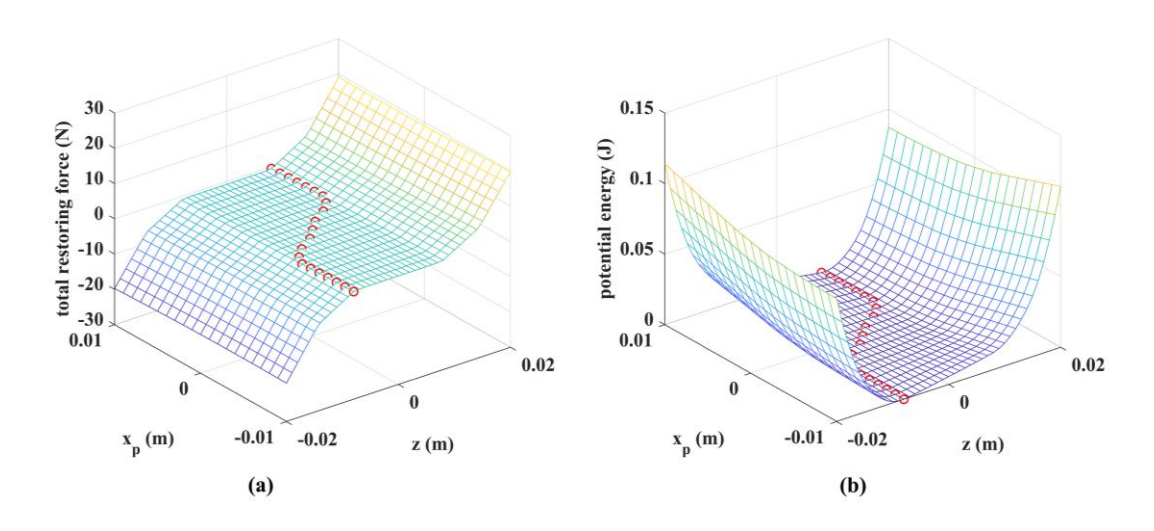


Figure 5.6 Illustration of  $f_{n1} + f_{n2}$ : (a) the force surface; (b) the potential energy surface.

To verify the accuracy of the nonlinear restoring force model, the equilibrium position of the MPLNES for different  $x_p$  are measured experimentally and compared with those obtained from the numerical model. In the experiment, to overcome challenge of achieving

a large deformation of the primary spring, an alternative method is employed. As illustrated in Figure 5.7(a), for each measurement, the primary block is fixed to the base, while magnet D is moved to a negative position in the x-axis. Such a setup simulates the scenario in which the primary block moves to a positive position in the x-axis. After the adjustment, the MPLNES is allowed to settle into its equilibrium position, and the final position of magnet D and the MPLNES are measured by the laser sensors. The comparison shown in Figure 5.7(b) indicates that there is a good agreement between the values predicted by the model and the values measured.

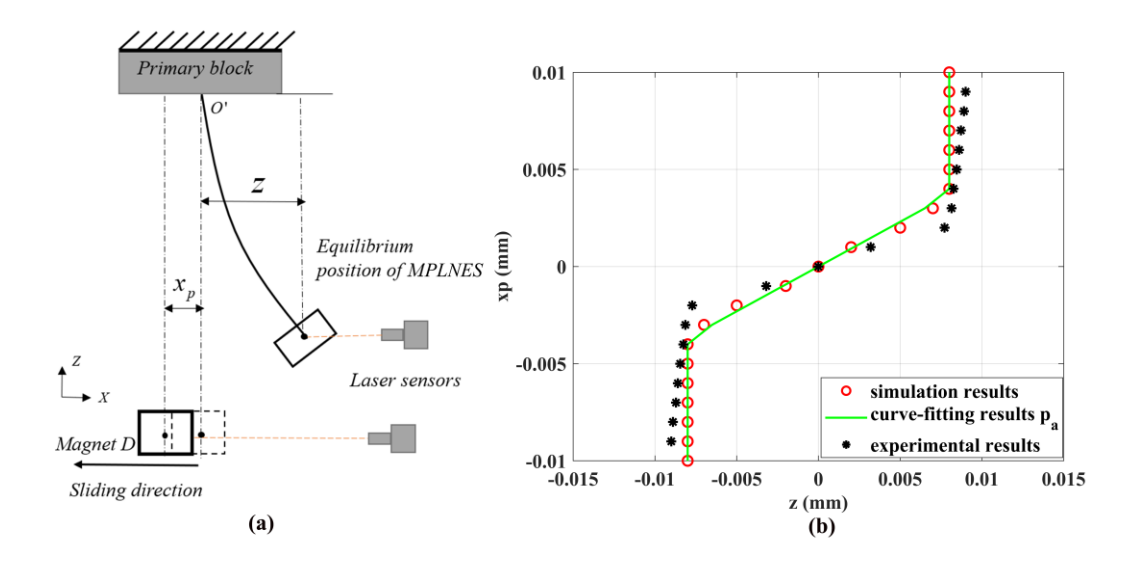


Figure 5.7 Validation of the equilibrium positions of the MPLNES: (a) the experimental setup; (b) comparison of the values from the model and the values measured experimentally.

## 5.2.3 Determination of the Transduction Factor

Due to the unique design, the transduction factor of the grounded EMEH is a function of both  $x_p$  and  $x_a$ . In what follows, the numerical method proposed in [49] is extended to determine the total transduction factor. As pointed out previously,  $K_t = 2(K_{t1} + K_{t2})$ . To determine  $K_{t1}$ , coil 1 is sliced into multiple layers. The magnetic flux in each layer is assumed to be uniformly distributed. Consequently,  $K_{t1}$  can be expressed as the rate of

change of the total magnetic flux within the coil with respect to the displacement  $x_a$ :

$$K_{t1} = -\frac{N_e}{n} \sum_{i=1}^n \frac{\partial \phi_{1j}}{\partial x_a}$$
 (5.15)

where n is the number of layers,  $N_e$  is the equivalent turns of the coil,  $\phi_{jj}$  is the magnetic flux in the z direction in the j<sup>th</sup> layer of coil 1, A finite element analysis software COMSOL Multiphysics is utilized to compute the change rates of the magnetic flux of coil 1 when magnet A oscillates over it. The detail of the modelling process and the parameters used in COMSOL is provided in Appendix 5C.

For each simulation run, the value of  $x_p$  is selected from the range -0.02 m to 0.02 m with an increment of 0.005 m. At each fixed  $x_p$  value, z varies from -0.04 m to 0.04 m. It should be noted that the chosen range of  $x_p$  extends beyond the actual displacement range of the primary mass, This extended range is used to better capture the overall trend of  $K_{t1}$  as a function of  $x_p$ . During each simulation, the change rate of the magnetic flux through each layer of the coil with the different  $x_a$  value is recorded. Then, based on Eq. (5.15), the transduction factor can be computed. Figure 5.8 illustrates  $K_{t1}$  verses  $x_a$  for various values of  $x_p$ . It can be observed that the shapes of the curves remain almost unchanged for different  $x_p$  values. For  $x_a < -0.05$  m or  $x_a > 0.02$  m, the  $K_{t1}$  values are almost zero. And for -0.05 m  $\le x_a \le -0.02$  m, each of the curves can be approximated as a sine function of  $x_a$  with its amplitude and phase affected by  $x_p$ .

To illustrate the  $K_{t1}$ 's dependence on  $x_p$ , the valley points of the curves are projected onto the  $x_a$ - $x_p$  plane, while both the peak and valley points of the curves are projected onto the  $x_p$  –  $K_{t1}$  plane. It can be found that the phase shift in  $x_a$  can be approximated as  $x_a$  –  $0.1x_p$ . The amplitude remains around 0.8 T·m with negligible variation for  $x_p$  < 0. However, as  $x_p$  increases from 0 m to 0.02 m, the amplitude decreases to approximately 80% of its original value.

Before curve-fitting  $K_{t1}$  with an interpretable expression, the accuracy of the numerical model obtained from the COMSOL simulation is experimentally validated. To this end,

three cases are considered:  $x_p = -0.02$  m, 0 m, and 0.02 m. The corresponding values of  $K_{t1}$  are obtained by using the experimental method described in [50]. Similar to the experimental setup shown in Figure 5.7(a), magnet D and the coils are moving with the stand in the opposite directions to simulate the movement of the primary block. As shown in Figure 5.9, overall, the experimental results agree well with the simulation ones.

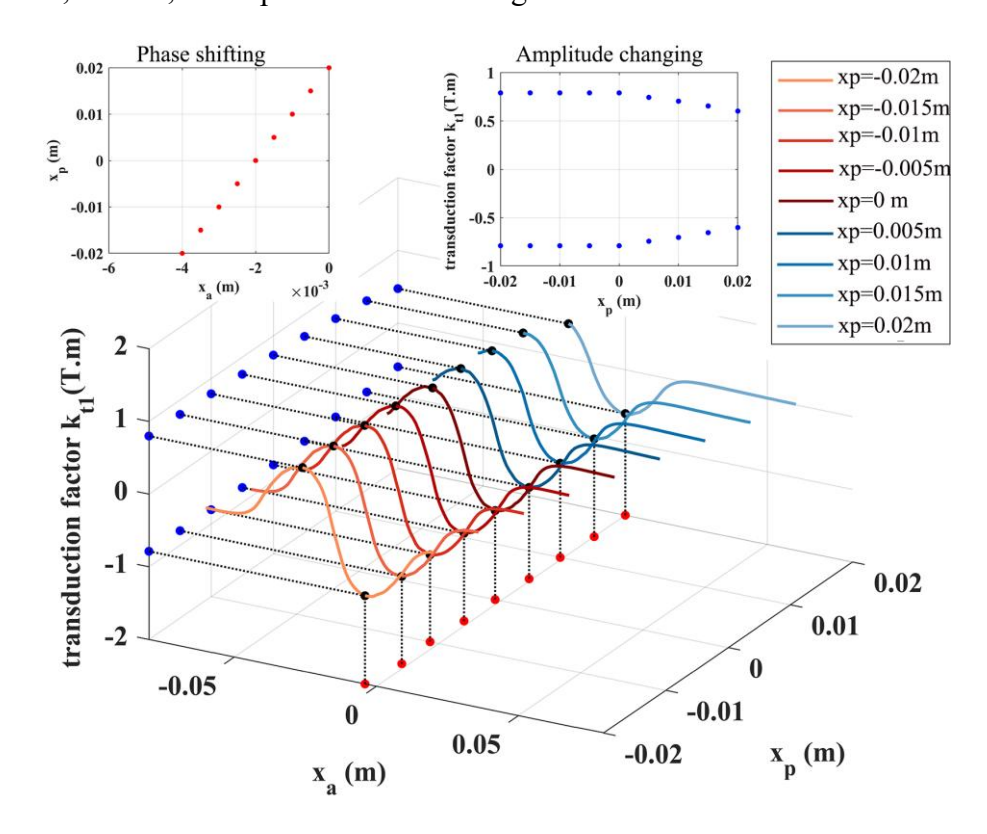


Figure 5.8 Transduction factor verses  $x_a$  of coil 1 for different  $x_p$ .

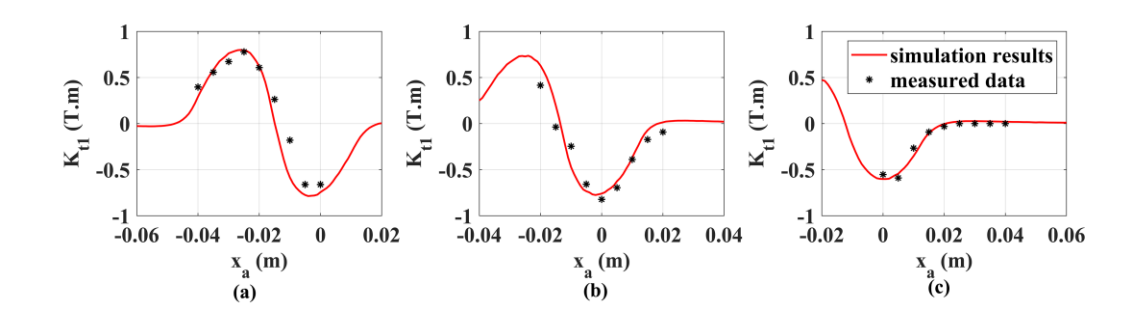


Figure 5.9 Experimental results of the  $K_{t1}$  when (a)  $x_p = -0.02$  m; (b)  $x_p = 0$  m; (c)  $x_p = 0.02$  m.

To derive an interpretable model for  $K_{t1}$ , the curves are approximated using a sum of three sine functions of the form:  $\sum_{j=1}^{3} a_j \sin(b_j x_a + c_j)$ , The curve corresponding to  $x_p = 0$  m is used as training data to determine the coefficients  $a_j$ ,  $b_j$ , and  $c_j$  via the least-squares optimization. The obtained values are listed in Table 5.1. By incorporating the effects of phase shift and amplitude modulation induced by  $x_p$ , the resulting expression for  $K_{t1}$  is given as follows:

$$K_{t1}(x_a, x_p) = \begin{cases} \sum_{j=1}^{3} (1 - 10x_p) a_j \sin(b_j (x_a - 0.1x_p) + c_j) & -0.05 \le x_a \le 0.02, x_p \ge 0 \\ \sum_{j=1}^{3} a_j \sin(b_j (x_a - 0.1x_p) + c_j) & -0.05 \le x_a \le 0.02, x_p < 0 \\ 0 & \text{otherwise} \end{cases}$$
 (5.16)

By following a similar process, the transduction factor for coil 2 can be derived as follows:

$$K_{t2}(x_a, x_p) = \begin{cases} \sum_{j=1}^{3} (1 + 10x_p) a_j \sin(b_j(0.1x_p - x_a) + c_j) & -0.02 \le x_a \le 0.05, x_p < 0 \\ \sum_{j=1}^{3} a_j \sin(b_j(0.1x_p - x_a) + c_j) & -0.02 \le x_a \le 0.05, x_p \ge 0 \\ 0 & \text{otherwise} \end{cases}$$
(5.17)

Figure 5.10 presents the numerical results of the total transduction factor along with the fitted surface. Overall, the curve-fitting functions show a good agreement with the numerical results. These functions will be used in the following simulations for both PLNES and MPLNES. Applicability of Eqs. (5.16) and (5.17) for the PLNES is justified by the fact that the magnetic flux within the coils is predominantly influenced by magnets A and C, making the effect of removing magnet D negligible.

Table 5.1 Curve-fitting constants of Eqs. (5.16) and (5.17).

Constants	$a_1$	$b_1$	$c_1$	$a_2$	$b_2$	<i>c</i> <sub>2</sub>	$a_3$	$b_3$	$c_3$
Value	-0.94	88.80	-0.29	179.47	-0.06	344.84	-1.06	99.08	-0.28

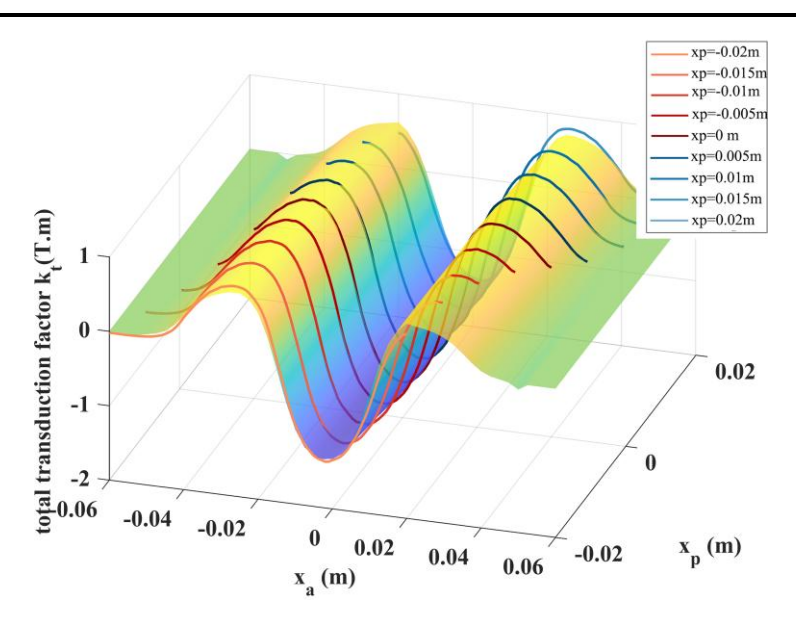


Figure 5.10 Curve fitting surface and the numerical results of the total transduction factor versus  $x_a$  for different  $x_p$ .

#### 5.3 Numerical Simulation

A numerical simulation is conducted to evaluate the performances of the PLNES and MPLNES. Note that the PLNES is achieved by removing magnet D so that  $f_{n2}=0$ . The parameter values used in the simulation are based on the developed apparatus. For the primary system,  $m_p=0.882~{\rm kg}$ ,  $k_p=4.605\times10^3~{\rm N/m}$ ,  $c_p=0.8604~{\rm Ns/m}$ . For both PLNES and MPLNES,  $m_a=0.09~{\rm kg}$  and  $c_{am}=0.0179~{\rm Ns/m}$ . The damping coefficient  $c_{am}$  is estimated from the small free responses of the PLNES by ensuring that the beam does not touch the tips of the DSBs. This damping coefficient corresponds to a damping ratio  $\zeta_{am}=0.0065~{\rm and}~a$  natural frequency  $f_a=5.05~{\rm Hz}$ . The resistance of one coil is  $R_{coil}=0.9~{\Omega}$ . Several load resistances are used in the simulation.

#### 5.3.1 Transient Performances

The transient performances are evaluated in terms of target energy transfer (TET) and energy harvesting (EH). The free responses are induced by specifying initial conditions: for the MPLNES  $x_p(0) = X$ ,  $x_a(0) = z_0(X) + X$ ,  $\dot{x}_p(0) = 0$  and  $\dot{x}_a(0) = 0$  and for the PLNES are  $x_p(0) = X$ ,  $x_a(0) = X$ ,  $\dot{x}_p(0) = 0$  and  $\dot{x}_a(0) = 0$ . The governing equations are numerically solved with the Matlab ODE45 function. To evaluate TET, the percentage of the instantaneous energy in the NES is defined by:

$$D_1 = \frac{E_a(t)}{E_p(t) + E_a(t)} \times 100\%$$
 (5.18)

where  $E_p$  is the instantaneous mechanical energy in the primary system defined by

$$E_{p}(t) = \frac{m_{p}\dot{x}_{p}^{2}}{2} + \frac{k_{p}x_{p}}{2}$$
 (5.19)

and  $E_a$  is the instantaneous mechanical energy in the NES which is defined by

$$E_a = \frac{m_a \dot{x}_a^2}{2} + \int f_{n1} dz + \int f_{n2} dz$$
 (5.20)

for the MPLNES and for the PLNES  $f_{n2}=0$ . In the following simulation, two initial energy levels are considered: X=3 mm for the low initial energy, X=7 mm for the medium-high initial energy level. The load resistor's resistance  $R_l$  is set as  $120 \Omega$ , resulting that the total damping is dominated by the mechanical damping.

Figures 5.11 and 5.12 shows the simulation results with X = 3 mm. Comparison of Figures 5.11(a)–(d) with Figures 5.12(a)–(d) reveals that the dynamic behaviours of the MPLNES and PLNES differ significantly. As shown in Figures 5.11(a) and 5.12(a), the response of the primary system with the MPLNES decreases quickly, while the response of the primary system with the PLNES is nearly identical to that without the NES. Figure 5.11(c) further illustrates that the instantaneous energy in the MPLNES rises from zero to approximately 90% within 1.2 seconds and reaches full energy transfer at 3.4 seconds,

confirming the fast establishment of TET. In contrast, Figure 5.12(c) shows no clear indication of TET in the PLNES. Figures 5.11(b) and 5.12(b) illustrate that the MPLNES performs large amplitude oscillation and exhibits typical nonlinear behaviours, while the PLNES maintains small, nearly linear oscillations. As a result, the MPLNES generates a much higher output voltage, as seen in Figures. 5.11(d) and 5.12(d).

Such differences stem from the presence of the GMS in the MPLNES. Even minor displacements in the primary system shift the MPLNES equilibrium position due to the influence of the GMS, Consequently, it forces the MPLNES into substantial motion. This mechanism ensures early engagement with the DSBs and facilitates the activation of nonlinearity. As a result, the MPLNES exhibits enhanced TET efficiency and high voltage output, particularly under low initial energy conditions.

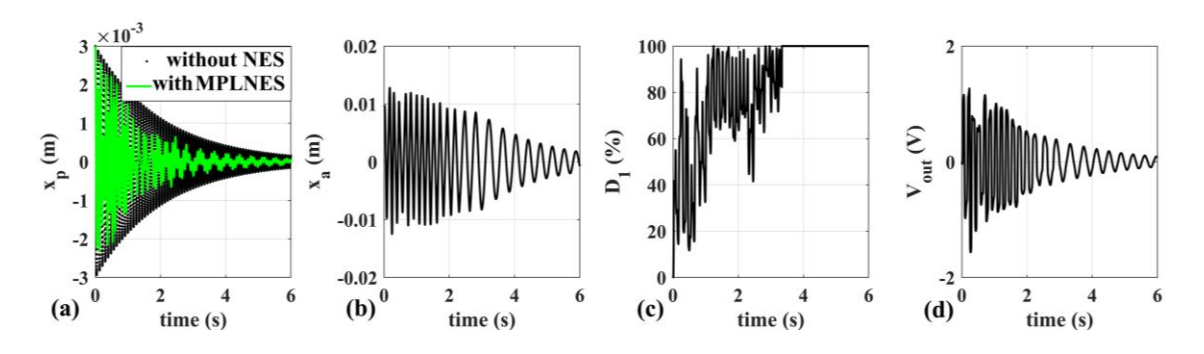


Figure 5.11 Simulation results with MPLNES and X = 3.0 mm: (a)  $x_p$ ; (b)  $x_a$ ; (c)  $D_1$ ; (d)  $V_{out}$ .

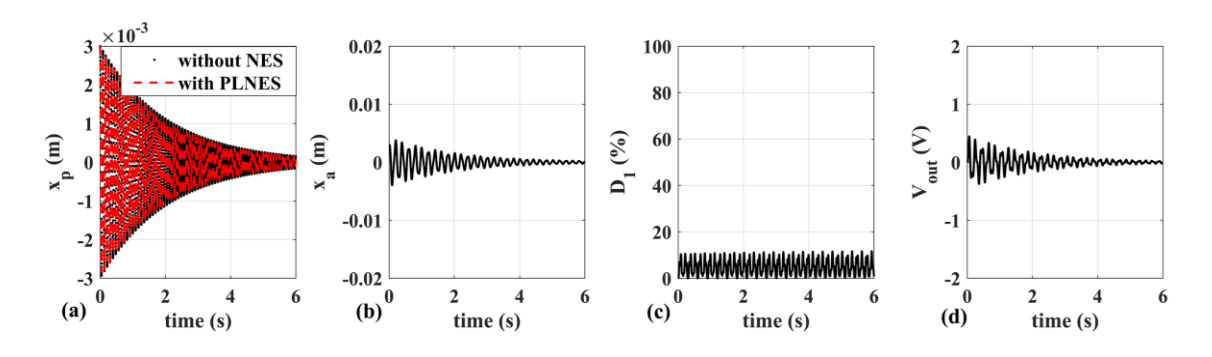


Figure 5.12 Simulation results with PLNES and X = 3.0 mm: (a)  $x_p$ ; (b)  $x_a$ ; (c)  $D_1$ ; (d)  $V_{out}$ .

The dominant frequencies of the responses can be revealed by the wavelet transform (WT) spectra. As shown in Figures 5.13 (a) and (c), the dominant frequency of the MPLNES mass's response originates from 6 Hz and then drops to around  $f_{a1}$  after 3 seconds, and the dominant frequency of the primary mass's response is around  $f_p$ . This indicates the initiation of TET, albeit without the full establishment of a 1:1 resonance condition. In contrast, Figures 5.13 (b) and (d) reveal that the dominant frequencies of the PLNES and the primary system are mainly around  $f_{a2}$  and  $f_p$ , respectively. This observation suggests that the PLNES's nonlinearity is not fully activated when the initial energy level is low.

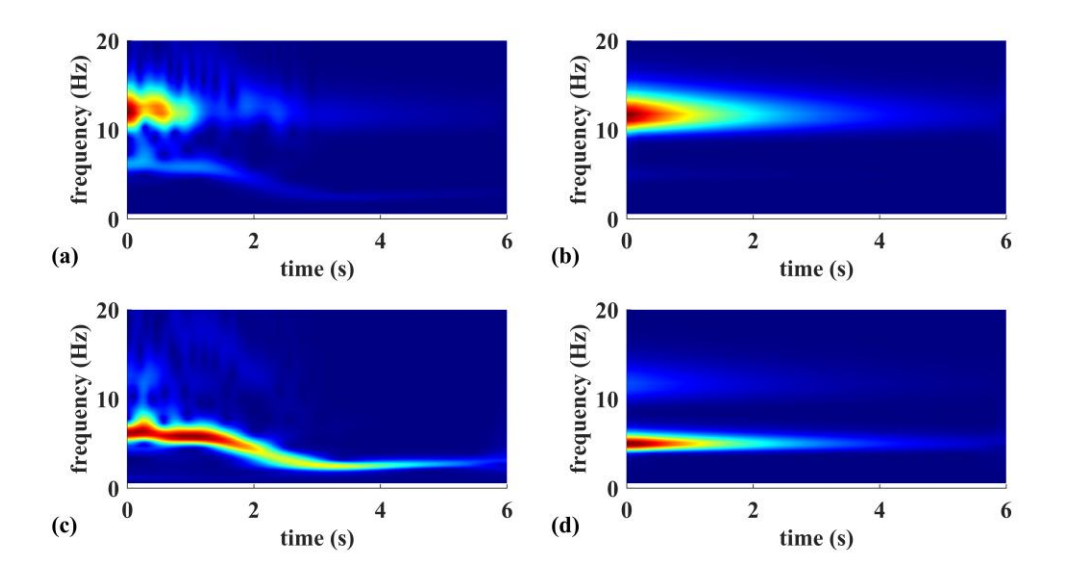


Figure 5.13 WT spectra of the responses with X = 3 mm: (a)  $x_p$  with MPLNES; (b)  $x_p$  with PLNES  $x_p$ ; (c)  $x_a$  with MPLNES; (d)  $x_a$  with PLNES.

Figures 5.14-16 present the simulation results with the medium-high initial energy level. As shown in Figures 5.14(c) and 5.15(c), TET is established in both configurations. The energy in the MPLNES undergoes three distinct stages: reversible energy exchange (0-2 seconds), irreversible energy exchange (2-4 seconds), and energy localization (4-6 seconds). On the other hand, a significant energy exchange exists between the PLNES and the primary system at the beginning, evidenced by the nonlinear beat phenomenon, and

then about 70% of the total energy is localized in the PLNES after 4 seconds.

Figure 5.16 highlights these differences in the frequency domain. As illustrated in Figures 5.16(a) and (c), the dominant frequency of the MPLNES varies from  $f_p$  to 6 Hz during the first stage, then it maintains such a high-frequency oscillation in the second stage, and after that, it drops to  $f_{a1}$  after 4 seconds. In contrast, as shown in Figures 5.16 (b) and (d), the dominant frequency of the PLNES decreases gradually from  $f_p$  to  $f_{a2}$  in 3 seconds. This difference indicates that the MPLNES remains at high frequencies for a longer duration, allowing more time for the effective establishment of TET.

The unique behaviours of the MPLNES arise from the effect of the GMS, which prolongs the duration of large-amplitude nonlinear response in the MPLNES. As a result, the EMEH in the MPLNES is capable of generating higher voltage output during 2-4 seconds than that in the PLNES, as shown in Figures 5.14 (d) and 5.15(d).

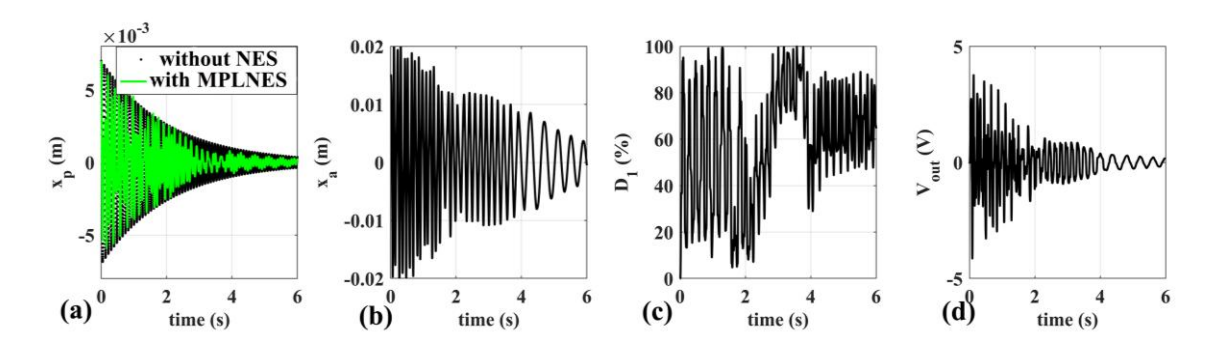


Figure 5.14 Simulation results with MPLNES and X = 7.0 mm: (a)  $x_p$ ; (b)  $x_a$ ; (c)  $D_1$ ; (d)  $V_{out}$ .

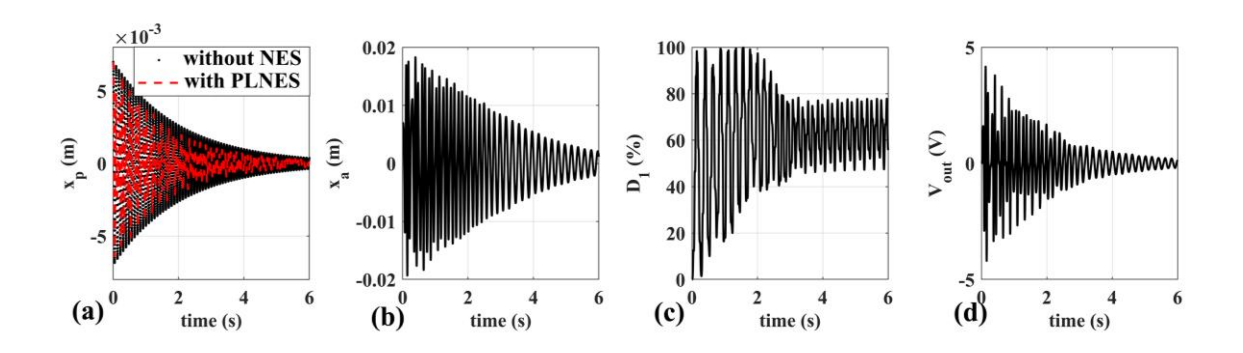


Figure 5.15 Simulation results with PLNES and X = 7.0 mm: (a)  $x_p$ ; (b)  $x_a$ ; (c)  $D_1$ ; (d)  $V_{out}$ .

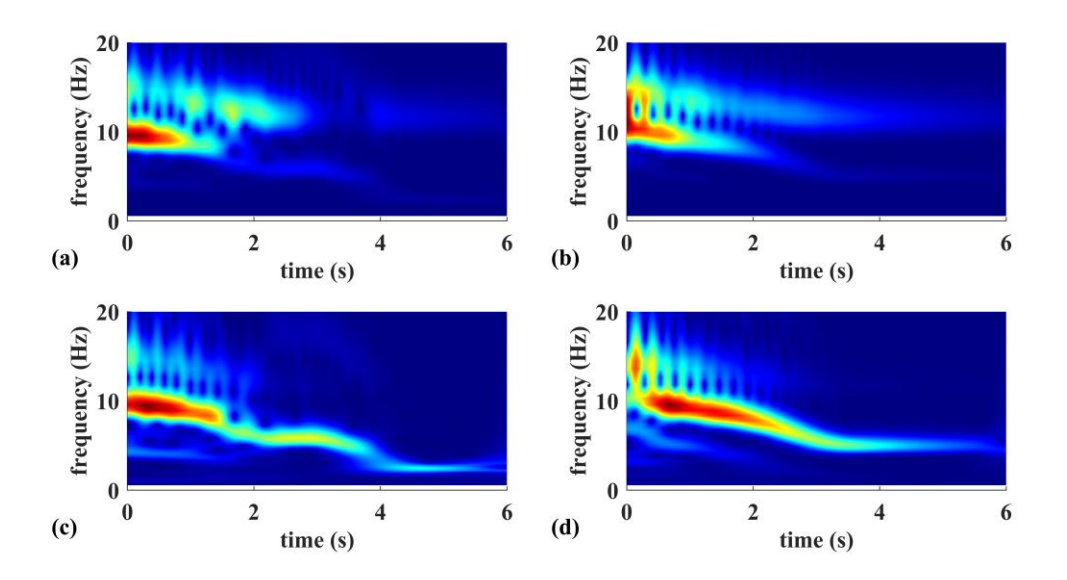


Figure 5.16 WT spectra of the responses with X = 7 mm: (a)  $x_p$  with MPLNES; (b)  $x_p$  with PLNES; (c)  $x_a$  with MPLNES; (d)  $x_a$  with PLNES.

## 5.3.2 Nonlinear Normal Mode (NNM) Analysis

To have a better understanding of the dynamics of the system, the NNM analysis is conducted for both the MPLNES and PLNES configurations. The frequency energy plot (FEP) is derived using the complexification-averaging technique (CX-A) [51], which reformulates the nonlinear system in the complex domain and applies an averaging procedure to approximate periodic solutions. Since the CX-A method requires continuous and analytically interpretable expressions for the nonlinear restoring forces in the dynamic model,  $f_{n1}$  and  $f_{n2}$  both are curve-fitted using polynomial functions.  $f_{n1}$  is curve fitted by an odd third-order polynomial as shown as follows:

$$\overline{f}_{n1} = k_1 z + k_3 z^3 \tag{5.21}$$

where  $k_1 = 85$  N/m and  $k_3 = 2.651 \times 10^6$  N/m. On the other hand, as  $f_{n2}$  depends on

both  $x_p$  and z, it must be represented by a multivariate polynomial in terms of  $x_p$  and z defined by the following expression:

$$\overline{f}_{n2} = \sum_{n=0}^{N} \sum_{m=0}^{M} b_{mn} z^{m} x_{p}^{n}$$
 (5.22)

where m and n are the non-negative integer indices, representing the polynomial orders with respect to z and  $x_p$ , respectively. The polynomial coefficients  $b_{mn}$  are corresponding to the term  $z^m x_p^n$ , with  $m \in (0, M)$ ,  $n \in (0, N)$ . To find the optimum values for M and N, two objective functions should be met:

$$J_{1} = M + N$$

$$J_{2} = \frac{1}{PQ} \sum_{p=1}^{P} \sum_{q=1}^{Q} (f_{n2}(p,q) - \overline{f}_{n2}(p,q))^{2}$$
(5.23)

The first objective function  $J_1$  denotes the maximum polynomial order in z and  $x_p$ . The second objective function  $J_2$  represents the root mean square error between  $f_{n2}$  and  $\bar{f}_{n2}$ , where p and q represents the position index of z and  $x_p$ , respectively. It is clear that the larger the  $J_1$  value, the smaller the  $J_2$  value. However, to simplify the NNM analysis, the value of  $J_1$  should be as low as possible. At the same time,  $J_2$  also should be sufficiently low to ensure accurate curve fitting. Figure 5.17 presents a heatmap of  $J_2$  for various combinations of M and N. The colour intensity indicates the magnitude of  $J_2$  in a logarithmic scale, with darker shades corresponding to smaller values. An optimal tradeoff is obtained at (M,N)=(5,5), where both objectives are satisfactorily reached. The absence of darker patches in the lower-left corner confirms that no better trade-off exists for smaller order numbers. By eliminating the terms with negligible coefficients,  $\bar{f}_{n2}$  can be expressed as:

$$\overline{f}_{n2} = b_{01}x_p + b_{03}x_p^3 + b_{05}x_p^5 + (b_{10} + b_{12}x_p^2 + b_{14}x_p^4)z + (b_{21}x_p + b_{23}x_p^3 + b_{25}x_p^5)z^2 
+ (b_{30} + b_{32}x_p^2 + b_{34}x_p^4)z^3 + (b_{41}x_p + b_{43}x_p^3 + b_{45}x_p^5)z^4 + (b_{50} + b_{52}x_p^2 + b_{54}x_p^4)z^5$$
(5.24)

where all the coefficient values are given in Table 5.2.

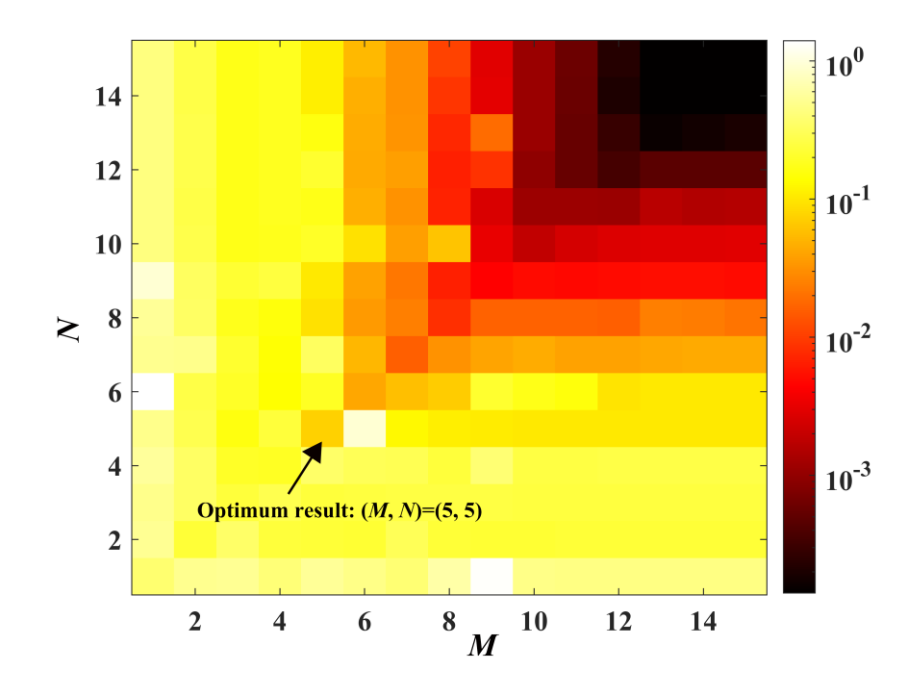


Figure 5.17 Heatmap of  $J_2$  for different M and N.

Table 5.2 Coefficient values in Eq. (5.24).

$b_{01}$	$b_{03}$	$b_{05}$	$b_{10}$	$b_{12}$	$b_{14}$
$5.121 \times 10^{1}$	$1.067 \times 10^{5}$	-1.953	$5.052 \times 10^{1}$	$3.428 \times 10^{5}$	-9.388
	b <sub>23</sub>	$\frac{\times 10^8}{b_{25}}$	b <sub>30</sub>	b <sub>32</sub>	$\frac{\times 10^8}{b_{34}}$
$3.537 \times 10^5$	-2.910	4.167	<i>D</i> 30	$\frac{b_{32}}{-3.254}$	7.204
	× 10 <sup>9</sup>	× 10 <sup>12</sup>	$1.491 \times 10^5$	× 10 <sup>9</sup>	$\times 10^{12}$
$b_{41}$	$b_{43}$	$b_{45}$	$b_{50}$	b <sub>52</sub>	b <sub>54</sub>
-1.024	6.917	-1.013	-2.655	5.034	-1.145
$\times 10^9$	$\times10^{12}$	$\times10^{16}$	$\times 10^8$	$\times 10^{12}$	$\times10^{16}$

Using the approximate restoring force models, the equations of motion for the undamped system with the MPLNES can be derived from Eqs. (5.1) and (5.2):

$$m_p \ddot{x}_p + k_p x_p - \bar{f}_{n1} = 0 ag{5.25}$$

$$m_a \ddot{x}_a + \bar{f}_{n1} + \bar{f}_{n2} = 0 ag{5.26}$$

Based on the CX-A technique, two complex variables are introduced as:

$$\psi_1 = \dot{x}_p + j\omega x_p, \psi_2 = \dot{x}_a + j\omega x_a \tag{5.27}$$

where  $\omega$  is the dominant fast frequency of the oscillation and  $j = \sqrt{-1}$ . Then, the displacement and acceleration can be obtained accordingly:

$$x_{p} = \frac{\psi_{1} - \psi_{1}^{*}}{2j\omega}, \ddot{x}_{p} = \dot{\psi}_{1} - \frac{j\omega}{2} (\psi_{1} + \psi_{1}^{*}),$$

$$x_{a} = \frac{\psi_{2} - \psi_{2}^{*}}{2j\omega}, \ddot{x}_{a} = \dot{\psi}_{2} - \frac{j\omega}{2} (\psi_{2} + \psi_{2}^{*})$$
(5.28)

where  $\psi_1^*$  and  $\psi_2^*$  are the complex conjugates of  $\psi_1$  and  $\psi_2$ , respectively. The slow-modulated amplitude can be defined as follows:

$$\psi_1(t) = \phi_1(t)e^{i\omega t}, \psi_2(t) = \phi_2(t)e^{i\omega t}$$
 (5.29)

Substituting Eq. (5.29) into Eq. (5.28), then into Eq. (5.25), the first governing equation can be rewritten as:

$$(1+j\omega)\phi_{1}e^{j\omega t} - \frac{j\omega}{2}\left(\phi_{1}e^{j\omega t} + \phi_{1}^{*}e^{-j\omega t}\right) + \frac{\phi_{1}e^{j\omega t} - \phi_{1}^{*}e^{-j\omega t}}{2j\omega}$$

$$-k_{1}\left(\frac{(\phi_{1}-\phi_{2})e^{j\omega t} + (\phi_{2}^{*}-\phi_{1}^{*})e^{-j\omega t}}{2j\omega m_{p}}\right) - k_{3}\left(\frac{\phi_{1}e^{j\omega t} - \phi_{1}^{*}e^{-j\omega t} - \phi_{2}e^{j\omega t} + \phi_{2}e^{-j\omega t}}{2j\omega m_{p}}\right)^{3} = 0$$

$$(5.30)$$

here, only the terms with fast frequency  $\omega$  are retained,

$$\dot{\phi}_{1} + \frac{jw}{2}\phi_{1} - \frac{j}{2\omega}\phi_{1} + \alpha_{2}\left(\frac{-j}{2\omega}\right)(\phi_{1} - \phi_{2}) 
+ \frac{k_{3}j}{8\omega^{3}m_{p}}\left(-3|\phi_{1}|^{2}\phi_{1} + 3\phi_{1}^{2}\phi_{2}^{*} + 6|\phi_{1}|^{2}\phi_{2} - 6\phi_{1}|\phi_{2}|^{2} - 3\phi_{1}^{*}\phi_{2}^{2} + 3|\phi_{2}|^{2}\phi_{2}\right) = 0$$
(5.31)

now the polar expression of the  $\phi_1$  and  $\phi_2$  are introduced as follows:

$$\phi_1 = Ae^{j\alpha}, \phi_2 = Be^{j\gamma} \tag{5.32}$$

where A and B are the real amplitude of the slow modulation,  $\alpha$  and  $\gamma$  represent the real phases of the modulation. Substituting Eq. (5.32) into Eq. (5.31) and retaining the real part of the equation yields,

$$\dot{A}\cos(\alpha) + \frac{A\sin(\alpha)}{2\omega} - A\dot{\alpha}\sin(\alpha) - \frac{A\omega\sin(\alpha)}{2} + \frac{k_1(A\sin(\alpha) - B\sin(\gamma))}{2\omega m_p} \\
-\frac{k_3}{8\omega^3 m_p} \Big[ \Big( 3B^3 \sin(\gamma) - 3A^3 \sin(\alpha) - 6AB^2 \sin(\alpha) \Big) \\
+ (6A^2 B\sin(\gamma) + 3AB^2 \sin(\alpha - 2\gamma) + 3A^2 B\sin(2\alpha - \gamma) \Big) \Big] = 0$$
(5.33)

To impose the stationarity condition, the time derivatives in the modulation equations are set to zero, enabling the computation of periodic solutions along the backbone branches. For simplification, a symmetric case is considered by assuming  $\alpha = \gamma$ . Under this assumption, Eq. (5.33) can be reformulated as follows:

$$\frac{A}{2\omega} - \frac{A\omega}{2} - \frac{k_3(3A^3 - 9A^2B + 9AB^2 - 3B^3)}{8\omega^3 m_p} + \frac{k_1(A - B)}{2\omega m_p} = 0$$
 (5.34)

By applying the same procedure to the second governing equation, Eq. (5.26) can be expressed as:

$$\frac{1}{8m_{a}B\omega^{3}} \left\{ \left[ -4Bm_{a}\omega^{4} + 4k_{1}\omega^{2}(B-A) + 3k_{3}(B-A)^{3} \right] \right. \\
+ \left[ -\frac{A\left(5b_{05}A^{4} + 6b_{03}A^{2}\omega^{2} + 8b_{01}\omega^{4}\right)}{2\omega^{2}} \right. \\
+ \frac{(A-B)(5b_{14}A^{4} + 6b_{12}A^{2}\omega^{2} + 8b_{10}\omega^{4})}{2\omega^{2}} \\
- \frac{A(A-B)^{2}(35b_{25}A^{4} + 40b_{23}A^{2}\omega^{2} + 48b_{21}\omega^{4})}{16\omega^{4}} \\
+ \frac{(A-B)^{3}(35b_{34}A^{4} + 40b_{32}A^{2}\omega^{2} + 48b_{30}\omega^{4})}{16\omega^{4}} \\
- \frac{A(A-B)^{4}(63b_{45}A^{4} + 70b_{43}A^{2}\omega^{2} + 80b_{41}\omega^{4})}{32\omega^{6}} \\
+ \frac{(A-B)^{5}(63b_{54}A^{4} + 70b_{52}A^{2}\omega^{2} + 80b_{50}\omega^{4})}{32\omega^{6}} \right] = 0$$

The amplitudes A and B in Eqs. (5.34) and (5.35) are solved for specified  $\omega$ . Then, the displacement and velocity can be derived as:

$$x_{p}(t) \approx X_{p} \cos(\omega t) = \frac{A}{\omega} \cos(\omega t), \qquad \dot{x}_{p}(t) \approx -\dot{X}_{p} \sin(\omega t) = -A \sin(\omega t),$$

$$x_{a}(t) \approx X_{a} \cos(\omega t) = \frac{B}{\omega} \cos(\omega t), \qquad \dot{x}_{a}(t) \approx -\dot{X}_{a} \sin(\omega t) = -B \sin(\omega t),$$

$$(5.36)$$

As the system is conservative, its total energy can be expressed as follows:

$$E_c = \frac{1}{2} m_p X_p^2 + \frac{1}{2} m_a X_a^2 \tag{5.37}$$

With a triplet of  $\omega$ , A and B in Eqs. (5.34) and (5.35), the FEP of the system with the MPLNES can be obtained, and the results are shown as black lines in Figure 5.18. To derive the FEP for the PLNES, the second square-bracketed term in Eq. (5.35) is removed since it is derived from  $\bar{f}_{n2}$ . The corresponding results are presented in Figure 5.19. Two black curves in Figures 5.18 and 5.19 present two primary NNM backbone branches: the upper one denoted as S11-, originating from  $f_p$ , is the out-of-phase branch, and the lower one denoted as S11+, originating from  $f_a$ , is the in-phase one. Additionally, the turning

point in S11— represents the energy threshold (ET) that is required to fully activate the 1:1 resonance.

The WT spectra contours of the relative displacement z at four different initial energy levels are overlaid on the FEPs to highlight the relationship between frequency components and displacement amplitude. Comparing Figures 5.18(a)-(b) and 5.19(a)-(b) reveal that when the initial energy is below the ET, the oscillation of the MPLNES tends to follow the S11+ backbone at the beginning, then follows a subharmonic branch (not shown). In contrary, the oscillation of the PLNES is mainly limited to its linear stiffness region. By comparing the two systems, it can be concluded that the MPLNES is able to show more nonlinearity under low and medium energy levels than the PLNES. As shown in Figures 5.18(c)-(d) and 5.19(c)-(d), when the initial energy exceeds the ET, the oscillations of both MPLNES and PLNES are attracted to their S11+ backbones, indicating that the desired 1:1 resonance has been established in both systems. Notably, the MPLNES shows immediate and steady 1:1 resonance compared to the PLNES, resulting in more effective TET from the primary system to the NES.

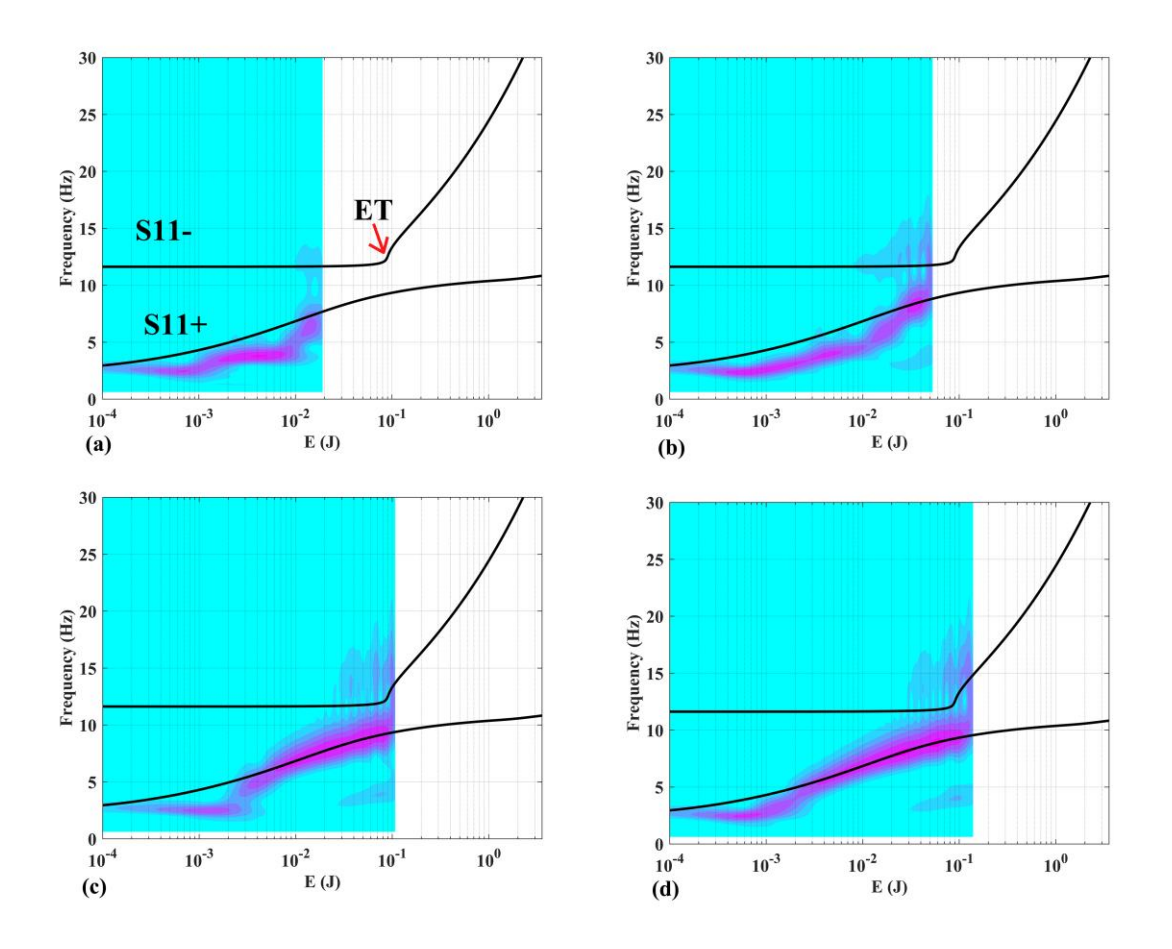


Figure 5.18 FEPs and WT spectra of the relative displacement z with MPLNES: (a) low initial energy X = 3 mm; (b) medium initial energy X = 5.0 mm; (c) medium-high initial energy X = 7.0 mm; (d) high initial energy X = 8.0 mm.

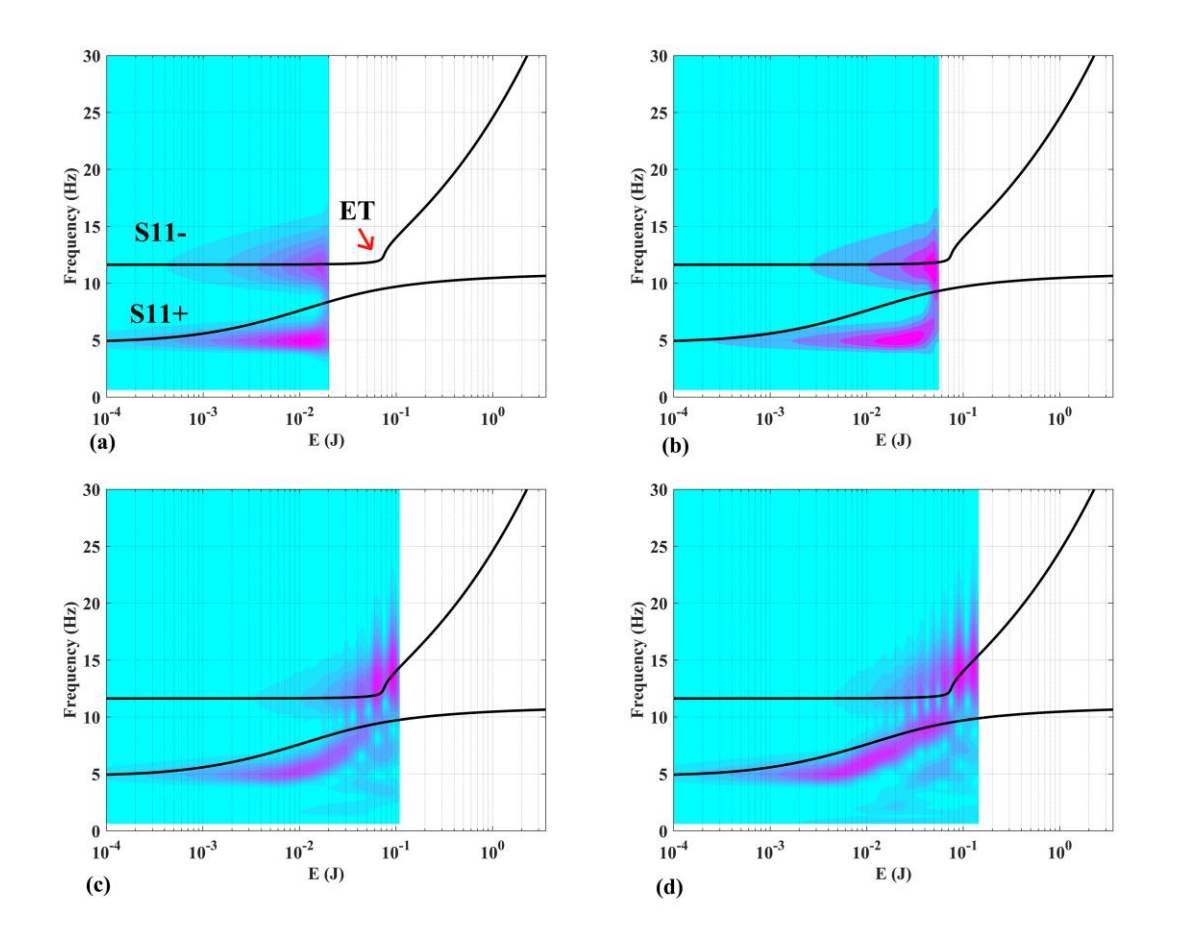


Figure 5.19 FEPs and WT spectra of the relative displacement z with PLNES: (a) low initial energy X = 3 mm; (b) medium initial energy X = 5.0 mm; (c) medium-high initial energy X = 7.0 mm; (d) high initial energy X = 8.0 mm.

## 5.4 VS and EH Trade-off Study

As shown in the previous studies [30, 52], the dual objective of maximizing VS and EH performances cannot be achieved simultaneously. It is imperative to maintain a proper trade-off between VS and EH. In addition, an investigation on this issue can further demonstrate the advantages of introducing the GMS. To better evaluate the VS performance, an index  $D_{c_a}$  is introduced:

$$D_{c_a} = D_{c_{am}} + D_{c_{ae}} (5.38)$$

where  $D_{c_{am}}$  represents the percentage of the initial energy dissipated by the mechanical damping over the time duration T defined as:

$$D_{c_{am}} = \frac{c_{am}}{E_i} \int_0^T \dot{z}^2 dt \times 100\%$$
 (5.39)

and  $D_{c_{ae}}$  represents the percentage of the initial energy harvested by the load resistor over the time duration T defined as:

$$D_{c_{ae}} = \frac{c_{ae}}{E_i} \int_0^T \dot{x}_a^2 dt \times 100\%$$
 (5.40)

Hereafter,  $D_{c_a}$  is referred to as the percentage of the initial energy dissipated by the NES. Note that as a key feature of the grounded EMEH,  $D_{c_{ae}}$  is related to  $\dot{x}_a$  instead of  $\dot{z}$ . A series of simulations are performed to evaluate  $D_{c_a}$  as a function of X under various  $R_l$  values. Figure 5.20 presents the simulation results. As shown,  $D_{c_a}$  sees a dramatic jump when X=2 mm for the MPLNES and X=5 mm for the PLNES, indicating that to activate the NES engagement, the MPLNES requires a lower initial energy threshold than the PLNES. The optimal VS performance is achieved at X=9 mm for the PLNES. Beyond this point, the performance shows a decreasing trend. In contrast, the MPLNES shows a more robust VS performance as it can maintain the peak VS performance over a wider range of initial displacements. Notably, the peak values of  $D_{c_a}$  for the two configurations are comparable.

Additionally, for both MPLNES and PLNES, within the range of  $R_l$  =30  $\Omega$  to 120  $\Omega$ , lower  $R_l$  values generally result in improvement of the VS performance. However, a comparison between the cases of  $R_l$ =20  $\Omega$  and 30  $\Omega$ , reveals a notable exception. When the initial energy is insufficient to fully activate the 1:1 resonance, the system with the higher  $R_l$  shows a better VS performance. This is because an excessively small  $R_l$  induces high electrical damping, which causes the NES to settle too quickly and prevents it from sustaining the dynamics necessary for an efficient TET. When the initial energy is sufficiently high to fully engage the 1:1 resonance, a lower  $R_l$  leads to an enhanced VS performance.

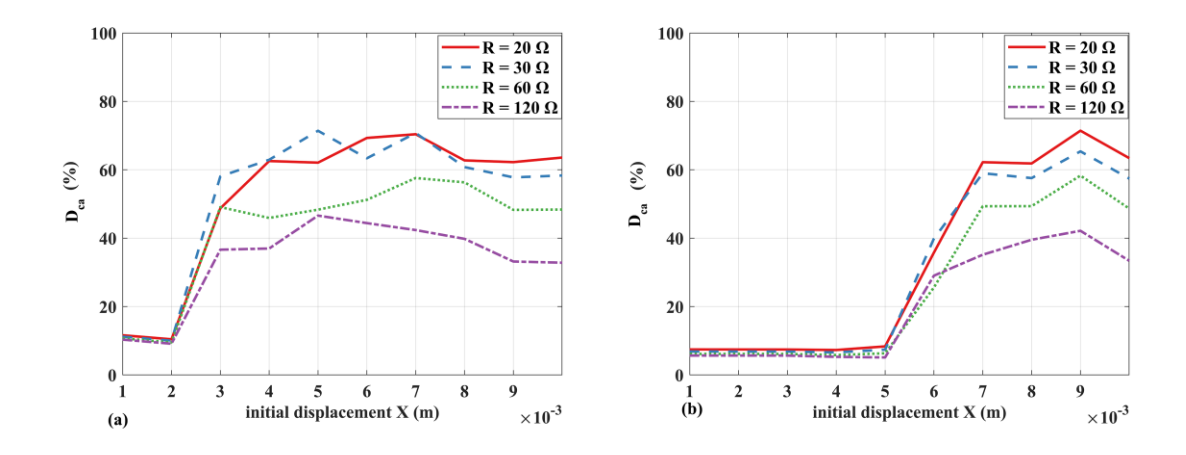


Figure 5.20 Percentage of the initial energy dissipated by the NES: (a) MPLNES; (b) PLNES.

To further illustrate the influence of  $R_l$ , simulations are repeated for both MPLNES and PLNES under the medium-high initial energy, by employing a lower load resistance value  $R_l = 20~\Omega$ . As shown in Figures 5.21(a) and 5.22(a), the oscillation amplitudes of the primary system in both configurations exhibit a more rapid decay compared to the cases in Figures 5.14(a) and 5.15(a). Due to high electrical damping, the oscillation of the MPLNES and PLNES stops early, consequently, the output voltage will also decrease rapidly.

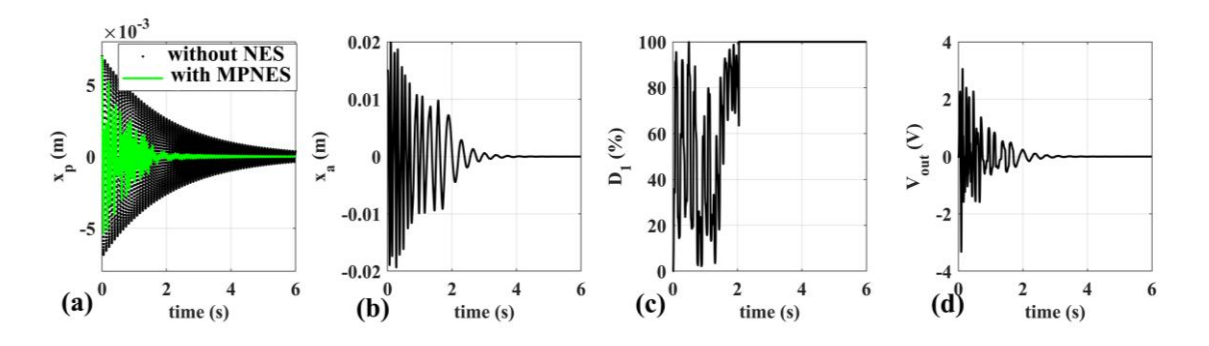


Figure 5.21 Simulation results with MPLNES and X = 7.0 mm,  $R_l = 20 \Omega$ : (a)  $x_p$ ; (b)  $x_a$ ; (c)  $D_1$ ; (d)  $V_{out}$ .

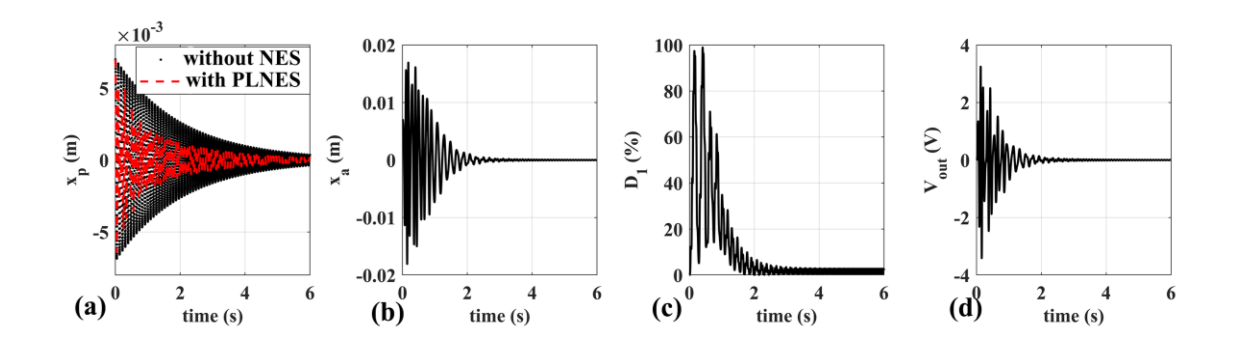


Figure 5.22 Simulation results with PLNES with X = 7.0 mm,  $R_l = 20 \Omega$ : (a)  $x_p$ ; (b)  $x_a$ ; (c)  $D_1$ ; (d)  $V_{out}$ .

Based on the investigation above, it is evident that the load resistance  $R_l$  affects both VS and EH performances. To better evaluate the energy harvesting efficiency, another index  $D_{load}$  is defined as:

$$D_{load} = \frac{1}{E_i} \int_0^T I^2 R_l dt = \frac{1}{E_i} \left[ \frac{K_t^2 R_l}{(4R_{coil} + R_l)^2} \int_0^T \dot{x}_a^2 dt \right] \times 100\%$$
 (5.41)

which measures the percentage of the energy harvested by the load resistance over the initial input energy. Comparing Eq. (5.41) and Eq. (5.40) reveals  $D_{load} = D_{c_{ae}}R_l/(4R_{coil}+R_l)$ , indicating that increasing  $R_l$  can enhance the power extraction from the load resistor. However, as mentioned above, a larger  $R_l$  value generally has an adversely effect on the VS performance of the system. Evidently, there is a trade-off between VS and EH when varying  $R_l$ 's value. To explore this trade-off, a multi-objective optimization is conducted to search for an optimal balance between VS and EH. For comparison, three NES configurations are considered, namely, MPLNES, PLNES and MPLNES without DSBs. It is worth mentioning that the modelling of the last configuration is achieved by using  $f_{n1} = k_{g1}z$  in Eqs. (5.1) and (5.2). For the optimization of each configuration,  $R_l$  and X are chosen to be the parameters to be optimized. The two objective functions are defined as follows:

$$J_1(R_l, X) = D_{c_a}(T) (5.42)$$

$$J_2(R_l, X) = D_{load}(T) (5.43)$$

where T=10 s. The MATLAB Global Optimization Toolbox is used to solve this 2-objective optimization problem. Since the program is based on minimization of the objective functions, the two objectives are set to  $-J_1$  and  $-J_2$ . The search range of the initial displacement is from X=1 mm to 3 mm for Case A (low initial energy) and from X=3 mm to 5 mm for Case B (medium initial energy), from X=5 mm to 7 mm for Case C (medium-high initial energy) and from X=7 mm to 10 mm for Case D (high initial energy). The search range of the load resistance is from  $R_1=1$   $\Omega$  to 150  $\Omega$ . The population size and the maximum number of generations are set to 500 and 50, respectively.

Figure 5.23 shows the so-called Pareto front for Case B for each of the three configurations. The best trade-off points marked as red circles are chosen as the ones that are closest to the origin of the plots. Table 5.3 summarizes the optimized values of  $R_l$  and X for the three configurations. It can be observed that the optimum  $R_l$  value generally exhibits a decreasing trend with increasing initial energy levels for all three NES configurations. This trend reflects a balance between the decay rate of the NES oscillation and the energy dissipated by the EMEH. An exception is observed in the case of the PLNES, where the optimum values for  $R_l$  remains relatively low in Cases A and B, as the system mainly exhibits linear behaviour under these conditions.

The bar chart shown in Figure 5.24 compares the optimum VS and EH performance of the three configurations under the different initial energy levels. It clearly demonstrates that the MPLNES exhibits outstanding VS and EH performance for all four cases. Due to the higher initial energy threshold required for establishing TET, the PLNES only shows comparable the VS and EH performance to the MPLNES under Cases C and D. In Case D, the VS performance of the two NES configurations is nearly identical, which can be attributed to the full establishment of the 1:1 resonance in both systems. The MPLNES without DSBs exhibits relatively low  $J_1$  and  $J_2$  values in the four cases, indicate that the TET can not be established even under the large initial energy level. However, it shows slightly better VS and EH performance than PLNES under Cases A and B due to the effect of the GMS. Two main observations can be drawn from the comparison. First, the

introduction of the GMS significantly enhances the VS and EH performance of the PLNES, particularly under low initial energy conditions. Second, the presence of a PLS between the primary system and the NES is crucial for enabling efficient engagement of TET.

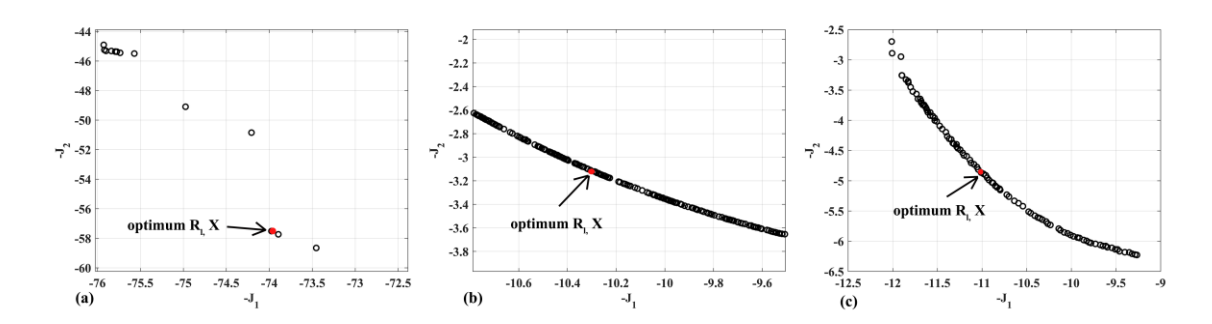


Figure 5.23 The Pareto fronts for Case B: (a) MPLNES; (b) PLNES and (c) MPLNES without DSBs.

Table 5.3 The optimization results for three NES configurations.

	MPLNES		PLNES		MPLNES without DSBs	
	$R_l(\Omega)$	X (mm)	$R_l(\Omega)$	X (mm)	$R_l(\Omega)$	X (m)
Case A	44.66	2.44	2.70	1.40	4.26	2.35
Case B	16.85	3.11	2.11	4.90	3.99	3.05
Case C	13.84	5.56	11.71	6.98	3.48	5.03
Case D	8.50	7.47	4.85	8.79	2.57	7.00

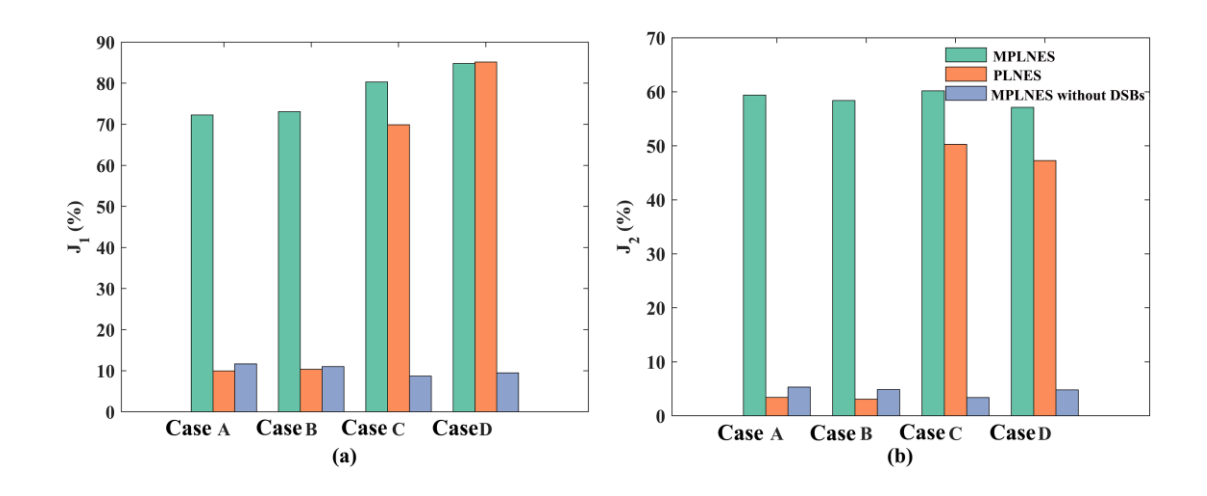


Figure 5.24 Comparison of the optimum results for the three configurations under different initial energy level ranges: (a)  $J_1$ ; (b)  $J_2$ .

## 5.5 Experimental Verification

An experimental study is conducted to verify the simulation results. Figure 5.25(a) shows a photo of the experimental setup to test the transient response of the primary system with the MPLNES. The base structure is fixed to the ground. The four coils are wired in series and connected to a variable resistor as shown in the bottom left of the figure. On the right, two laser reflex sensors (CP24MHT80, Wenglor) are used to measure the displacement of the primary block and the NES's mass, respectively. A computer equipped with the dSPACE dS1104 data acquisition board is used to collect the displacement signals from the laser sensors and the voltage signals of the EMEH's load resistor. To control the experiment, a program is developed by using the MATLAB Simulink which is interfaced with dSPACE Controldesk Desktop software. To have a better view of the MPLNES, Figure 5.25(b) shows the close-up view of the apparatus. For comparison, the primary system with the PLNES is also tested experimentally. This configuration is achieved by removing magnet D. The transient responses of both configurations are tested under the same load resistance value and initial conditions as those used in the simulation presented in Section 5.3.

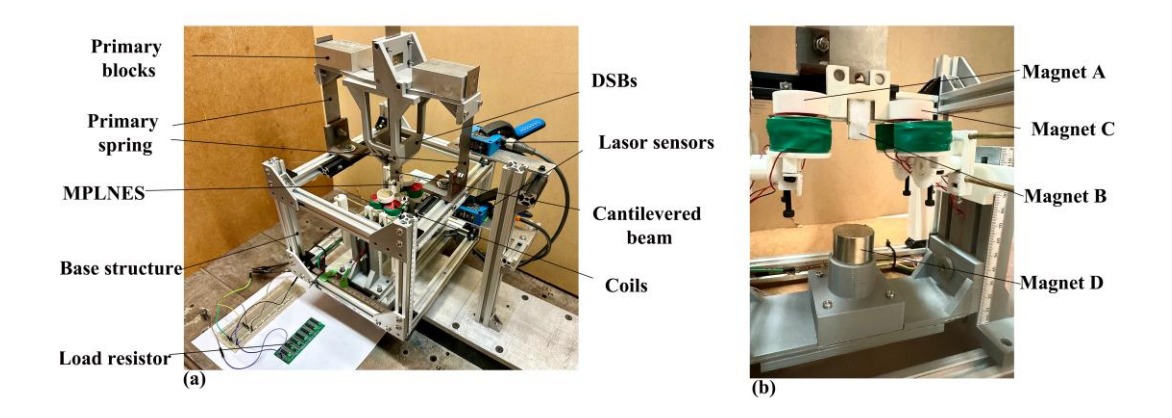


Figure 5.25 The experimental setup: (a) the entire system; (b) a close-up view of the MPLNES and magnet D.

Comparison of Figures 5.26-28 with Figures 5.11-13 reveals that overall, the experimental results agree with the simulation ones, confirming that the MPLNES's nonlinearity can is activated under the low initial energy level. However, as a notable difference, the responses obtained from the experiment decay faster than those from the simulation. This difference is primarily attributed to the energy loss caused by impacts between the beam and the DSBs,a dissipation mechanism not accounted for in the modeling. As a result, the output voltage from the experiment also exhibits a more rapid decay, suggesting that the actual energy harvested by the EMEH is lower than that predicted by the simulation.

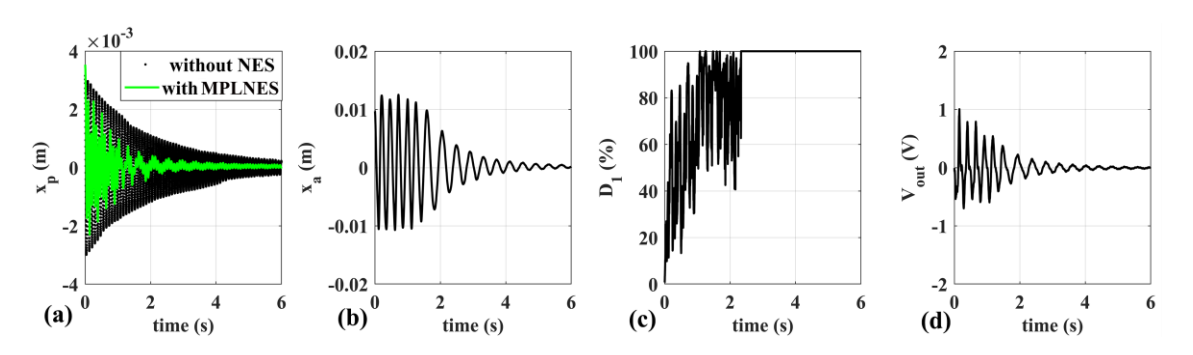


Figure 5.26 Experimental results with MPLNES and X = 3.53 mm: (a)  $x_p$ ; (b)  $x_a$ ; (c)  $D_1$ ; (d)  $V_{out}$ .

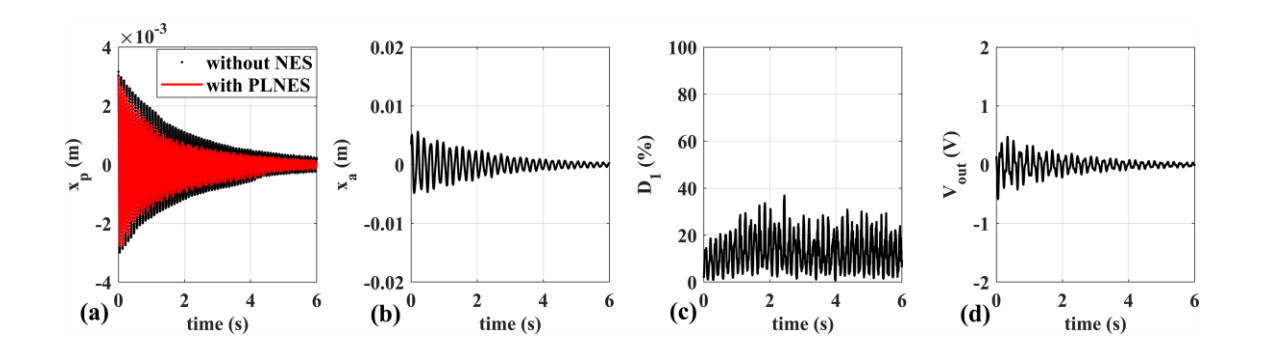


Figure 5.27 Experimental results with PLNES and X = 2.99 mm: (a)  $x_p$ ; (b)  $x_a$ ; (c)  $D_1$ ; (d)  $V_{out}$ .

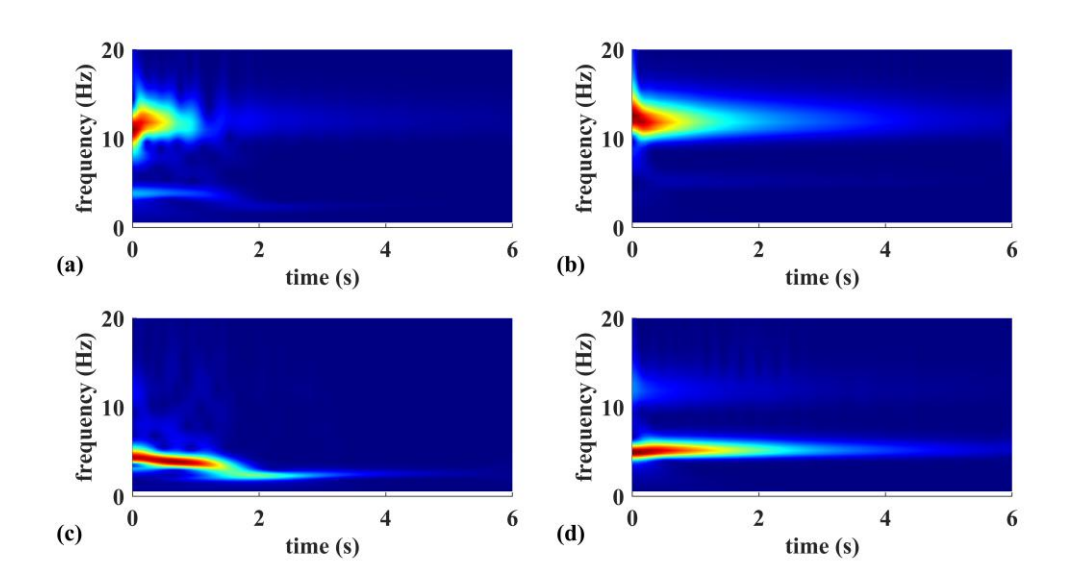


Figure 5.28 WT spectra of the experimental responses: (a)  $x_p$  with MPLNES; (b)  $x_p$  with PLNES  $x_p$ ; (c)  $x_a$  with MPLNES; (d)  $x_a$  with PLNES.

Comparison of Figures 5.29–5.31 with Figures 5.14–5.16 also reveals that the experimental results follow the general trends predicted in the simulation, confirming that under the medium-high initial energy, the 1:1 resonance is activated for both systems. However, due to the additional damping introduced by impact, the responses in the experiment decay more rapidly than those in the simulations. This suggests that TET exists for a shorter duration than predicted by the simulation.

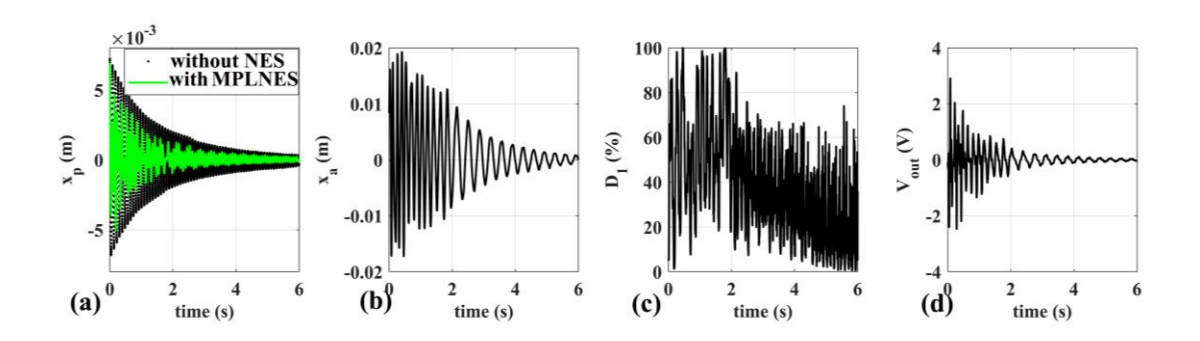


Figure 5.29 Experimental results with MPLNES and X = 6.87 mm: (a)  $x_p$ ; (b)  $x_a$ ; (c)  $D_1$ ; (d)  $V_{out}$ .

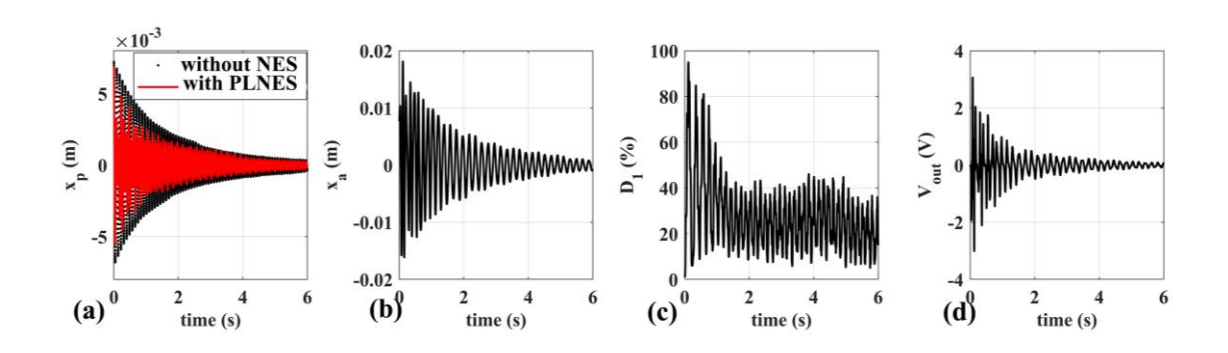


Figure 5.30 Experimental results with PLNES and X = 6.93 mm: (a)  $x_p$ ; (b)  $x_a$ ; (c)  $D_1$ ; (d)  $V_{out}$ .

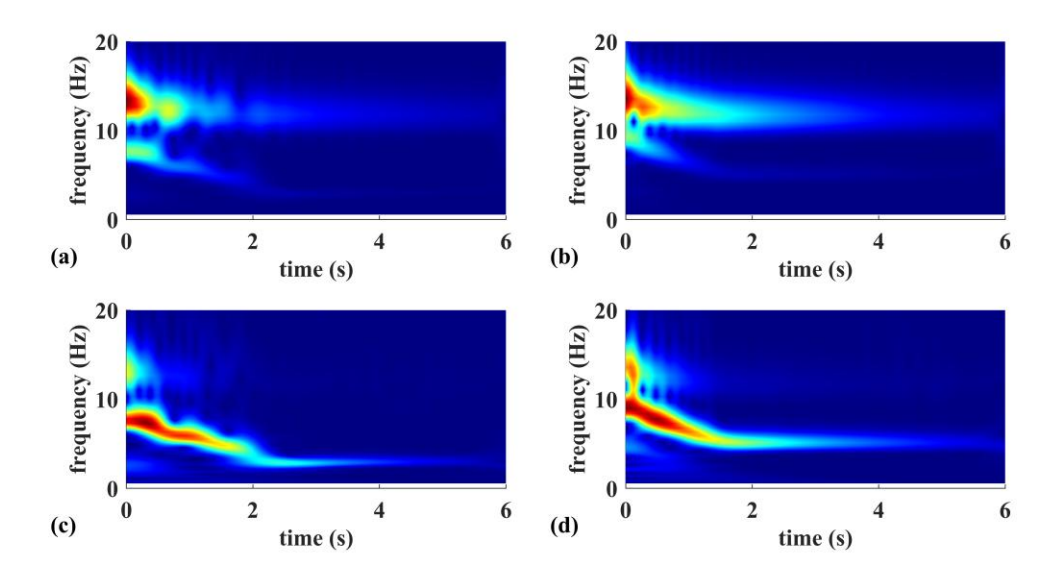


Figure 5.31 WT spectra of the experimental responses: (a)  $x_p$  with MPLNES; (b)  $x_p$  with PLNES; (c)  $x_a$  with MPLNES; (d)  $x_a$  with PLNES.

Figures 5.32 and 5.33 show the FEPs and WT spectra for the relative displacement for the system with the MPLNES and the PLNES, respectively. By comparing them with Figures 5.18-5.19, it can be found that the experimental results show a good agreement with the simulation ones when the initial energy is lower than the ET. However, under the medium-to-high and high initial energy conditions, the oscillation amplitudes of both MPLNES and PLNES are somewhat lower than the S11+ backbone curves. This discrepancy can be attributed to the additional damping induced by repeated impacts, which suppresses the dynamic response of the NESs and prevents a full establishment of the 1:1 resonance.

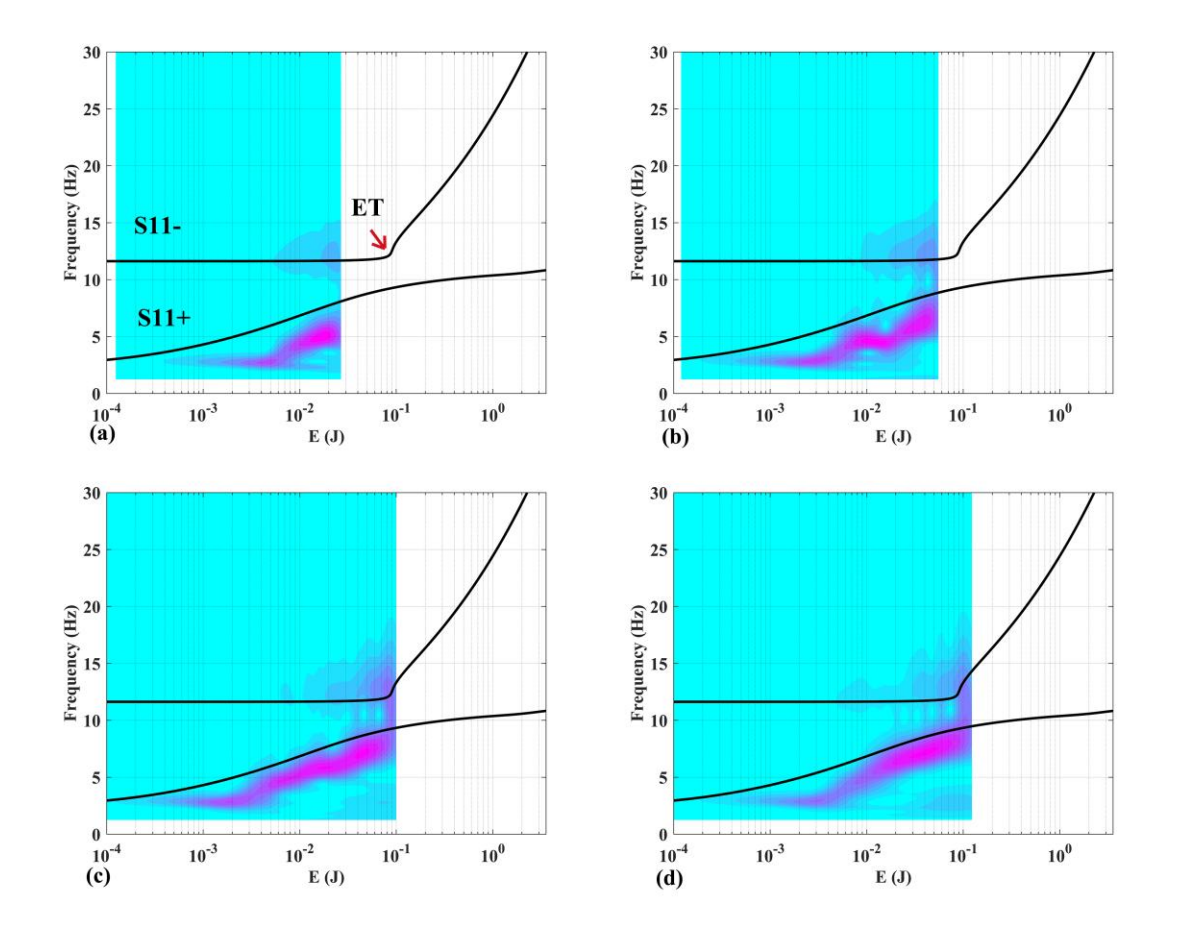


Figure 5.32. FEPs and WT spectra for the experimental relative displacement z with MPLNES: (a) low initial energy X = 3.53 mm; (b) medium initial energy X = 5.21 mm; (c)medium-high initial energy X = 6.87 mm and (d) high initial energy X = 8.50 mm.

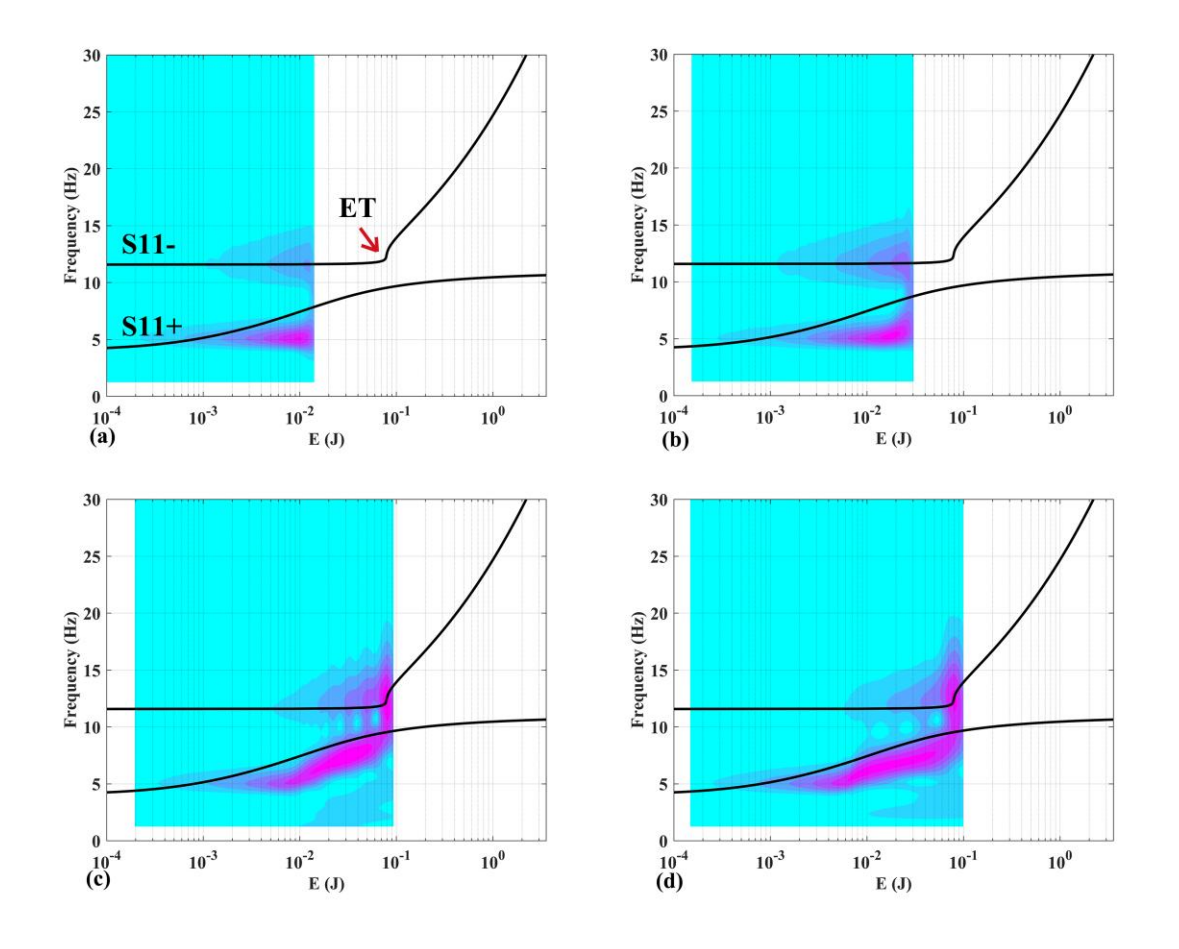


Figure 5.33 FEPs and WT spectra for the experimental relative displacement z with PLNES: (a) low initial energy X = 2.99 mm; (b) medium initial energy X = 4.78 mm; (c) medium-high initial energy X = 6.93 mm and (d) high initial energy X = 8.11 mm.

#### 5.6 Conclusions

In this study, a magnetically enhanced piecewise-linear nonlinear energy sink (MPLNES) was developed to achieve simultaneous vibration suppression (VS) and energy harvesting (EH). The MPLNES is connected between the primary system and the ground through a piecewise-linear spring (PLS) and a grounded magnetic spring (GMS), and incorporates a grounded electromagnetic energy harvester (EMEH). A detailed design procedure was established for both the PLS and GMS. For the PLS, the NES frequency at maximum displacement is tuned to match the natural frequency of the primary system.

Using the derived two-variable model, the GMS is designed based on two criteria—maintaining mono-stable behavior and enhancing the essential nonlinearity of the NES—by appropriately selecting the parameters *d* and *h*. The transduction factor of the EMEH is determined through COMSOL simulations and expressed as a function of the positions of both the MPLNES and the primary mass, with experimental results confirming the model's accuracy.

In the performance evaluation, a comparative analysis between the MPLNES and a conventional piecewise-linear nonlinear energy sink (PLNES) was conducted. The transient behaviors of both configurations were examined through time responses, wavelet transform spectra, and frequency energy plots under various initial energy levels. The results show that the MPLNES requires a lower energy threshold to initiate targeted energy transfer (TET) compared to the PLNES. This advantage arises from the GMS, which introduces a position-dependent restoring force that dynamically shifts the NES's equilibrium position in response to the primary mass motion. This unique feature amplifies the relative displacement under low initial energy, promoting earlier activation of the nonlinear regime and thus reducing the TET threshold.

To address the trade-off between VS and EH, a multi-objective optimization was performed to identify the optimal initial displacements and load resistances for three NES configurations: the PLNES, the MPLNES, and the MPLNES without double stop blocks (DSBs). Three key observations emerged from the results: (1) the MPLNES not only achieves a better balance between VS and EH than the other two configurations but also maintains robust performance across a wide range of initial energy levels; (2) the optimal load resistance generally decreases as the initial energy level increases for all three configurations; and (3) the MPLNES without DSBs is inefficient for both VS and EH under various initial conditions, highlighting that the hardening effect introduced by the PLS is essential for sustaining effective TET.

Experimental tests were performed at various initial energy levels, and the results showed good agreement with numerical predictions. The presence of double stop blocks introduced impact damping, resulting in additional energy dissipation and slightly faster

decay compared to the simulations. Nevertheless, the measured transient responses confirmed that the developed apparatus is capable of achieving efficient VS and EH even under low initial energy levels.

## Appendix 5A. Parameters of the apparatus

Table 5.4 The parameters of the PLSs with DSBs.

paramete	rs of PLS	Geometry parameters of the blocks		
Symbols	values	Symbols	values	
$k_{gl}$ (N/m)	90.205	<i>l</i> <sub>1</sub> (m)	0.0116	
$z_{gl}(m)$	0.008	$g_1$ (m)	0.004	
$k_{g2}$ (N/m)	985.764	$l_2$ (m)	0.136	
$z_{g2}$ (m)	0.0143	g <sub>2</sub> (m)	0.007	
$k_{g3}$ (N/m)	2370.967			

# Appendix 5B. The Amplitudes of the Position Vectors of Magnets

The expressions of the amplitudes of position vectors of magnets shown in Eqs. (5.10) and (5.12) can be defined as follows:

$$|\mathbf{r}_{15}| = \left\{ \left\{ -\left[ d - \frac{l_D}{2} \right] - \left( l - \left( l - \frac{l_B}{2} \right) \cos \theta \right) \right\}^2 + \left( x_p + z - \frac{l_B}{2} \sin \theta \right)^2 \right\}^{1/2}$$
 (5B.1)

$$|\mathbf{r}_{16}| = \left\{ \left\{ -\left[d + \frac{l_D}{2}\right] - \left(l - \left(l - \frac{l_B}{2}\right)\cos\theta\right) \right\}^2 + \left(x_p + z - \frac{l_B}{2}\sin\theta\right)^2 \right\}^{1/2}$$
 (5B.2)

$$|\mathbf{r}_{25}| = \left\{ \left\{ -\left[d - \frac{l_D}{2}\right] - \left(l - \left(l + \frac{l_B}{2}\right)\cos\theta\right) \right\}^2 + \left(x_p + z + \frac{l_B}{2}\sin\theta\right)^2 \right\}^{1/2}$$
 (5B.3)

$$|\mathbf{r}_{26}| = \left\{ \left\{ -\left[ d + \frac{l_D}{2} \right] - \left( l - \left( l + \frac{l_B}{2} \right) \cos \theta \right) \right\}^2 + \left( x_p + z + \frac{l_B}{2} \sin \theta \right)^2 \right\}^{1/2}$$

$$(5B.4)$$

$$|\mathbf{r}_{35}| = \left\{ \left\{ -\left[ d - \frac{l_D}{2} \right] - \left( l - \left( l - h - \frac{l_A}{2} \right) \cos \theta \right) \right\}^2 + \left( x_p + z - h \sin \alpha - \frac{l_A}{2} \sin \alpha \right)^2 \sin^2 \theta + w^2 \right\}^{1/2}$$

$$(5B.5)$$

$$|\mathbf{r}_{36}| = \left\{ \left\{ -\left[ d + \frac{l_D}{2} \right] - \left( l - \left( l - h - \frac{l_A}{2} \right) \cos \theta \right) \right\}^2 + \left( x_p + z - h \sin \theta - \frac{l_A}{2} \sin \theta \right)^2 \sin^2 \theta + w^2 \right\}^{1/2}$$

$$(5B.6)$$

$$|\mathbf{r}_{45}| = \left\{ \left\{ -\left[ d - \frac{l_D}{2} \right] - \left( l - \left( l - h + \frac{l_A}{2} \right) \cos \theta \right) \right\}^2 + \left( x_p + z - h \sin \theta + \frac{l_A}{2} \sin \theta \right)^2 \sin^2 \theta + w^2 \right\}^{1/2}$$

$$(5B.7)$$

$$|\mathbf{r}_{46}| = \left\{ \left\{ -\left[ d + \frac{l_D}{2} \right] - \left( l - \left( l - h + \frac{l_A}{2} \right) \cos \theta \right) \right\}^2 + \left( x_p + z - h \sin \theta + \frac{l_A}{2} \sin \theta \right)^2 \sin^2 \theta + w^2 \right\}^{1/2}$$

$$(5B.8)$$

# Appendix 5C. Determination of the EMEH's Transduction Factor in COMSOL

In this study, a finite element analysis software COMSOL Multiphysics is utilized to compute the change rates of the magnetic flux of coils 1 and 2 when magnets A and B are oscillating through them. For the sake of simplicity, the influence of magnet C on the coils 1 and 2 is ignored. The geometry of the model built in COMSOL is shown in Figure 5B.1(a). It should be noted that each of the coils is modelled as n disks to represent the n layers and meshed individually. As shown in Figure 5B.1(b),  $D_{coil}$  and  $h_{coil}$  are the diameter and height of the coil, respectively,  $d_g$  is the air gap between the end surfaces of magnet C and the coils 1 and 2, All the values of the parameters of the coils and magnets used in the simulation are summarized in Tables 3.1 and 3.2, respectively. In the simulation, each coil is modelled with 12 layers, the x-axis positions of magnets B and C are expressed as  $x_a =$ 

 $x_p + z$ , while the z-axis position on is given by  $\delta(z) = l - \sqrt{l^2 - z^2}$ , and  $\theta$  is set as the angle of magnets A and B from the horizontal.

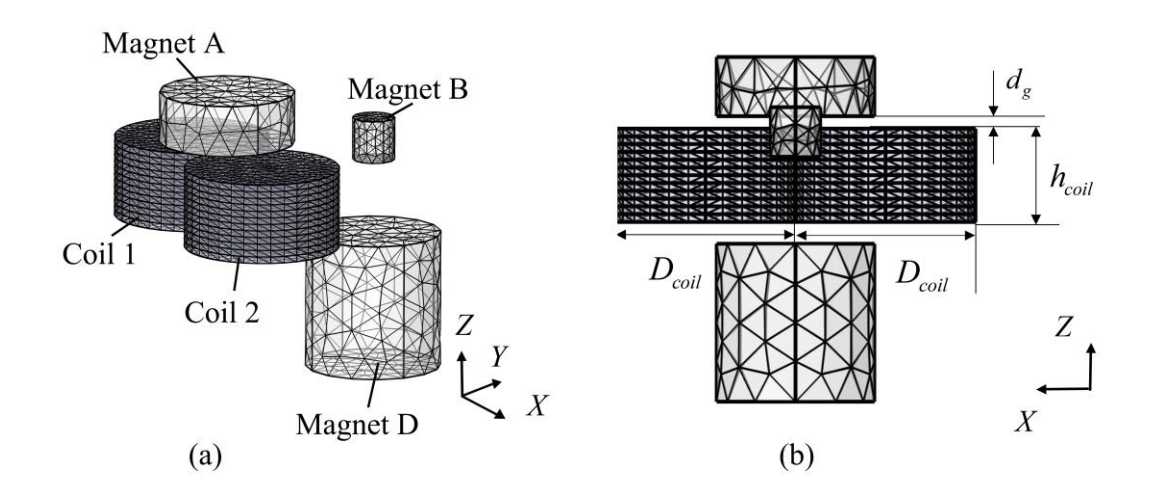


Figure 5B.1 COMSOL model used to determine  $K_{ti}$ : (a) isometric view; (b) side view.

#### References

- [1] P. S. Balaji and K. Karthik SelvaKumar, "Applications of nonlinearity in passive vibration control: a review," *Journal of Vibration Engineering & Technologies*, vol. 9, no. 2, pp. 183-213, 2020, doi: 10.1007/s42417-020-00216-3.
- [2] C. R. Bowen, H. A. Kim, P. M. Weaver, and S. Dunn, "Piezoelectric and ferroelectric materials and structures for energy harvesting applications," *Energy Environ. Sci.*, vol. 7, no. 1, pp. 25-44, 2014, doi: 10.1039/c3ee42454e.
- [3] A. Muscat, S. Bhattacharya, and Y. Zhu, "Electromagnetic Vibrational Energy Harvesters: A Review," *Sensors (Basel)*, vol. 22, no. 15, Jul 25 2022, doi: 10.3390/s22155555.
- [4] F. U. Khan and M. U. Qadir, "State-of-the-art in vibration-based electrostatic energy harvesting," *Journal of Micromechanics and Microengineering*, vol. 26, no. 10, 2016, doi: 10.1088/0960-1317/26/10/103001.
- [5] N. Tran, M. H. Ghayesh, and M. Arjomandi, "Ambient vibration energy harvesters: A review on nonlinear techniques for performance enhancement," *International Journal of Engineering Science*, vol. 127, pp. 162-185, 2018, doi: 10.1016/j.ijengsci.2018.02.003.

- [6] S. F. Ali and S. Adhikari, "Energy harvesting dynamic vibration absorbers," *Journal of Applied Mechanics*, vol. 80, no. 4, 2013, doi: 10.1115/1.4007967.
- [7] M. J. Brennan, B. Tang, G. P. Melo, and V. Lopes, "An investigation into the simultaneous use of a resonator as an energy harvester and a vibration absorber," *Journal of Sound and Vibration*, vol. 333, no. 5, pp. 1331-1343, 2014, doi: 10.1016/j.jsv.2013.10.035.
- [8] Z. Chen, Z. Chen, and Y. Wei, "Quasi-zero stiffness-based synchronous vibration isolation and energy harvesting: a comprehensive review," *Energies*, vol. 15, no. 19, 2022, doi: 10.3390/en15197066.
- [9] M. Rezaei, R. Talebitooti, W.-H. Liao, and M. I. Friswell, "A comparative study on vibration suppression and energy harvesting via mono-, bi-, and tri-stable piezoelectric nonlinear energy sinks," *Nonlinear Dynamics*, vol. 112, no. 13, pp. 10871-10910, 2024, doi: 10.1007/s11071-024-09562-3.
- [10] P. V. R. Raj and B. Santhosh, "Parametric study and optimization of linear and nonlinear vibration absorbers combined with piezoelectric energy harvester," *International Journal of Mechanical Sciences*, vol. 152, pp. 268-279, 2019, doi: 10.1016/j.ijmecsci.2018.12.053.
- [11] Y. S. Lee *et al.*, "Passive non-linear targeted energy transfer and its applications to vibration absorption: A review," *Proceedings of the Institution of Mechanical Engineers, Part K: Journal of Multi-body Dynamics*, vol. 222, no. 2, pp. 77-134, 2008, doi: 10.1243/14644193jmbd118.
- [12] A. F. Vakakis, "Inducing passive nonlinear energy sinks in vibrating systems," *Journal of Vibration and Acoustic.*, vol. 123, no. 3, pp. 324-332, 2001, doi: 10.1115/1.1368883.
- [13] A. F. Vakakis, "Designing a linear structure with a local nonlinear attachment for enhanced energy pumping," *Meccanica*, vol. 38, pp. 677-686, 2003, doi: 10.1023/A:1025829425349.
- [14] H. Yao, Y. Cao, Z. Ding, and B. Wen, "Using grounded nonlinear energy sinks to suppress lateral vibration in rotor systems," *Mechanical Systems and Signal Processing*, vol. 124, pp. 237-253, 2019, doi: 10.1016/j.ymssp.2019.01.054.
- [15] H. Zhao, J. Li, S. Zhu, and Y. Zhang, "Research on damping region on grounded damping nonlinear energy sink," *Nonlinear Dynamics*, vol. 113, no. 14, pp. 17725-17746, 2025, doi: 10.1007/s11071-025-11113-3.
- [16] A. F. Vakakis and R. H. Rand, "Nonlinear dynamics of a system of coupled oscillators with essential stiffness nonlinearities," in *International Design Engineering Technical Conferences and Computers and Information in Engineering Conference*, 2003, vol. 37033, pp. 1209-1220.
- [17] Y. S. Lee, G. Kerschen, A. F. Vakakis, P. Panagopoulos, L. Bergman, and D. M. McFarland, "Complicated dynamics of a linear oscillator with a light, essentially

- nonlinear attachment," *Physica D: Nonlinear Phenomena*, vol. 204, no. 1, pp. 41-69, 2005/05/01/2005, doi: https://doi.org/10.1016/j.physd.2005.03.014.
- [18] X. Geng, H. Ding, X. Mao, and L. Chen, "A ground-limited nonlinear energy sink," *Acta Mechanica Sinica*, vol. 38, no. 5, 2022, doi: 10.1007/s10409-022-09027-x.
- [19] Y. Shen, P. Sui, and X. Wang, "Performance analysis and optimization of bimodal nonlinear energy sink," *Nonlinear Dynamics*, vol. 111, no. 18, pp. 16813-16830, 2023, doi: 10.1007/s11071-023-08737-8.
- [20] P. Sui, Y. Shen, and X. Wang, "Study on response mechanism of nonlinear energy sink with inerter and grounded stiffness," *Nonlinear Dynamics*, vol. 111, no. 8, pp. 7157-7179, 2023, doi: 10.1007/s11071-022-08226-4.
- [21] X.-F. Geng, H. Ding, J.-C. Ji, K.-X. Wei, X.-J. Jing, and L.-Q. Chen, "A state-of-the-art review on the dynamic design of nonlinear energy sinks," *Engineering Structures*, vol. 313, 2024, doi: 10.1016/j.engstruct.2024.118228.
- [22] F. Zhao, J. C. Ji, K. Ye, and Q. Luo, "Increase of quasi-zero stiffness region using two pairs of oblique springs," *Mechanical Systems and Signal Processing*, vol. 144, 2020, doi: 10.1016/j.ymssp.2020.106975.
- [23] F. Zhao, J. Ji, K. Ye, and Q. Luo, "An innovative quasi-zero stiffness isolator with three pairs of oblique springs," *International Journal of Mechanical Sciences*, vol. 192, 2021, doi: 10.1016/j.ijmecsci.2020.106093.
- [24] J. Zhou, X. Wang, D. Xu, and S. Bishop, "Nonlinear dynamic characteristics of a quasi-zero stiffness vibration isolator with cam-roller-spring mechanisms," *Journal of Sound and Vibration*, vol. 346, pp. 53-69, 2015, doi: 10.1016/j.jsv.2015.02.005.
- [25] X. Wang, J. Zhou, D. Xu, H. Ouyang, and Y. Duan, "Force transmissibility of a two-stage vibration isolation system with quasi-zero stiffness," *Nonlinear Dynamics*, vol. 87, no. 1, pp. 633-646, 2016, doi: 10.1007/s11071-016-3065-x.
- [26] X. Geng, H. Ding, X. Jing, X. Mao, K. Wei, and L. Chen, "Dynamic design of a magnetic-enhanced nonlinear energy sink," *Mechanical Systems and Signal Processing*, vol. 185, 2023, doi: 10.1016/j.ymssp.2022.109813.
- [27] Y. Sun, "Experimental Modelling and Amplitude-frequency response analysis of a piecewise linear vibration system," *IEEE Access*, vol. 9, pp. 4279-4290, 2021, doi: 10.1109/access.2020.3047655.
- [28] H. Li, K. Liu, and J. Deng, "Using a piecewise-linear spring to approximate an essentially nonlinear spring: design and validation," *Transactions of the Canadian Society for Mechanical Engineering*, 2024, doi: 10.1139/tcsme-2024-0163.
- [29] X. Shui and S. Wang, "Investigation on a mechanical vibration absorber with tunable piecewise-linear stiffness," *Mechanical Systems and Signal Processing*, vol. 100, pp. 330-343, 2018, doi: 10.1016/j.ymssp.2017.05.046.

- [30] X. Li, K. Liu, L. Xiong, and L. Tang, "Development and validation of a piecewise linear nonlinear energy sink for vibration suppression and energy harvesting," *Journal of Sound and Vibration*, vol. 503, 2021, doi: 10.1016/j.jsv.2021.116104.
- [31] Y. Cao, H. Yao, H. Li, and J. Dou, "Torsional vibration dynamics of a gear-shafting system attaching a nonlinear energy sink," *Mechanical Systems and Signal Processing*, vol. 176, 2022, doi: 10.1016/j.ymssp.2022.109172.
- [32] X. Liu, H. Ding, X. Geng, K. Wei, S. Lai, and L. Chen, "A magnetic nonlinear energy sink with quasi-zero stiffness characteristics," *Nonlinear Dynamics*, vol. 112, no. 8, pp. 5895-5918, 2024, doi: 10.1007/s11071-024-09379-0.
- [33] B. P. Mann and N. D. Sims, "Energy harvesting from the nonlinear oscillations of magnetic levitation," *Journal of Sound and Vibration*, vol. 319, no. 1-2, pp. 515-530, 2009, doi: 10.1016/j.jsv.2008.06.011.
- [34] Z. Li, L. Xiong, L. Tang, W. Yang, K. Liu, and B. Mace, "Modeling and harmonic analysis of energy extracting performance of a piezoelectric nonlinear energy sink system with AC and DC interface circuits," *Mechanical Systems and Signal Processing*, vol. 155, 2021, doi: 10.1016/j.ymssp.2021.107609.
- [35] S. Wang, W. Xin, Y. Ning, B. Li, and Y. Hu, "Design, experiment, and improvement of a quasi-zero-stiffness vibration isolation system," *Applied Sciences*, vol. 10, no. 7, 2020, doi: 10.3390/app10072273.
- [36] M. Rezaei, R. Talebitooti, and W.-H. Liao, "Exploiting bi-stable magneto-piezoelastic absorber for simultaneous energy harvesting and vibration mitigation," *International Journal of Mechanical Sciences*, vol. 207, 2021, doi: 10.1016/j.ijmecsci.2021.106618.
- [37] Y.-Y. Chen, Z.-C. Qian, W. Zhao, and C.-M. Chang, "A magnetic bi-stable nonlinear energy sink for structural seismic control," *Journal of Sound and Vibration*, vol. 473, 2020, doi: 10.1016/j.jsv.2020.115233.
- [38] Y.-c. Zeng and H. Ding, "A tristable nonlinear energy sink," *International Journal of Mechanical Sciences*, vol. 238, 2023, doi: 10.1016/j.ijmecsci.2022.107839.
- [39] M. Lallart, S. Zhou, Z. Yang, L. Yan, K. Li, and Y. Chen, "Coupling mechanical and electrical nonlinearities: The effect of synchronized discharging on tristable energy harvesters," *Applied Energy*, vol. 266, 2020, doi: 10.1016/j.apenergy.2020.114516.
- [40] Z. Nili Ahmadabadi and S. E. Khadem, "Nonlinear vibration control and energy harvesting of a beam using a nonlinear energy sink and a piezoelectric device," *Journal of Sound and Vibration*, vol. 333, no. 19, pp. 4444-4457, 2014, doi: 10.1016/j.jsv.2014.04.033.
- [41] J. Shen, S. Wan, J. Fu, S. Li, D. Lv, and K. Dekemele, "A magnetic plucking frequency up-conversion piezoelectric energy harvester with nonlinear energy sink structure," *Applied Energy*, vol. 376, 2024, doi: 10.1016/j.apenergy.2024.124326.

- [42] K. Remick, D. Dane Quinn, D. Michael McFarland, L. Bergman, and A. Vakakis, "High-frequency vibration energy harvesting from impulsive excitation utilizing intentional dynamic instability caused by strong nonlinearity," *Journal of Sound and Vibration*, vol. 370, pp. 259-279, 2016, doi: 10.1016/j.jsv.2016.01.051.
- [43] H. Li, A. Li, X. Kong, and H. Xiong, "Dynamics of an electromagnetic vibro-impact nonlinear energy sink, applications in energy harvesting and vibration absorption," *Nonlinear Dynamics*, vol. 108, no. 2, pp. 1027-1043, 2022, doi: 10.1007/s11071-022-07253-5.
- [44] J. Xu, Y. Leng, X. Su, and X. Chen, "Efficiency evaluation of the enhanced nonlinear energy sink with electromagnetic energy harvesting mechanism," *Journal of Vibration and Control*, vol. 31, no. 3-4, pp. 384-397, 2024, doi: 10.1177/10775463241227336.
- [45] H. Li, K. Liu, J. Deng, and B. Li, "A grounded and tunable multi-stable nonlinear energy sink: transient responses," *In Proceedings of the Canadian Society for Mechanical Engineering International Congress* 2022, June 5-8, 2022, Edmonton, Canada, doi: 10.7939/r3-d4rz-jr10.
- [46] T. Yang, T. Liu, Y. Tang, S. Hou, and X. Lv, "Enhanced targeted energy transfer for adaptive vibration suppression of pipes conveying fluid," *Nonlinear Dynamics*, vol. 97, no. 3, pp. 1937-1944, 2018, doi: 10.1007/s11071-018-4581-7.
- [47] S. Wang and M. Wiercigroch, "Forced oscillators with non-linear spring: A simple analytical approach," *Chaos, Solitons & Fractals*, vol. 41, no. 4, pp. 1784-1790, 2009, doi: 10.1016/j.chaos.2008.07.048.
- [48] G. Wang, H. Wu, W.-H. Liao, S. Cui, Z. Zhao, and J. Tan, "A modified magnetic force model and experimental validation of a tri-stable piezoelectric energy harvester," *Journal of Intelligent Material Systems and Structures*, vol. 31, no. 7, pp. 967-979, 2020, doi: 10.1177/1045389X2090597.
- [49] M. A. Al-Shudeifat and A. S. Saeed, "Frequency–energy plot and targeted energy transfer analysis of coupled bistable nonlinear energy sink with linear oscillator," *Nonlinear Dynamics*, vol. 105, no. 4, pp. 2877-2898, 2021, doi: 10.1007/s11071-021-06802-8.
- [50] H. Li, K. Liu, and J. Deng, "Modeling and evaluation of a multi-stable hybrid energy harvester," *Vibration*, vol. 7, no. 3, pp. 662-686, 2024, doi: 10.3390/vibration7030035.
- [51] G. Kerschen, J. J. Kowtko, D. M. McFarland, L. A. Bergman, and A. F. Vakakis, "Theoretical and Experimental Study of Multimodal Targeted Energy Transfer in a System of Coupled Oscillators," *Nonlinear Dynamics*, vol. 47, no. 1-3, pp. 285-309, 2006, doi: 10.1007/s11071-006-9073-5.
- [52] D. Kremer and K. Liu, "A nonlinear energy sink with an energy harvester: Transient responses," *Journal of Sound and Vibration*, vol. 333, no. 20, pp. 4859-4880, 2014, doi: 10.1016/j.jsv.2014.05.010.

### **Chapter 6 Conclusions and Future Works**

#### 6.1 Conclusions

This thesis has systematically addressed the modelling, design, analysis and experimental validation of a nonlinear energy sink (NES) that is capable of simultaneously achieving vibration suppression (VS) and energy harvesting (EH). Motivated by the high initial energy threshold of the existing NES designs, the research focused on integrating a grounded magnetic spring (GMS) and an energy harvester into a conventional piecewise linear NES (PLNES). Four interrelated objectives were pursued, each corresponding to a dedicated study: developing an accurate magnetic force model, comparing the characteristics of different energy harvesting mechanisms, establishing a systematic design process for a piecewise linear spring (PLS), and proposing a magnetically enhanced PLNES.

Firstly, A tunable multi-stable piezoelectric energy harvester (PEH) was developed, comprising a cantilever beam and an adjustable magnetic assembly capable of achieving mono-, bi-, and tri-stable states by tuning geometric parameters. Two magnetic restoring force models (the equivalent magnetic point model as 1<sup>st</sup> model and the equivalent magnetic 2-point dipole model as the 2<sup>nd</sup> model) were derived and validated experimentally. The models were further optimized using a multi-population genetic algorithm (MPGA). The results show that a five-parameter optimized 2<sup>nd</sup> model achieves the highest accuracy. Parametric sensitivity analysis revealed that the tri-stable configuration is more sensitive to parameter variations. The stability state region demonstrates that the developed apparatus possesses a large parameter tuning space.

Secondly, A multi-stable hybrid energy harvester (MSHEH) combining a PEH and an electromagnetic energy harvester (EMEH) is developed. The MSHEH incorporates a novel coil arrangement in the EMEH to enhance power output. The EMEH transduction factor is calculated numerically and validated experimentally. The magnetic restoring force is

modelled via a 2-point dipole approach, and the accuracy of the model is further improved by the genetic algorithm identification approach. This refined model was used to map the stability state region Performance evaluations under high and low excitation levels demonstrated configuration-dependent advantages: the tri-stable state achieved the widest bandwidth (2.36 Hz) and highest total harvested energy (3.86 J) under high excitation, while the bi-stable state outperformed others in low excitation with an effective bandwidth of 2.65 Hz and 9.35×10<sup>-2</sup> J accumulated energy, primarily due to the EMEH's power peaks near side equilibria. In addition, Pareto front optimization is conducted to determine the optimal load resistances for both transducers, showing dependence on the amplitude and frequency of the excitation.

Thirdly, A systematic design procedure for a PLS to emulate an essentially nonlinear stiffness (ENS) is proposed. The PLS consists of a cantilever beam constrained by either single- or double-stop blocks (DBSs), which convert the beam into a fixed-pinned type with an overhang upon contact. The single-stop configuration is defined by two parameters (h and d), while the double-stop configuration requires four parameters  $(h_1, d_1, h_2)$  and  $(h_2, h_2)$ . The process begins with defining the desired ENS restoring force using the equivalent stiffness concept, which approximates a cubic nonlinearity. A least squares optimization is then used to obtain the optimal stiffness and switching positions for both PLS types. Finally, the geometric parameters are derived from the optimized values. Numerical analysis confirmed that the double-stop configuration provides a closer match to the desired restoring force and potential energy distribution, and produces smoother, longer instantaneous frequency (IF) transitions compared to the single-stop configuration. Experimental validation confirmed the static accuracy of the designed model and demonstrated dynamic force-displacement agreement within the achievable excitation range. A redesign with reduced displacement limit improved attainable IF range and restoring force coverage. Observed discrepancies in decay rates suggested variable damping and non-negligible impact effects, which warrant further investigation.

Finally, a magnetically enhanced piecewise linear NES (MPLNES) is developed. The MPLNES integrates a GMS and a grounded EMEH into a conventional PLNES with a

DBSs. Based on the theoretical foundation built in chapters 2 and 4, the PLS and GMS are designed to maintain mono-stable behaviour while enhancing the essential nonlinearity of the NES. COMSOL simulation is used to model the position-dependent EMEH transduction factor, with experimental verification confirming accuracy. Comparative studies against a conventional PLNES show that the MPLNES requires a lower energy threshold to trigger TET, achieving more robust VS and EH performance over varying excitation levels. This advantage arises from the GMS, which introduces a positiondependent restoring force that dynamically shifts the NES's equilibrium position in response to the primary mass motion. This unique feature amplifies the relative displacement under low initial energy, promoting earlier activation of the nonlinear regime and thus reducing the TET threshold. To balance VS and EH performance, a multiobjective optimization was carried out across three configurations: PLNES, MPLNES, and MPLNES without DSBs. The results showed that: (1) MPLNES offers the best trade-off between VS and EH and remains robust over varying energy levels; (2) optimal load resistance tends to decrease with higher initial energy; and (3) removing DSBs significantly reduces system efficiency, highlighting the essential role of the PLS-induced hardening effect. Experimental results matched simulations and confirmed efficient dual-function operation even at low excitation levels, with impact damping from double stops contributing to slightly faster decay.

#### 6.2 Recommendations for Future Work

The research objectives set out in this thesis have been successfully achieved. Building upon these results, several directions for future investigation are proposed:

1. The current modelling for the MPLNES does not explicitly account for impact dynamics, which may be the reason for the discrepancy between the simulated responses and the experimental responses in terms of decay rate. Future work could consider energy dissipation due to impact to improve model accuracy. Additionally, material selection and structural adjustments could be explored to better control or utilize impact-induced damping for enhanced energy transfer.

- 2. The current analysis for the MPLNES only focuses on transient responses. Future studies could evaluate its performance under harmonic excitation. Additionally, More realistic excitations, such as colored noise excitation, could be considered to provide deeper insight into its practical performance in real-world environments.
- 3. The proposed MPLNES belongs to the mono-stable nonlinear system. Since the GMS is tunable, the bi-stable or tri-stable configuration could also be investigated to explore its potential. Such studies could further elucidate the role of multi-stability in optimizing performance, enhancing robustness, or enabling adaptive behaviour under varying excitation conditions.
- 4. Since the present analysis primarily compares the EH performance of the MPLNES and PLNES, a basic resistive load is adopted for simplicity. Future work could incorporate rectifier circuits and energy storage modules to regulate and store harvested power, enabling direct use by low-power sensors or control electronics. Application-specific prototypes could be developed and demonstrated in real-world scenarios, such as building health monitoring.

## **Appendices**

Appendix A. A Grounded and Tunable Multi-Stable Nonlinear

**Energy Sink: Transient Responses** 

#### A.1 Introduction

Vibration widely exists in machines and civil structures. Such ambient vibration may be caused by wind, operation of the machine or human activity. A vibration energy harvester (VEH) is a device that converts mechanical motion to electricity, which can solve the battery changing issue for the wireless sensor network.

A traditional VEH consists of a linear oscillator that operates in a narrow frequency bandwidth. In order to widen the bandwidth, various nonlinear VEHs have been proposed [1]. According to the system stability, the nonlinear VEHs can be classified as mono-stable and multi-stable such as bi-stable or tri-stable. A piezoelectric vibration energy harvester (PVEH) reported in [2] consists of a piezoelectric cantilever beam with a tip magnet subjected to an external magnetic field generated by a pair of fixed magnets. Such a monostable system can exhibit softening or hardening behaviors when the magnetic interaction is adjusted. By applying different external magnet tuning strategies, a bi-stable energy harvester (BEH) can be achieved. As shown in [3], the BEH can enhance the power output performance. Further, tri-stable energy harvesters (TEHs) have been proposed in order to reduce the depth of the BEH's potential wells. Based on the configuration of the BEH in [3], a TEH was achieved by tuning the angular orientations [4] or the spatial positions [5] of the fixed magnets. The studies showed that the optimally designed TEHs outperform the BEHs in terms of the voltage output.

On the other hand, vibration that exists in machines and civil structure is harmful, and it may cause resonance and even failure of the system. A vibration absorber is a device used to suppress the vibration of the primary system. A traditional linear vibration absorber mainly operates in the narrow frequency bandwidth. The nonlinear energy sink (NES) was proposed for the purpose of achieving wideband vibration suppression (VS). The NES consists of a small mass and essential nonlinear spring so that it can be weakly coupled with the primary system. The NES possesses some unique features such as target energy transfer (TET) and strongly modulate resonance (SMR) which can significantly enhance the vibration suppression performance. For the past two decades, various kinds of NES have been proposed by researchers, such as rotational NES [6], mono-stable NES (MNES) [7] and multi-stable NES such as bi-stable NES (BNES) [8, 9] and tri-stable NES (TNES) [10]. The study has shown that the multi-stable NES can achieve highly efficient TET in a wider band.

Since the 2-degree-of-freedom PVEH and NES share a similar structure, it is much desirable to achieve VS and energy harvesting (EH) simultaneously by a well-designed NES. An MNES based PVEH has been proposed in [11]. The apparatus possesses the characteristics of the 1:1 resonance TET and initial energy dependence. The study shows a significant VS effect and the broadband voltage output can also be achieved. The study reported in [12] proposed a PVEH with BNES. The VS and EH performance of the proposed PVEH is compared with that of a linear absorber under the impact excitation. Besides, a tuned BNES was proposed in [13] to further improve the VS and EH performances.

So far, the proposed MNESs and multi-stable NESs that can achieve VS and EH simultaneously are considered to be ungrounded as the nonlinear spring is connected between the NES mass and the primary mass. In this study, a grounded PVEH with a tunable multi-stable NES is proposed. The proposed NES consists of one stationary magnet and a cantilever beam whose free end is attached by a moveable assembly of two magnets and one tip magnet. By varying the gap between the stationary magnet and the tip magnet, and the distance between the magnet assembly and the tip magnet, the NES can assume three states: mono-stable, bi-stable or tri-stable. The rest of the chapter is organized as follows: Section 2 presents the proposed apparatus, and derives the electromechanical

model based on the lumped parameter model of the system, and then the magnetic force model is derived according to the magnetic dipole approach. Section 3 evaluates the performance under the transient responses by conducting the numerical simulation. Section 4 draws the main conclusions of the study.

## A.2 The Apparatus and Electromechanical Model

Figure A.1(a) shows a CAD drawing of the apparatus developed for this study. The primary system consists of a top block and base block which are connected by four stainless-steel beams. The proposed tunable multi-stable NES comprises a cantilever beam attached with a tip magnet and a movable assembly of 2 magnets. The cantilever beam is composed of a unimorph piezoelectric transducer (S128-J1FR-1808YB, Midé Corporation) and a stainless-steel beam. One end of the cantilever beam is clamped to the top block while its other end is attached with a small cylindrical magnet B and a holder for two identical cylindrical magnets A and C. The holder for magnets A and C can slide along the beam. A large cylindrical magnet D is fixed in a holder that can slide vertically inside a stand fastened to the base block. When the primary beams and the cantilever beam are at their equilibrium position or undeflected, the four magnets are situated on the same vertical plane and magnets B and D are colinear. By sliding the holder of magnet D, the distance between magnet B and magnet D can be adjusted. Figure A.1(b) shows the lumped parameter model of the proposed apparatus, where x and  $x_a$  represent the displacement of the primary mass and NES mass, respectively, the magnetic interaction is considered as a nonlinear spring with the nonlinear stiffness  $k_n$ . The equations governing the dynamics of the system can be represented by:

$$m\ddot{x} + c\dot{x} + kx - (c_a\dot{u} + k_au + \theta v) = 0 \tag{A.1}$$

$$m_a \ddot{x}_a + (c_a \dot{u} + k_a u + \theta v) - f_n = 0 \tag{A.2}$$

$$c_p \dot{v} + \frac{v}{R_t} - \theta \dot{u} = 0 \tag{A.3}$$

where m, c, and k are the mass, damping coefficient and stiffness of the primary system, respectively;  $m_a$ ,  $c_a$  and  $k_a$  is the mass, damping coefficient and stiffness of the NES system, respectively;  $\theta$  is the electromechanical coupling coefficient of the PEH,  $f_n$  denotes the nonlinear magnetic force applied to the NES mass,  $R_l$  is the load resistance,  $c_p$  is the capacitance of the PEH, and  $u = x_a - x$  represents the relative displacement between the primary mass and the NES mass.

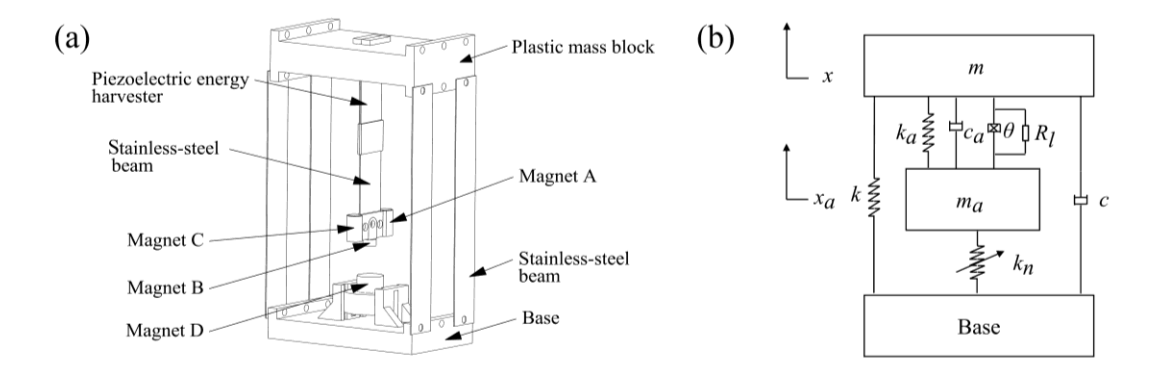


Figure A.1(a) 3D CAD drawing of a primary system attached by a tunable multistable NES, (b) lumped parameter model.

Figure A.2 illustrates two symmetric situations of the deformed cantilever beam as the primary mass moves identically to the negative or the positive position on X-axis where O' represents the middle point of the fixed end of the cantilever beam. And the central axis of the cantilever beam will always be on plane XZ. The figure also depicts the spatial positions and polarities of the four magnets where  $m_A$ ,  $m_B$ ,  $m_C$ ,  $m_D$  are the magnetic moment vectors, A, B, C and D are the center positions of magnets,  $r_{DA}$  represents a vector from A to D,  $r_{DB}$  represents a vector from B to D, and vector  $r_{DA}$ 's projection on the x-z plane is represented by  $r_{DAxz}$ . Note that the direction of  $m_B$  is opposite to that of  $m_A$ ,  $m_C$  and  $m_D$ .

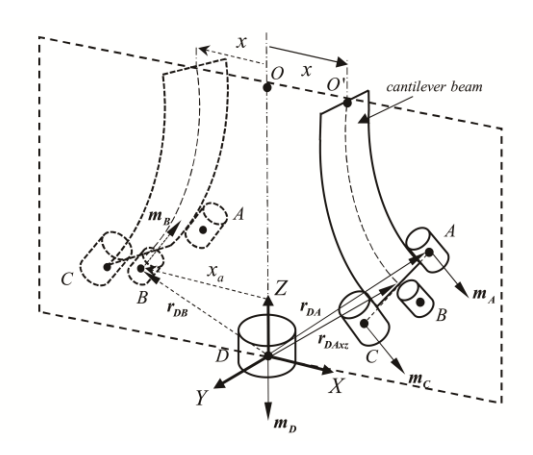


Figure A.2 Spatial positions of the magnets.

The total nonlinear magnetic force  $f_n$  in the x-direction consists of an attractive magnetic force  $f_{DBx}$  between magnet D and magnet B, and two repulsive magnetic forces:  $f_{DAx}$  between magnet D and magnet A and  $f_{DCx}$  between magnet D and magnet C. Since magnets A and C are identical and symmetrical about the central line of the beam, the values of  $f_{DAx}$  and  $f_{DCx}$  are equal. Then the total nonlinear magnetic force can be expressed as:

$$f_n = f_{DBx} + f_{DAx} + f_{DCx} = f_{DBx} + 2f_{DAx}.$$
 (A.4)

Figure A.3(a) shows the side view of Figure A.2 when the cantilever beam is undeformed, where d is the vertical distance between magnet D and magnet B, h is the gap between the center of magnet A or C and the center of magnet B, l is the length of the cantilever beam, and w is the distance between the axis of magnet B and that of magnet A or C. Figure A.2(b) shows the front view of Figure A.2 when the cantilever beam is deformed to the right side and the primary mass's displacement x is positive, where  $\alpha$  is the angle between  $m_B$  and  $m_D$ , and  $\beta$  is the supplement of the angle between  $m_D$  and  $r_{DB}$ , r and r are the transverse and longitudinal displacements of the center of magnet B, respectively.

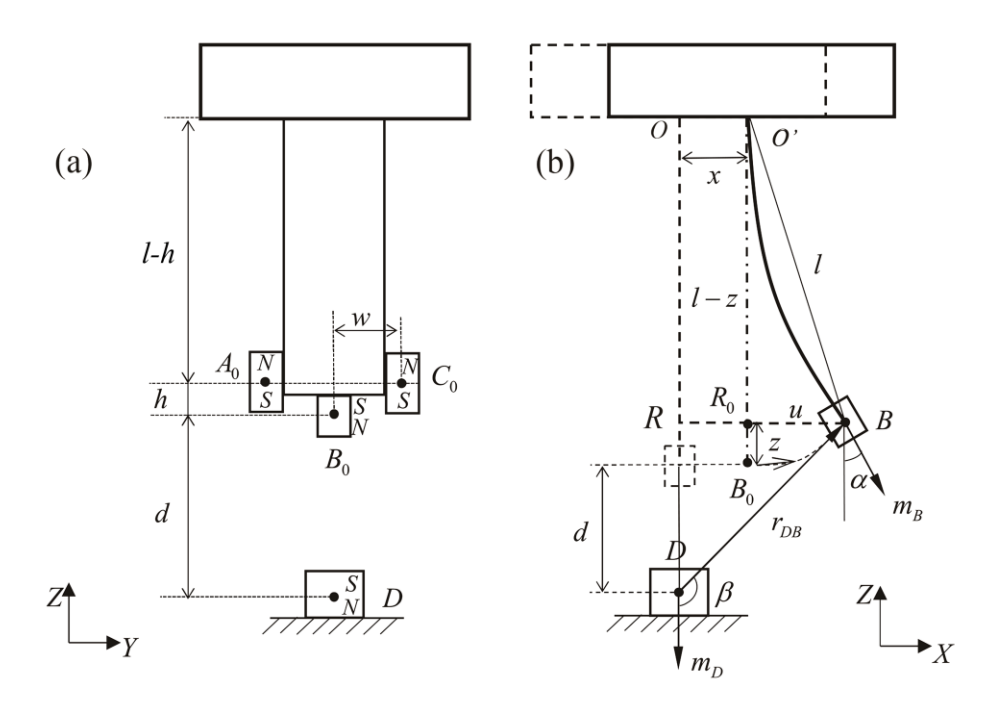


Figure A.3(a) Side view and (b) front view of the apparatus.

In this paper, the magnetic dipole approach [14] is used to determine the magnetic force between two magnets. Firstly, the magnetic force between magnet D and magnet B is considered. According to the dipole assumption, the force exerted by magnet D on magnet B is given by:

$$\boldsymbol{f}_{DB} = \nabla \left( \boldsymbol{B}_{DB} \cdot \boldsymbol{m}_{B} \right) \tag{A.5}$$

where  $B_{DB}$  is the magnetic flux density generated by magnet D upon B. Equation. (A.5) can be expanded as:

$$\boldsymbol{f}_{DB} = \frac{3\mu_0 m_D m_B}{4\pi r_{DB}^4} \left[ \hat{\boldsymbol{r}}_{DB} \left( \hat{\boldsymbol{m}}_B \cdot \hat{\boldsymbol{m}}_D \right) - 5\hat{\boldsymbol{r}}_{DB} \left( \hat{\boldsymbol{m}}_D \cdot \hat{\boldsymbol{r}}_{DB} \right) \left( \hat{\boldsymbol{r}}_{DB} \cdot \hat{\boldsymbol{m}}_B \right) + \hat{\boldsymbol{m}}_B \left( \hat{\boldsymbol{m}}_D \cdot \hat{\boldsymbol{r}}_{DB} \right) + \hat{\boldsymbol{m}}_D \left( \hat{\boldsymbol{m}}_B \cdot \hat{\boldsymbol{r}}_{DB} \right) \right] (A.6)$$

where  $m_B$ ,  $m_D$ , and  $r_{BD}$  are the magnitude of  $m_B$ ,  $m_D$ , and  $r_{DB}$ , respectively;  $\hat{m}_B$ ,  $\hat{m}_D$ , and  $\hat{r}_{BD}$  are the unit vector of  $m_B$ ,  $m_D$ , and  $r_{DB}$ , respectively. These unit vectors can be expressed as:

$$\hat{\boldsymbol{m}}_{B} = [\sin(\alpha) - \cos(\beta) \ 0], \ \hat{\boldsymbol{m}}_{D} = [0 \ -1 \ 0],$$

$$\hat{\boldsymbol{r}}_{DB} = [-\sin(\beta) \cos(\beta) \ 0].$$
(A.7)

Substituting the above unit vectors in the dot products of Eq. (A.6) and the magnetic force in the x-direction can be obtained in the following form:

$$f_{DBx} = -\frac{3\mu_0 m_D m_B}{4\pi r_{BD}^4} \left\{ \sin(\beta) \left[ \cos(\alpha) - 5\cos(\beta)\cos(\beta - \alpha) \right] + \sin(\alpha)\cos(\beta) \right\}.$$
 (A.8)

Since the slope of the beam's tip is relatively small, it is assumed that  $\angle BOB_0 \approx \alpha$ . Also, it is noted that  $\beta$  can be found from the triangle DRB in Figure A.3(b). The trigonometric relationship in Eq. (A.8) can be expressed as follows:

$$\sin(\alpha) = \frac{u}{l}; \cos(\alpha) = \frac{l-z}{l}; \tag{A.9}$$

$$\sin(\beta) = \frac{x_a}{r_{DB}}; \cos(\beta) = -\frac{z+d}{r_{DB}}; \tag{A.10}$$

$$\cos(\beta - \alpha) = \cos(\alpha)\cos(\beta) + \sin(\alpha)\sin(\beta)$$

$$= \frac{l - z}{l} \left( -\frac{z + d}{r_{DR}} \right) + \frac{x_a}{r_{DR}} \frac{x_a}{l} = \frac{x_a^2 - lz - ld + zd + z^2}{lr_{DR}}.$$
(A.11)

where  $z = l - \sqrt{l^2 - u^2}$ . Substituting the above expressions into (A.8) yields

$$f_{DBx} = -\frac{3\mu_0 m_D m_B}{4\pi r_{DB}^5} \left\{ x_a (l-z) - u(d+z) - \frac{5}{r_{DB}^2} \left[ -z^3 + (l-2d)z^2 + (2dl - ux_a - d^2)z + d^2l - ux_a d \right] \right\}$$
(A.12)

Similarly, the magnetic force between magnet A and magnet D in the *x*-direction can be found as:

$$f_{DAx} = \frac{3\mu_0 m_D m_A}{4\pi r_{0A}^4} \left\{ \frac{x_a (l-z) - u(d+z)}{r_{DAx}} - \frac{5}{r_{DAx}^3} \left[ -z^3 + (l-2d_0)z^2 + (2d_0l - ux_a - d_0^2)z + d_0^2l - ux_a d \right] \right\}$$
(A.13)

where  $d_0=d+h$ . Substituting Eqs. (A.12) and (A.13) into Eq. (A.4), then the nonlinear magnetic force model can be obtained. All the parameters' values are listed in Table A.1.

Note that the amplitudes of magnetic moment vectors for magnets A, B, C and D are obtained by an experimental identification given in [15]. For the sake of comparison, there are three configurations of the NESs are considered in this study: MNES d=0.0487 m, h=0.0187 m; BNES d=0.0467 m, h=0.0157 m; TNES d=0.0367 m, h=0.0197 m. The potential energy of the NES can be obtained by taking the integral of the total restoring force of the NES  $f_a$  which can be expressed as follows:

$$f_a = k_a \left( x_a - x \right) - f_n \tag{A.14}$$

Note that the total restoring force is related to three factors: the displacement of the primary system x; the displacement of NES  $x_a$ ; and the magnetic force  $f_n$ . In other words, the position of the primary system will affect the potential energy of the NES. Figures A.4(a) (b) and (c) show the potential energy verse  $x_a$  of the MNES, BNES and TNES for three different values of x. It can be observed that the NESs are in symmetrical mono-stable, bistable and tri-stable stability states when x=0, and they become asymmetric mono-stable, bi-stable and tri-stable systems as the absolute value of x increases to 0.003 m. It should be mentioned that Figure A.4 only shows the local potential of the grounded NESs. It cannot tell where the NESs will finally rest according to the local potentials. To get the global potentials of the grounded NES systems, the equilibrium positions of the primary systems that they are attached to need to be considered. The primary systems with the grounded MNES, BNES and TNES will have multiple equilibrium positions due to the changing elastic forces induced by the NESs. And the equilibrium position of the primary system  $x_e$  fulfills the following condition:

$$kx_e = k_a(x_{ae} - x_e) \tag{A.15}$$

where  $x_{ae}$  is the equilibrium position of the NES. Accordingly, the global potential of the grounded NESs can be determined, which can tell the positions that the primary system and the NES will finally rest.

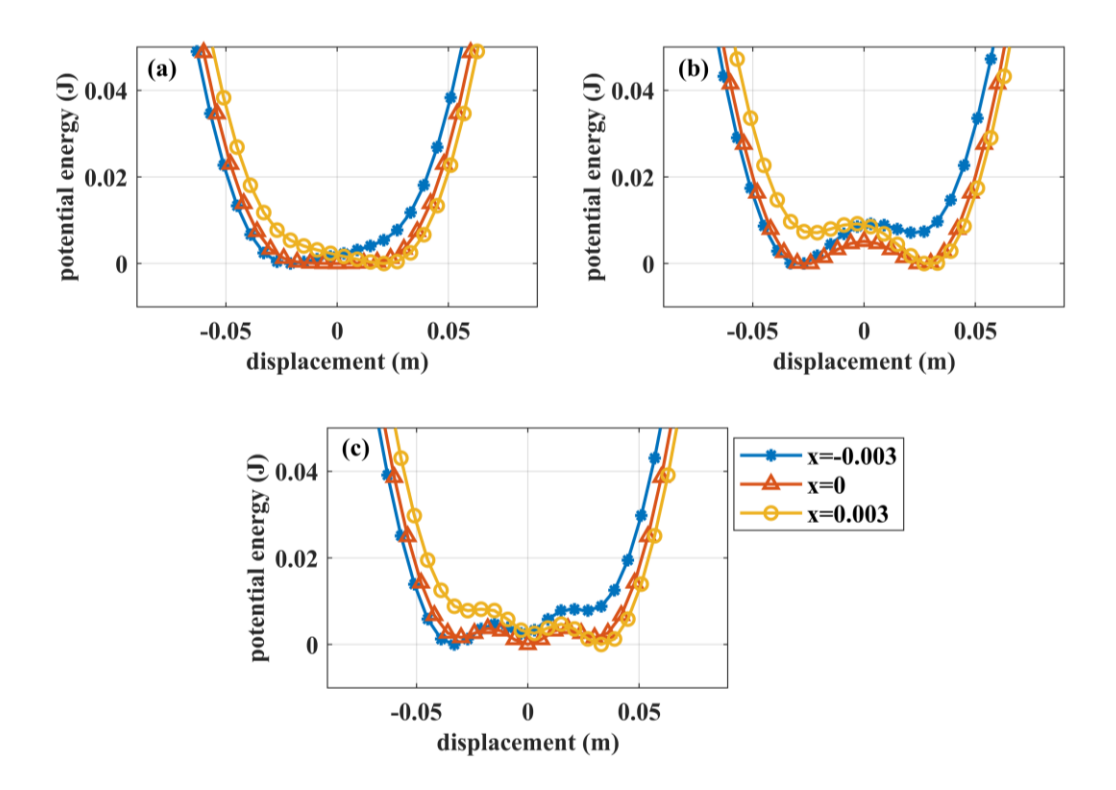


Figure A.4 The potential energy of the different NESs verse  $x_a$  when varying x: (a) MNES; (b) BNES; (c)TNES.

#### A.3 Numerical Simulation

To compare the VS and EH performance of the system with the MNES BNES and TNES, a series of simulations to get their transient responses is conducted. In the simulation, the impulsive force  $f_p(t)$  which is applied to the primary system is a half-sine signal with amplitude A and period T:

$$f_p(t) = \begin{cases} A\sin\left(\frac{2\pi t}{T}\right), & 0 < t < \frac{T}{2} \\ 0, & t \ge \frac{T}{2} \end{cases}$$
(A.16)

where the period T=0.3 s. Two initial energy levels are considered in the simulations: the low initial energy level (A=1.2 N) and high initial energy level (A=8 N). In this case, the

electromechanical equations of the system Eqs. (A.1) - (A.3) can be rewritten as follows:

$$m\ddot{x} + c\dot{x} + kx - (c_a\dot{u} + k_au + \theta v) = f_n(t) \tag{A.17}$$

$$m_a \ddot{x}_a + (c_a \dot{u} + k_a u + \theta v) - f_n = 0 \tag{A.18}$$

$$c_p \dot{v} + \frac{v}{R_l} - \theta \dot{u} = 0. \tag{A.19}$$

The values of the parameters in the above equations are listed in Table A.1. By solving Eqs. (A.17) - (A.19) with the zero initial condition for the system with the TNES, and the initial conditions of  $(x, \dot{x}, x_a, \dot{x}_a, v) = (0.003, 0, 0.022, 0, 0)$  and (0.004, 0, 0.031, 0, 0) for the systems with the MNES and BNES, respectively, in the period of 20 s using the MATLAB ODE45 solver, the transient responses of the primary system, NES and load voltage can be obtained. Besides, the EH performance is evaluated by the accumulated energy in NES E, which is defined as follows:

$$E(t) = \int_0^t \frac{v(t)^2}{R_t} dt \tag{A.20}$$

where t is the duration of the simulation, v is the load voltage and  $R_l$  represents the resistance of the load resistor.

Table A.1 Parameters value of the apparatus.

gymh al	Parameters		
symbol	Parameter name	value	
$\mu_0$	Vacuum permeability	4π×10 <sup>-7</sup>	
$m_A$ ,	Magnitudes of magnetic moment vector of magnet A and C	4.30	
$m_C$	(H.m/T)		
$m_B$	Magnitude of magnetic moment vector of magnet B (H.m/T)	0.83	
$m_D$	Magnitude of magnetic moment vector of magnet D (H.m/T)	18.00	
14)	Distance between the axis of magnet B and magnet A or C	0.025	
W	(m)		
$k_a$	Stiffness of the cantilever beam (N/m)	47.39	
l	Length of the cantilever beam (m)	0.12	
k	Stiffness of the primary system (N/m)	189	
m	Mass of the primary system(kg)	0.44	
$m_a$	Mass of the NES (kg)	0.066	
С	Damping coefficient of the primary system (Ns/m)	0.125	
$c_a$	Daping coefficient of the NES (Ns/m)	0.067	
θ	Electromechanical coupling coefficient of the piezoelectric	1.88×10 <sup>-4</sup>	
U	transducer (N/V)		
$R_{I}$	Load resistance (ohm)	5×10 <sup>6</sup>	

When the amplitude of the impulsive force A=1.2 N, the time responses of the displacements of the primary systems with locked NES, MNES, BNES and TNES, and the displacements of the MNES, BNES and TNES are shown in Figure A.5. Note that to conduct the simulation of the system with a locked NES is by solving Eq. (A.17) with the primary mass equal to  $m+m_a$ , and setting u and v to zero. Figure A.5 shows that the MNES performs the snap-through motion between its equilibrium positions initially, and it dissipates the impulse energy rapidly within 11.8 s to decrease the initial amplitude of the primary system to 4%. By contrast, it takes 13.24 s and 19.5 s for the systems with the BNES and TNES to dissipate the initial amplitude to 4%. And it also can be seen that the BNES and TNES are only oscillating in one of their potential wells.

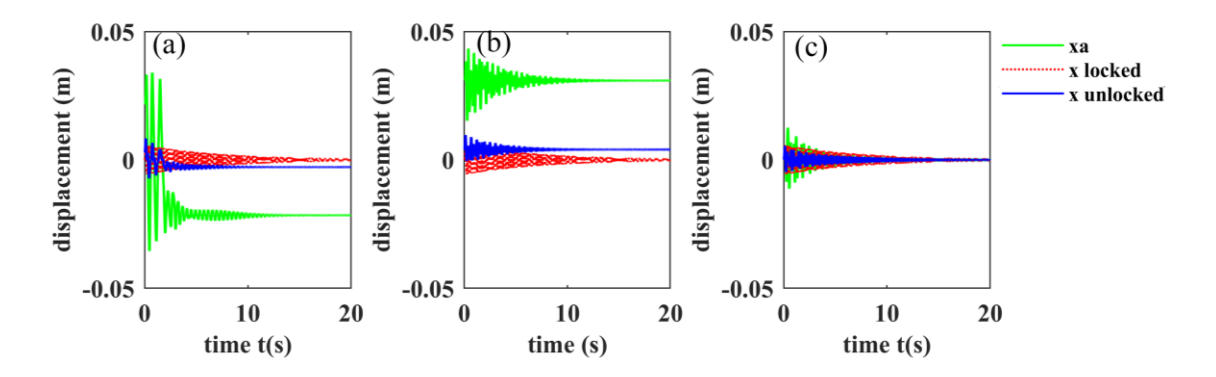


Figure A.5 Transient responses of the systems with four different NESs when A=1.2 N, red dash line and blue solid for the displacement of primary mass with locked and unlocked NES, green solid line for the NES's displacement: (a) MNES; (b) BNES; (c) TNES.

Figures A.6(a)-(c) show the wavelet transform (WT) spectra of the displacements of the primary systems with the MNES, BNES and TNES, and the WT spectra of the displacements for their corresponding NESs are shown in Figures A.6(d)-(f). It can be seen in Figures A.6(a) and (d) that the 1:1 internal resonance occurs between the MNES and the primary system when the MNES performs the snap-through motion at the first 1.5 s. As shown in Figures A.6(b) and (e), although the 1:1 resonance phenomenon occurs in the system with the BNES initially. However, the nonlinearity does not activate due to the BNES only oscillating in the single stability potential well. Figures A.6(c) and (f) show the primary system and TNES oscillates at their own natural frequencies, which means the TET does not occur.

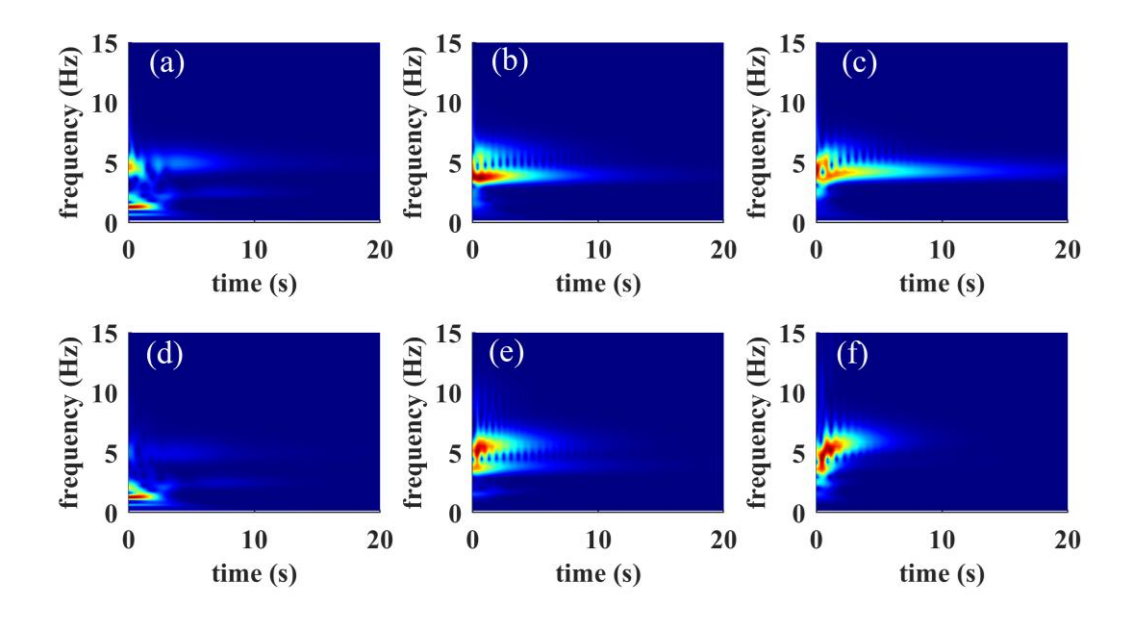


Figure A.6 WT spectra of the transient responses of the systems with four different NESs when A=1.2 N, upper plots for the primary displacements and lower plots for the NES displacements: (a)(d) MNES; (b)(e) BNES; (c)(f) TNES.

Figure A.7 shows the accumulated energy for systems with different NESs under the low-level impact excitation. It shows that the system with the MNES is the most efficient in EH. Due to MNES performing the snap-through movement at the beginning, the accumulated energy of MNES shows a rapid rise initially and then stops at 0.52 mJ. By contrast, the systems with BNES and TNES are far less efficient in EH with merely 0.06mJ and 0.04mJ total accumulated energy, respectively.

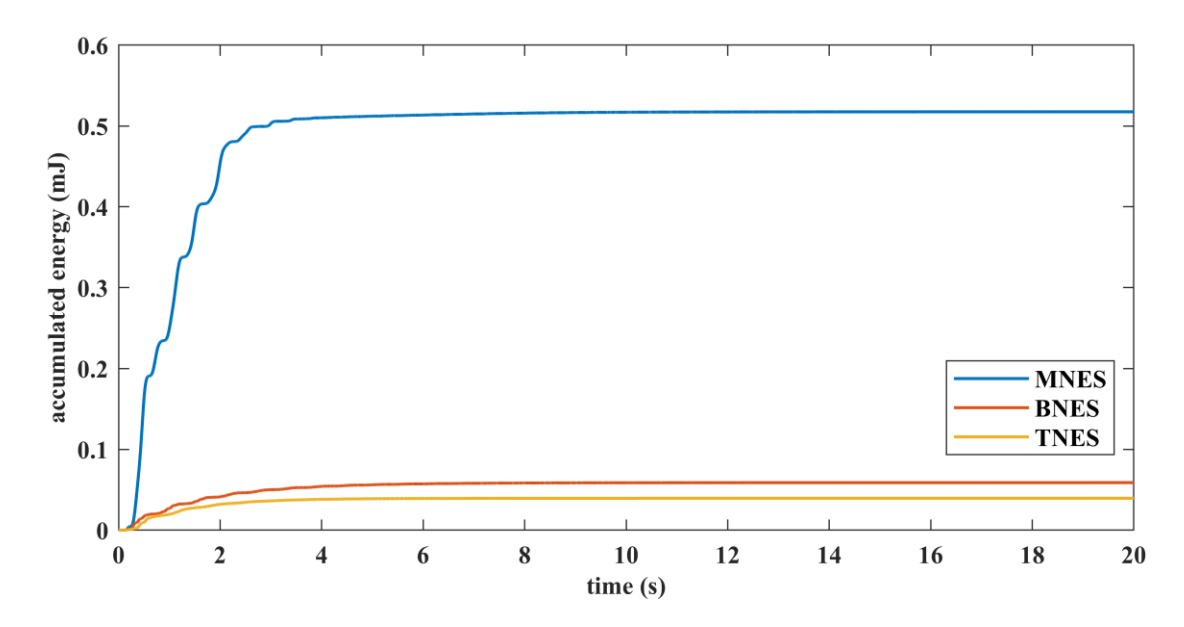


Figure A.7 Accumulated energy of the systems with different NESs when A=1.2 N.

For the case of the system under the high-level impact excitation, The time responses of the displacements of the primary systems with the locked NES, MNES, BNES and TNES, and the displacements of the corresponding NESs are shown in Figure A.8. As shown the system with the MNES, BNES and TNES perform the snap-through motion initially and then rest in one of their equilibrium positions. The VS effect can be clearly observed from the transient responses of the three systems. It takes 14.04 s, 9.55 s and 13.58 s to decrease the initial amplitude to 4% for systems with the MNES, BNES and TNES, respectively. Thus, the system with the BNES is the most efficient in VS among the three systems.

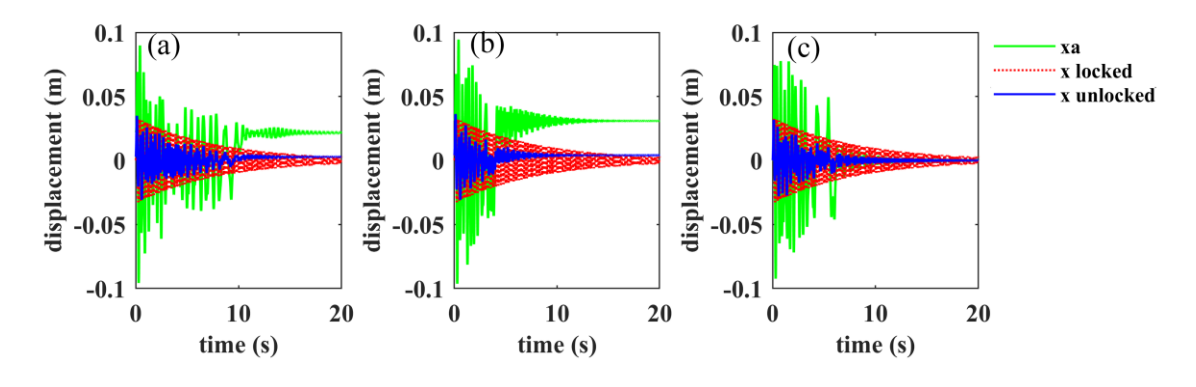


Figure A.8 Transient responses of the systems with four different NESs when A=8 N,

red dash line and blue solid for the displacement of primary mass with locked and unlocked NES, green solid line for the NES's displacement: (a) MNES; (b) BNES; (c) TNES.

Figures A.9(a)-(c) show the WT spectra of the displacements of the primary systems with the MNES, BNES and TNES, and the WT spectra of the displacements of their corresponding NESs are shown in Figures A.9(d)-(f). It can be observed in Figure 5.9 that the 1:1 resonance has been triggered and the TET has been established between the primary systems and NESs of the three systems. Taking the system with the BNES for example, it can be seen in Figures 5.9(b) and (e) that the dominant frequencies of the primary system and BNES are located around their natural frequencies, which indicates the TET occur. And such a phenomenon can also be observed in the other two systems.

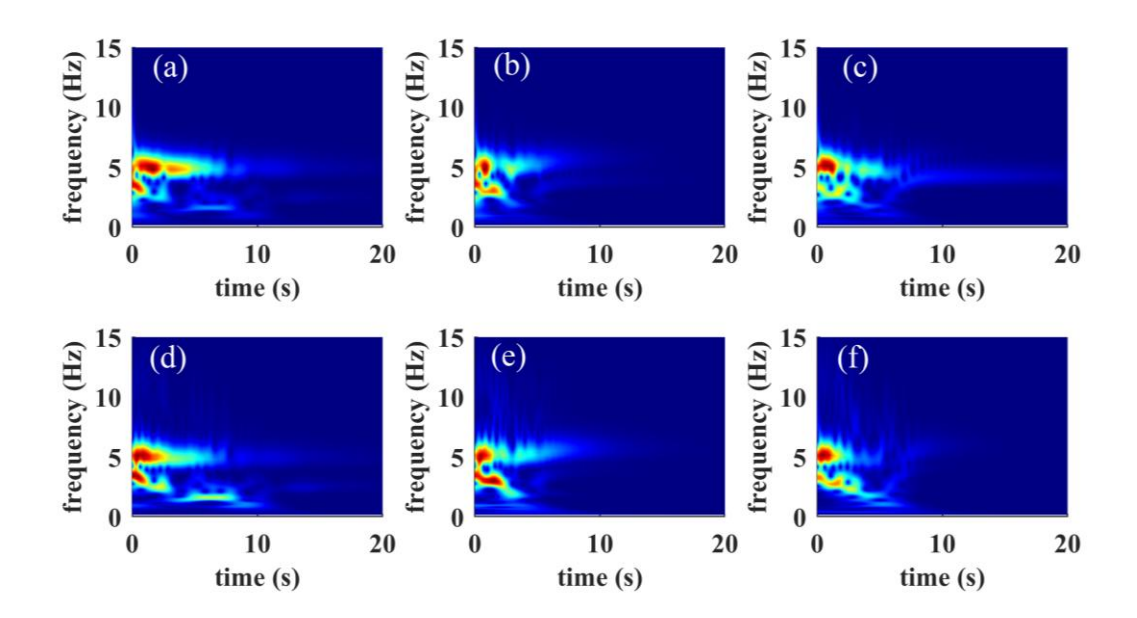


Figure A.9 WT spectra of the transient responses of the systems with four different NESs when A=8 N, upper plots for the primary systems' displacements and lower plots for the NESs' displacements: (a)(d) MNES; (b)(e) BNES; (c)(f) TNES.

Figure 5.10 shows the accumulated energy for the systems with different NESs under the high-level impact excitation. It depicts that the system with the MNES is the most efficient in EH with 4.55 mJ of total accumulating energy. And the total accumulated

energy for the systems with the BNES and TNES is 3.97 mJ and 4.45 mJ, respectively. The arrows A, B and C in Figure 5.10 point out the end of the rapid increase period of the accumulated energy, which is at 10.37 s, 4.52 s and 6.06 s for the systems with the MNES, BNES and TNES, respectively. It can be found that the system with the TNES has better EH performance than the systems with the BNES and MNES at the first 9 s since it has larger separation distances between its two side potential wells. After that, the system with the MNES outperforms in EH since it lasts longer to perform in the snap-through movement.

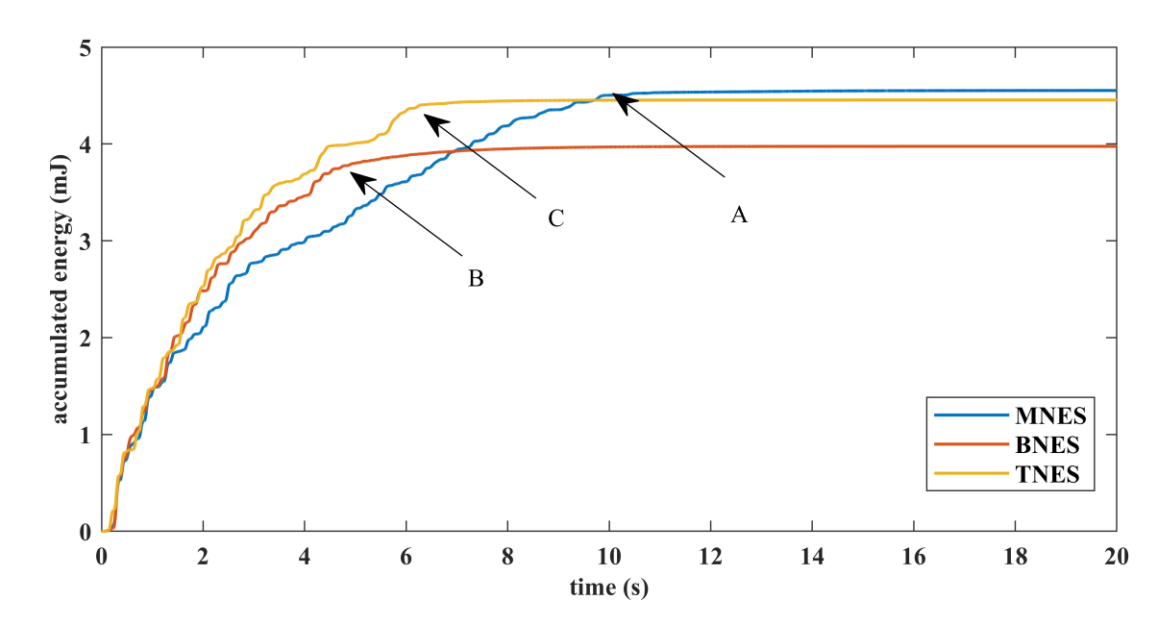


Figure A.10 Accumulated energy of the systems with different NESs when A=8 N.

### A.4 Conclusions

In this study, a PVEH with a grounded multi-stable NES has been developed. The NES can be manually tuned to achieve three different stability states referred to as MNES, BNES, and TNES, respectively. The electromechanical model of the system is derived from the lumped parameter model, and the magnetic force model is established based on the magnetic dipole approach. The simulation is conducted to investigate the VS and EH performances of the systems with MNES, BNES and TNES under the low and high-level impact excitation. The results depict that under the low-level impact excitation, the system

with the MNES has the lowest energy threshold to engage the high-efficiency TET. Thus, it outperforms in VS among the three systems, and it also has a better performance in EH due to its low energy threshold to operate in the snap-through oscillation. When the initial energy level is high enough, the MNES, BNES and TNES can both perform the snap-through motion initially. In this case, the system with the BNES has better VS performance among the three systems. On the other hand, the systems with the BNES and TNES perform better in EH initially since they have larger separation distances between their two side potential wells. However, the system with the MNES can harvest more energy eventually because it lasts longer to perform the snap-through motion.

### References

- [1] Z. Yang, S. Zhou, J. Zu, and D. Inman, "High-Performance Piezoelectric Energy Harvesters and Their Applications," *Joule*, vol. 2, no. 4, pp. 642-697, 2018, doi: 10.1016/j.joule.2018.03.011.
- [2] S. C. Stanton, C. C. McGehee, and B. P. Mann, "Reversible hysteresis for broadband magnetopiezoelastic energy harvesting," *Applied Physics Letters*, vol. 95, no. 17, 2009, doi: 10.1063/1.3253710.
- [3] A. Erturk, J. Hoffmann, and D. J. Inman, "A piezomagnetoelastic structure for broadband vibration energy harvesting," *Applied Physics Letters*, vol. 94, no. 25, 2009, doi: 10.1063/1.3159815.
- [4] J. Cao, S. Zhou, W. Wang, and J. Lin, "Influence of potential well depth on nonlinear tristable energy harvesting," *Applied Physics Letters*, vol. 106, no. 17, p. 173903, 2015, doi: 10.1063/1.4919532.
- [5] L. Haitao, Q. Weiyang, L. Chunbo, D. Wangzheng, and Z. Zhiyong, "Dynamics and coherence resonance of tri-stable energy harvesting system," *Smart Materials and Structures*, vol. 25, no. 1, p. 015001, 2016, doi: 10.1088/0964-1726/25/1/015001.
- [6] A. S. Saeed, M. A. Al-Shudeifat, and A. F. Vakakis, "Rotary-oscillatory nonlinear energy sink of robust performance," *International Journal of Non-Linear Mechanics*, vol. 117, 2019, doi: 10.1016/j.ijnonlinmec.2019.103249.
- [7] Z. Zhang, Z.-Q. Lu, H. Ding, and L.-Q. Chen, "An inertial nonlinear energy sink," *Journal of Sound and Vibration*, vol. 450, pp. 199-213, 2019/06/23/ 2019, doi: https://doi.org/10.1016/j.jsv.2019.03.014.

- [8] G. Habib and F. Romeo, "The tuned bistable nonlinear energy sink," *Nonlinear Dynamics*, vol. 89, no. 1, pp. 179-196, 2017, doi: 10.1007/s11071-017-3444-y.
- [9] D. Qiu, T. Li, S. Seguy, and M. Paredes, "Efficient targeted energy transfer of bistable nonlinear energy sink: application to optimal design," *Nonlinear Dynamics*, vol. 92, no. 2, pp. 443-461, 2018, doi: 10.1007/s11071-018-4067-7.
- [10] H. Yao, Y. Cao, Y. Wang, and B. Wen, "A tri-stable nonlinear energy sink with piecewise stiffness," *Journal of Sound and Vibration*, vol. 463, 2019, doi: 10.1016/j.jsv.2019.114971.
- [11] Y. Zhang, L. Tang, and K. Liu, "Piezoelectric energy harvesting with a nonlinear energy sink," *Journal of Intelligent Material Systems and Structures*, vol. 28, no. 3, pp. 307-322, 2016, doi: 10.1177/1045389x16642301.
- [12] M. Rezaei, R. Talebitooti, and W.-H. Liao, "Exploiting bi-stable magneto-piezoelastic absorber for simultaneous energy harvesting and vibration mitigation," *International Journal of Mechanical Sciences*, vol. 207, p. 106618, 2021/10/01/ 2021, doi: https://doi.org/10.1016/j.ijmecsci.2021.106618.
- [13] S. Fang, K. Chen, J. Xing, S. Zhou, and W.-H. Liao, "Tuned bistable nonlinear energy sink for simultaneously improved vibration suppression and energy harvesting," *International Journal of Mechanical Sciences*, vol. 212, 2021, doi: 10.1016/j.ijmecsci.2021.106838.
- [14] K. W. Yung, P. B. Landecker, and D. D. Villani, "An analytic solution for the force between two magnetic dipoles," *Physical Separation in Science and Engineering*, vol. 9, no. 1, pp. 39-52, 1998.
- [15] H. Li, "A tunable multi-stable piezoelectric vibration energy harvester," Mechanical engineering, Lakehead University, published, 2021. [Online]. Available: https://knowledgecommons.lakeheadu.ca/handle/2453/4966

# Appendix B. Identification of The Restoring Force of A Grounded Nonlinear Energy Sink

### **B.1** Introduction

With the rapid evolution of Internet of Things (IoT) technology, the demand for a self-sustaining power source for wireless sensor networks has become increasingly critical. A vibration energy harvester (VEH) is a viable solution to address this need. Such a device can scavenge mechanical energy from ambient vibrations and converting it into electricity, offering a sustainable and efficient alternative to conventional power sources such as battery and wired power supply.

A traditional VEH consists of a linear oscillator that operates in a narrow frequency bandwidth. In order to widen the bandwidth, various nonlinear VEHs have been proposed [1]. According to the system stability, the nonlinear VEHs can be classified as mono-stable and multi-stable such as bi-stable or tri-stable. A VEH reported in [2] consists of a piezoelectric cantilever beam with a tip magnet subjected to an external magnetic field generated by a pair of fixed magnets. Such a mono-stable system can exhibit softening or hardening behaviors when the magnetic interaction is adjusted. By applying different external magnet tuning strategies, a bi-stable energy harvester (BEH) can be achieved. As shown in [3], the BEH can enhance the power output performance. Further, tri-stable energy harvesters (TEHs) have been proposed in order to reduce the depth of the BEH's potential wells. Based on the configuration of the BEH in [3], a TEH was achieved by tuning the angular orientations [4] or the spatial positions [5] of the fixed magnets. The studies showed that the optimally designed TEHs outperform the BEHs in terms of the voltage output.

On the other hand, vibrations present in machinery and civil structures can be detrimental, potentially leading to resonance and system failure. To counter this, the concept of a Nonlinear Energy Sink (NES) has been introduced for the purpose of

achieving wideband vibration suppression (VS) through the target energy transfer (TET) phenomenon. Various kinds of NES have been proposed by researchers, such as rotational NES [6], mono-stable NES (MNES) [7] and multi-stable NES such as bi-stable NES (BNES) [8, 9] and tri-stable NES (TNES) [10]. The study has shown that the multi-stable NES can achieve highly efficient TET in a wider band. In recent years, a NES is able to achieving VS and energy harvesting (EH) simultaneously has attracted the attention of many researchers [11]. An mono-stable NES(MNES) based VEH has been proposed in [12], the apparatus shows a significant VS effect and the broadband voltage output can also be achieved. In addition, a VEH with bi-stable NES(BNES) has been proposed in [13], the study shows the multiple stability bring benefits in both EH and VS performance.

In many cases, the complexity of the restoring force of the NES's spring makes it impossible to apply analytical methods such as harmonic balance method. Model interpretability is a concept employed in machine learning techniques. A polynomial is considered to be interpretable. It is desirable to use a polynomial to represent the restoring force of the NES's spring. Most existing studies have dealt with the identification of a polynomial of a single variable. The grounded NES under consideration of this study imposes a challenge as the restoring force of the magnetic spring employed is a function of two variables. Various approaches have been proposed to identify an interpretable model for a nonlinear dynamic system, such as nonparametric identification technique [14] and sparse identification method [15]. This study is focused on the linear regression based identification. The rest of the paper is organized as follows: Section II presents the apparatus used in this study, and its dynamic model, and the magnetic force model of the magnetic spring. Section III investigates the identification of a polynomial model for the restoring force using free responses of the system. Section IV draws the main conclusions of the study.

## B.2 Apparatus and Modelling

Figure B.1 shows a CAD drawing of the apparatus developed for the study of vibration suppression and energy harvesting. It consists of a primary system and a grounded NES.

The primary system is formed by using four stainless-steel beams referred to as primary beams to connect a primary block and a base block. The grounded NES comprises a cantilever beam attached with a tip magnet B and a movable assembly of 2 magnets A and C and a magnet D that is fixed in a holder that can slide vertically inside a stand fastened to the base block. The upper end of the cantilever beam is clamped to the primary block and a unimorph piezoelectric energy harvester (PEH) (S128-J1FR-1808YB, Midé Corporation) is glued to the beam as shown. When the primary beams and the cantilever beam are at their equilibrium position or undeflected, the four magnets are situated on the same vertical plane and magnets B and D are colinear. By sliding the holder of magnet D, the distance between magnet B and magnet D can be adjusted. By sliding the assembly of magnets A and C along the beam, the distance between A/C and B can be varied.

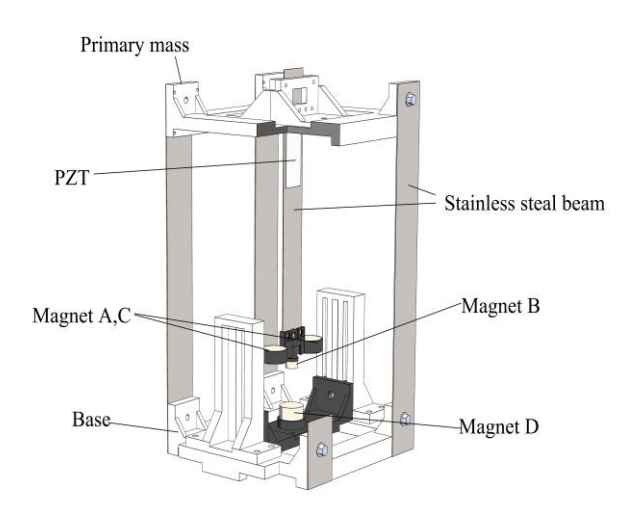


Figure B.11 3D CAD drawing of the apparatus

Figure B.2 shows the lumped parameter model of the apparatus, where  $x_p$  and  $x_a$  represent the displacement of the primary mass and NES mass, respectively, the magnetic interaction is considered as a nonlinear spring with the nonlinear stiffness  $k_n$ . Since the focus of this study is identification of the nonlinear restoring force, the model does not include the PEH. Based on the model, the equations of motion governing the system dynamics are defined as follows:

$$m_{p}\ddot{x}_{p} + c\dot{x}_{p} + kx_{p} - (c_{a}\dot{u} + k_{a}u) = 0$$
 (B.1)

$$m_a \ddot{x}_a + \left(c_a \dot{u} + k_a u\right) + f_n = 0 \tag{B.2}$$

where  $m_p$ ,  $c_p$  and  $k_p$  are the mass, damping coefficient and stiffness of the primary system, respectively;  $m_a$ ,  $c_a$  and  $k_a$  are the mass, damping coefficient, and stiffness of the NES system, respectively;  $f_n$  denotes the nonlinear magnetic force applied to the NES mass, and  $u = x_a - x_p$  represents the relative displacement between the primary mass and the NES mass.

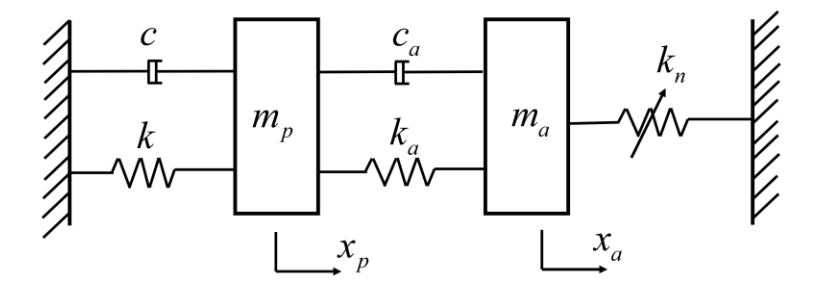


Figure B.12 Lumped parameter model of the apparatus.

The total nonlinear magnetic force  $f_n$  in the x-direction consists of an attractive magnetic force  $f_{DBx}$  between magnet D and magnet B, and two repulsive magnetic forces:  $f_{DAx}$  between magnet D and magnet A and  $f_{DCx}$  between magnet D and magnet C. Since magnets A and C are identical and symmetrical about the central line of the beam, the values of  $f_{DAx}$  and  $f_{DCx}$  are equal. Then, the total nonlinear magnetic force can be expressed as:

$$f_n = f_{DBx} + f_{DAx} + f_{DCx} = f_{DBx} + 2f_{DAx}.$$
 (B.3)

The magnetic restoring force can be found using the equivalent magnetic 2-point dipole model proposed in [16]. As shown in Figure B.3, O' represents the middle point of the fixed end of the cantilever beam. And O is the central point of the primary mass when it is at the zero position. the origin of the coordinate system is located at  $B_0$ , the centers of magnet A,

magnet B, and magnet D are represented by points A, B and D, respectively, points  $A_0$  and  $B_0$  depict the positions of magnets A and B when the beam is undeformed,  $l_B$ ,  $l_D$  and  $l_A$  are the length of magnet B, magnet D and magnet A, respectively, and h is the distance between magnet A/C and magnet B in the z-direction, l is the length of the cantilever beam,  $r_{15}$ ,  $r_{25}$ ,  $r_{35}$  and  $r_{45}$  are the vectors from  $Q_5$  to  $Q_1$ ,  $Q_2$ ,  $Q_3$  and  $Q_4$ , respectively, and  $r_{16}$ ,  $r_{26}$ ,  $r_{36}$  and  $r_{46}$  are the vectors from  $Q_6$  to  $Q_1$ ,  $Q_2$ ,  $Q_3$  and  $Q_4$  respectively,  $Q_1$  and  $Q_2$  are the total charges of the top and the bottom surfaces of magnet B, respectively,  $Q_3$  and  $Q_4$  are the total charges of the top and the bottom surfaces of magnet A, respectively,  $Q_5$  and  $Q_6$  are the total charges of the top and the bottom surfaces of magnet D, respectively. The total surface charges can be expressed as follows:

$$Q_1 = -MS_B$$
  $Q_2 = MS_B$   $Q_3 = MS_A$   $Q_4 = -MS_A$   $Q_5 = -MS_D$   $Q_6 = MS_D$  (B.4)

where  $S_A = 5.07 \times 10^{-4} \text{ m}^2$ ,  $S_B = 4.95 \times 10^{-5} \text{ m}^2$  and  $S_D = 5.07 \times 10^{-4} \text{ m}^2$  are the surface area of magnets B, A and D, respectively,  $M = B_r / \mu$  is the magnetization of magnets A, B and D, where  $B_r$  is the magnetic residual flux density, their values are listed in Table B.1, and  $\mu = 4\pi \times 10^{-7} \text{H/m}$  is the vacuum permeability.

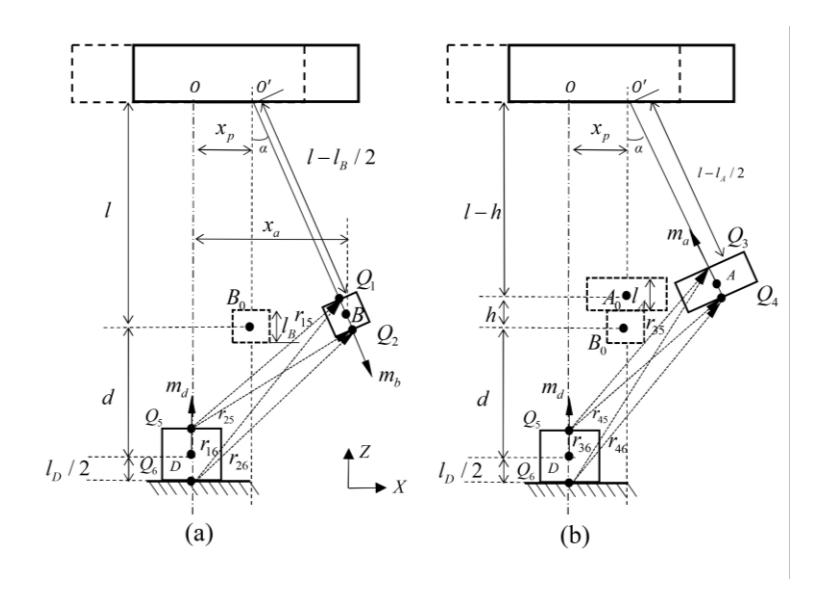


Figure B.3 Illustration of the equivalent magnetic 2-point dipole model:(a) magnets B and D; (b) magnets A and D.

The magnetic force between magnet B and magnet D is considered first. Based on the Boit-Savart law, the magnetic force exerted by magnet B on magnet D is the combination of the magnetic force exerted from  $Q_1$  and  $Q_2$  to  $Q_5$  and  $Q_6$ , which is given in the following equation:

$$f_{DB} = Q_1 \frac{\mu_0}{4\pi} \left( Q_5 \frac{\mathbf{r}_{15}}{|\mathbf{r}_{15}|^3} + Q_6 \frac{\mathbf{r}_{16}}{|\mathbf{r}_{16}|^3} \right) + Q_2 \frac{\mu_0}{4\pi} \left( Q_5 \frac{\mathbf{r}_{25}}{|\mathbf{r}_{25}|^3} + Q_6 \frac{\mathbf{r}_{26}}{|\mathbf{r}_{26}|^3} \right)$$
(B.5)

where  $r_{15}$ ,  $r_{16}$ ,  $r_{25}$  and  $r_{26}$  can be derived from the are the position vectors of  $Q_1$ ,  $Q_2$ ,  $Q_5$  and  $Q_6$ , respectively, According to (A.4), to obtain the total restoring force, only the  $f_{DBx}$  is considered, which can be expressed as follows [17]:

$$f_{DBx} = -\frac{\mu_0}{4\pi} \left[ Q_1 \left( x_a - \frac{l_B}{2} \sin \alpha \right) \left( \frac{Q_5}{\gamma_1} + \frac{Q_6}{\gamma_2} \right) + Q_2 \left( x_a + \frac{l_B}{2} \sin \alpha \right) \left( \frac{Q_5}{\gamma_3} + \frac{Q_6}{\gamma_3} \right) \right]$$
(B.6)

where the  $\sin \alpha = u/l$ , and the expression  $\gamma_1$ ,  $\gamma_2$ ,  $\gamma_3$  and  $\gamma_4$  can be found in [17]. Further, the magnetic force between magnets A and D in the x-direction can also be obtained as:

$$f_{DAx} = -\frac{\mu_0}{4\pi} \left[ Q_3 \left( x_a - h \sin \alpha - \frac{l_A}{2} \right) \left( \frac{Q_5}{\gamma_5} + \frac{Q_6}{\gamma_6} \right) + Q_4 \left( x_a - h \sin \alpha + \frac{l_A}{2} \right) \left( \frac{Q_5}{\gamma_7} + \frac{Q_6}{\gamma_8} \right) \right]$$
(B.7)

where  $\gamma_5$ ,  $\gamma_6$ ,  $\gamma_7$  and  $\gamma_8$  are also defined in [17], By substituting (5.11) and (5.12) into (A.4), the total restoring force can be obtained. All the parameters' values are listed in Table B.1. Note that the values of the surface charges are obtained by an experimental identification method given in [18]. For the sake of comparison, two configurations of the NESs are considered in this study: case I: d=0.0487 m, h=0.01 m; case II d=0.0507 m, h=0.005 m. And the 3D plot of  $f_n$  versus u and  $x_p$  for both cases are shown in Figure B.4.

Table B.1 Paramters value of the grounded NES.

symbol	Parameters		
	Parameter name	value	
$Q_3$	Total charges of the top surfaces of magnet A/C	642.36	
$Q_4$	Total charges of the bottom surfaces of magnet A/C	903.53	
$Q_1$	Total charges of the top surfaces of magnet B	0	
$Q_2$	Total charges of the bottom surfaces of magnet B	35.62	
$Q_5$	Total charges of the top surfaces of magnet D	353.39	
$Q_6$	Total charges of the bottom surfaces of magnet D	577.56	
$k_a$	Stiffness of the cantilever beam (N/m)	90.00	
1	Length of the cantilever beam (m)	0.12	
$k_p$	Stiffness of the primary system (N/m)	1924.40	
$m_p$	Mass of the primary system(kg)	0.45	
$m_a$	Mass of the NES (kg)	0.09	
$c_p$	Damping coefficient of the primary system (Ns/m)	0.58	
$c_a$	Daping coefficient of the NES (Ns/m)	0.0342	

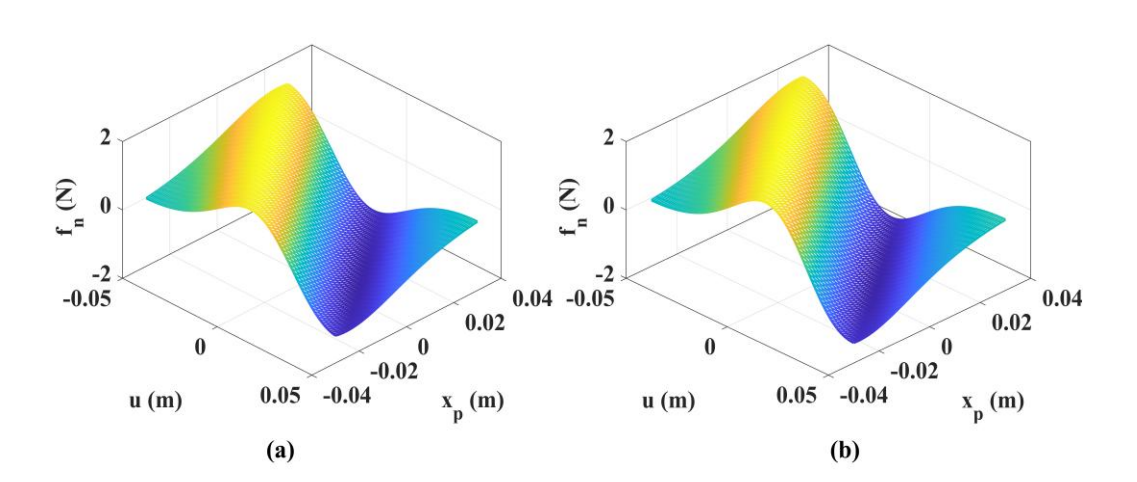


Figure B.4 3D plot of the nonlinear restoring force surface of the: (a) case I; (b) case II.

### B.3 Fundamental of the linear regression method

The complex expression of Eqs. (B.6) and (B.7) makes it impossible to apply analytical methods, such as the harmonic balance method. A common approach to deal with this issue is to approximate the nonlinear restoring force by using a high order polynomial. Techniques such as the force surface method [19] or direct force measurement [20] can be employed to identify the actual nonlinear restoring force, after which the polynomial curve-fitting can be applied. However, for the system under consideration, the nonlinear restoring force is influenced by both  $x_p$  and u, which makes the traditional methods invalid. As proposed in [21], the polynomial approximation for an unknown nonlinear restoring force can be achieved through a linear regression by using the time series of the free responses, which provides a solution to the current issue. The following develops a suitable identification procedure.

As this study focuses on the identification of  $f_n$  from free responses, (B.2) can be reformulated as:

$$g(\ddot{x}_a, \dot{u}, u) = -(m_a \ddot{x}_a + c_a \dot{u} + k_a u) = f_n$$
 (B.8)

by assuming that  $m_a$ ,  $c_a$ ,  $k_a$  are available. After collecting the time series of the free responses  $x_p$  and  $x_a$ , the velocity  $\dot{x}_a$  and  $\dot{x}_p$ , and acceleration  $\ddot{x}_a$  and  $\ddot{x}_p$  can be obtained by using numerical differentiation. Then, the known function can be written as a column vector form:

$$G = \begin{bmatrix} g(\ddot{x}_{a}(t_{1}), \dot{u}(t_{1}), u(t_{1})) \\ g(\ddot{x}_{a}(t_{2}), \dot{u}(t_{2}), u(t_{2})) \\ \vdots \\ g(\ddot{x}_{a}(t_{q}), \dot{u}(t_{q}), u(t_{q})) \end{bmatrix}$$
(B.9)

where q is the length of the time series. The right-hand term in (8) is the unknown nonlinear restoring force  $f_n$ , which can be approximated by a polynomial that can be represented as:

$$f_n = \mathbf{\Theta} \boldsymbol{\xi} \tag{B.10}$$

where  $\Theta$  is the candidate functions matrix, and  $\xi$  is the coefficient vector. First, we assume that the candidate functions are related to only the variable u, and the maximum order of the polynomial is n. Thus, the candidate function matrix and coefficient vector can be given as:

$$\boldsymbol{\Theta}(u) = \begin{bmatrix} 1, u(t_1), u^2(t_1), u^3(t_1), \dots, u^n(t_1) \\ 1, u(t_2), u^2(t_3), u^3(t_4), \dots, u^n(t_5) \\ \vdots \\ 1, u(t_q), u^2(t_q), u^3(t_q), \dots, u^n(t_q) \end{bmatrix}$$
(B.11)

and

$$\boldsymbol{\xi} = [\xi_1, \xi_2, \xi_3, \xi_4, \dots, \xi_{n+1}]^{\mathrm{T}}$$
(B.12)

respectively. The coefficient vector can be obtained by solving the following equation:

$$\boldsymbol{\xi} = \boldsymbol{\Theta}^{+} \boldsymbol{G} \tag{B.13}$$

where '+' represents the pseudo inverse of the matrix. After obtaining the coefficient vector, the approximate nonlinear restoring force model can be found.

## B.4 Application of the linear regression method

In this study, the time series of the free responses of the system are obtained through a numerical simulation. By solving Eqs. (B.1) and (B.2) with the initial condition of ( $x_p$ ,  $\dot{x}_p$ ,  $x_a$ ,  $\dot{x}_a$ )=(-0.02, 0, -0.02, 0) for the system of case I, in the period of 20 s using the MATLAB ODE45 solver, the free responses of the primary system and NES can be obtained. Then, the known function matrix **G** is calculated based on the collected data. By setting the maximum order number n=7, the candidate function matrix  $\Theta$  can be formulated, the coefficients vector can be obtained by solving Eq. (B.13).

To verify the accuracy of the estimated system, two sets of simulations are conducted. The first one is by using the actual nonlinear restoring force model shown in Eq. (B.3), and the second one is using the estimated nonlinear restoring force model, with the initial conditions of  $(x_p, \dot{x}_p, x_a, \dot{x}_a) = (-0.01, 0, -0.017, 0)$  for both two systems in the period of 20 s. Note that the initial conditions used for verification are different from those used to generate the responses for identification. The two simulation results are compared in Figure B.5. Additionally, to better estimate the accuracy of the prediction, The error of the estimated  $x_p$  and  $x_a$  can be derived by the following equations:

$$\varepsilon_{p} = \frac{\left\| \boldsymbol{x}_{p} - \boldsymbol{x}_{p}' \right\|_{2}}{\left\| \boldsymbol{x}_{p}' \right\|_{2}}, \varepsilon_{a} = \frac{\left\| \boldsymbol{x}_{a} - \boldsymbol{x}_{a}' \right\|_{2}}{\left\| \boldsymbol{x}_{a}' \right\|_{2}}$$
(B.14)

where  $x'_p, x'_a, x_p$  and  $x_a$  are the time series vectors of  $x_p$  and  $x_a$  of the real system and estimated system, respectively, and  $\|\mathbf{e}\|_2$  denote the second norm of the vector. As shown in Figure B.5, the estimated force model basically failed to predict the time responses of the real system, and the errors  $\varepsilon_p = 0.378$ ,  $\varepsilon_a = 1.02$  are notably big, indicating that using a polynomial of a single variable to approximate the restoring force cannot result in an acceptable approximation.

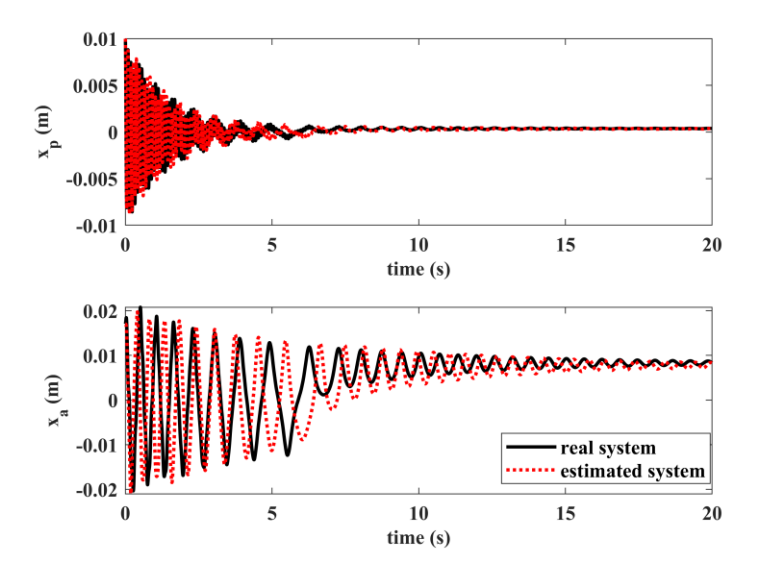


Figure B.5 Free responses of the Case I system with the real force model and the

estimated force model by using the single variable in the candidate functions matrix.

To improve the accuracy of identification, both  $x_p$  and u should be considered when building the candidate function matrix. One convenient choice for the candidate functions is a polynomial of the products of  $x_p$  and u with different orders. As shown in Figure B.4, when fixing the value of  $x_p$ , the changing of u will significantly influence the shape of  $f_n$ . However, varying  $x_p$  does not alter the shape of the curve significantly, but mainly results in a shift of the curve. This implies that the order of  $x_p$  should be much lower than that of u. Assuming the maximum orders of u and  $x_p$  are n and m (n > m), respectively. Then, the modified candidate function matrix can be written in the following form:

$$\boldsymbol{\Theta}(u, x_p) = \left[\boldsymbol{\Theta}_1, \boldsymbol{\Theta}_2, \boldsymbol{\Theta}_3, \dots, \boldsymbol{\Theta}_{n+1}\right]$$
 (B.15)

where the matrix's elements  $\theta_i$  (i = 1,2,3...n + 1) are given as:

$$\boldsymbol{\Theta}_{i}(u,x_{p}) = \begin{bmatrix} u^{i-1}(t_{1}), u^{i-1}(t_{1})x_{p}(t_{1}), & \cdots, u^{i-1}(t_{1})x_{p}^{m}(t_{1}) \\ u^{i-1}(t_{2}), u^{i-1}(t_{2})x_{p}(t_{2}), & \cdots, u^{i-1}(t_{2})x_{p}^{m}(t_{2}) \\ & \vdots \\ u^{i-1}(t_{q}), u^{i-1}(t_{q})x_{p}(t_{q}), & \cdots, u^{i-1}(t_{q})x_{p}^{m}(t_{q}) \end{bmatrix}$$
(B.16)

and the coefficient vector becomes:

$$\boldsymbol{\xi} = [\xi_1, \xi_2, \xi_3, \xi_4, \dots, \xi_{(n+1)(m+1)}]^{\mathrm{T}}$$
(B.17)

By setting the order numbers n = 7, m = 5 in the modified  $\boldsymbol{\theta}$  and following the same data training procedure, the new coefficient vector can be obtained, and the verification results are shown in Figure B.6. It can be seen that the identified model is capable of accurately predicting the time responses of the actual system, and the errors  $\varepsilon_p = 0.0327$ ,  $\varepsilon_a = 0.105$  are reduced to an acceptable level.

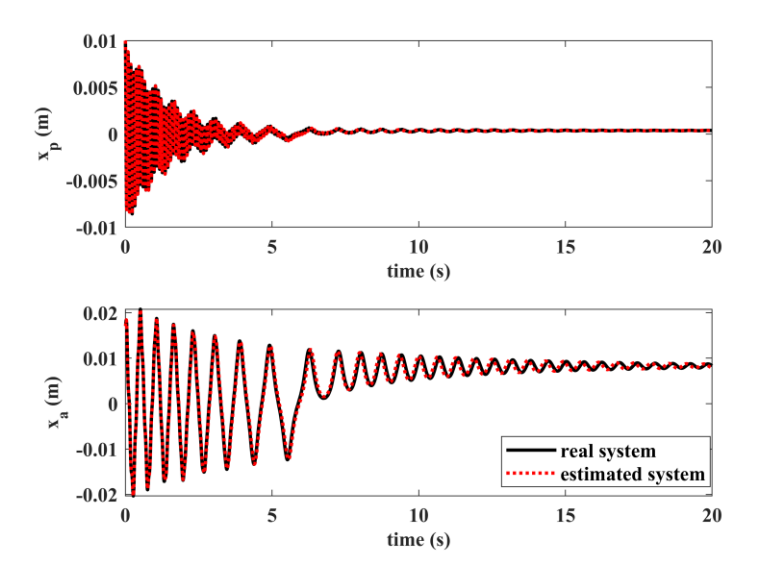


Figure B.6 Free responses of the Case I system with the real force model and the estimated force model by using a modified candidate functions matrix.

The identification of the nonlinear restoring force of case II follows the same procedure as mentioned in the last section, by using the modified candidate function matrix, and the initial conditions ( $x_p$ ,  $\dot{x}_p$ ,  $x_a$ ,  $\dot{x}_a$ )=(-0.035, 0, -0.035, 0) to obtain the training data, then verified with the initial condition of ( $x_p$ ,  $\dot{x}_p$ ,  $x_a$ ,  $\dot{x}_a$ )=(-0.015, 0, -0.02, 0). As shown in Figure B.7, there is a huge difference between the free responses of the estimated system and those of the real system, and the errors  $\varepsilon_p = 0.739$ ,  $\varepsilon_a = 1.94$  are unacceptably large. This may be caused by insufficience of the current training data set. To improve the identification accuracy, the training data much be sufficiently richin the dynamics of case II.

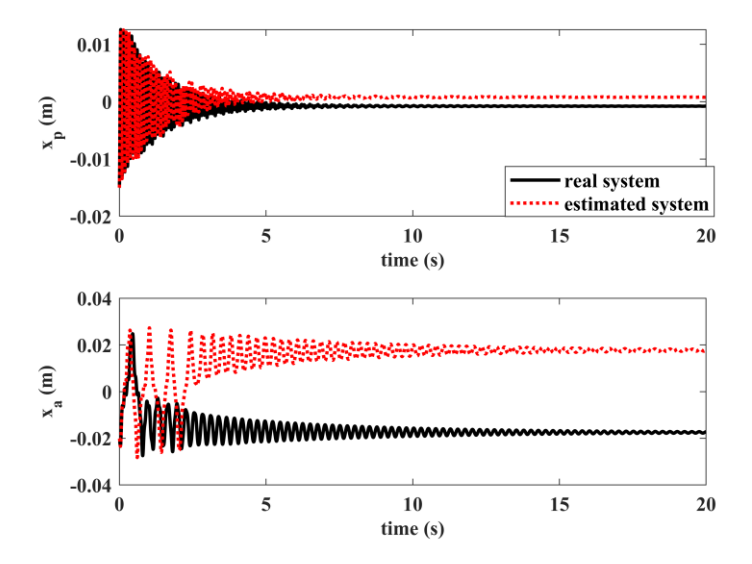


Figure B.7 Free responses of the Case II system with the real force model and the estimated force model trained by one data set.

Based on the identification method proposed in [22], multiple training data sets are employed to overcome such a problem. To achieve that, multiple sets of simulations with different initial conditions are conducted and collect the multiple sets of time series of a free response to assemble of the new known function matrix and candidate functions matrix as:

$$G = \begin{bmatrix} g(\ddot{x}_{a}(t_{11}), \dot{u}(t_{11}), u(t_{11})) \\ \vdots \\ g(\ddot{x}_{a}(t_{1q}), \dot{u}(t_{1q}), u(t_{1q})) \\ \vdots \\ g(\ddot{x}_{a}(t_{r1}), \dot{u}(t_{r1}), u(t_{r1})) \\ \vdots \\ g(\ddot{x}_{a}(t_{rq}), \dot{u}(t_{rq}), u(t_{rq})) \end{bmatrix}$$
(B.18)

and

$$\boldsymbol{\Theta}_{i}(u,x_{p}) = \begin{bmatrix} u^{i-1}(t_{11}), u^{i-1}(t_{11})x_{p}(t_{11}), & \cdots, & u^{i-1}(t_{11})x_{p}^{m}(t_{11}) \\ \vdots & & & \\ u^{i-1}(t_{1q}), u^{i-1}(t_{1q})x_{p}(t_{1q}), & \cdots, & u^{i-1}(t_{1q})x_{p}^{m}(t_{1q}) \\ \vdots & & & \\ u^{i-1}(t_{r1}), u^{i-1}(t_{r1})x_{p}(t_{r1}), & \cdots, & u^{i-1}(t_{r1})x_{p}^{m}(t_{r1}) \\ \vdots & & & \\ u^{i-1}(t_{rq}), u^{i-1}(t_{rq})x_{p}(t_{rq}), & \cdots, & u^{i-1}(t_{rq})x_{p}^{m}(t_{rq}) \end{bmatrix}$$
(B.19)

respectively, where r is the number of the training data set used in the identification. In this study, three different sets of training data are considered, namely, r=1, r=2 and r=3. The first training data is obtained by the simulation with the initial condition of  $(x_p, \dot{x}_p, x_a, \dot{x}_a) = (-0.035, 0, -0.035, 0)$ , the second one with  $(x_p, \dot{x}_p, x_a, \dot{x}_a) = (-0.02, 0, -0.015, 0)$ , and the third one with  $(x_p, \dot{x}_p, x_a, \dot{x}_a) = (-0.01, 0, -0.01, 0)$ . The verification results of the estimate system trained with the first two data sets and three data sets are shown in Figures B.8 and B.9, respectively. and the errors for the three training conditions are collected in the bar chart shown in Figure B.10. It clearly shows that using more training data leads to better prediction results.

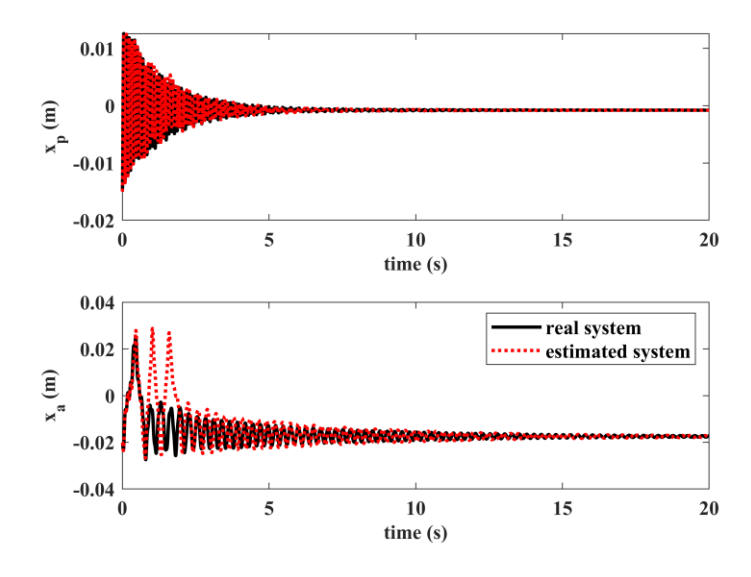


Figure B.8 Free responses of the Case II with the real force model and the estimated force model trained by two data sets.

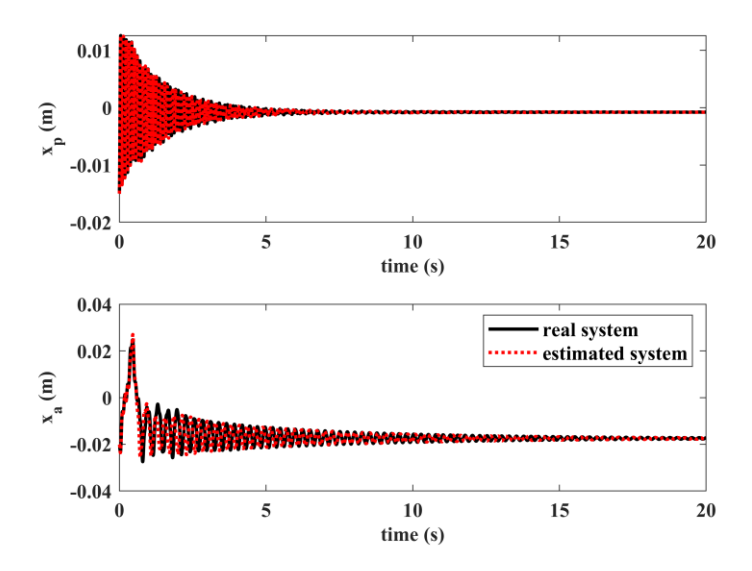


Figure B.9 Free responses of the Case II with the real force model and the estimated force model trained by three data sets.

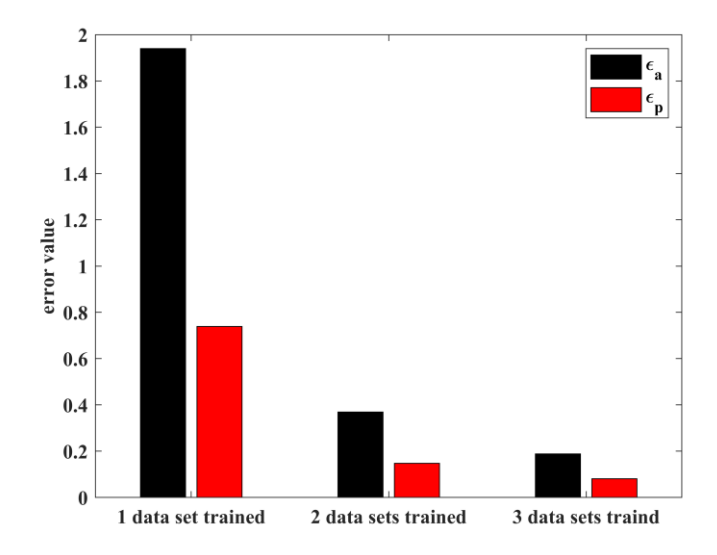


Figure B.10 The error of the prediction of the Case II system with identified force model trained by three different sets of data.

### **B.5** Conclusions

In this study, a regression-based identification approach has been proposed to find the polynomial approximation of the nonlinear restoring force of a grounded MS-NES. Firstly, the apparatus is introduced briefly, then the dynamic model of the system is derived from the lumped parameter model, and the magnetic force model is established based on an equivalent magnetic 2-point dipole approach. Two bis-table configurations have been chosen to evaluate the approach.

For Case I, the results show that considering a single variable u in the candidate function matrix is not sufficient to predict the free responses of the real system. To improve the accuracy, two variables u and  $x_p$  are considered when building the candidate function matrix. By considering the influence of the two variables on the shape of the nonlinear restoring force, the maximum order number of  $x_p$  is chosen much lower than that of u. And the validation results show that the accuracy of the identified model has been significantly improved by introducing the modified candidate function matrix. As for Case II, even by using the modified candidate function matrix, the predictions remain unsatisfactory. The solution is integrating multiple training data sets which encompass a broader range of system behaviours, and the results show that more comprehensive training data sets lead to a more robust and accurate identified model.

### References

- [1] Z. Yang, S. Zhou, J. Zu, and D. Inman, "High-performance piezoelectric energy harvesters and their applications," *Joule*, vol. 2, no. 4, pp. 642-697, 2018, doi: 10.1016/j.joule.2018.03.011.
- [2] S. C. Stanton, C. C. McGehee, and B. P. Mann, "Reversible hysteresis for broadband magnetopiezoelastic energy harvesting," *Applied Physics Letters*, vol. 95, no. 17, 2009, doi: 10.1063/1.3253710.
- [3] A. Erturk, J. Hoffmann, and D. J. Inman, "A piezomagnetoelastic structure for broadband vibration energy harvesting," *Applied Physics Letters*, vol. 94, no. 25, 2009, doi: 10.1063/1.3159815.
- [4] J. Cao, S. Zhou, W. Wang, and J. Lin, "Influence of potential well depth on

- nonlinear tristable energy harvesting," *Applied Physics Letters*, vol. 106, no. 17, p. 173903, 2015, doi: 10.1063/1.4919532.
- [5] L. Haitao, Q. Weiyang, L. Chunbo, D. Wangzheng, and Z. Zhiyong, "Dynamics and coherence resonance of tri-stable energy harvesting system," *Smart Materials and Structures*, vol. 25, no. 1, p. 015001, 2016, doi: 10.1088/0964-1726/25/1/015001.
- [6] A. S. Saeed, M. A. Al-Shudeifat, and A. F. Vakakis, "Rotary-oscillatory nonlinear energy sink of robust performance," *International Journal of Non-Linear Mechanics*, vol. 117, 2019, doi: 10.1016/j.ijnonlinmec.2019.103249.
- [7] Z. Zhang, Z.-Q. Lu, H. Ding, and L.-Q. Chen, "An inertial nonlinear energy sink," *Journal of Sound and Vibration*, vol. 450, pp. 199-213, 2019/06/23/ 2019, doi: 10.1016/j.jsv.2019.03.014.
- [8] G. Habib and F. Romeo, "The tuned bi-stable nonlinear energy sink," *Nonlinear Dynamics*, vol. 89, no. 1, pp. 179-196, 2017, doi: 10.1007/s11071-017-3444-y.
- [9] D. Qiu, T. Li, S. Seguy, and M. Paredes, "Efficient targeted energy transfer of bistable nonlinear energy sink: application to optimal design," *Nonlinear Dynamics*, vol. 92, no. 2, pp. 443-461, 2018, doi: 10.1007/s11071-018-4067-7.
- [10] H. Yao, Y. Cao, Y. Wang, and B. Wen, "A tri-stable nonlinear energy sink with piecewise stiffness," *Journal of Sound and Vibration*, vol. 463, 2019, doi: 10.1016/j.jsv.2019.114971.
- [11] X. Kang *et al.*, "Design, optimization, and application of nonlinear energy sink in energy harvesting device," *International Journal of Energy Research*, vol. 2024, pp. 1-33, 2024, doi: 10.1155/2024/2811428.
- [12] Y. Zhang, L. Tang, and K. Liu, "Piezoelectric energy harvesting with a nonlinear energy sink," *Journal of Intelligent Material Systems and Structures*, vol. 28, no. 3, pp. 307-322, 2016, doi: 10.1177/1045389x16642301.
- [13] M. Rezaei, R. Talebitooti, and W.-H. Liao, "Exploiting bi-stable magneto-piezoelastic absorber for simultaneous energy harvesting and vibration mitigation," *International Journal of Mechanical Sciences*, vol. 207, p. 106618, 2021/10/01/2021, doi: 10.1016/j.ijmecsci.2021.106618.
- [14] S. F. Masri and T. K. Caughey, "A nonparametric identification technique for nonlinear dynamic problems," *Journal of Applied Mechanics*, vol. 46, no. 2, pp. 433-447, 1979, doi: 10.1115/1.3424568.
- [15] Y. Zhang, J. Duan, Y. Jin, and Y. Li, "Discovering governing equation from data for multi-stable energy harvester under white noise," *Nonlinear Dynamics*, vol. 106, no. 4, pp. 2829-2840, 2021, doi: 10.1007/s11071-021-06960-9.
- [16] G. Wang, H. Wu, W.-H. Liao, S. Cui, Z. Zhao, and J. Tan, "A modified magnetic force model and experimental validation of a tri-stable piezoelectric energy harvester," *Journal of Intelligent Material Systems and Structures*, vol. 31, no. 7,

- pp. 967-979, 2020.
- [17] H. Li, K. Liu, J. Deng, and B. Li, "Validation and optimization of two models for the magnetic restoring forces using a multi-stable piezoelectric energy harvester," *Journal of Intelligent Material Systems and Structures*, vol. 34, no. 14, pp. 1688-1701, 2023, doi: 10.1177/1045389x221151064.
- [18] H. Li, "A tunable multi-stable piezoelectric vibration energy harvester," Mechanical engineering, Lakehead University, published, 2021. [Online]. Available: https://knowledgecommons.lakeheadu.ca/handle/2453/4966
- [19] K. Worden, "Data processing and experiment design for the restoring force surface method, part I: integration and differentiation of measured time data," *Mechanical Systems and Signal Processing*, vol. 4, no. 4, pp. 295-319, 1990, doi: 10.1016/0888-3270(90)90010-I.
- [20] S. Zhou, J. Cao, D. J. Inman, J. Lin, S. Liu, and Z. Wang, "Broadband tristable energy harvester: Modeling and experiment verification," *Applied Energy*, vol. 133, pp. 33-39, 2014, doi: 10.1016/j.apenergy.2014.07.077.
- [21] P. Wulff, L. Lentz, and U. von Wagner, "Determination of the polynomial restoring force of a one DoF bistable Duffing oscillator by linear regression," *Acta Mechanica*, pp. 1-17, 2023, doi: 10.1007/s00707-022-03462-6.
- [22] J. Qian, X. Sun, and J. Xu, "A data-driven reconstruction method for dynamic systems with multistable property," *Nonlinear Dynamics*, vol. 111, no. 5, pp. 4517-4541, 2022, doi: 10.1007/s11071-022-08082-2.

# Appendix C. Design and Evaluation of Three Variant Nonlinear Energy Sinks

### **Abstract**

The traditional nonlinear energy sink (NES) consists of an essentially nonlinear spring (ENS). In this study, three variant NESs without an ENS are considered, namely mono-stable NES, bi-stable NES, and tri-stable NES. A method is proposed to design these variant NESs for the dual purpose of vibration suppression (VS) and energy harvesting (EH). The proposed method can ensure that the designed variant NES closely emulates the behaviors of a true NES. The design starts with defining a NES with a desired ENS using the concept of equivalent stiffness. Then, by forcing the restoring force of the variant NES at the maximum displacement equal to that of the desired NES, the key parameters of the variant NES are determined. A numerical simulation is conducted to compare the variant NESs with the desired NES in terms of VS under transient responses. The VS performances are evaluated by the targeted energy transfer, the wavelet transform spectra, and the frequency-energy plots. To investigate the trade-off issue, two objective functions are defined to measure VS and EH performances, respectively. Then a two-objective optimization is conducted for the case of the NES equipped with a piezoelectric energy harvester and the case of the NES equipped with an electromagnetic energy harvester. The Pareto fronts are generated for all four NESs to reveal the best NES in terms of VS or EH.